Finanziato dall'Unione Europea
NextGenerationEU

UNIVERSITÀ DEGLI STUDI DI BRESCIA

DIPARTIMENTO DI INGEGNERIA MECCANICA E INDUSTRIALE

DOTTORATO DI RICERCA IN
TRANSIZIONE ENERGETICA E SISTEMI PRODUTTIVI SOSTENIBILI

settore scientifico disciplinare
CHEM-06/A

CICLO
XXXVIII

TITOLO TESI

Innovative electrolyte materials used to build large batteries

"Case study of Titanium–Iron Flow Batteries Using Sulfuric Acid and EDTA as Complexing Agents"

NOME DELLA DOTTORANDA

Maria Viviana Scopelliti

SUPERVISORE
Laura Borgese

"Whatever our souls are made of, his and mine are the same."

— Emily Brontë, Wuthering Heights (1847)

Ringraziamenti

Sono trascorsi tre anni da quel giorno in cui, dalla mia amata Sicilia, ho scelto di partire per intraprendere un nuovo percorso che si è trasformato nel mio Dottorato. Fin dall'inizio è stato un cammino impegnativo: nuove conoscenze da acquisire, ambiti sconosciuti da esplorare, la necessità di rimettermi in gioco e di studiare materie di cui ignoravo persino l'esistenza.

Lontana dalla mia famiglia e dalla mia terra, in un luogo tutto da scoprire, ho affrontato difficoltà, dubbi e momenti di smarrimento. Eppure, proprio quelle incertezze hanno rafforzato il mio essere e mi hanno ricondotta alla mia più grande passione: la ricerca, lo studio, la curiosità verso ciò che ancora non conosco.

Ho compreso che la ricerca non è soltanto un lavoro, ma un modo di guardare il mondo: con domande aperte, con il coraggio di non avere subito risposte, con la pazienza di costruirle nel tempo. Questo dottorato non è stato semplicemente un titolo da conseguire, ma un viaggio interiore che mi ha insegnato che la vera conquista non è arrivare, ma diventare.

Per questo, un sentito ringraziamento va alla mia professoressa e tutor, ***Laura Borgese***, che mi ha sostenuta e mi ha dato spazio per dare forma alle mie idee. Il suo supporto e la fiducia mi hanno permesso di affrontare questo percorso con maggiore consapevolezza e responsabilità, incoraggiandomi a perseverare anche nei momenti più complessi.

Ringrazio la professoressa ***Laura Eleonora Depero***, che in una giornata di inizio agosto dell'ormai lontano 2022, ha creduto in me, offrendomi l'opportunità di intraprendere questo percorso di dottorato.

Un grazie sincero ad ***Antonella Cornelio, Mattia Massa, Esenina Stroka e a tutti i colleghi di dottorato***. In questi anni ho trovato non solo colleghi, ma amici. Sono stati il mio sostegno nei momenti difficili e la mia gioia in quelli più sereni. Sono stati la mia valvola di sfogo e mi hanno aiutato a vedere il bicchiere sempre mezzo pieno. Con loro ho imparato che condividere rende ogni fatica più leggera e ogni successo più grande.

Ringrazio ***AB Impianti***, che mi ha permesso di fare questo dottorato e mi ha proposto il tema delle Redox Flow Batteries. Non avevo mai studiato elettrochimica, ma ho accettato la sfida e ho scoperto un mondo affascinante, capace di appassionarmi oltre ogni aspettativa.

Un grazie speciale al ***CIC energiGUNE***, dove ho trascorso otto mesi. Ricordo il primo giorno: la nuova lingua, le abitudini diverse, la nostalgia di casa. Eppure, proprio lì ho incontrato persone straordinarie che mi hanno accolta e sostenuta. Non dimenticherò mai l'aiuto di ***Asier, Amaia e Seda***, sempre presenti con disponibilità e generosità. Sono stati amici, colleghi e il mio supporto.

E poi ***Fengjing Jiang***, mio supervisor e guida in questo percorso. Mi ha trasmesso la vera passione per lo studio delle batterie, contribuendo in modo decisivo alla mia formazione scientifica. Mi ha insegnato il rigore, la dedizione e la perseveranza. Anche quando appariva severo, non ha mai smesso di credere in me e di spronarmi a dare il meglio. Di questo gli sarò sempre grata e porterò sempre con me i suoi insegnamenti.

Il grazie più grande, però, va ai miei genitori. ***A mio Padre e a mia Madre***, che mi hanno accompagnata fin da bambina, condividendo le mie scelte anche quando non erano semplici da comprendere. Mi hanno lasciata libera di sbagliare, di cadere e di rialzarmi, insegnandomi a essere forte e a diventare la donna che desideravo essere. Sono stati, e saranno sempre, il mio punto fermo, la mia roccia e il mio porto sicuro

E poi ci sei tu, amore mio, ***Daniele La Corte***. A te, che sei stato il mio porto nelle tempeste e la mia quiete dopo ogni battaglia, va il mio grazie più profondo, e a te dedico questa tesi. Se questo cammino mi ha resa più forte, è perché al mio fianco ho avuto te, capace di sostenermi quando vacillavo e di credere in me oltre ogni incertezza. Se la ricerca è stata la mia sfida, tu sei stato la mia certezza. Con la tua presenza, ogni ostacolo è diventato affrontabile e ogni traguardo condiviso. E se oggi questo traguardo porta il mio nome, appartiene anche a te, che hai camminato accanto a me, mano nella mano, sostenendomi in silenzio lungo questo percorso, restando al mio fianco passo dopo passo, giorno dopo giorno.

Oggi si chiude un capitolo importante della mia vita. Non è un punto di arrivo, ma una soglia: oltre di essa si apre il futuro, che affronterò con la stessa passione che mi ha guidata fin qui. Perché la ricerca non termina con una tesi, ma continua a vivere nella curiosità, nel dubbio e nel desiderio costante di andare oltre.

Non è una fine. È un nuovo inizio.

"*La cosa più bella che possiamo provare è il mistero. È la fonte di ogni vera arte e di ogni vera scienza*."

Cit. Albert Einstein

Acknowledgements

Three years have passed since the day I left my beloved Sicily to embark on a new journey that eventually became my PhD. From the very beginning, it was a demanding path: new knowledge to acquire, unfamiliar fields to explore, and the need to challenge myself by studying subjects I had never even imagined before. Far from my family and my homeland, in a place entirely new to discover, I faced difficulties, doubts, and moments of uncertainty. Yet it was precisely those challenges that strengthened me and led me back to my greatest passion: research, study, and the curiosity for what I still do not know. I came to understand that research is not merely a profession, but a way of looking at the world: with open questions, with the courage not to have immediate answers, and with the patience to build them over time. This PhD has not simply been a degree to obtain, but an inner journey that taught me that true achievement is not about arriving, but about becoming.

For this reason, I would like to express my sincere gratitude to my professor and supervisor, ***Laura Borgese***, who supported me and gave me the space to give shape to my ideas. Her guidance and trust allowed me to approach this path with greater awareness and responsibility, encouraging me to persevere even in the most challenging moments.

I would also like to thank ***Professor Laura Eleonora Depero***, who, on in early August back in 2022, believed in me and offered me the opportunity to undertake this PhD journey.

My heartfelt thanks go to ***Antonella Cornelio, Mattia Massa, Esenina Stroka, and all my PhD colleagues***. Over these years, I have found not only colleagues, but friends. They have been my support during difficult times and my joy during the happiest ones. They were my outlet and helped me always see the glass as half full. With them, I learned that sharing makes every hardship lighter and every success greater.

I am grateful to ***AB Impianti***, who made this PhD possible and introduced me to the topic of Redox Flow Batteries. I had never studied electrochemistry before, but I embraced the challenge and discovered a fascinating world that captured my interest beyond all expectations.

A special thanks goes to ***CIC energiGUNE***, where I spent eight months. I still remember the first day: a new language, different habits, and the longing for home. Yet it was there that I met extraordinary people who welcomed and supported me. I will never forget the help of ***Asier, Amaia, and Seda***, always present with generosity and kindness. They were friends, colleagues, and a constant source of support.

And then Fengjing Jiang, my supervisor and guide throughout this journey. He transmitted to me a true passion for battery research and contributed decisively to my scientific growth. He taught me rigor, dedication, and perseverance. Even when he appeared strict, he never stopped believing in me and pushing me to give my best. For this, I will always be grateful and will carry his teachings with me.

The greatest thanks, however, go to my parents. To my ***Father and my Mother***, who have supported me since childhood, sharing my choices even when they were not easy to understand. They allowed me the freedom to make mistakes, to fall and rise again, teaching me to be strong and to become the woman I wished to be. They have been, and always will be, my foundation, my rock, and my safe harbor.

And then there is you, my love, ***Daniele La Corte***. To you, who have been my harbor in the storm and my peace after every battle, goes my deepest gratitude, and to you I dedicate this thesis. If this journey has made me stronger, it is because I had you by my side, supporting me when I faltered and believing in me beyond every doubt. If research has been my challenge, you have been my certainty. With your presence, every obstacle became manageable and every achievement shared. And if today this milestone bears my name, it also belongs to you, who have walked beside me, hand in hand, supporting me silently throughout this journey, staying by my side step by step, day after day.

Today an important chapter of my life comes to an end. It is not a final destination, but a threshold: beyond it lies the future, which I will face with the same passion that has guided me this far. Because research does not end with a thesis; it continues to live in curiosity, in doubt, and in the constant desire to go beyond.

It is not an end. It is a new beginning.

"*The most beautiful thing we can experience is the mysterious. It is the source of all true art and science*."

— **Albert Einstein**

Abstract

La crescente integrazione delle fonti di energia rinnovabile nei moderni sistemi elettrici richiede lo sviluppo di tecnologie di accumulo energetico efficienti, scalabili e sostenibili, in grado di compensare l'intrinseca intermittenza della generazione da fonte fotovoltaica ed eolica. Tra le soluzioni disponibili, le batterie a flusso redox (RFB) rappresentano una tecnologia particolarmente promettente per l'accumulo stazionario su larga scala, grazie alla possibilità di disaccoppiare potenza ed energia, alla lunga vita ciclica e all'elevato livello di sicurezza operativa. Tuttavia, i sistemi commerciali più maturi, come quelli basati sul vanadio, sono limitati dall'elevato costo e dalla disponibilità ridotta del materiale attivo.

In questo contesto, la presente tesi indaga sistemi elettrolitici alternativi basati sulle coppie redox Ti(IV)/Ti(III) e Fe(III)/Fe(II), costituiti da metalli abbondanti in natura, a basso costo e ambientalmente sostenibili. Lo studio è stato condotto attraverso un approccio comparativo, analizzando il comportamento del sistema Ti–Fe in due differenti ambienti: un mezzo fortemente acido a base di acido solforico e un sistema complessato basato su specie Ti–EDTA e Fe–EDTA, con l'obiettivo di ridurre la corrosività dell'elettrolita e migliorarne la stabilità chimica. La stabilità e la solubilità dei complessi Ti–EDTA e Fe–EDTA sono state investigate in funzione del pH e della concentrazione dell'elettrolita di supporto (KCl), individuando condizioni operative ottimali in grado di mantenere le specie in soluzione e garantire una risposta elettrochimica riproducibile. Le proprietà diffusionali e cinetiche sono state valutate mediante voltammetria ciclica, confermando la reversibilità delle coppie redox Ti(IV)/Ti(III) e Fe(III)/Fe(II) nell'ambiente complessato. I test di cella hanno evidenziato che il sistema Ti–Fe in acido solforico raggiunge elevate efficienze elettrochimiche, mentre il sistema complessato Ti–EDTA/Fe–EDTA mostra una migliore stabilità ciclica e una maggiore compatibilità operativa. Il confronto tra le due formulazioni mette in luce vantaggi e limitazioni di ciascun approccio, fornendo indicazioni utili per future ottimizzazioni del sistema.

Nel complesso, sebbene siano ancora necessari ulteriori miglioramenti, i sistemi Ti–EDTA e Fe–EDTA possono rappresentare un'alternativa più sicura e sostenibile agli elettroliti fortemente acidi, aprendo nuove prospettive per lo sviluppo di batterie a flusso redox più economiche ed ecocompatibili nel contesto della transizione energetica.

Summary

Introduction *1*

1 Energy System Overview and Storage Technologies *3*

1.1 Trends in Global Energy Consumption 3

1.2 Climate Crisis and Decarbonization 5

1.3 Energy Storage Technologies: A Key Enabler for the Transition 6

1.4 Redox flow batteries and the role of electrolytes 8

1.4.1 General Introduction to Redox Flow Batteries 8

1.4.2 Historical Evolution and Role of the Vanadium Redox Flow Battery (VRFB): State of the Art and Critical Issues 11

1.5 The Role of Electrolytes in RFBs 13

1.6 Research Objectives and Scope of the Thesis 14

2 Characterization of redox-active systems and flow battery components: techniques and methods *16*

2.1 Electrochemical techniques 17

2.1.1 Cyclic voltammetry (CV) 17

2.1.2 Calculation of diffusive and kinetic parameters: Randles–Ševčík and Laviron equations 19

2.1.3 Electrochemical Impedance Spectroscopy (EIS) 21

2.1.4 Charge and Discharge Cycles in Redox Flow Batteries 23

2.2 Morphological and compositional analysis techniques 26

2.2.1 Scanning Electron Microscopy (SEM) 26

2.2.2 Total Reflection X-Ray Fluorescence (TXRF) 28

2.2.3 Raman Spectroscopy 29

3 Analysis and Development of the Ti–Fe Redox System in Sulfuric Acid *31*

3.1 The Choice of the Ti–Fe System: State of the Artand Application Perspectives 31

3.2 Chemical and Electrochemical Behavior of Titanium in Sulfuric Acid 32

3.3 Preliminary Electrochemical Study of Titanium in Sulfuric Acid 34

3.3.1 Experimental Setup and Instrumentation 34

3.3.2 Preparation of the Solutions and Operating Conditions 36

3.4 Voltammetric Behavior of the Ti(IV)/Ti(III) Redox Couple as a Function of Electrolyte Composition 37

3.4.1 Influence of Scan Rate on the Electrochemical Behavior of the Ti(IV)/Ti(III) Redox Couple (1 M $TiOSO_4$) in Sulfuric Acid 39

3.5 Spectroscopic and Voltammetric Investigation: Molecular Compatibility of Ti–Fe Electrolytes . 43

3.6 Battery Testing of the Ti^{3+}/TiO^{2+}–Fe^{3+}/Fe^{2+} System in Sulfuric Acid Medium: Design and Performance Evaluation 46

3.7 Redox reactions and chemical composition of the anodic and cathodic compartments 47

3.7.1 Cell Configuration and Employed Materials 49

3.7.2 Electrolyte Preparation and Tested Configurations 51

3.8 In-cell performance of the Ti–Fe battery with mixed electrolytes: evaluation of the effect of bismuth 54

3.8.1 Evaluation of Baseline Performance of the Ti–Fe Redox Flow Battery Without Bismuth 55

3.8.2 In-cell performance of the Ti–Fe battery with bismuth: catalytic effect and long-term stabilization 60

3.8.3 Electrochemical Impedance Spectroscopy (EIS) Analysis 63

3.8.4 Post-cycle morphological analysis of electrodes by SEM 65

3.9 Performance Evaluation of the Ti–Fe System Using Mixed Electrolytes at 0.5 M Ti with Bismuth 68

3.10 Electrochemical Evaluation of the Ti–Fe Cell with Separated Electrolytes 72

3.11 Post-cycling elemental analysis by TXRF 77

3.12 Comparison of the performance of different Ti–Fe battery configurations 80

4 Study of Titanium Complexes and Application in the Ti–Fe Battery with EDTA Complexes 82

4.1 Theoretical background on coordination chemistry 83

4.2 Experimental Procedure for the Preparation and Electrochemical Characterization of Titanium Complexes 85

4.3 Electrochemical Study of Titanium Complexes: Objectives and Experimental Studies 88

4.3.1 Electrochemical behavior of the Ti–bipyridine complex 89

4.3.2 Electrochemical Behavior of the Ti–HEDP Complex 92

4.3.3 Electrochemical Behavior of the Ti–EDTA Complex 97
4.4 Study of Ti–EDTA and Fe–EDTA Complexes for Redox Flow Batteries 101
4.5 Study of Ti–EDTA/Fe–EDTA Battery 106
4.5.1 Ionic Conductivity Study of the Ti–EDTA and Fe–EDTA Complexed Electrolytes 106
4.5.2 Electrochemical performance of Ti–EDTA/Fe–EDTA battery 110
4.5.3 Influence of temperature on Ti–EDTA/Fe–EDTA battery performance 115
4.5.4 Influence of flow rate on Ti–EDTA/Fe–EDTA battery performance 116
5 Comparative Assessment of Sulfate-Based and EDTA-Complexed Electrolytes for Ti–Fe Redox Flow Batteries 119
5.1 Chemical and Electrochemical Comparison Between Sulfate-Based and EDTA-Complexed Electrolytes 119
5.2 Ionic Conductivity 121
5.3 Short-Run Comparison of Sulfuric Acid and EDTA-Based Ti–Fe Batteries 123
5.4 Long-run Comparison Between H_2SO_4 and EDTA Systems 125
5.5 Comparative analysis of different electrolyte configurations 127
5.6 Comparison of active material costs 129
Conclusions 131

Introduction

The large-scale integration of renewable energy sources, such as photovoltaic and wind power, is increasingly highlighting the need for energy storage systems that are efficient, scalable, and capable of compensating for the intrinsic intermittency of renewable generation, thereby ensuring grid stability and supporting the progressive decarbonization of the energy sector. Among the available technologies, Redox Flow Batteries (RFBs) stand out as one of the most promising solutions for stationary energy storage, thanks to their operational flexibility, the intrinsic decoupling between power and energy, their long cycle life, and the high level of safety resulting from the use of liquid electrolytes. The vanadium-based flow battery (VRFB) currently represents the most consolidated commercial standard; however, the high cost of vanadium, its notable price volatility, and its limited availability significantly hinder large-scale deployment, particularly in scenarios where electrolyte cost strongly influences the overall economic competitiveness of the system. For these reasons, growing research efforts have been directed toward developing RFB chemistries based on abundant, inexpensive, and environmentally sustainable metals such as iron, manganese, copper, and titanium. Among these alternatives, the Ti(IV)/Ti(III) – Fe(III)/Fe(II) redox couple has shown significant potential: both metals are naturally abundant, have a low environmental impact, and exhibit good electrochemical reversibility in acidic media. The use of H_2SO_4 stabilizes Ti(IV) by suppressing hydrolysis phenomena, but the high corrosivity of this environment poses critical challenges in terms of material compatibility and long-term durability. To overcome these limitations, increasing attention has been devoted to coordination complexes capable of stabilizing metal ions under milder conditions. In this context, EDTA has proven to be an effective ligand for forming stable and soluble complexes with Ti(IV) and Fe(III) in slightly acidic media, thereby enabling the development of fully complexed systems that are chemically safer and more compatible with cost-effective cell components. Building on these premises, the present work investigates the Ti–Fe chemistry in a systematic and comparative manner in two distinct electrolyte environments: 1) a strongly acidic sulfuric system, used to evaluate titanium speciation, kinetic limitations, intermetal compatibility, and flow-cell performance, including the catalytic effect of Bi^{3+}; 2) a complexed Ti–EDTA/Fe–EDTA system, used to assess chemical stability, solubility, redox behavior, and operational response under different temperatures and flow conditions. The overall aim of the thesis is to provide an in-depth understanding of the mechanisms governing stability, redox reversibility, ionic transport, and interactions with electrodes and membranes in both formulations, linking chemical and physical properties to real flow-cell performance through voltammetric, spectroscopic, morphological, and galvanostatic analyses.

The thesis is organized into five chapters that guide the reader through a coherent and progressive research path.

Chapter 1 contextualizes the study within the current energy landscape, discusses the strategic role of RFBs in the transition toward renewable-based systems, analyzes their operating principles, and outlines the motivations behind the search for new chemistries based on abundant metals such as titanium and iron.

Chapter 2 presents the experimental techniques employed, including cyclic voltammetry, electrochemical impedance spectroscopy, scanning electron microscopy, TXRF analysis, and the methodology used for galvanostatic flow-cell tests, providing the conceptual tools required to interpret the subsequent results. Chapter 3 forms the core of the first experimental section and investigates the Ti–Fe system in sulfuric acid, detailing titanium speciation as a function of acidity, the voltammetric behavior of the Ti(IV)/Ti(III) and Fe(III)/Fe(II) couples, the stability of the mixed electrolyte, the kinetic limitations of the titanium anodic process, and the catalytic action of bismuth in reducing overpotentials and enhancing cell performance, including comparisons between mixed, diluted, and separated configurations.

Chapter 4 focuses on titanium complexes—Ti–bpy, Ti–HEDP, and especially Ti–EDTA. This chapter examines their solubility, chemical stability, redox potentials, and voltammetric responses, along with the preparation and characterization of the Ti–EDTA/Fe–EDTA flow battery. Special attention is devoted to the influence of temperature and electrolyte flow rate on cell voltage, efficiency, and mass-transport phenomena.

Chapter 5 provides a direct and critical comparison between the sulfuric and complexed systems, integrating chemical, electrochemical, operational, and techno-economic considerations. Stability, reversibility, energy efficiencies, and active-material costs are examined to identify the operational conditions and application scenarios in which each chemistry is most advantageous, establishing the basis for further development of Ti–Fe–based flow batteries.

Taken together, these elements offer a comprehensive and coherent picture of the opportunities and challenges associated with Ti–Fe chemistry for flow battery applications. This introduction therefore prepares the reader for a detailed evaluation of a promising emerging system by illustrating how fundamental aspects of speciation, redox kinetics, ionic transport, and material interactions determine the practical performance of these electrolyte formulations.

1 Energy System Overview and Storage Technologies

1.1 Trends in Global Energy Consumption

In recent decades, the global energy system has undergone profound transformations, both in quantitative and qualitative terms. According to data from the International Energy Agency (IEA), global primary energy consumption has steadily increased, driven by population growth, industrialization in emerging countries, and the rising energy demand of the residential, transport, and industrial sectors. Between 2000 and 2019, global energy demand grew by approximately 50%, a trend that, despite the temporary contraction caused by the COVID-19 pandemic, is expected to continue in the coming decades. Projections to 2040 indicate a sustained increase in demand, although at a slower pace than in the past, due in part to improvements in energy efficiency and evolving consumption patterns [1].

As shown in Figure 1.1 (data updated to 2023), the composition of the global energy mix remains heavily dominated by fossil fuels, despite the growth of renewable sources. The figure highlights that the combined share of oil, coal, and natural gas continues to exceed that of traditional renewable sources.

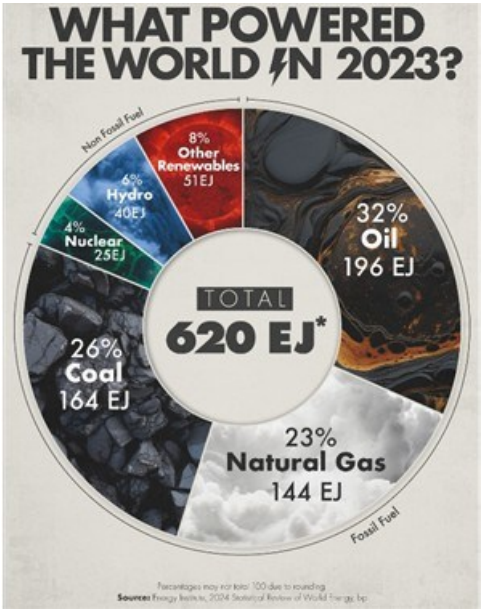


Figure 1.1: Composition of the Global Energy Mix by Source (2023). Source: IEA, World Energy Balances: Overview 2023.

A significant indicator of this evolution is the growing role of electricity. The transition towards a digital economy, the electrification of transport, and the widespread adoption of technologies such as heat pumps, data centers, and smart home devices have led to an increasingly pronounced demand for electricity compared to other forms of energy carriers. At the European level, electricity currently accounts for over 20% of final energy consumption, and this share is expected to exceed 30% by 2040 according to the most advanced decarbonization scenarios [2]. In countries such as China and India, per capita electricity consumption has increased at an exponential rate, significantly contributing to the overall growth in global demand. The rise of

electrification and the evolution of global electricity consumption are summarized in Figure 1.2, which illustrates both the increase in total electricity demand and the shift in regional shares. In particular, a sharp rise is observed in Asia, with China alone projected to account for 33% of global electricity consumption by 2025, far surpassing the United States and Europe.

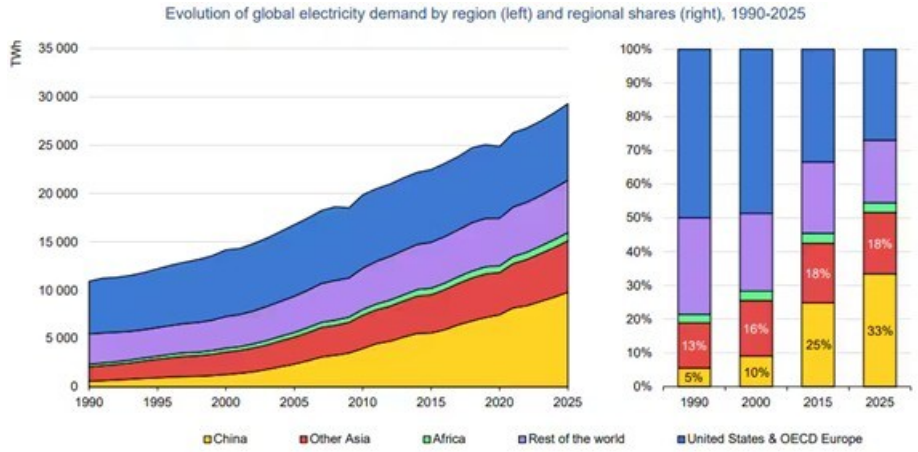


Figure 1.2: Evolution of Global Electricity Demand by Region (left) and Regional Percentage Distribution (right), 1990–2025.
Source: International Energy Agency (IEA), World Energy Outlook 2020

Greater electrification of energy consumption represents a significant opportunity for reducing greenhouse gas emissions, especially when electricity is generated from renewable sources. However, it also introduces new challenges for the energy system, which must now handle more variable and less predictable demand, increasingly influenced by climatic and behavioral factors. Furthermore, the expansion of renewable energy sources brings high variability in power generation, requiring increasingly sophisticated tools for grid management and balancing. In parallel, the structure of energy supply is also undergoing a transformation. The growing penetration of renewable sources, particularly solar photovoltaics and wind power, has led to a gradual decline in the use of fossil fuels in many national energy systems. According to data published by REN21 and the IEA, in 2022 renewable energy sources accounted for over 29% of global electricity generation, with peaks exceeding 50% in some Northern European countries [3]. This shift has been driven by the declining cost of renewable technologies, especially photovoltaic modules and wind turbines, as well as by increasingly stringent regulations and incentive policies. Nonetheless, this transformation presents a range of new challenges associated with the intermittency and non-dispatchable nature of renewable generation. Although solar and wind energy are abundant and environmentally friendly, they are not always available during peak demand periods, making it essential to implement systems capable of balancing generation and consumption. This has led to the growing importance of grid flexibility, understood as the system's ability to rapidly adapt to fluctuations in supply and demand while maintaining reliability and quality of service [4].This trend is also evident in the Italian context. According to Terna, the company responsible for high-voltage electricity transmission in Italy, national electricity consumption increased by 53% between 1987 and 2017, with a growing share supplied by renewable sources, which in 2022 accounted for more than 35% of domestic

electricity generation [5]. Solar power has seen particularly significant growth, with an installed capacity exceeding 25 GW, followed by wind and hydropower. At the same time, the complexity of electricity system management has also increased, in a context that demands greater flexibility, rapid response capabilities, and enhanced resilience. These developments highlight how the energy system has entered a phase of structural transition, marked by increasing electrification, decarbonization of energy supply, and digitalization of the grid. In this scenario, electrical energy storage plays a strategic role in ensuring reliability, efficiency, and sustainability. The following sections will explore issues related to the climate crisis and the decarbonization of the energy sector, before providing a detailed analysis of the main energy storage technologies currently available and the role of redox flow batteries within the new energy paradigm.

1.2 Climate Crisis and Decarbonization

As highlighted in the previous section, the continuous increase in global energy demand continues to be met largely through the use of fossil fuels. This has led, over the past decades, to a parallel rise in greenhouse gas (GHG) emissions, particularly carbon dioxide (CO_2), which is the main driver of global warming. The energy sector currently accounts for approximately 75% of global GHG emissions, making it one of the primary contributors to the climate crisis. According to data from the International Energy Agency (IEA), in 2023 global energy-related CO_2 emissions reached a record high of 37.4 billion tonnes, marking a further increase compared to the previous year, despite the continued growth of renewable energy sources [6].
The historical evolution of these emissions is well illustrated in Figure 1.3, which shows the cumulative contribution of the world's major regions from 1950 to 2022. It is clearly evident that, in the early decades, the United States and Europe were the dominant contributors. However, from the late 20th century onward, China has emerged as a major emitter, followed, albeit to a lesser extent, by India and other Asian countries.

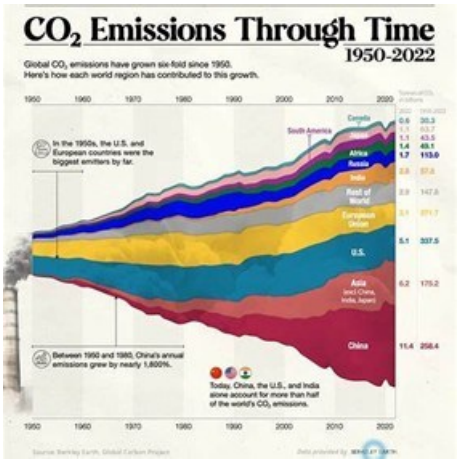


Figure 1.3: The chart illustrates the cumulative contribution of major world regions to global CO_2 emissions since 1950. Initially dominated by the U.S. and Europe, emissions have shifted significantly in recent decades, with China now accounting for the largest share.Source: Berkeley Earth, Global Carbon Project (data provided by Our World in Data / Visual Capitalist).

The shift in the geography of emissions reflects the broader economic and industrial evolution of the world. Between 1950 and 1980, for example, China's emissions increased by approximately 1,800%. Today, China

alone is responsible for more than one-quarter of global emissions [7]. The rapid industrialization of emerging economies, combined with a strong reliance on fossil fuels, has consequently shifted the center of gravity of emissions toward East Asia. Contributing to this trend is the rising atmospheric concentration of CO_2, which in 2025 exceeded 430 ppm, compared to approximately 280 ppm in the pre-industrial era, according to measurements from the Mauna Loa Observatory (NOAA). The resulting increase in global temperatures is closely linked to these concentration levels. According to the IPCC, without drastic intervention, global warming could exceed 2 °C by the end of the century, with potentially irreversible impacts on ecosystems, food security, and social stability [8]. To address this trajectory, the international community has set a series of ambitious targets. The 2015 Paris Agreement established the goal of keeping the increase in global average temperature "well below 2 °C" and ideally limiting it to 1.5 °C [9]. The European Union has translated these targets into the Green Deal and the legislative package Fit for 55, which aims for a 55% reduction in emissions by 2030 and climate neutrality by 2050 [10]. In Italy, these targets have been adopted through the Integrated National Energy and Climate Plan (PNIEC) [11] and the National Recovery and Resilience Plan (PNRR), which allocate strategic investments in renewable energy, energy efficiency, and sustainable mobility [11].
However, the current pace of decarbonization remains insufficient to meet climate goals. A structural transformation of the entire energy system is required, one based on the electrification of end-use sectors, the gradual phase-out of fossil fuels, and the integration of enabling technologies such as energy storage, smart grids, and demand-side management. Within this framework, energy storage plays a strategic role, which will be explored in greater detail in the following sections. A comparison of the main climate and energy policies at the European and national levels is provided in Table 1.1 and implementation measures adopted to support the decarbonization pathway.

Table 1.1 Comparison of Climate and Energy Policies (EU and Italy).

Policy / Plan	Main Target Year	Key Emission Targets	Main Measures
***EU Green Deal** [12]*	2050	Climate neutrality by 2050	Decarbonization, clean energy, circular economy, biodiversity protection
***Fit for 55 (EU)** [13]*	2030	–55% GHG emissions (vs. 1990) by 2030	Carbon pricing, renewables, energy efficiency, transport electrification
Italian NECP**[14] **(PNIEC, 2023 draft)	2030	–43.7% GHG emissions (vs. 2005) by 2030	65% RES in electricity, efficiency improvements, fossil fuel reduction
Italian NRRP** [15] **(PNRR, 2023 revision)	2026	Strategic support to decarbonization and energy transition	Investments in renewables, grids, sustainable mobility and buildings

1.3 Energy Storage Technologies: A Key Enabler for the Transition

In response to the climate emergency and the decarbonization targets discussed in the previous section, the evolution of energy systems is increasingly oriented toward the electrification of end uses and the progressive replacement of fossil fuels with renewable energy sources. In particular, solar photovoltaics and wind power have experienced unprecedented growth, driven by falling costs, improved technological efficiency, and

increasingly robust incentive policies. However, the intermittent and non-dispatchable nature of these sources introduces new challenges for grid management, which must balance highly variable generation with a demand that remains relatively stable on daily and seasonal timescales.

To ensure the reliability and security of the power system, it is therefore essential to deploy technologies capable of absorbing surplus energy during periods of low demand and releasing it when needed, while also supporting frequency and voltage regulation. In this context, Energy Storage Systems (ESS) play a key role in the energy transition. Storage enables the temporary accumulation of energy, reduces dependence on fossil resources, supports the integration of renewables, and provides a wide range of ancillary services to the power grid [16], [17].

Energy storage technologies can be classified according to their underlying physical principles and the form of energy stored. In particular, the following categories can be identified:

- Mechanical storage systems, including Pumped Hydro Storage (PHS), flywheels, and Compressed Air Energy Storage (CAES);
- Thermal storage systems, which use sensible or latent heat through phase-change materials or molten salt tanks;
- Chemical storage systems, based on the production and reconversion of energy carriers such as hydrogen or synthetic fuels (power-to-gas);
- Electrochemical storage systems, including batteries (lead-acid, lithium-ion, sodium-sulfur, zinc-air), supercapacitors, and redox flow batteries (RFBs) [18].

Each of these technologies presents specific advantages and limitations depending on the application context, with significant differences in energy density, round-trip efficiency, cycle life, response time, scalability, and Levelized Cost of Storage (LCOS) [19]. As a result, energy storage systems are deployed across a range of scales:

- Small scale (up to a few tens of kWh): typically used in residential settings or microgrids, where compact, safe devices with rapid response times are required. Common solutions include lithium-ion batteries, supercapacitors, and flywheels;
- Medium scale (10 kWh to 1 MWh): suited for commercial facilities, isolated local grids, or industrial plants. In these cases, the trade-off between autonomy, cost, and cycle life is crucial. Technologies such as compact CAES systems, fuel cells, and flow batteries are often employed;
- Large scale (above 1 MWh): designed for utility-scale plants aimed at grid balancing, system stabilization, and renewable integration support. Leading technologies include pumped hydro, hydrogen-based storage, and flow batteries, due to their capacity to manage large energy volumes over extended periods [20].

A summary representation of the various storage technologies in terms of energy and power density is shown in Figure 1.4, which illustrates the application domains of each solution and highlights their operational limits.

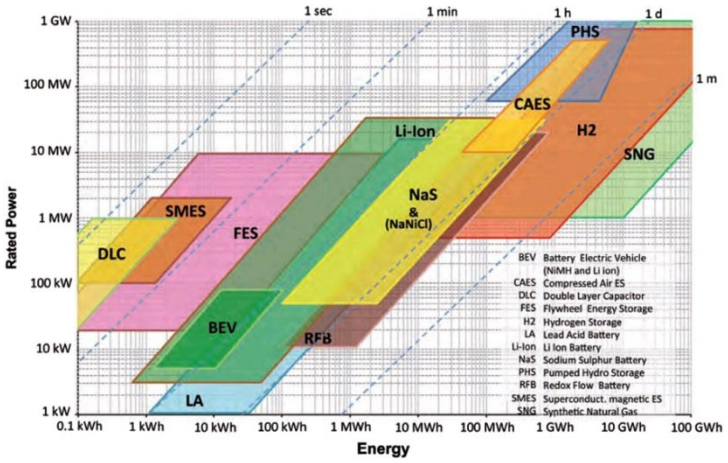


Figure 1.4: ESS's comparison by rated power, energy, and discharge duration [21].

According to estimates by the International Energy Agency, achieving full integration of renewable energy sources and meeting global climate targets will require the deployment of more than 600 GW of new storage capacity worldwide by 2030, with a growing role for stationary batteries [17]. Within this framework, the development of technologies that are sustainable, scalable, and based on non-critical materials is a key priority. Among these, Redox Flow Batteries (RFBs) are emerging as one of the most promising solutions for large-scale grid storage, thanks to their ability to decouple energy and power, long cycle life, and flexible architecture, which enables modular, scalable, and safe energy management [22].

1.4 Redox flow batteries and the role of electrolytes

1.4.1 General Introduction to Redox Flow Batteries

Redox Flow Batteries (RFBs) represent one of the most promising technologies for large-scale electrical energy storage, owing to their design flexibility, long operational lifetime, and intrinsic safety [22], [23]. Unlike conventional batteries, where energy is stored in solid electrode materials, RFBs store energy in two separate liquid electrolytes that continuously circulate through an electrochemical cell where redox (oxidation–reduction) reactions occur. These solutions, known respectively as the anolyte and catholyte, contain the active redox couples responsible for the energy conversion process [24].

During the charging phase, electrical energy from an external source drives the oxidation of the reduced species in the anolyte and, simultaneously, the reduction of the oxidized species in the catholyte. During discharge, the process is reversed, allowing the stored chemical energy to be converted back into electrical energy [23].

The redox reactions occurring in the two half-cells can be expressed in general form as follows (Equations 1.1 and 1.1.2):

Anolyte (oxidation):

$$R^{n-} \rightarrow O^{(n+1)} + e^{-} \qquad \text{Eq. 1.1}$$

Catholyte (reduction):

$$O'^{(m+1)-} + e^{-} \rightarrow R'^{m-} \qquad \text{Eq. 1.2}$$

Where:

- R^{n-} is the reduced species in the anolyte;
- $O^{(n+1)}$ is the oxidized form resulting after the loss of one electron;
- $O'^{(m+1)-}$ is the oxidized species in the catholyte;
- R'^{m-} is the reduced species formed in the catholyte;
- e^- represents the electron transferred through the external circuit.
- n and m indicate the negative charge of the reduced redox species;
- the indices (n+1) and (m+1) reflect the increase in oxidation state during the redox process.

The two electrolytes are separated by an ion-selective membrane, which allows the controlled passage of charge-balancing ions, typically protons or anions, while preventing the direct mixing of electroactive species. This balance between electronic flow through the external circuit and ionic flow across the membrane enables the reversible conversion between chemical and electrical energy [25].

A schematic representation of the general operating principle of a redox flow battery is shown in Figure 1.5, highlighting the electrolyte tanks containing the anolyte and catholyte, the circulation pumps, the electrochemical stack, and the external electrical circuit.

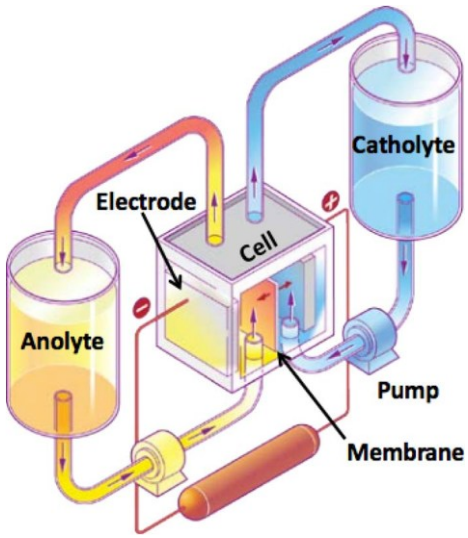


Figure 1.5: Schematic of a generic redox flow battery system. Source: Sandia National Laboratories, 2013 [26].

The core of the system is the electrochemical stack, composed of a series of individual cells connected in series. Each cell consists of two porous electrodes (typically made of carbon felt or graphite), separated by an ion-selective membrane and sandwiched between bipolar plates that serve as current collectors and flow distributors [27]. These plates feature engraved flow fields designed to ensure a uniform distribution of the electrolyte across the electrode surface. Common geometries include serpentine, interdigitated, and mesh-type patterns; these play a critical role in stack design, as they directly affect fluid distribution, pressure drop, and hydraulic losses within the system [28], [29]. A homogeneous flow of anolyte and catholyte ensures uniform utilization of the electrode's active surface, minimizes stagnant zones, and improves overall cell efficiency.

A schematic of a single cell within the stack, showing the main components such as porous electrodes, ion-selective membrane, bipolar plates, and flow channels, is presented in Figure 1.6,

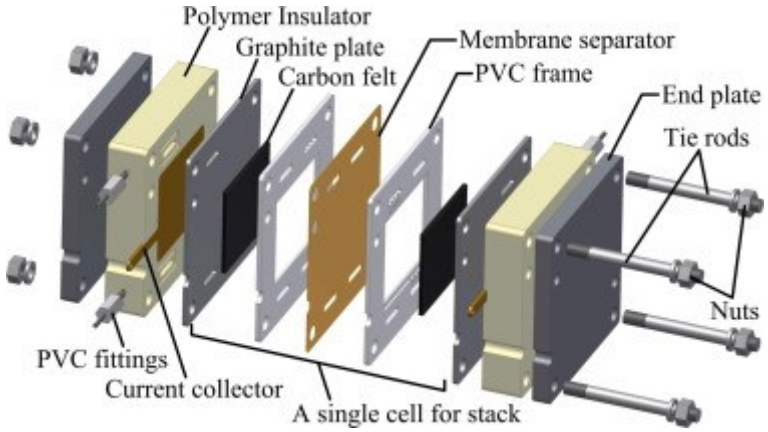


Figure 1.6: Schematic of the VRB single cell assembly structure [30]

The porous electrodes, characterized by high specific surface area and good electrical conductivity, provide the sites where redox reactions occur. Their microstructure, composition, and surface treatment strongly influence reaction kinetics and, consequently, the overall performance of the battery. The entire stack is enclosed by end plates, which provide mechanical rigidity and ensure fluid tightness, while the electrical interconnection of the cells allows the voltages generated by each unit to be summed. A typical stack can contain from a few dozen to more than one hundred cells, reaching modular voltages of 50–100 V; multiple stacks can be connected in series or parallel to increase voltage or power, respectively [31].

From a hydraulic standpoint, the anolyte and catholyte are pumped in a closed loop between the storage tanks and the stack, flowing through the anodic and cathodic compartments before returning to the tanks for continuous recirculation. Control of flow rate and pressure is essential to ensure uniform distribution and minimize energy losses due to pumping [32]. Meanwhile, the membrane must provide high ionic selectivity and low ohmic resistance to prevent efficiency losses and crossover phenomena, i.e., the undesired migration of redox-active species between compartments. If uncontrolled, crossover can lead to capacity loss and alter the chemical balance of the electrolytes over time [33].

One of the most distinctive features of RFBs is the decoupling of energy and power, a major advantage over solid-state batteries. The power output depends on the active electrode area and the number of cells in the stack, while the energy capacity is determined by the volume and concentration of the electrolyte solutions stored in the tanks. This allows for highly modular and scalable system design, suitable for applications ranging from microgrids to large utility-scale installations [34].

RFBs exhibit coulombic efficiencies above 90% and overall energy efficiencies between 70% and 85%, with operational lifetimes exceeding 10.000 charge–discharge cycles [23], [35]. Because all reactions occur in the liquid phase, structural changes in electrode materials are avoided, thereby minimizing degradation and ensuring high operational stability. Moreover, the use of aqueous electrolytes makes these systems inherently safe, as they are not prone to thermal runaway phenomena typical of lithium-based batteries [36].

Nevertheless, RFBs still face some limitations. The most significant is their low volumetric energy density (20–50 Wh L^{-1}), which requires large electrolyte volumes to store substantial amounts of energy, making them unsuitable for mobile or space-constrained applications [37]. High capital costs also remain a challenge, arising from system complexity, active material costs, and the need for pumps, piping, and advanced control systems [38]. Additionally, species crossover, thermal management, and ohmic and hydraulic losses continue to be active areas of research and optimization.

Despite these challenges, the combination of flexibility, long cycle life, and intrinsic safety makes Redox Flow Batteries one of the most promising technologies for renewable energy management, energy self-sufficiency, and grid support in the context of the global energy transition.

1.4.2 Historical Evolution and Role of the Vanadium Redox Flow Battery (VRFB): State of the Art and Critical Issues

The history of redox flow batteries (RFBs) dates back to the 1970s, when NASA first explored the possibility of using electrochemical flow systems for energy storage in aerospace applications. Among the earliest chemistries investigated was the Iron-Chromium (Fe/Cr) couple, selected for its low cost and material abundance, but limited by poor coulombic efficiency and sluggish redox kinetics [23], [39]. A major paradigm shift occurred in the following decade thanks to the pioneering work of Maria Skyllas-Kazacos and her team at the University of New South Wales [40]. Their research led to the development of the Vanadium Redox Flow Battery (VRFB), which remains one of the most extensively studied and commercially implemented systems to date. The VRFB is characterized by the use of a single element, Vanadium, in four different oxidation states (V(II), V(III), V(IV), V(V)), dissolved in sulfuric acid (H_2SO_4). This configuration enables the use of a single bifunctional electrolyte, minimizing cross-contamination between half-cells and simplifying the maintenance of ionic balance. During operation, the redox reactions proceed as follows (Equations 1.1.3 and 1.1.4):

Anolyte (discharge):

$$V^{2+} \rightarrow V^{3+} + e^- \qquad \text{Eq. 1.3}$$

Catholyte (discharge):

$$VO_2^+ + 2H^+ + e^- \rightarrow VO^{2+} + H_2O \qquad \text{Eq. 1.4}$$

These fully reversible reactions occur in a strongly acidic environment (typically H_2SO_4), where Vanadium species remain chemically stable and soluble at relatively high concentrations. The system architecture comprises two storage tanks, an electrochemical cell equipped with porous electrodes (commonly graphite felt), and an ion-selective membrane (generally Nafion), which allows for the selective transfer of H^+ ions to maintain electroneutrality between the compartments. The strengths of this technology are numerous: high chemical reversibility and cycling stability; long operational lifetime (over 10,000 charge/discharge cycles); modularity and scalability (power and capacity are independent variables); intrinsic safety due to the use of

aqueous, non-flammable electrolytes; absence of memory effect; and good tolerance to deep cycling [22], [25], [41]. However, VRFBs also face several major challenges: the cost of vanadium, subject to market volatility and supply constraints; the highly acidic environment, which requires corrosion-resistant and therefore expensive materials for tanks, tubing, electrodes, and membranes; the low volumetric energy density (20–50 Wh L^{-1}), which limits their use in mobile applications or where space is constrained; and the need for precise operational control, including temperature, state of charge, and chemical balance between the reservoirs [22]. A comparative summary of the main RFB technologies currently studied is reported in the Table 1.2:

Table 1.2: Comparison among main redox flow technologies.

Redox system	Development status	Advantages	Drawbacks
VRFB (V^{2+}/VO_2^+)	Commercial	High reversibility, long lifetime, safety	Vanadium cost, low energy density
Fe/Cr	Prototype	Low material cost	Slow kinetics, low efficiency
Zn/Br	Commercial	High energy density	Corrosion, Zn dendrite formation
Organic	Laboratory	High molecular flexibility	Low stability, electrochemical degradation
Metal–organic	Laboratory	Chemical tunability	Limited stability

Over the past decades, the RFB family has expanded considerably, giving rise to a wide range of technological solutions differing in architecture, solvent, and redox-active species.

A first classification criterion concerns the physical phase of the active materials: classical systems employ liquid electrolytes in both half-cells; hybrid systems use one solid-phase electrode—for instance, zinc/bromine (Zn/Br) batteries, where metallic zinc is plated on the electrode during charging; and semi-flow or slurry-based systems employ either a single soluble redox species or solid particles suspended in a carrier fluid, configurations attracting increasing interest due to their potential for higher energy density [42].

A second criterion relates to the type of solvent. Aqueous RFBs are currently the most mature commercially, offering safety, chemical stability, and low cost, though limited by a narrow electrochemical stability window. Non-aqueous systems, still under development, can achieve higher theoretical cell voltages and better solubility for certain redox species, albeit at the expense of ionic conductivity and material compatibility [43].

From the standpoint of redox chemistry, numerous systems have been investigated in addition to the VRFB: the aforementioned Fe/Cr system, cost-effective but inefficient; the Zn/Br system, offering high energy density but operational complexity; organic and metal-organic systems, providing tunable molecular design yet hampered by chemical degradation; and alternative couples based on copper, manganese, or titanium, which are currently under study for their potential sustainability and elemental abundance [23], [44].

The following Table 1.3 shows the main types of electrolytes studied for RFB, with their characteristics and state of development:

Table 1.3: Redox electrolytes studied in RFBs.

Electrolyte type	Key features	Development status
Aqueous (H_2SO_4)	High conductivity Safety Low cost	Commercial
Non-aqueous (carbonates)	Higher theoretical energy density Wide electrochemical window	Experimental
Deep Eutectic Solvents (DES)	Enhanced solubility Sustainability Low environmental impact	Emerging
Organic electrolytes	High molecular versatility Tunable synthesis	Laboratory
Hybrid electrolytes	Balance between performance Safety Environmental compatibility	Laboratory

Among all these systems, the VRFB remains the technological benchmark for redox flow batteries. Its robust engineering design, combined with extensive accumulated experimental knowledge, makes it an ideal platform for exploring new solutions, particularly regarding electrode materials, membranes, and, most importantly, electrolytes.

Indeed, beyond the specific redox chemistry employed, it is now widely recognized that the performance, lifetime, and safety of an RFB are critically dependent on the nature of the electrolyte. The electrolyte directly affects energy density, coulombic efficiency, chemical stability of active species, ionic conductivity, and interactions with other cell components. Furthermore, it represents one of the main cost drivers and a central factor in assessing the environmental and economic sustainability of the system.

In light of these considerations, the scientific community has progressively focused on the design of innovative electrolytes, both aqueous and non-aqueous, to overcome the limitations of existing systems and enable new battery architectures. It is within this framework that the work presented in this thesis is situated, with the following sections devoted to a detailed analysis of the composition, performance, and evolution of electrolytes for redox flow batteries.

1.5 The Role of Electrolytes in RFBs

As previously discussed, beyond the specific redox chemistry employed, it is now widely recognized that the performance, durability, and safety of a RFB critically depend on the nature of the electrolyte. In these systems, energy is not stored in solid materials but in redox-active species dissolved in the liquid phase. Consequently, electrolyte design is not a secondary aspect but rather a central determinant of the overall performance of the battery [45].

From a chemical and functional standpoint, the electrolyte must simultaneously ensure the stability of the redox species and efficient ionic conduction across the cell. Multiple parameters influence system performance: volumetric energy density, coulombic efficiency, cycling capacity, redox reversibility, and

compatibility with electrodes and membranes all depend strongly on the physicochemical properties of the electrolyte solution [23].

An effective electrolyte must satisfy a set of stringent requirements, including high solubility of active species, to maximize the amount of storable energy, good redox reversibility to minimize losses and improve cycle life, chemical and electrochemical stability under operating conditions, high ionic conductivity, low viscosity, and the absence of precipitation or irreversible degradation phenomena [46].

However, these criteria are often mutually conflicting. For instance, increasing solubility may lead to chemical instability or higher viscosity, while solvents with a wide electrochemical window often exhibit poor ionic conductivity. For these reasons, the design of an "optimal" electrolyte remains one of the most significant open challenges in the field of RFBs. The main issues typically encountered in RFB electrolytes include the chemical or electrochemical degradation of active species, the precipitation or formation of solid phases, the cross-over of redox species through the membrane, electrode or membrane fouling, and long-term incompatibility with cell components [47]. To address these challenges, recent research has increasingly focused on advanced strategies such as the molecular complexation of redox species (to improve solubility and stability), the use of functional additives (to reduce degradation or enhance redox kinetics), and the adoption of alternative solvents, including deep eutectic solvents (DES) and organic solvent mixtures [48].

Within this framework, the present thesis aims to contribute to the development of innovative electrolytes for RFBs, with particular focus on the Ti/Fe redox couple, selected for the abundance, cost-effectiveness, and sustainability profile of the constituent elements. Although the titanium/iron system is less established than others, such as the VRFB, it represents a promising alternative based on earth-abundant metals whose efficiency and stability are strongly dependent on electrolyte optimization.

The objective of this work is therefore to explore new approaches for the rational design of the Ti/Fe electrolyte, assessing its performance in terms of solubility, redox reversibility, and chemical stability, with the ultimate goal of improving its suitability for large-scale stationary energy storage applications.

1.6 Research Objectives and Scope of the Thesis

As discussed in the previous sections, Redox Flow Batteries (RFBs) represent one of the most promising technologies for large-scale stationary energy storage, owing to their design flexibility, long operational lifetime, and intrinsic safety. However, their industrial deployment is still hindered by several challenges, including limited energy density, system complexity, and, most critically, the nature and behavior of the electrolytes. In this context, the present thesis aims to contribute to the development of innovative electrolytes for RFBs through the experimental investigation of the Titanium/Iron (Ti/Fe) redox couple. This chemistry, based on earth-abundant and low-cost metals, offers interesting prospects in terms of sustainability and material accessibility, while simultaneously posing significant challenges related to chemical stability, redox reversibility, and solubility of the active species.

The main objective of this work is to optimize the electrolyte formulation for the Ti/Fe battery by adopting a systematic approach encompassing:

- The analysis of solubility and stability of the redox species under various chemical conditions;
- The evaluation of coulombic efficiency and electrochemical reversibility;
- The study of interactions among electrolyte, electrodes, and membranes;
- The use of additives, complexing agents, or pH modifiers to enhance overall system performance.

Among the planned research activities, particular attention has been devoted to the study of titanium-containing chemical complexes, with the goal of assessing their stability in solution, electrochemical behavior, and potential applicability as active redox species. This investigation is crucial because, despite its abundance and promising characteristics, titanium exhibits significant limitations associated with the instability of its oxidation state, poor redox reversibility, and a tendency to form precipitates or colloidal species. The analysis of different complex formulations has therefore represented a key aspect of the adopted methodology, aimed at identifying stabilization strategies and solubility enhancement approaches. These aspects will be further discussed in the subsequent chapters, which are specifically dedicated to the detailed study of the Ti/Fe redox couple and its potential application in RFB systems.

Through electrochemical testing, characterization analyses, and operational simulations, this thesis seeks to provide new insights into the limiting mechanisms and possible improvement strategies, with the ultimate goal of making the Ti/Fe couple competitive with more mature redox chemistries such as the vanadium-based system (VRFB).

Ultimately, the work aims to assess the feasibility of the Ti/Fe battery as a sustainable, scalable, and low-impact energy storage solution, contributing to the scientific and technological advancement of redox flow battery systems.

2 *Characterization of redox-active systems and flow battery components: techniques and methods*

Understanding the electrochemical, structural, and compositional behavior of materials used in redox flow batteries (RFBs) requires the application of a broad spectrum of characterization techniques, each designed to analyze specific aspects of the system under investigation. Before presenting the experimental results, this chapter provides a systematic overview of the methodologies employed to investigate the fundamental properties of redox-active couples, electrolytes, electrodes, and ion-selective membranes. The aim is to offer a coherent and comprehensive methodological framework that supports and contextualizes the observations discussed in the following chapters. The techniques described include classical electrochemical methods such as cyclic voltammetry (CV) and electrochemical impedance spectroscopy (EIS), as well as operational charge–discharge tests performed in full-cell configuration. These methods allow not only the evaluation of redox reversibility and the overall energy performance of the system, but also the identification of limiting mechanisms, such as charge transfer resistance, ion diffusion, or degradation of active species. Morphological and compositional analysis techniques also play a central role in this work, particularly scanning electron microscopy (SEM) and total reflection X-ray fluorescence spectroscopy (TXRF). These analytical tools provide critical information on the distribution of electrochemical deposits, the structural stability of the electrodes, and the long-term behavior of the membrane. In particular, the ability to combine high-resolution morphological observations with chemical-elemental data makes it possible to directly correlate surface structure with electrochemical performance. The integration of complementary techniques—each focused on different levels of analysis, from macroscopic to microscopic to molecular—constitutes a key aspect of the experimental strategy adopted in this work. Such a multidisciplinary approach is especially suited to the study of complex systems like those based on the Ti/Fe couple, where chemical, physical, and electrokinetic phenomena interact simultaneously. This methodological articulation also reflects the need to address the open challenges in the field of RFBs, such as the instability of metal complexes, degradation of active materials, species crossover through the membrane, and chemical compatibility between the various cell components.

Ultimately, the detailed description of the techniques employed not only supports the interpretation of the experimental data but also serves as a reference for comparison with the literature and for ensuring the reproducibility of the results. The methodological choices made were guided by the need to obtain reliable, comparable, and representative measurements under realistic operating conditions, with particular attention to cross-validation and internal consistency of the data. The following sections will explore, in a logical and functional order, the operating principles, analytical parameters, and experimental configurations of the main characterization techniques used in this work, with the goal of establishing a solid foundation for the critical interpretation of the phenomena described in the subsequent chapters.

2.1 Electrochemical techniques

2.1.1 Cyclic voltammetry (CV)

Cyclic voltammetry (CV) is one of the most widely employed techniques in electrochemistry for the characterization of redox systems in solution, owing to its ability to rapidly and simultaneously provide thermodynamic, kinetic, and mass-transport information. According to the classical treatment by Bard and Faulkner [49], CV can be regarded as a form of "electrochemical spectroscopy" that allows the investigation of electron-transfer mechanisms and coupled chemical reactions through the analysis of the current response to a controlled variation of the electrode potential.

The experimental setup used in cyclic voltammetry typically consists of a three-electrode electrochemical cell, comprising a working electrode, a reference electrode, and a counter electrode. The working electrode, commonly made of glassy carbon, platinum, or gold, provides the surface on which the redox process of the electroactive species under investigation takes place. The reference electrode (Ag/AgCl or saturated calomel electrode, SCE) supplies a constant and well-defined potential, against which the applied potential is measured. The counter electrode, an inert conductor (usually platinum or stainless steel), completes the electrical circuit and balances the current flowing through the working electrode. The cell also contains a supporting electrolyte at high concentration (≥ 0.1 M), which is essential to ensure that mass transport of the electroactive species occurs exclusively via diffusion. The transport mechanisms involved include diffusion, migration, and convection; however, under ideal cyclic voltammetry conditions, diffusion is the predominant mode of transport [50], [51].

The potentiostat is the fundamental instrument that enables the execution of a cyclic voltammetry experiment. It precisely regulates the potential between the working and reference electrodes and measures the current flowing between the working and counter electrodes. It operates as a feedback-controlled circuit, capable of maintaining the desired potential, compensating for ohmic drops (iR drop), and ensuring signal stability even in low-conductivity solutions [52]. The use of a three-electrode potentiostatic configuration allows for the separation of potential control from current measurement, significantly improving the accuracy and reliability of the acquired data.

During a cyclic voltammetry (CV) experiment, the potential of the working electrode is varied linearly with time following a triangular waveform, starting from an initial potential E_i up to a switching potential E_s, and then returning to the initial value. Figure 2.1 schematically illustrates the operating principle of cyclic voltammetry.

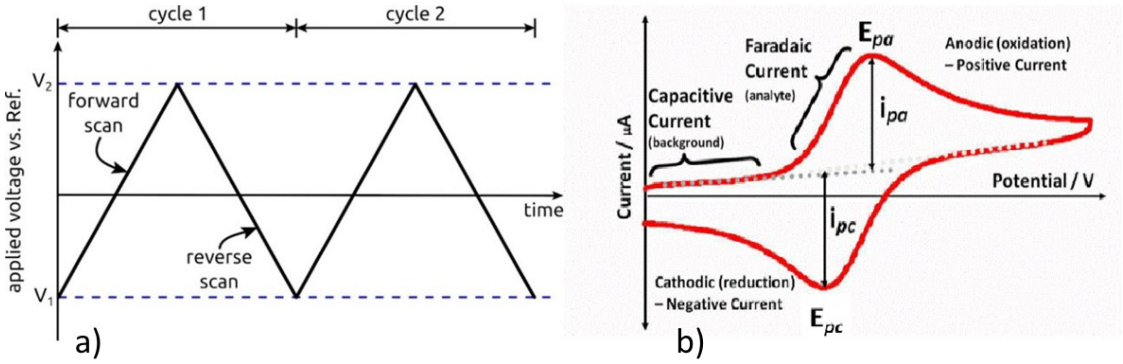


Figure 2.1 : (a) Cyclic potential sweep and (b) a resulting cyclic [49], [53].

On the left (Figure 2.1a), the triangular potential waveform is shown: the potential increases linearly until it reaches a predefined switching value, then decreases at the same scan rate. This cycle can be repeated multiple times, if necessary, to monitor the system's evolution. On the right (Figure 2.1b), an ideal cyclic voltammogram is shown. According to the IUPAC nomenclature, anodic current (oxidation) is reported as positive, while cathodic current (reduction) is reported as negative. During the forward scan, a reduction peak (E_{pc}) is observed, while in the reverse scan, the corresponding oxidation peak (E_{pa}) appears. The peak current intensities (i_{pc} and i_{pa}) are related to the concentration of the electroactive species and the rate of the process. The area under the peaks is proportional to the number of electrons exchanged. The shape and symmetry of the voltammogram provide valuable information on the system's reversibility, electron transfer kinetics, and redox species stability.

From a theoretical standpoint, the analysis is based on the Nernst equation (equation 2.1), which describes the dependence of the electrode potential on the concentration of the redox species [1,4]:

$$E = E^0 + \frac{RT}{nF} \ln \left(\frac{[Ox]}{[Red]}\right) \qquad \text{Eq 2.1}$$

where E is the applied potential, E^0 is the standard potential, n is the number of electrons transferred, F is the Faraday constant, R is the universal gas constant, and T is the absolute temperature.

This relationship is particularly relevant under reversible conditions, when the redox equilibrium is maintained at the electrode, solution interface and the current is controlled by the diffusive transport of the species. The standard potential (E^0) can be estimated as the average of the anodic peak (E_{pa}) and cathodic peak (E_{pc}) potentials (Equation 2.2).

$$E^0 = \frac{E_{pa} + E_{pc}}{2} \qquad \text{Eq 2.2}$$

This expression is valid for reversible or quasi-reversible systems, in which the electron transfer is sufficiently fast to maintain redox equilibrium at the electrode–solution interface during the potential sweep. Moreover, in a fully reversible system, the ratio between the anodic and cathodic peak currents approaches unity (Equation 2.3):

$$\frac{i_{pa}}{i_{pc}} \approx 1 \qquad \text{Eq 2.3}$$

Deviations from these theoretical values are indicative of kinetic limitations or surface adsorption phenomena [53], [54]. Bard and Faulkner [49], as well as Heinze [54] and Kissinger & Heineman [53], have extensively analyzed the criteria that distinguish reversible, quasi-reversible, and irreversible systems based on the current–potential response and the influence of the scan rate.

The scan rate (ν, expressed in V/s) is a critical parameter, as it determines the time scale of the process and significantly influences the shape of the voltammogram. At low scan rates, the system tends to behave reversibly, whereas at high scan rates, capacitive effects and kinetic limitations become more prominent.

The time-dependent potential profile can be described by the following equation 2.4 and 2.5:

$$E(t) = E_i + \nu t \ (forward\ sweep) \qquad \text{Eq. 2.4}$$

$$E(t) = E_s - \nu t \ (reverse\ sweep) \qquad \text{Eq. 2.5}$$

The total current measured during a cyclic voltammetry experiment is the sum of a faradaic component, arising from electron transfer reactions, and a capacitive component, associated with the formation of the electrical double layer at the electrode/solution interface. The latter can become predominant at high scan rates, potentially masking faradaic information and requiring careful selection of experimental parameters [50], [53].

Before the working electrode is connected to the potentiostat and immersed in solution, the electrons in the metallic electrode occupy a continuous distribution of energy levels, with the highest occupied level, known as the Fermi level, representing the energy of the most easily removable electron [49], [52]. The application of an external potential modulates the energy of the electrons in the metal and thus their ability to transfer to or from redox species in solution.

When the applied potential is sufficiently negative, the energy of the electrons in the electrode increases, enabling transfer to oxidized species in solution and generating a reduction current. Conversely, a positive potential lowers the electronic energy, facilitating the transfer of electrons from reducing species in solution to the electrode, resulting in oxidation. In both cases, the magnitude of the current measured is proportional to the number of electrons transferred and, therefore, to the amount of reactive species involved in the process [49], [51]. In the presence of adsorbed species on the electrode surface, the peak current is proportional to the scan rate ($i_p \propto \nu$), while in diffusion-controlled systems, it follows the relation $i_p \propto \nu^{1/2}$, thereby enabling identification of the dominant mass transport mechanism [51].

2.1.2 Calculation of diffusive and kinetic parameters: Randles–Ševčík and Laviron equations

In the context of cyclic voltammetry, the quantitative analysis of peak current provides fundamental information about the diffusive and kinetic behavior of the redox species under investigation. Specifically, under reversible and diffusion-controlled conditions, the peak current observed in the voltammogram can be described by the Randles–Ševčík equation (2.6), which, at 25 °C, takes the following form [49]:

$$i_p = (2.69 * 10^5) n^{\frac{3}{2}} A D^{\frac{1}{2}} C \nu^{\frac{1}{2}} \qquad \text{Eq. 2.6}$$

where i_p is the peak current (Ampere), n is the number of electrons transferred, A is the electrode area (cm^2), D is the diffusion coefficient (cm^2/s), C is the concentration of the redox species (mol/cm^3), and ν is the scan rate (V/s).

Using the Randles–Ševčík equation, the diffusion coefficient (D) can be experimentally determined by plotting i_p as a function of $\nu^{1/2}$; the linearity of the resulting curve and its slope provide a direct indication of the mobility of the redox species. However, this relationship is valid only for reversible systems, in which the separation between redox peaks remains constant (ideally ~59/n mV at 25 °C), the ratio of anodic to cathodic peak currents is close to unity, and no significant adsorption or chemical instability effects are observed [50].

When studying systems that deviate from ideal reversibility, for instance, an increase in peak separation ΔEp with increasing scan rate or asymmetric peak shapes, it becomes necessary to adopt models that incorporate the kinetics of electron transfer. In such cases, the Laviron model enables the extraction of key kinetic parameters, namely the standard heterogeneous rate constant k^0 (cm/s) and the electron transfer coefficient α (dimensionless) [52]. The method is based on the observation that, under slow electron transfer conditions, the peak potential shifts with scan rate according to a logarithmic relation 2.7 :

$$E_p = E^0 + \frac{RT}{\alpha n F} \ln\left(\frac{RTk^0}{\alpha n F}\right) \qquad \text{Eq. 2.7}$$

where E_p is the peak potential (anodic or cathodic) (V), E^0 is the standard potential of the redox couple (V), R is the universal gas constant 8.314 ($J \cdot mol^{-1} \cdot K^{-1}$), T is the absolute temperature (K), F is the Faraday constant 96485 ($C \cdot mol^{-1}$), ν is the scan rate (V/s), α is the transfer coefficient, and k^0 is the standard rate constant (cm/s). This equation is applicable in the quasi-reversible regime and in the absence of mass transport limitations, such as for adsorbed systems or high scan rate experiments [49]

Experimentally, the method involves recording a series of voltammograms at increasing scan rates and plotting E_p as a function of ln (ν). Linear analysis of the resulting data allows the extraction of α and k^0 from the slope and intercept of the line, which describe the asymmetry of the reaction energy profile and the rate of electron transfer at the electrode–solution interface, respectively. Values of $k^0 > 10^{-2}$ cm/s indicate fast electrochemical reactions, whereas values below 10^{-2} cm/s are typical of slow, kinetically hindered systems [[49]]. The combined use of the Randles–Ševčík and Laviron equations provides a comprehensive overview of the electrochemical behavior of redox species, enabling the distinction between diffusion-limited and kinetically limited processes. This approach is particularly valuable in the investigation of new electrolytes for redox flow batteries, where an in-depth understanding of transport properties and interfacial kinetics is a fundamental criterion for the selection of efficient and stable redox couples.

2.1.3 Electrochemical Impedance Spectroscopy (EIS)

Electrochemical Impedance Spectroscopy (EIS) is an analytical technique widely employed to investigate the dynamic processes occurring at the electrode/electrolyte interfaces in electrochemical systems. Its versatility makes it an essential tool for the characterization of batteries, supercapacitors, fuel cells, and in particular redox flow batteries (RFBs), where it enables the separation and quantification of resistive and capacitive contributions responsible for ohmic losses and kinetic limitations within the cell [49], [55].

The technique is based on the application of a small-amplitude sinusoidal voltage signal, typically a few millivolts, to the system under investigation, and the measurement of the resulting current. In the linear regime, the system responds with a sinusoidal current that is phase-shifted with respect to the applied signal by an angle φ, from which the complex impedance Z(ω) (Ω) can be defined as (equation 2.8):

$$Z(\omega) = \frac{E(\omega)}{I(\omega)} Z'(\omega) + jZ''(\omega) \qquad \text{Eq. 2.8}$$

where Z' is the real (resistive) component (Ω), Z'' is the imaginary (reactive) component (Ω), I is the resulting current (A), ω=2πf is the angular frequency of the applied signal (rad/s), f is the frequency (Hz) and j is the imaginary unit (j^2=-1).

This impedance is typically analyzed through graphical representations, each highlighting specific aspects of the electrochemical response. Figure 2.2 shows a Nyquist plot representing the typical frequency response of an electrochemical system, accompanied by its corresponding equivalent circuit. In this type of plot, the imaginary component of the impedance (−Z'') is shown on the y-axis, while the real component (Z') is shown on the x-axis.

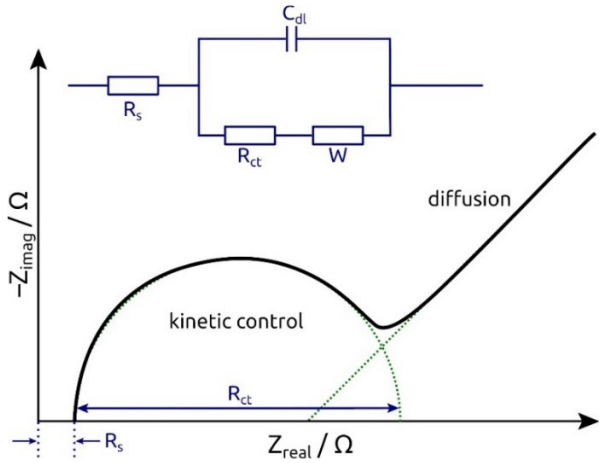


Figure 2.2: Nyquist Plot fitted with an equivalent electrical circuit model [56].

At high frequencies, the trace starts at a point on the real axis corresponding to the ohmic resistance R_s, which includes the contributions from the electrolyte, membrane, and contact resistances. As the frequency decreases, a semicircular arc appears, representing the capacitive behavior of the electrical double layer and the charge

transfer resistance R_{ct}. The size of the arc is directly related to the value of R_{ct}, while its shape may be influenced by non-ideal effects such as surface roughness or distributions in time constants.

The equivalent circuit shown at the top of the figure reproduces this behavior using a classical model known as the Randles circuit. It consists of a resistance R_s in series with a parallel branch formed by the charge transfer resistance R_{ct} and the double-layer capacitance C_{dl}; these elements are followed by a Warburg element W, which accounts for the diffusion-related impedance that becomes significant at low frequencies.

Indeed, at low frequencies, the plot extends into a straight line with a slope of approximately 45°, characteristic of semi-infinite linear diffusion. This portion of the curve reflects mass transport limitations of redox species within the cell and is mathematically described by the Warburg impedance (equation 2.9) [49], [57].

$$Z_W(\omega) = \frac{\sigma}{\sqrt{(j\omega)}} \qquad \text{Eq. 2.9}$$

where $Z_W(\omega)'$ is the Warburg diffusion impedance (Ω), σ is Warburg coefficient ($\Omega \cdot s^{1/2}$), ω is the angular frequency (rad/s), and j is the imaginary unit (j^2=-1).

Figure 2.3 shows the Bode plot (magnitude), a complementary representation in which the magnitude of the impedance |Z| is plotted as a function of frequency (on a logarithmic scale).

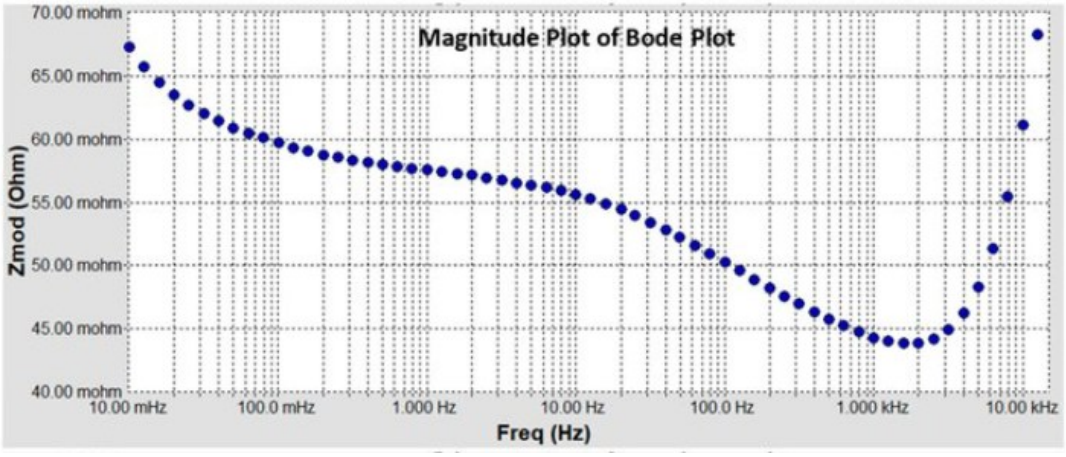


Figure 2.3: Impedance magnitude as a function of frequency (Bode plot) [58].

At low frequencies, the impedance increases due to slow diffusive and capacitive processes, while at high frequencies, the ohmic component dominates. This behavior helps to identify the dominant regimes of ionic conduction, redox reactions, and diffusion across the frequency spectrum [59].

Figure 2.4 shows the Bode plot (phase), which illustrates the phase angle variation between voltage and current as a function of frequency.

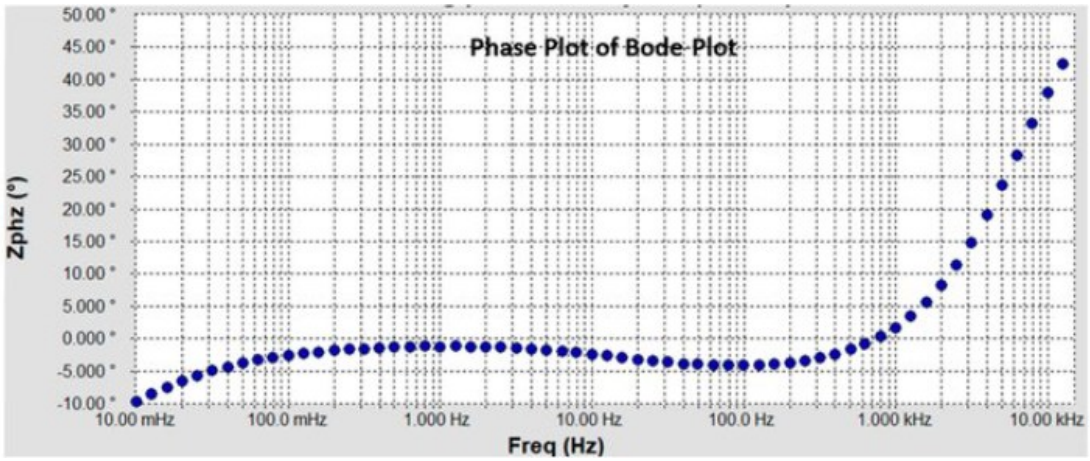


Figure 2.4: Phase angle as a function of frequency (Bode plot) [58].

Phase angles near 0° indicate resistive behavior, while those approaching −90° are typical of capacitive response. The evolution of the phase angle across the frequency range allows for identifying the dominant mechanisms and distinguishing between RC-type and mixed responses.

EIS is particularly valuable for the characterization of ion exchange membranes and electrolytes in redox flow batteries. Membranes significantly contribute to the internal resistance of the cell and may undergo chemical degradation over time. Measurements performed on symmetric cells, in which both compartments contain identical electrolyte and electrode materials, allow for the exclusion of redox reaction contributions, isolating the membrane's resistive and capacitive response. This enables the evaluation of membrane stability, ionic conductivity, and selectivity over time. Similarly, EIS enables the comparison of different electrolyte systems. The chemical nature of redox species, their mobility, and the degree of complexation influence the charge transfer resistance and diffusional processes. Impedance analysis thus provides a powerful tool to assess the efficiency of different electrolytes, facilitating the selection of species that are more reactive, stable, and less resistive [57], [60]. Over time, EIS has established itself not only as a technique for equilibrium characterization but also as a diagnostic tool under operational conditions. In particular, the application of low-amplitude signals superimposed on a constant charge or discharge current (galvanostatic mode) enables real-time monitoring of internal resistance evolution, interfacial layer formation, or variations in membrane conductivity throughout the battery's operating cycle. This approach is increasingly used in the development and testing of redox flow batteries at both laboratory and pre-industrial scales [56].

2.1.4 Charge and Discharge Cycles in Redox Flow Batteries

Charging a battery involves applying a potential difference between the electrodes to convert electrical energy from an external source into chemical energy stored within the electrochemical system. Discharging is the reverse process, in which the stored chemical energy is released as electrical current to power an external load. In redox flow batteries (RFBs), energy is not stored in solid materials but in liquid electrolytes containing redox-active species, which continuously circulate through the electrochemical cell during the charge–discharge process. The electrolytes are pumped from external reservoirs through porous carbon felt electrodes

separated by an ion-selective membrane that allows ionic conduction while preventing the crossover of redox species [37], [61].

Charge–discharge tests are typically performed under galvanostatic conditions, i.e., at constant current, using a potentiostat/galvanostat capable of precisely controlling both voltage and current limits of the cell.

In this work, the experiments were conducted using a Neware CT-4008Tn-5V6A-S1 potentiostat, shown in Figure 2.5, a high-precision instrument designed for battery and electrochemical cell characterization, capable of operating over a wide current and voltage range with excellent measurement accuracy.



Figure 2.5: Neware CT-4008Tn-5V6A-S1 potentiostat/galvanostat used for the charge–discharge cycling tests of redox flow battery cells.

During the charging phase, the applied current induces oxidation of the reduced species in the anolyte and reduction of the oxidized species in the catholyte. During discharge, the reactions are reversed, releasing the stored energy back to the external circuit. The cell voltage is continuously monitored as a function of time, producing characteristic voltage–time profiles for each cycle [62]. The electrochemical performance of the battery is evaluated in terms of efficiencies and capacities, parameters that provide insight into the reversibility of the system and its overall energy losses.

The coulombic efficiency (CE), also referred to as amp-hour efficiency, expresses the degree of reversibility of the redox process and is defined as in the equation 2.10 [63]:

$$CE = \frac{Q_{\text{disch}}}{Q_{ch}} * 100 \qquad \text{Eq. 2.10}$$

Where Q_{disch} and Q_{ch} are the total charges transferred during discharge and charge, respectively, expressed in Coulomb (C).

The voltaic efficiency (VE) quantifies the effect of ohmic, activation, and mass-transport losses, and is defined as in the equation 2.11 [63]:

$$VE = \frac{V_{\text{avg,disch}}}{V_{avg,ch}} * 100 \qquad \text{Eq. 2.11}$$

where $V_{avg,disch}$ and $V_{avg,ch}$ are the average discharge and charge voltages, respectively, expressed in volts (V).

The energy efficiency (EE) provides a global assessment of the system's ability to store and recover energy, accounting for both charge-transfer and voltage losses as in the equation 2.12 [63]:

$$EE = CE * VE \qquad \text{Eq. 2.12}$$

The capacity retention represents the conservation of discharge capacity over cycling and is defined as in the equation 2.13 [63]:

$$Capacity\ Retention = \frac{Q_{\text{disch,n}}}{Q_{\text{disch,1}}} * 100 \qquad \text{Eq. 2.13}$$

where $Q_{disch,n}$ (C or Ah) is the discharge capacity at the *n*-th cycle and $Q_{disch,1}$ (C o Ah) is the capacity at the first cycle .

A high-capacity retention and stable efficiency values indicate good redox reversibility, chemical stability of the active species, and mechanical integrity of the separator membrane [64], [65].

During cycling, the voltage window is strictly controlled to prevent overcharging or over-discharging, which can lead to degradation of the active materials or side reactions. Typical current densities applied in RFB testing range from 10 to 100 $mA \cdot cm^{-2}$, depending on the electrolyte composition and operating conditions.

Lower current densities yield smaller overpotentials and higher VE, while higher current densities improve CE but reduce VE due to increased ohmic polarization [66].

The evolution of CE, VE, EE, and capacity retention as a function of cycle number provides direct insight into the cycling stability and long-term durability of the RFB. In general, stable systems exhibit CE > 95%, VE > 80%, and overall EE > 75% after tens or hundreds of cycles[41].

In addition to galvanostatic cycling, polarization (I–V) and power-density curves are often recorded by varying the applied current incrementally, enabling the determination of internal resistance, maximum power density ($W \cdot cm^{-2}$), and overall efficiency under different loads. These measurements complete the electrochemical characterization of the redox flow cell and enable comparison of different redox couples and membranes under realistic operating conditions [67].

2.2 Morphological and compositional analysis techniques

2.2.1 Scanning Electron Microscopy (SEM)

Morphological analyses of the electrodes were carried out using a Scanning Electron Microscope (SEM, model SNE-Alpha, SEC Co., Ltd., South Korea), shown in Figure 2.6.



Figure 2.6: SNE-Alpha Scanning Electron Microscope (SEC Co., Ltd., South Korea) used for morphological characterization of the electrodes used at University of Brescia.

The SNE-Alpha is a high-resolution, compact benchtop SEM offering comparable performance to floor-standing instruments. It provides a resolution down to 5 nm and a magnification range up to 250,000×, operating within an accelerating voltage range of 1–30 kV. The system is equipped with detectors for secondary electrons (SE) and backscattered electrons (BSE), enabling both topographical and compositional

imaging. It features a 5-axis motorized stage with sub-5 μm positioning precision and supports automated multi-position scanning. Advanced functionalities such as Auto Gun Align and Auto Focus enhance the repeatability and accuracy of image acquisition. The operating parameters, accelerating voltage, beam current, and working distance, were optimized according to the sample conductivity and the desired level of resolution. Prior to observation, the samples were dried and, when necessary, coated with a thin conductive layer of carbon or gold to minimize surface charging effects and improve image quality.

Its operating principle is based on the interaction between a focused electron beam and the sample surface: the incident electrons, accelerated by a controlled electric field, penetrate the upper layers of the material, generating a variety of secondary signals, secondary electrons, backscattered electrons, and characteristic X-rays, that are detected and converted into images or emission spectra [68], [69]. Secondary electrons (SE) provide topographical information and highlight fine surface details with resolutions down to a few nanometres, while backscattered electrons (BSE) produce compositional contrast, as their intensity is strongly dependent on the average atomic number of the analyzed region. The combined acquisition of both signals enables a simultaneous visualization of surface microstructure and compositional heterogeneity [68].

In this work, SEM was employed to characterize the surface of the carbon felt electrode used during charge–discharge cycling tests in the redox flow battery. The main objective of these analyses was to detect the presence of bismuth (Bi) deposits formed during the electrochemical cycling. As reported by Qiao et al. [70], in the Fe/Ti redox system, bismuth can be electrodeposited in situ onto the surface of the felt during the charging phase, forming a thin metallic layer that acts as a catalyst for the Ti^{3+}/TiO^{2+} redox couple. This deposit facilitates electron transfer and decreases interfacial resistance, thereby enhancing the electrocatalytic activity of the electrode material and improving the reversibility of the redox reactions. The presence of Bi has been correlated with a significant increase in peak currents and with higher coulombic efficiency during long-term cycling tests [71], [72]. SEM imaging enabled the identification of Bi particles distributed across the surface of the carbon felt, allowing evaluation of their homogeneity and size.

Post-cycling morphological observations also made it possible to verify the structural stability of the carbon substrate and to identify possible degradation phenomena, such as surface roughening, fragmentation, or the formation of thin surface films. Such morphological information was essential to correlate electrode microstructure with the electrochemical behavior observed in the flow cell tests, providing direct evidence of the link between surface architecture and catalytic performance.

Therefore, the use of SEM provided a non-destructive, high-resolution morphological characterization of the electrodes, offering experimental evidence of the effectiveness of bismuth deposition as a catalyst and of the structural role of the carbon felt substrate. These morphological investigations are crucial to understanding the activation and stability mechanisms of the Ti^{3+}/TiO^{2+} couple and represent a key complement to the electrochemical and spectroscopic analyses presented in this study.

2.2.2 Total Reflection X-Ray Fluorescence (TXRF)

The compositional analysis of the electrolytes was performed by means of Total Reflection X-Ray Fluorescence (TXRF) spectroscopy, a highly sensitive and non-destructive analytical technique used for the identification and quantification of metallic elements and trace components in both liquid and solid matrices. Measurements were carried out using a benchtop TXRF spectrometer (model Horizon, G.N.R. S.r.l., Italy), shown in Figure 2.7, equipped with a molybdenum X-ray tube coupled to a W/Si multilayer monochromator to generate a Mo-Kα excitation beam (17.44 keV).



Figure 2.7: Horizon TXRF spectrometer (G.N.R. S.r.l., Italy) used for compositional analysis of the electrolytes used at University of Brescia.

The instrument operates at an accelerating voltage of 40 kV and a current of 15 mA in air. It is fitted with a high-resolution silicon drift detector (SDD), which enables simultaneous multi-element detection with detection limits below the ppb range. The Horizon system combines compact design with high analytical performance, allowing accurate quantification of trace elements in small liquid aliquots while minimizing sample consumption.

TXRF operates on the same physical principle as conventional X-Ray Fluorescence (XRF), but under total reflection conditions. The primary X-ray beam impinges on the sample at an incidence angle smaller than the critical angle for total reflection (typically < 0.1°), thus avoiding penetration into the substrate and interacting only with the thin sample layer deposited on a highly polished reflector, usually made of quartz or silicon.

This geometry drastically reduces background scattering, improving the signal-to-noise ratio and enabling accurate quantitative determination of trace elements with excellent precision [73], [74].

In this work, TXRF was employed for two main purposes. Firstly, it was used to detect the presence of bismuth (Bi) in the liquid electrolytes collected after electrochemical testing, in order to monitor the stability of the metal in solution and any release of Bi^{3+} ions during charge–discharge cycling. Secondly, TXRF was crucial to evaluate the ionic crossover phenomenon in separated-electrolyte tests, in which the Fe/Ti flow battery was formulated with $TiOSO_4$ in sulfuric acid as the anolyte and $FeSO_4$ in sulfuric acid as the catholyte. The purpose of these tests was to determine whether Fe^{2+}/Fe^{3+} ions crossed the ion-exchange membrane and migrated into the anodic compartment, or conversely, whether traces of titanium species were detected in the catholyte. The detection of even small amounts of iron in the anolyte, or titanium in the catholyte, was interpreted as evidence of cross-transfer between the two compartments, a phenomenon that can compromise the long-term stability and coulombic efficiency of the Fe/Ti redox flow battery.

Thanks to the high sensitivity of TXRF, it was possible to quantify these metallic species with great accuracy, providing clear evidence of any diffusion phenomena through the membrane and assessing the efficiency of ionic separation. The results obtained offered valuable insight into the chemical stability of the electrolyte systems and supported the optimization of the membrane materials employed in the flow battery [71].

2.2.3 Raman Spectroscopy

Raman analyses were performed at the CIC energiGUNE Research Center (Vitoria-Gasteiz, Spain) within the framework of a scientific collaboration, using a Renishaw InVia confocal Raman spectrometer coupled with a Nanonics Multiview 2000 microscope for Tip-Enhanced Raman Spectroscopy (TERS) measurements, as shown in Figure 2.Z.

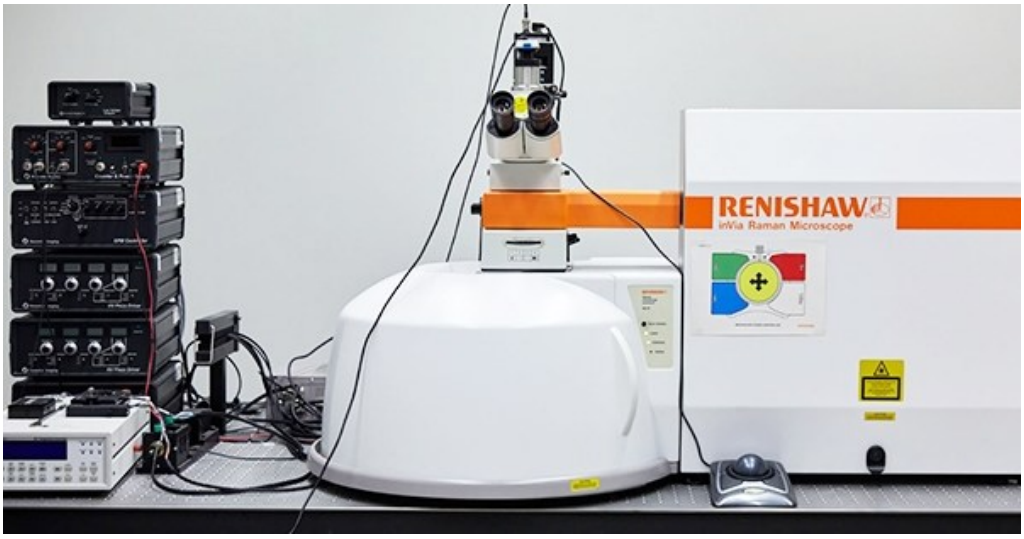


Figure 2.8: Renishaw InVia *confocal Raman spectrometer coupled with Nanonics* Multiview 2000 TERS *microscope used at the CIC energiGUNE Research Center (Vitoria-Gasteiz, Spain).*

This instrument allows both conventional Raman measurements in confocal configuration and high-spatial-resolution analyses through the combination with an AFM probe, enabling the acquisition of TERS spectra with nanometric resolution. It is equipped with excitation lasers at 532 nm and 785 nm, a high-resolution

diffraction grating (1200 l/mm), and a thermoelectrically cooled CCD detector that ensures high sensitivity even for weak signals. The confocal optics, combined with an automatic focusing system, allow spectral resolution below 1 cm^{-1} and spatial resolution on the micrometres scale. Raman spectroscopy is a non-destructive analytical technique based on the inelastic scattering of monochromatic light (Raman effect). When a laser beam interacts with the sample, a small fraction of the scattered radiation experiences an energy shift corresponding to the vibrational and rotational modes of the molecules. The analysis of these energy shifts provides detailed information on the chemical structure, bonding environment, coordination state, and molecular symmetry of the analyzed species [75], [76]. Compared with other spectroscopic techniques, Raman spectroscopy stands out for its high vibrational specificity, its ability to analyze samples in concentrated or strongly acidic solutions, and its sensitivity to ionic interactions and structural modifications without requiring complex sample preparation or causing any alteration to the sample. The confocal optical configuration enables three-dimensional chemical mapping, while the integration with the TERS mode allows nanoscale characterization, combining the topographic resolution of AFM with the molecular sensitivity of Raman spectroscopy [77].

In this work, Raman spectroscopy was employed as a complementary characterization tool to electrochemical and TXRF analyses, with the aim of achieving a molecular-level description of the electrolyte system used in the Ti–Fe redox flow batteries [78], [79]. The technique was used to identify the predominant chemical species in titanium- and iron-based electrolytes, verify the structural integrity of the metal complexes in sulfuric acid environment, and exclude the formation of mixed complexes or unwanted interactions between the two redox couples in the mixed electrolyte configuration. More broadly, the Raman approach allowed the correlation between the molecular structure in solution and the electrochemical behavior observed during galvanostatic tests, providing an integrated view of the system and an experimental foundation for understanding the stability and reversibility of the Ti^{3+}/Ti^{4+} and Fe^{2+}/Fe^{3+} redox couples.

3 *Analysis and Development of the Ti–Fe Redox System in Sulfuric Acid*

3.1 The Choice of the Ti–Fe System: State of the Artand Application Perspectives

Within the expanding landscape of stationary energy storage technologies, redox flow batteries (RFBs) have emerged as one of the most versatile solutions to manage the intermittency of renewable energy sources. Among the most established systems, the vanadium redox flow battery (VRFB) has long represented the benchmark due to its high chemical stability and reversible redox behavior. However, the high cost of vanadium, its limited availability, and environmental concerns associated with its life cycle have progressively driven research toward alternative chemistries based on more abundant and sustainable elements. In this context, the hybrid Titanium/Iron (Ti–Fe) redox system offers a promising configuration that combines two well-known redox couples, Ti (IV)/Ti (III) and Fe (III)/Fe (II), operating in a strongly acidic medium, typically sulfuric acid. This system emerges as a viable alternative to VRFBs, offering a more favorable economic and environmental profile. The decision to investigate the Ti–Fe system stems from an integrated evaluation of raw material availability, electrolyte simplicity, and practical feasibility. Titanium is a non-critical, non-toxic element, abundantly present in the Earth's crust (~0.6 wt%) and commercially available in soluble forms such as $TiOSO_4$. Iron, on the other hand, is already extensively employed in redox systems due to its excellent reversibility, ultra-low cost, and operational stability. The combination of these two half-cells allows for the design of a redox battery operating in acidic conditions, using abundant, low-impact, and inexpensive materials. However, despite its potential, the Ti–Fe system still presents several limitations that have so far hindered its technological maturity. In particular, the Ti (IV)/Ti (III) redox couple suffers from intrinsically slow electron-transfer kinetics, resulting in poor charge/discharge efficiency unless appropriate electrocatalysts are employed [70]. Furthermore, the speciation of Ti(IV) is highly pH-dependent and requires extremely acidic environments to avoid irreversible hydrolysis and precipitation as colloidal TiO_2 [80], [81]. In addition, the high concentrations of sulfuric acid needed to stabilize titanium raise serious corrosion concerns, requiring careful selection of cell materials and membranes Reduction of Ti(IV) species in aqueous sulfuric and hydrochloric acids Titanium speciation [82].

Despite these challenges, the Ti–Fe system retains strong potential, and addressing these open issues constitutes a timely and relevant scientific goal and the starting point of the present research. Before undertaking the experimental investigation of the complete flow cell, an in-depth characterization of the titanium-based anodic half-cell was conducted, in order to elucidate its solution chemistry, redox stability, and, above all, the kinetics of the electron transfer process in sulfuric acid media.

To fully understand the limitations associated with the use of titanium in redox batteries, it is helpful to briefly retrace the scientific development of this metal, highlighting the key challenges reported in the literature and the strategies proposed in recent studies.

3.2 Chemical and Electrochemical Behavior of Titanium in Sulfuric Acid

Titanium in its oxidized form, Ti(IV), is one of the most chemically complex redox-active species to manage in aqueous systems, especially when compared to more established elements used in redox flow batteries, such as vanadium. Unlike vanadium, which exhibits well-defined and reversible redox couples in strongly acidic media, titanium poses multiple challenges related to its solution-phase stability and its electron transfer kinetics. In sulfuric acid, Ti(IV) exists not as a free ion but primarily as the titanyl ion (TiO^{2+}), a linear and highly electrophilic species that readily coordinates with sulphate (SO_4^{2-}) and bisulphate (HSO_4^-) anions, forming a range of complexes such as $[TiO(SO_4)]$, $[TiO(SO_4)_2]^{2-}$, $[Ti(OH)_2(SO_4)_2]^{2-}$ and polynuclear structures [71], [80], [83]. The distribution and prevalence of these species are critically dependent on the acid concentration and Ti/SO_4 molar ratio, which directly affect the solubility, redox potential, and speciation stability. At pH values above 1.5, these complexes rapidly lose stability, and Ti(IV) undergoes hydrolysis, forming colloidal $TiO_2 \cdot xH_2O$ precipitates and effectively removing the active species from solution. This behavior significantly limits the operational window for titanium-based systems and demands highly acidic conditions ($\geq$ 3–4 M H_2SO_4) to maintain chemical speciation under control. Moreover, identifying the specific solution-phase species is complex: spectroscopic techniques such as FT-Raman, UV-Vis, and EXAFS, along with theoretical simulations, have shown that the equilibrium between monomeric and polynuclear forms is highly dynamic and influenced by parameters such as temperature, ionic strength, and trace metal contaminants [84]. This behavior is well summarized by the Pourbaix diagram of titanium, which outlines the thermodynamic stability domains of Ti(IV), Ti(III), and solid TiO_2 as a function of pH and electrochemical potential (Figure 3.1). In highly acidic and oxidizing conditions (pH < 1.5 and E > 0.1 V vs. SHE), Ti(IV) exists as soluble TiO^{2+}. Ti(III), conversely, is only stable under more reducing conditions, and both forms tend to precipitate as TiO_2 at pH values above ~2 [85].

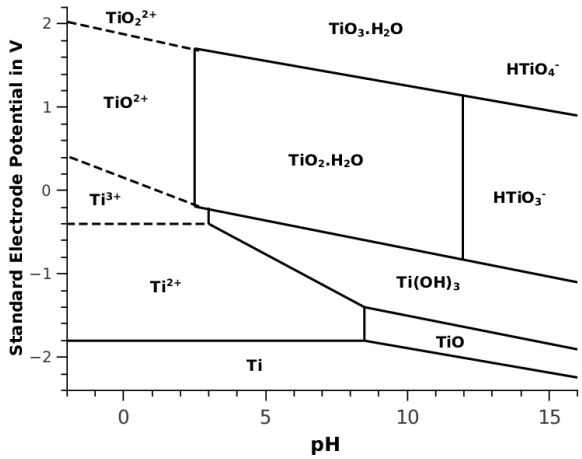


Figure 3.1: Pourbaix-diagram of titanium[86] .

Thermodynamically, the Ti(IV)/Ti(III) redox couple is suitable for use in flow battery systems (~0.1–0.2 V vs. SHE), but its electron transfer kinetics are inherently sluggish. Electrochemical studies report broad peak

separations, low peak currents, and the absence of diffusion-limited plateaus, features characteristic of slow and partially irreversible redox systems governed by multi-step ECE (Electron–Chemical–Electron) mechanisms [87], [88]. These limitations are further exacerbated by electrode surface fouling or the presence of impurities such as Fe^{3+}, Cu^{2+}, and Al^{3+}. Although improvements in reversibility have been achieved through the use of purified sulfuric acid and surface-modified electrodes (e.g., carbon felt coated with Bi or Sb), the overall reversibility of the titanium system remains limited. Furthermore, sulfuric acid, while essential for stabilizing Ti(IV) complexes, contributes to electrolyte corrosivity and places constraints on material compatibility for electrodes, membranes, and cell components.

A central role in Ti(IV) stabilization is played by its complexation with sulphate species. Recent spectroscopic and theoretical studies have confirmed the presence of coordination structures such as $[TiO(SO_4)]$, $[TiO(SO_4)_2]^{2-}$, $[Ti(OH)_2SO_4]$, and $[Ti(OH)_2(SO_4)_2]^{2-}$ [70], [85]. These complexes act as stabilizing agents, limiting hydrolysis and increasing the solubility of Ti(IV) in sulfuric acid. Their formation can be tracked by FT-Raman spectroscopy, where Ti–O–S symmetric stretch bands appear in the range of 995–1010 cm^{-1}. The nature of the coordination (monodentate vs. bidentate) is influenced by acid concentration and temperature. A schematic representation of these coordination modes is shown in Figure 3.2.

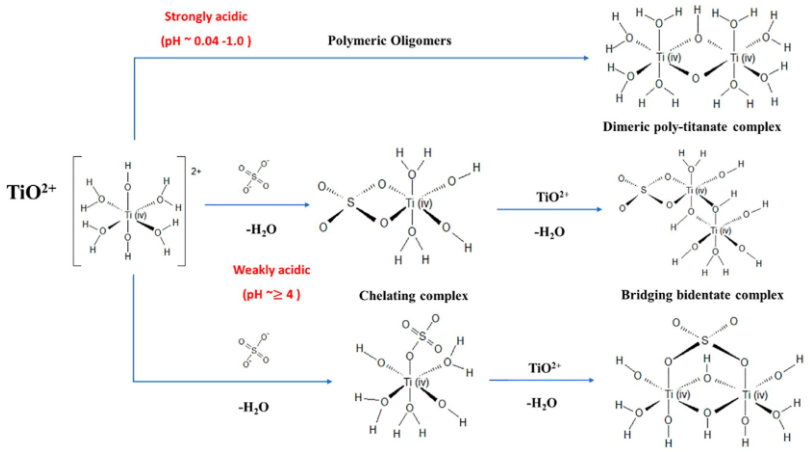


Figure 3.2: Schematic representation of various Ti4+ complexes under weakly and strongly acidic conditions [80].

Furthermore, Figure 3.3 reports a representative FT-Raman spectrum acquired at different H_2SO_4 concentrations. As acidity increases, the intensity of the band at ~1010 cm^{-1} becomes more pronounced, indicating a shift in equilibrium toward the formation of stable bisulphate complexes such as $[Ti(OH)_2(SO_4)_2]^{2-}$ [84].

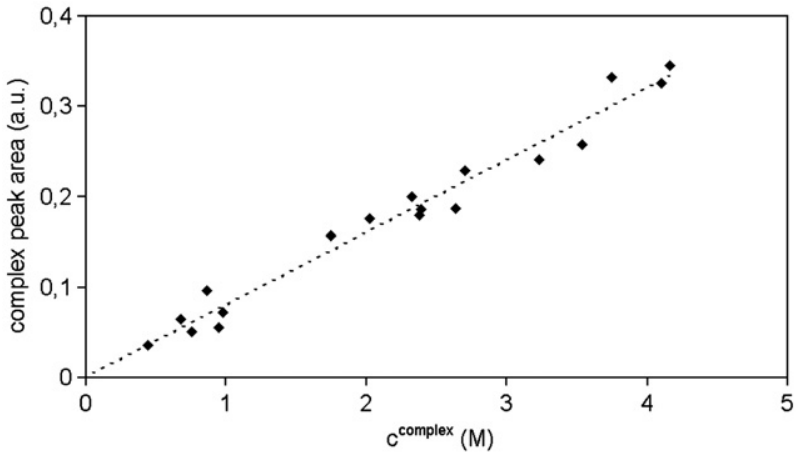


Figure 3.3: FT-Raman spectra of Ti(IV) species in H_2SO_4 solutions at varying acid concentrations.

The band at ~1010 cm^{-1} increases with acidity, indicating the formation of bisulphate-coordinated titanyl complexes [84].

Altogether, these findings underscore the complexity and sensitivity of titanium chemistry in acidic media. Its strong oxygen affinity, dynamic speciation, and kinetic challenges necessitate strict control of formulation parameters. As such, this work includes a dedicated preliminary investigation of the titanium anolyte in sulfuric acid, aiming to define its redox boundaries, evaluate its coordination behavior, and identify optimal conditions for integration into the Ti–Fe redox flow system.

3.3 Preliminary Electrochemical Study of Titanium in Sulfuric Acid

Following the detailed discussion in the previous section on the complex speciation of titanium in sulfuric acid and the thermodynamic constraints affecting its stability, it became essential to experimentally assess its actual redox behavior under controlled conditions. To this end, a preliminary investigation was carried out using cyclic voltammetry, a reference electrochemical technique for qualitatively evaluating the reversibility of redox couples, electron transfer kinetics, and the influence of operating conditions. The objective of this phase was twofold: on one hand, to determine whether the Ti(IV)/Ti(III) redox couple exhibits voltammetric behavior compatible with redox flow battery requirements (in terms of stability, reversibility, and peak definition); on the other, to identify the main operational limitations associated with managing titanium in aqueous H_2SO_4 solutions. The results obtained serve as a foundational benchmark for justifying, in the following sections, the adoption of corrective strategies such as the use of metallic catalysts or electrode surface modifications aimed at improving the performance of the titanium-based system.

3.3.1 Experimental Setup and Instrumentation

The initial experimental campaign aimed at investigating the electrochemical behavior of titanium in sulfuric acid media was conducted at the electroanalytical chemistry laboratories of the University of Brescia. The objective was to obtain a preliminary yet systematic characterization of the Ti(IV)/Ti(III) redox system by evaluating the influence of electrolyte composition on the voltammetric response under simplified and controlled conditions. A classical three-electrode electrochemical cell setup was adopted in order to isolate the

redox couple's behavior in homogeneous solution, avoiding complications related to full-cell configurations, membrane effects, or convective flow. The measurements were performed using a portable PalmSens EmStat Blue potentiostat, a compact single-channel device equipped with a USB interface and PS Trace software for data acquisition and control. The software allowed real-time recording of voltammograms, baseline correction (e.g., zero-current adjustment), and export of data in formats compatible with further analysis. The instrument proved particularly suitable for preliminary studies due to its ease of use and reliability, even in non-shielded laboratory environments.

Figure 3.4 shows the PalmSens EmStat Blue potentiostat used for the electrochemical measurements.

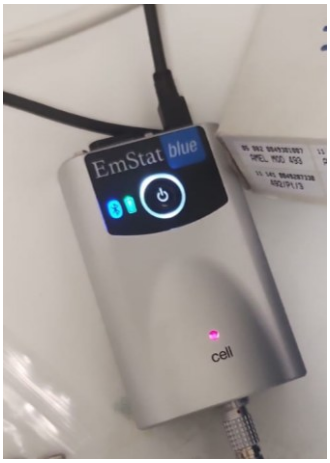


Figure 3.4: PalmSens EmStat Blue portable potentiostat used for voltammetric measurements of the Ti(IV)/Ti(III) redox couple

Experiments were conducted at room temperature (approximately 25 °C). Prior to each scan, the solutions were deoxygenated by continuous nitrogen purging for approximately 15 minutes in order to remove dissolved oxygen, which can interfere with redox processes in acidic media. The voltammetric tests were carried out using a three-electrode electrochemical cell, consisting of a transparent cylindrical container sealed with a threaded cap featuring three separate ports for the electrodes and an additional port for the nitrogen inlet. A photograph of the actual setup is shown in Figure 3.5.



Figure 3.5: Three-electrode electrochemical cell used for voltammetric investigation of the Ti(IV)/Ti(III) redox couple. The image shows the saturated calomel reference electrode (SCE), the glassy carbon working electrode (GC), and the platinum wire counter electrode.

The working electrode was a 3 mm diameter glassy carbon disk, selected for its chemical inertness and wide potential window in acidic environments. The reference electrode was a saturated calomel electrode (SCE), inserted directly into the electrolyte without an external salt bridge. The counter electrode consisted of a platinum wire, also immersed directly into the solution. All electrodes were fixed using sealed adapters integrated into the cap, ensuring mechanical stability and effective isolation from the external environment.

3.3.2 Preparation of the Solutions and Operating Conditions

The working solutions were prepared by dissolving titanium oxysulfate ($TiOSO_4$, ACS reagent, ≥99%, Sigma–Aldrich, Germany) in aqueous sulfuric acid (H_2SO_4, ACS reagent, 95–98%, Sigma–Aldrich, Germany), systematically varying the concentrations of both components. Specifically, for each of the tested titanium concentrations (0.25 M, 0.5 M, 0.75 M, and 1 M), solutions were prepared under four different acidic conditions: 1 M, 2 M, 3 M, and 4 M H_2SO_4. All solutions were prepared in 50 mL volumetric flasks, using ultrapure Millipore (Mill-Q) water for dilution. The preparation procedure involved the initial addition of approximately 50 mL of water, followed by weighing and gradual dissolution of the required amount of $TiOSO_4$ under magnetic stirring. The complete set of electrolyte formulations is summarized in Table 3.1.

Table 3.1: Summary of $TiOSO_4$–H_2SO_4 Electrolyte Preparation Variables

$TiOSO_4$ concentration	**H_2SO_4 concentration**	**Final Volume**
M	**M**	mL
0.25	1	50
	2	
	3	
	4	
0.5	1	50

	2 3 4	
0.75	1 2 3	50
1	1 2 3	50

Upon initial contact with water, the titanium salt imparted a milky-white appearance to the solution, with evident turbidity. However, upon continued stirring, the turbidity gradually disappeared, yielding a clear and transparent solution, with no visible suspended particles or residual solids.

Once complete dissolution of the salt was achieved, the calculated volume of concentrated sulfuric acid was added to reach the desired final molarity. This order of addition, $TiOSO_4$ first, then H_2SO_4, was maintained throughout all experiments, as it was found to favour solution stabilization and to prevent undesired effects such as partial hydrolysis or gel formation.

All solutions were used immediately after preparation, without prolonged storage. In some cases, a nitrogen purging step (approximately 15 minutes) was performed prior to measurement in order to remove dissolved oxygen and minimize unwanted redox activity. Voltammetric measurements were carried out by scanning a potential window between –0.7 V and +0.5 V vs SCE, at scan rates ranging from 5 mV s^{-1} to 60 mV s^{-1}. This experimental setup allowed for the collection of preliminary but significant insights into the reaction kinetics, the definition of the redox peaks, and the possible emergence of secondary phenomena. The results will be discussed in the following section, in light of literature data and the hypotheses outlined previously.

3.4 Voltammetric Behavior of the Ti(IV)/Ti(III) Redox Couple as a Function of Electrolyte Composition

To better understand the influence of electrolyte composition on the electrochemical behavior of the Ti(IV)/Ti(III) redox couple, cyclic voltammetry (CV) measurements were performed on solutions containing various concentrations of $TiOSO_4$ (0.25 M, 0.5 M, 0.75 M, and 1 M) prepared in sulfuric acid (H_2SO_4) at increasing concentrations (1 M, 2 M, 3 M, and 4 M) (see Table 3.1). The results are presented in Figure 3.6, where each panel (a–d) shows the voltammetric response of a given $TiOSO_4$ concentration as a function of the acid strength of the medium.

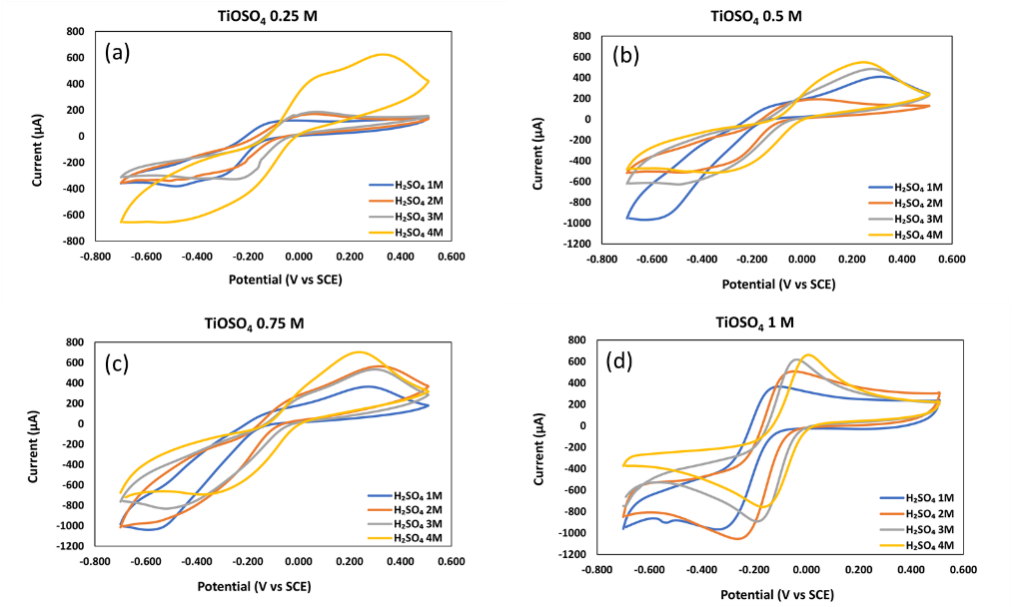


Figure 3.6: Cyclic voltammetry of the Ti(IV)/Ti(III) system obtained for solutions of (a)0.25M,(b)0.5M,(c)0.75M, and(d)1M $TiOSO_4$, each tested in 1 – 4M H_2SO_4. Measurements were conducted at 10mV s^{-1} in a three-electrode half-cell (GC, Pt, SCE) in the range from –0.7 to +0.5V vs SCE.

As the concentration of sulfuric acid increases, the voltammetric curves display a progressive enhancement of the redox peak currents (both anodic and cathodic), along with an improved definition of the peaks, suggesting an increase in the system's reversibility and a higher electron transfer efficiency. As shown in Figure 3.6a, the response for 0.25 M $TiOSO_4$ is characterized by broad and poorly defined redox waves at low acidity, whereas in the presence of 4 M H_2SO_4 a marked increase in peak currents and a more symmetric shape of the redox waves are observed. This behavior is consistent with literature reports indicating that higher sulfuric acid concentrations favour the formation of stable complexes between TiO^{2+} and SO_4^{2-}, such as $[Ti(OH)_2SO_4]$ and $[Ti(OH)_2(SO_4)_2]^{2-}$, which prevent Ti(IV) hydrolysis and enhance the electrochemical stability of the electrolyte [71], [80]. In the case of 0.5 M $TiOSO_4$ (Figure 3.6b), the voltammetric response becomes more intense and regular, with a reduced peak-to-peak separation (ΔE_p) and increased current intensity. The increase in acidity causes a shift of the cathodic peak toward less negative potentials, indicating a more reversible and kinetically favorable redox process. As previously reported by Lisitsyn et al. [85], acidic media promote the stabilization of coordinated sulfate complexes that improve the electron transfer kinetics of the Ti(IV)/Ti(III) system, resulting in behavior closer to ideal reversibility. At higher concentrations, 0.75 M $TiOSO_4$ (Figure 3.6c) shows a further increase in peak current, consistent with the higher concentration of redox-active species in solution, and a further narrowing of the peak separation. The voltammetric curves become more symmetric and defined at 3 M and 4 M H_2SO_4, indicating more efficient diffusion and reduced charge transfer resistance, in agreement with the findings of Ahmed et al. [89]. However, a slight broadening of the redox waves is sometimes observed, possibly due to overlapping redox processes associated with multiple titanium complexes, as suggested by speciation studies [84], [90]. At the highest concentration examined, 1 M $TiOSO_4$ (Figure 3.6d), the voltammetric response features well-defined peaks with significant current intensity, particularly in 3 M and 4 M H_2SO_4, where the best compromise between signal intensity, symmetry, and reproducibility is achieved.

Under these conditions, the reduction of Ti(IV) to Ti(III) appears faster and more reversible, supporting the idea that high acid concentrations stabilize the TiO^{2+} species and suppress hydrolysis or insoluble complex formation [81]. Nonetheless, at high concentrations of both $TiOSO_4$ and H_2SO_4, slight distortions in the voltammetric baseline may arise, potentially due to surface adsorption phenomena on the electrode surface or increased viscosity of the electrolyte, which can affect the diffusivity of the redox species [82].

Overall, the voltammetric analysis clearly demonstrates that both $TiOSO_4$ and H_2SO_4 concentrations critically influence the redox behavior of the system. The most intense, stable, and reproducible responses were obtained with 1 M $TiOSO_4$, particularly in combination with 3 M or 4 M H_2SO_4. These conditions were therefore selected as reference for further kinetic and diffusional investigations, which will be explored in the following section through the application of the Randles–Ševčík and Laviron equations.

3.4.1 Influence of Scan Rate on the Electrochemical Behavior of the Ti(IV)/Ti(III) Redox Couple (1 M $TiOSO_4$) in Sulfuric Acid

Building upon the observations discussed in the previous section, which highlighted how the sulfuric acid concentration strongly affects the reversibility and definition of the redox peaks, the system containing 1 M $TiOSO_4$ was selected as the reference composition for a more detailed investigation of the electron transfer kinetics. This concentration was chosen as it represents the optimal compromise between current intensity, solution stability, and signal reproducibility.

In this subsequent phase, the objective was to evaluate the influence of the scan rate on the electrochemical behavior of the Ti(IV)/Ti(III) couple, in order to distinguish between diffusional and kinetic control and to quantitatively determine the main electrochemical parameters of the process.

For this purpose, cyclic voltammetry measurements were performed at scan rates ranging from 5 mV s^{-1} to 60 mV s^{-1}, keeping the $TiOSO_4$ concentration constant at 1 M while varying the H_2SO_4 concentration between 1 M and 4 M. The peak currents and corresponding potentials were subsequently analyzed according to the Randles–Ševčík and Laviron equations, previously described in the section 2.1.2, in order to determine the apparent diffusion coefficient and the kinetic parameters α (electron transfer coefficient) and k (heterogeneous rate constant). Before discussing the experimental results, it is important to briefly clarify the meaning of the Laviron and Randles–Ševčík plots presented in this section. These graphical analyses allow distinguishing whether the electrochemical response of the Ti(IV)/Ti(III) couple is governed primarily by charge-transfer kinetics or by mass-transport processes. In the Laviron representation, the linear trends obtained by plotting the peak potentials as a function of the logarithm of the scan rate indicate how the electron-transfer kinetics influence the position and separation of the redox peaks. A well-defined linearity reveals that the system follows the behaviour expected for a quasi-reversible electron-transfer process, providing insight into the energetic barrier and the efficiency of charge transfer at the electrode interface. Conversely, the Randles–Ševčík plot relates the peak current to the square root of the scan rate. When a linear relationship is observed, it signifies that the voltammetric response is mainly controlled by diffusion of the electroactive species in solution. The degree of linearity therefore reflects the effectiveness of mass transport and the accessible

concentration of electroactive titanium species near the electrode surface. Together, the straight lines obtained in these plots offer a visual confirmation of the dominant mechanism governing the redox process and allow interpreting the subsequent voltammograms in terms of reversibility, kinetic limitations, and diffusion effects[49]. Figure 3.7 shows the cyclic voltammograms of the Ti(IV)/Ti(III) system recorded at different scan rates for the four investigated H_2SO_4 concentrations.

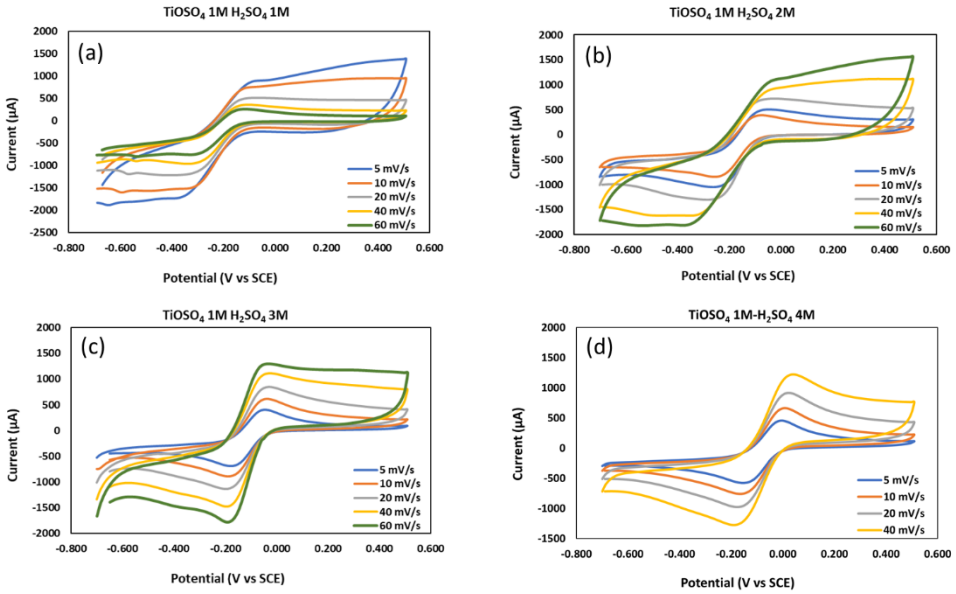


Figure 3.7: Cyclic voltammograms of the Ti(IV)/Ti(III) redox couple (1 M $TiOSO_4$) at different scan rates in sulfuric acid solutions of (a) 1 M, (b) 2 M, (c) 3 M, and (d) 4 M H_2SO_4, using a three-electrode setup with a glassy carbon working electrode, platinum counter electrode, and SCE reference electrode. Measurements were carried out between −0.7 and +0.5 V vs SCE.

The curves obtained in 1 M H_2SO_4 (Figure 3.7a) display broad and poorly defined anodic and cathodic peaks, with a peak-to-peak separation (ΔE_p) of approximately 206 mV at 10 mV s^{-1}, which further increases at higher scan rates. This behavior is typical of a slow and partially irreversible electron-transfer process, in which the overall kinetics are governed primarily by the charge-transfer step rather than by diffusion. The Laviron plot (Figure 3.8a) yields an α value of about 0.30 and a k value of 1×10^{-3} cm s^{-1}, while the diffusion coefficient derived from the Randles–Ševčík plot (Figure 3.8b) is 4.5×10^{-8} cm^2 s^{-1}. These results confirm the low efficiency of the electron transfer in weakly acidic conditions, in agreement with Lisitsyn et al. [85], who reported that the formation of hydrolyzed or polynuclear titanium species significantly decreases the availability of electroactive TiO^{2+} ions at the electrode interface.

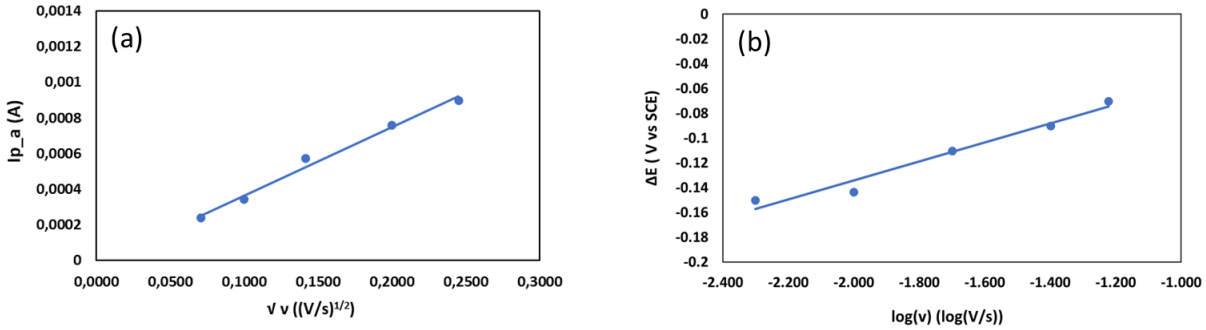


Figure 3.8: (a) Randles–Ševčík plot (i_p vs $v^{1/2}$) and (b) Laviron plot (ΔE_p vs log v) for the Ti(IV)/Ti(III) redox couple (1 M $TiOSO_4$) in 1 M H_2SO_4. Data were obtained from cyclic voltammetry measurements performed between −0.7 V and +0.5 V vs SCE using a glassy carbon working electrode, platinum counter electrode, and SCE reference electrode.

Upon increasing the acidity to 2 M H_2SO_4, the voltammetric profiles become more symmetric and exhibit higher peak currents, accompanied by a reduction of the potential separation, which decreases to about 190 mV at 10 mV s^{-1} (Figure 3.7b). The linear relationship between the peak current (i_p) and the square root of the scan rate ($v^{1/2}$) observed in Figure 3.9a confirms confirms that the electrochemical process remains diffusion-controlled. Compared to the corresponding behavior at lower acid concentration (Figure 3.8a), a steeper slope is obtained, indicating an increase in the diffusion coefficient (3.2×10^{-8} cm^2 s^{-1}). The Laviron analysis (Figure 3.9b) provides $\alpha \approx 0.39$ and $k \approx 2 \times 10^{-3}$ cm s^{-1}, indicating more favorable charge-transfer kinetics. These findings suggest that the higher proton concentration promotes the stabilization of TiO^{2+}–HSO_4^- complexes, reducing hydrolysis and improving the availability of redox-active species, thereby enhancing the apparent reversibility of the system.

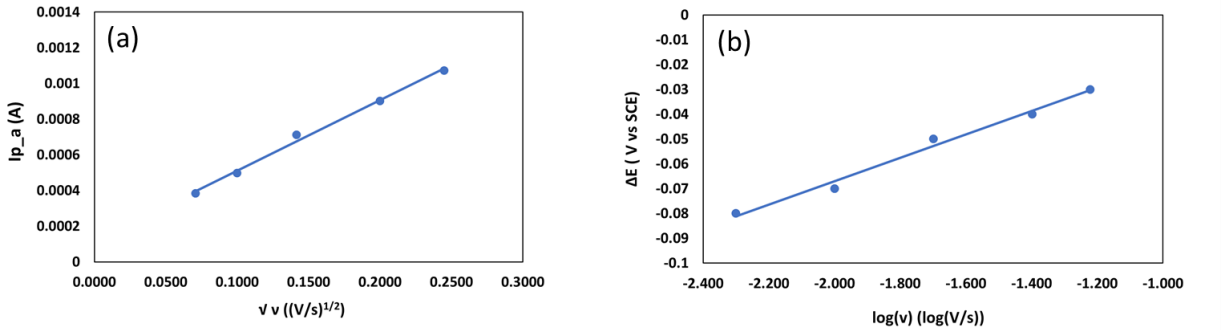


Figure 3.9: (a) Randles–Ševčík plot (i_p vs $v^{1/2}$) and (b) Laviron plot (ΔE_p vs log v) for the Ti(IV)/Ti(III) redox couple (1 M $TiOSO_4$) in 2 M H_2SO_4. Data were obtained from cyclic voltammetry measurements performed between −0.7 V and +0.5 V vs SCE using a glassy carbon working electrode, platinum counter electrode, and SCE reference electrode.

In 3 M H_2SO_4, the voltammetric response clearly evolves toward a quasi-reversible behavior. The anodic and cathodic peaks become sharper and more closely spaced (Figure 3.7c), with a ΔE_p value of about 190 mV at 10 mV s^{-1} and a peak current ratio (i_{pa}/i_pc) close to unity. The kinetic parameters obtained from Laviron (Figure 3.10b) are $\alpha \approx 0.45$ and $k \approx 4 \times 10^{-3}$ cm s^{-1}, while the diffusion coefficient from Randles–Ševčík (Figure 3.10a)

increases to 4.3 × 10^{-8} cm^2 s^{-1}, confirming improved charge-transport properties. These conditions correspond to the stability domain of bisulfate titanyl complexes, such as $[Ti(OH)_2(SO_4)_2]^{2-}$, as reported by Baillon et al. [84]. The predominance of such monomeric species under highly acidic conditions allows for faster charge transfer and a mainly diffusion-controlled mechanism.

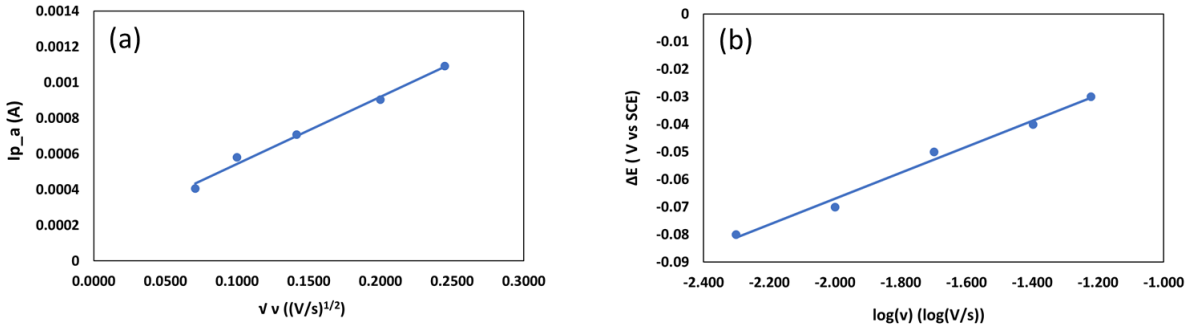


Figure 3.10: (a) Randles–Ševčík plot (i_p vs $v^{1/2}$) and (b) Laviron plot (ΔE_p vs log v) for the Ti(IV)/Ti(III) redox couple (1 M $TiOSO_4$) in 3 M H_2SO_4. Data were obtained from cyclic voltammetry measurements performed between −0.7 V and +0.5 V vs SCE using a glassy carbon working electrode, platinum counter electrode, and SCE reference electrode

Finally, the system in 4 M H_2SO_4 (Figure 3.7d) exhibits the most stable and reproducible electrochemical response. The voltammograms display sharp and symmetric peaks with a ΔE_p value of about 172 mV , while the Randles and Laviron analyses (Figure 3.11a and Figure 3.11b) confirm a diffusion-controlled regime with improved kinetic parameters (α ≈ 0.50, k ≈ 6–7 × 10^{-3} cm s^{-1}) and a higher diffusion coefficient (9.3 × 10^{-8} cm^2 s^{-1}).

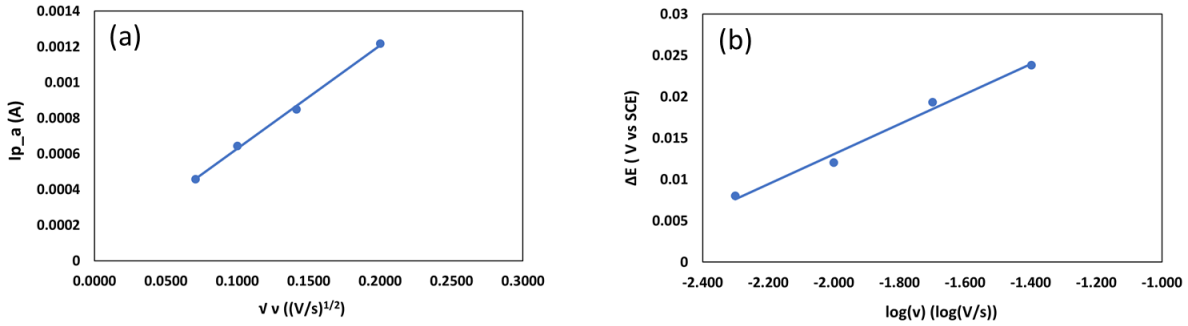


Figure 3.11: (a) Randles–Ševčík plot (i_p vs $v^{1/2}$) and (b) Laviron plot (ΔE_p vs log v) for the Ti(IV)/Ti(III) redox couple (1 M $TiOSO_4$) in 4 M H_2SO_4. Data were obtained from cyclic voltammetry measurements performed between −0.7 V and +0.5 V vs SCE using a glassy carbon working electrode, platinum counter electrode, and SCE reference electrode

However, in this condition, the peak-to-peak separation remains around 172 mV, and a noticeable increase in electrolyte viscosity was observed, which introduced experimental difficulties in maintaining signal stability and linearity in the Randles plot. As discussed by Qiao et al. [71], increasing acid concentration can reduce ionic mobility and lead to partial diffusional limitations, particularly in highly concentrated systems. Moreover,

at 60 mV s^{-1}, it was not possible to record a complete voltammogram: the high current densities generated at this scan rate exceeded the instrument's measurable current range, leading to signal saturation and preventing accurate data acquisition. This limitation, although instrumental in nature, is likely accentuated by the higher conductivity and viscosity of the concentrated solution. Nonetheless, the voltammetric behavior observed at lower scan rates remains fully representative of the system's overall trend.

To provide a clearer overview of the electrochemical performance under the different conditions, the main kinetic and diffusional parameters extracted from the Randles–Ševčík and Laviron analyses are summarized in Table 3.2.

Table 3.2: Summary of electrochemical parameters (ΔE_p, α, k, and D) of the Ti(IV)/Ti(III) redox couple (1 M $TiOSO_4$) obtained from cyclic voltammetry and Laviron/Randles–Ševčík analysis in 1–4 M H_2SO_4.

H_2SO_4 concentration	**ΔE_p**	**α**	**k**	**D**	**Electrochemical behavior**
M	mV		cm s^{-1}	cm^2 s^{-1}	
1 M	206	0.30	1.0×10^{-3}	4.51×10^{-8}	Strongly irreversible; sluggish charge transfer; hydrolyzed Ti species reduce reactivity
2 M	190	0.39	2.0×10^{-3}	3.20×10^{-8}	Improved reversibility; stabilization of TiO^{2+}–HSO_4^- complexes
3 M	190	0.45	4.0×10^{-3}	4.28×10^{-8}	Quasi-reversible system; bisulfate complexes enhance charge transfer
4 M	172	0.50	6.0×10^{-3}	9.31×10^{-8}	Highest stability and kinetics; slight viscosity increase limits diffusion

Overall, the analysis of cyclic voltammetry at different scan rates confirms that the kinetics of the Ti(IV)/Ti(III) system are strongly influenced by the acidity of the medium. The progressive increase of α, k, and D with rising H_2SO_4 concentration demonstrates that a strongly protonic environment not only suppresses titanium hydrolysis but also facilitates faster and more symmetric electron transfer. This behavior is consistent with the proton-assisted mechanism proposed by Bishop [88] and Cservenyak [87]. The condition at 3 M H_2SO_4 therefore represents an effective compromise between chemical stability, kinetic efficiency, and electrochemical compatibility, serving as the optimal starting point for the subsequent optimization of the Ti–Fe redox flow battery anolyte.

3.5 Spectroscopic and Voltammetric Investigation: Molecular Compatibility of Ti–Fe Electrolytes

In addition to the electrochemical investigation of the titanium-based electrolyte, this work also included tests aimed at evaluating the behavior and compatibility of the iron-based counterpart. The selection of the Fe^{3+}/Fe^{2+} redox couple is a precise choice: it is a well-established system, extensively employed in the literature for redox flow batteries due to its high reversibility, stability in acidic environments, and favorable charge-transfer

kinetics [91], [92]. Numerous studies have shown that the Fe^{3+}/Fe^{2+} couple in aqueous solution delivers stable electrochemical behavior even under challenging operating conditions, making it a promising candidate for large-scale stationary energy storage. In particular, Gong et al. demonstrated the feasibility of a fully soluble all-iron redox flow battery, reporting high coulombic efficiency and excellent cycling stability [93]. Similarly, recent work has focused on developing iron-based catholytes to optimize redox performance in relation to pH, solubility, and compatibility with various cell materials [92]. A more comprehensive analysis of the electrochemical behavior of iron was recently presented by Zhang et al., who reviewed iron-based redox flow batteries and highlighted their advantages in terms of cost, availability, and environmental sustainability compared to conventional vanadium systems [94]. The abundant availability of literature data on iron was one of the factors that supported its selection for this study. Nonetheless, the combination of iron and titanium within a single system remained an open question, particularly regarding the molecular compatibility of the two electrolytes and their ability to coexist in acidic solution without forming unwanted interactions. Furthermore, the low cost of iron, combined with its good solubility and favorable redox properties, made it a suitable candidate for investigation in mixed electrolyte configurations. For these reasons, the inclusion of iron in this work was also necessary to experimentally verify its interaction with titanium, both in separated and combined systems.

As a first step, cyclic voltammetry of 1 M $FeSO_4$ in 3 M H_2SO_4 was performed, as shown in Figure 3.12.

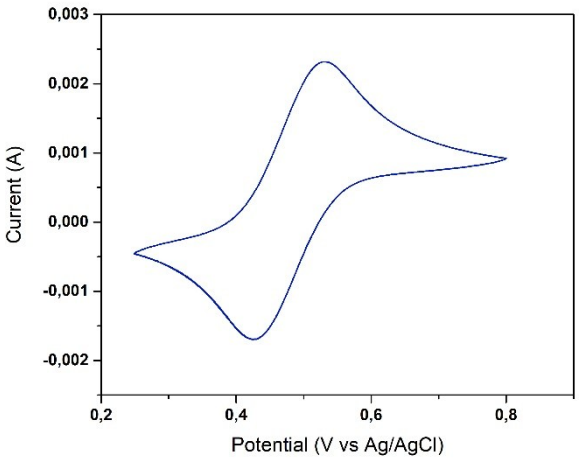


Figure 3.12: Cyclic voltammogram of 1 M $FeSO_4$ in 3 M H_2SO_4 at 25 mV s^{-1} using a three-electrode setup with a glassy carbon working electrode, platinum counter electrode, and Ag/AgCl reference electrode. The redox peaks are well-defined and reversible, confirming the electrochemical stability of the Fe^{3+}/Fe^{2+} couple.

The voltammogram displays a well-defined, symmetric redox couple, consistent with the expected behavior of the Fe^{3+}/Fe^{2+} system in acidic media, as reported in previous studies [95].

To complement the electrochemical analysis, FT-Raman spectroscopy was conducted on three electrolytes: (i) titanium-only (1 M $TiOSO_4$), (ii) iron-only (1 M $FeSO_4$), and (iii) a mixed solution containing 1 M Ti and 1 M Fe, all prepared in 3 M H_2SO_4. Raman and voltammetric measurements of the mixed electrolyte were carried

out at the CIC energiGUNE research center (Vitoria-Gasteiz, Spain) as part of a scientific collaboration. The results are shown in Figure 3.13.

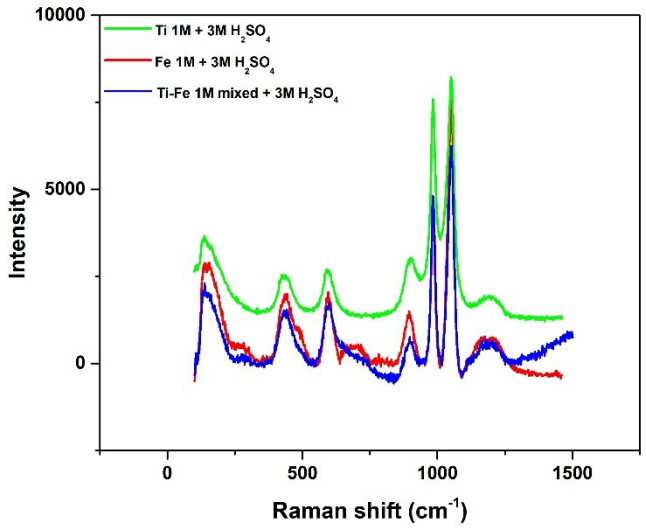


Figure 3.13: FT-Raman spectra of the electrolytes: green is 1 M $TiOSO_4$ in 3 M H_2SO_4, red is 1 M $FeSO_4$ in 3 M H_2SO_4 and blue is mixed solution with 1 M Ti + 1 M Fe in 3 M H_2SO_4. The absence of new bands in the blue spectrum suggests structural independence between the two species.

To better understand potential interactions between the redox species and the acidic environment, the Raman spectra were compared to reference literature data. In the case of the iron-based electrolyte (Figure 3.13 red), intense bands are observed in the 980–1020 cm^{-1} region, attributed to the symmetric stretching vibration $\nu_1(SO_4^{2-})$, along with signals around 420–490 cm^{-1} associated with bending vibrations $\nu_2(SO_4^{2-})$, consistent with the Raman study on hydrated ferrous sulfate by Chi et al. [96] and Sharma et al. [97]. For the titanium-based solution (Figure 3.13 green), a main band centered around 1010 cm^{-1} is observed, associated with the coordinated sulfate group, and secondary bands between 365 and 785 cm^{-1} attributed to Ti–O modes and sulfate deformation [84]. These features agree with the results reported by Noda et al., who identified the formation of species such as $[TiO(SO_4)]$ and $[TiO(SO_4)_2]^{2-}$ in $TiOSO_4$ solutions [98]. In the mixed system (Figure 3.13 blue), the Raman spectrum appears as a superposition of the two individual spectra, with no new bands or significant shifts. This indicates the absence of detectable Ti–Fe complex formation or structural interaction, and confirms that the two cations coexist in solution as independent species. These observations are consistent with previous studies by Rudolph et al., which show that metal–sulfate interactions can be spectroscopically distinguished even in concentrated solutions [99].

Finally, the cyclic voltammogram of the mixed electrolyte, shown in Figure 3.14, further confirms the electrochemical independence of the two systems.

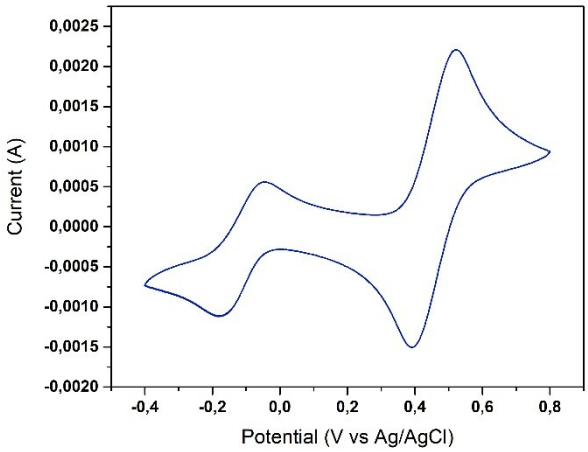


Figure 3.14: Cyclic voltammogram of the mixed electrolyte containing 1 M $TiOSO_4$ and 1 M $FeSO_4$ in 3 M H_2SO_4 using a three-electrode setup with a glassy carbon working electrode, platinum counter electrode, and Ag/AgCl reference electrode. The two well-separated redox couples confirm the electrochemical compatibility of titanium and iron in acidic solution.

The voltammogram clearly displays two distinct and well-separated redox couples, attributable to titanium and iron, respectively. The absence of overlapping signals or anomalous distortions indicates that both redox processes occur independently and reversibly, even in the presence of both species in the same acidic environment.

Overall, the combination of spectroscopic and voltammetric results confirms that titanium and iron can coexist stably in sulfuric acid without forming unwanted structural or chemical interactions. This demonstration of molecular and electrochemical compatibility provides the necessary foundation for the design and operation of the Ti–Fe redox flow battery, which will be presented in the following section.

3.6 Battery Testing of the Ti^{3+}/TiO^{2+}–Fe^{3+}/Fe^{2+} System in Sulfuric Acid Medium: Design and Performance Evaluation

After demonstrating the electrochemical and structural compatibility between the Ti(IV)/Ti(III) and Fe(III)/Fe(II) redox couples in sulfuric acid medium, through cyclic voltammetry and Raman measurements, the experimental work proceeded with cell-based testing, aimed at studying the behavior of the system under redox flow battery operating conditions. This phase focused not only on validating the redox reversibility and stability within the cell, but also on evaluating coulombic, voltaic, and energy efficiencies over multiple charge–discharge cycles. At the same time, a systematic investigation was carried out on the influence of key operating parameters, such as electrolyte composition, the presence of metallic catalysts, and the anode/cathode configuration, with the aim of identifying the limits and potential of the Ti–Fe system in view of its possible deployment in stationary energy storage applications. The Ti^{3+}/TiO^{2+}–Fe^{3+}/Fe^{2+} system is considered one of the most promising alternatives to conventional vanadium-based redox flow batteries, due to the higher abundance of the active materials involved, their lower cost, and their greater environmental sustainability. The theoretical cell voltage, approximately 0.67 V, represents a suitable compromise between

energy density, operational safety, and suppression of unwanted side reactions such as hydrogen evolution. As reported in the literature, similar systems have achieved high charge/discharge efficiencies and excellent long-term stability, even in the absence of complex management strategies, with consistent performance maintained newover more than one hundred continuous cycles [25], [37], [71], [80].

The first test was carried out using an equimolar mixed electrolyte containing 1 M $TiOSO_4$ and 1 M $FeSO_4$ in 3 M H_2SO_4. The use of a mixed electrolyte was specifically intended to avoid crossover phenomena between redox-active species across the proton exchange membrane. In this configuration, both compartments contain the same chemical composition, eliminating the concentration gradient that typically drives ion migration. This approach reduces chemical imbalance and improves the long-term stability of the system [47]. The cell was tested both in the absence and in the presence of metallic bismuth, which was added to the negative compartment to evaluate its catalytic effect on the Ti^{3+}/TiO^{2+} redox couple, known to be kinetically slower than the ferric counterpart [71], [72]. Subsequently, the same mixed electrolyte system was tested at reduced concentration, with 0.5 M of each metal salt, in order to examine the effect of dilution on solution stability and charge transfer kinetics. Finally, tests were conducted using separated electrolytes: the anodic compartment contained only the titanium species, while the cathodic compartment contained only iron, both at 1 M concentration. In this configuration as well, tests were performed with and without the addition of bismuth, to assess its impact on the electrochemical performance of the cell.

All tests were carried out at the CIC energiGUNE research center in Vitoria-Gasteiz (Spain), using a laboratory-scale redox flow cell equipped with a peristaltic pump, proton exchange membrane, and real-time data acquisition system. The following sections describe in detail the cell configuration, redox reactions involved, operating conditions, and experimental results, with particular attention to the effect of the metallic catalyst and a critical comparison with literature data on analogous Fe–Ti and vanadium-based systems.

3.7 Redox reactions and chemical composition of the anodic and cathodic compartments

This section provides a detailed description of the electrochemical reactions occurring in the anodic and cathodic compartments of the Ti–Fe redox flow battery system investigated in this work. Following the electrochemical characterization of the individual redox couples in acidic media, the focus now shifts to the interaction between the two half-reactions within the actual battery configuration. The objective is to understand how the redox properties of iron and titanium combine in a working system, and what the chemical and thermodynamic implications are of their pairing. Figure 3.15 shows a schematic diagram of the studied Ti–Fe flow system, highlighting the two compartments, the direction of electron and ion flow, and the redox-active species involved. Both the anolyte and the catholyte consist of an acidic solution containing the Fe^{3+}/Fe^{2+} and TiO^{2+}/Ti^{3+} redox couples, which participate in the charge transfer processes in a complementary manner.

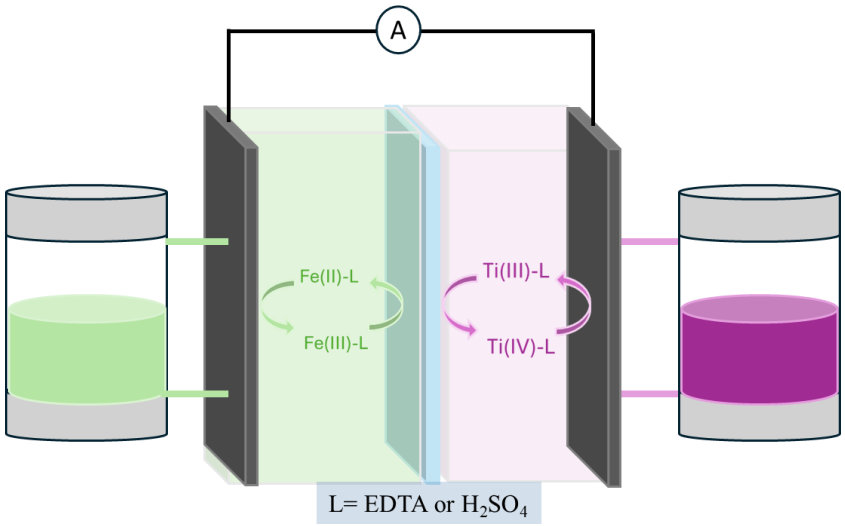


Figure 3.15: Schematic representation of the Ti–Fe redox flow battery. The diagram illustrates the two tanks with the Ti/Fe solution, recirculating pumps, proton exchange membrane, and external electronic circuit.

During battery operation, two main phases alternate, charging and discharging, corresponding to the storage and release of energy. In the charging phase, electrical energy supplied from an external source is stored in the form of chemical energy via electron transfer between the redox-active species. In the cathodic compartment, Fe^{2+} is oxidized to Fe^{3+}, while in the anodic compartment, TiO^{2+} is reduced to Ti^{3+}. This results in an increased concentration of Fe^{3+} in the catholyte and Ti^{3+} in the anolyte. During the discharge phase, the process is reversed: Ti^{3+} is oxidized back to TiO^{2+}, releasing electrons to the external circuit, while Fe^{3+} is reduced to Fe^{2+}, thereby restoring the initial chemical balance and generating usable electrical energy. The battery operates through the simultaneous utilization of the Fe^{3+}/Fe^{2+} and TiO^{2+}/Ti^{3+} redox couples, both active under strongly acidic conditions. The fundamental electrochemical reactions governing the system are as follows:

Anode (reduction reaction)

$$TiO^{2+} + 2H^{+} + e^{-} \rightleftharpoons Ti^{3+} + H_2O \qquad E° \approx +0.10 \text{ V vs SHE}$$

Cathode (oxidation reaction):

$$Fe^{2+} \rightleftharpoons Fe^{3+} + e^{-} \qquad E° \approx +0.77 \text{ V vs SHE}$$

Overall cell reaction:

$$TiO^{2+} + 2H^{+} + Fe^{2+} \rightleftharpoons Ti^{3+} + Fe^{3+} + H_2O \qquad \Delta E° \approx 0.67 \text{ V}$$

The theoretical cell voltage, derived from the difference in standard potentials between the two half-reactions, is approximately 0.67 V. While this value is lower than that of traditional vanadium redox flow batteries (VRFBs), which can reach up to 1.26 V when pairing V^{2+}/V^{3+} at the anode with V^{5+}/V^{4+} at the cathode, it remains suitable for stationary applications. This is especially true when considering the chemical simplicity and reduced cost of the Ti–Fe system. Both iron and titanium are among the ten most abundant metals in the Earth's crust, offering significant economic and resource advantages over strategic and volatile materials such as vanadium, whose fluctuating market price and limited supply have hindered the widespread deployment of

VRFBs. From a chemical standpoint, both redox couples are known for their stability in sulfuric acid. The Fe^{3+}/Fe^{2+} couple is extensively used in electrochemical research as a model redox system due to its high reversibility, fast electron transfer kinetics, and excellent solubility in H_2SO_4. Titanium, although kinetically slower, exhibits valuable redox properties: the oxidized TiO^{2+} species can be stabilized in solution through the formation of sulfate complexes that inhibit hydrolysis and support redox reversibility. The reduced form, Ti^{3+}, is thermodynamically stable but more reactive toward dissolved oxygen and other oxidants, necessitating carefully controlled working conditions. An important consideration is the proximity of the Ti(IV)/Ti(III) redox potential to the lower boundary of the water stability window. This means that, under suboptimal conditions, the reduction of TiO^{2+} may compete with hydrogen evolution, thereby decreasing the system's coulombic efficiency. However, studies have shown that the addition of metallic additives such as bismuth to the negative electrode can modulate overpotential, shifting the effective reduction potential and mitigating side reactions. The coupling of the two half-reactions also allows the system to operate with a bifunctional electrolyte, simultaneously serving as both anolyte and catholyte. This feature not only reduces the impact of ionic crossover but also simplifies electrolyte management, which is a significant operational concern in conventional VRFB systems that require separate tanks, rebalancing strategies, and volume compensation. Moreover, using the same solution in both compartments helps to maintain stable composition over extended operation, contributing to long-term electrochemical reliability. Functionally, the Ti–Fe system supports low-voltage operation with high coulombic efficiency and streamlined maintenance, features that are critical for medium-scale, stationary storage applications. The complementary redox behavior of iron and titanium, along with their compatibility with acidic media and commercial proton exchange membranes, makes this system a promising candidate for cost-effective and sustainable energy storage. Having clarified the redox mechanisms underlying the battery's operation, the next section will present the experimental configuration used during the electrochemical tests, including cell design, materials, and operating parameters.

3.7.1 Cell Configuration and Employed Materials

Before detailing the operating conditions and the electrochemical results, it is useful to present the experimental configuration of the Ti–Fe flow battery used in this study. The setup, shown in Figure 3.16, was designed to provide precise control over both hydraulic and electrical parameters, ensuring measurement repeatability and data reliability.

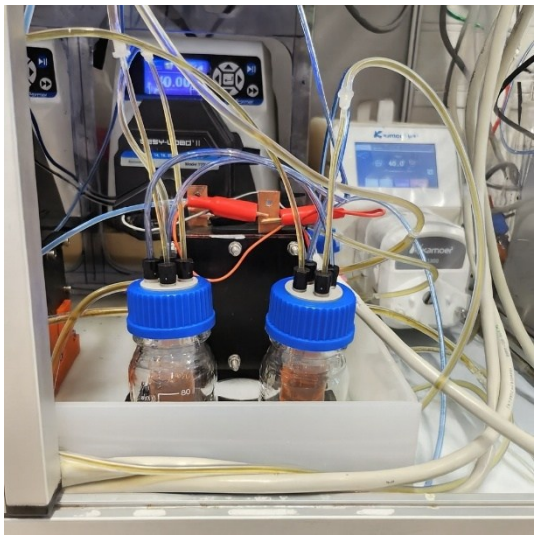


Figure 3.16: Laboratory setup used for the charge–discharge tests of the Ti–Fe redox flow battery.

The core of the system was a custom-made single flow cell with an active area of 4 cm², connected via PTFE tubing to two 100 mL borosilicate glass reservoirs containing the anolyte and catholyte, respectively. Electrolyte circulation was maintained by Masterflex™ L/S™ peristaltic pumps equipped with Easy-Load™ II pump heads, operating at a constant flow rate of 40 mL min^{-1}. The electrochemical control and data acquisition were managed using a Neware CT-4008Tn-5V6A-S1 testing system, which enabled galvanostatic charge–discharge cycling with real-time monitoring of current, voltage, and capacity. The compact architecture and functional arrangement of the components helped reduce dead volumes and improve the system's dynamic response during operation.

The main mechanical components of the cell are illustrated in Figure 3.17, where each section highlights a key element of the assembly.

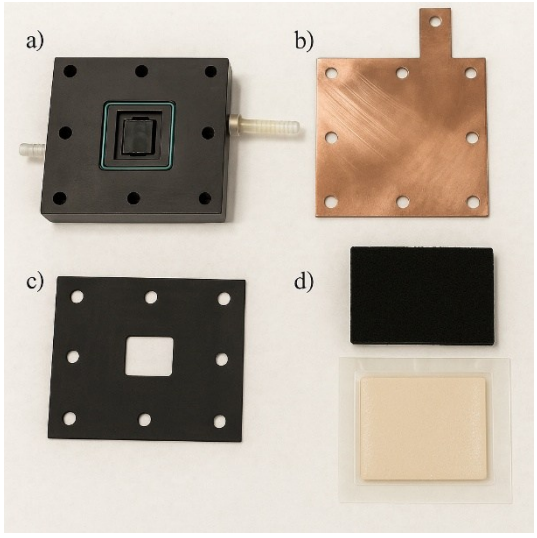


Figure 3.17: Main components of the Ti–Fe single flow cell: (a) Graphite bipolar plate with flow channels and sealing ports; (b) copper current collector; (c) rubber gasket for compartment separation and hydraulic sealing; (d) carbon felt electrode and proton exchange membrane.

At the heart of the structure are the graphite bipolar plates (Figure 3.17a), which provide the mechanical framework of the cell. These plates, precisely machined with internal linear flow channels, ensure homogeneous distribution of the electrolyte across the electrode surface, minimizing concentration gradients and enhancing ion-exchange efficiency [100]. Assembly was secured using stainless steel bolts and insulating spacers, ensuring both uniform compression of the stack and effective hydraulic sealing of the compartments. The current collector, shown in Figure 3.17b, is made of copper and serves to establish electrical contact between the electrode and the external circuit. Copper was selected due to its excellent electrical conductivity and sufficient chemical resistance in acidic environments, helping to minimize contact resistance and enhance electron transfer efficiency during operation [101], [102]. Among the functional components, the black rubber gasket shown in Figure 3.17c plays a crucial role in sealing and isolating the anodic and cathodic compartments. Tailored to the cell geometry and equipped with holes for alignment and assembly, this component prevents electrolyte leakage and ensures effective compartmental separation while maintaining mechanical integrity. Figure 3.17d displays two critical electrochemical components: the electrode and the proton exchange membrane. The electrode consists of a highly porous carbon felt with a three-dimensional structure that offers a large active surface area and excellent electrical conductivity. The felts, cut to 2 × 2 cm with a thickness of 5 mm, were supplied pre-activated by the manufacturer. This condition improves wettability and increases the surface density of oxygen-containing functional groups, thereby enhancing charge transfer kinetics and improving the reversibility of the Ti(IV)/Ti(III) redox reaction. The use of carbon felt electrodes is well-established in flow battery research due to their high electrochemical surface area, stability, and compatibility with acidic electrolytes [103], [104].

Beneath the electrode, the proton exchange membrane can be seen—a 50 µm thick Nafion™ N212 film used to physically separate the anodic and cathodic compartments while allowing selective proton transport. Prior to assembly, the membrane underwent a chemical activation treatment consisting of sequential immersion in 3% hydrogen peroxide for 1hour, ultrapure water at 80 °C for 1 hour, and finally 1 M sulfuric acid for another hour, followed by thorough rinsing in ultrapure water. This process removed any organic contaminants and restored the sulfonic acid groups (–SO_3H) to their protonated form, maximizing proton conductivity and ensuring long-term membrane stability under acidic conditions [105], [106], [107].

Taken together, the components were selected and integrated to ensure mechanical robustness, chemical compatibility, efficient fluid distribution, and electrochemical functionality. This structural configuration provides the technical foundation for the subsequent analysis of the Ti–Fe system's electrochemical performance, discussed in the following sections.

3.7.2 Electrolyte Preparation and Tested Configurations

The Ti–Fe redox system was investigated through a series of electrolyte configurations designed to explore how electrolyte composition influences electrochemical performance in a flow battery setup. Electrolyte preparation involved the dissolution of high-purity salts in concentrated sulfuric acid, in order to ensure the stability of the redox species and to establish reproducible working conditions. Although experimentally

straightforward, this phase is critical for interpreting electrochemical performance correctly, since even small variations in concentration or purity can affect redox reversibility and long-term system stability. Specifically, titanium oxysulfate ($TiOSO_4$, ACS reagent, ≥99%, Sigma–Aldrich, USA) was used for the titanium-containing anolyte, while ferrous sulfate heptahydrate ($FeSO_4 \cdot 7H_2O$, ACS reagent, ≥99.0%, Sigma–Aldrich, USA) was employed as the iron precursor for the catholyte. Both salts were sourced from Sigma–Aldrich, and the sulfuric acid (H_2SO_4, 95–97%, analytical grade, Scharlau, Spain) was obtained from VWR Chemicals. The solutions were prepared in 3 M H_2SO_4, using ultrapure water (18.2 MΩ·cm) to avoid contamination that could compromise redox purity. Figure 3.18 visually presents the prepared solutions: (a) the mixed electrolyte containing 1 M Ti and 1 M Fe in 3 M H_2SO_4; (b) the solution containing only 1 M $FeSO_4$; and (c) the solution containing only 1 M $TiOSO_4$. The different coloration of the three solutions reflects the presence and oxidation states of the active redox species in solution, providing initial visual confirmation of correct formulation.

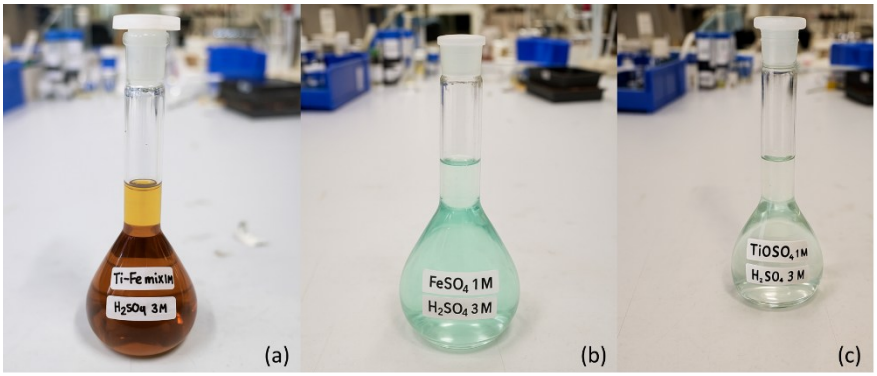


Figure 3.18: Electrolyte solutions used for flow battery testing. (a) Mixed solution containing 1 M Ti and 1 M Fe in 3 M H_2SO_4; (b) solution containing only 1 M $FeSO_4$ in 3 M H_2SO_4 (catholyte); (c) solution containing only 1 M $TiOSO_4$ in 3 M H_2SO_4 (anolyte).

From an experimental standpoint, the first set of tests was conducted using an equimolar mixed formulation, consisting of a single solution containing 1 M Ti^{3+}/TiO^{2+} and 1 M Fe^{2+}/Fe^{3+} in 3 M H_2SO_4. This configuration simplifies electrolyte handling and is often adopted to minimize crossover phenomena through the membrane and to improve coulombic efficiency [108]. Additionally, it enables the direct study of the interaction between the two redox couples in a unified chemical environment, allowing for simplified energy balancing and easier interpretation of charge/discharge curves. In this condition, the influence of a metallic catalyst in the anodic compartment was also investigated, by adding 16 mg of bismuth (Bi^{3+}) directly to the solution, in the form of bismuth (III) sulfate ($Bi_2(SO_4)_3$, 99%, Alfa Aesar, Thermo Fisher Scientific, USA). Bismuth is well known for its ability to spontaneously deposit onto carbon felts, forming a thin electroactive layer that significantly enhances the kinetics of the Ti(IV)/Ti(III) redox couple, which is typically limited by slow electron-transfer rates. Its effectiveness has been well demonstrated in the literature in various multivalent redox flow systems[72]. A second configuration tested involved the use of diluted mixed electrolytes (0.5 M Ti + 0.5 M Fe in 3 M H_2SO_4), in order to investigate how redox species concentration affects energy efficiency and cell polarization. While lower concentration may reduce ohmic resistance, it can also lead to a drop in theoretical capacity and potentially worsen system stability at higher current densities. Moreover, this condition is helpful

in understanding the operational limits of the system under low ionic charge conditions, such as those that may occur after prolonged cycling in real-world stationary energy storage applications. Finally, a separated-electrolyte configuration was explored, in which the anolyte contained only 1 M $TiOSO_4$ in 3 M H_2SO_4 and the catholyte only 1 M $FeSO_4$ in 3 M H_2SO_4. This setup allowed for a more independent evaluation of the two half-cell reactions, making it possible to assess the redox reversibility and long-term stability of each couple individually, as well as to characterize degradation phenomena specific to each compartment. Separated systems are also strategically relevant for studying the proton-exchange membrane's selectivity and ion crossover effects under realistic conditions. All electrochemical tests were carried out in a single flow cell, operated at a constant temperature of 25 °C and with a flow rate of 40 mL min^{-1}. These operating conditions were selected to simulate the real-world environment of a flow battery, while maintaining consistent experimental parameters across the different electrolyte configurations. The cell was subjected to galvanostatic charge/discharge cycles at 40, 60, and 80 mA cm^{-2}, to evaluate performance under varying current densities. Additionally, for the mixed electrolyte conditions (with and without bismuth), a long-term test of up to 100 cycles at 80 mA cm^{-2} was carried out, aimed at monitoring capacity evolution, coulombic and voltage efficiency, and long-term degradation. The tests carried out are summarised in

Table 3.3, which briefly reports the electrolyte formulations, the presence of bismuth in the anode compartment, the applied current intensities, the number of cycles and the total duration of the tests.

Table 3.3: Composition of electrolytes and experimental parameters used in the single-cell tests.

	Electrolytes		**Bi**	**Tempertature**	**Flux**	**Current**	**Cycles**	**Time**
Support Electrolytes	**Anolyte**	**Catholyte**	**[mg]**	**[°C]**	**[mL/min]**	**[A]**	**[n°]**	**[h]**
H_2SO_4 3M	Ti 1M	Fe 1M	0.16	25	40	0.16 0.24 0.32	6 6 106	83
	Ti-Fe mix 0.5M	Ti-Fe mix 0.5M	0.16	25	40	0.16 0.24 0.32	6 6 106	100
	Ti-Fe mix 1M	Ti-Fe mix 1M	0.16	25	40	0.16 0.24 0.32	6 6 106	230
	Ti-Fe mix 1M	Ti-Fe mix 1M	-	25	40	0.16 0.24 0.32	6 6 106	80

Overall, these experiments provided a systematic and comparative assessment of the Ti–Fe system as a function of electrolyte formulation and catalyst presence. They serve as a solid basis for further discussion and

optimization of the system, not only in terms of electrochemical performance but also with respect to its potential application in stationary energy storage.

3.8 In-cell performance of the Ti–Fe battery with mixed electrolytes: evaluation of the effect of bismuth

Building on recent literature concerning the use of mixed titanium and iron electrolytes for electrochemical energy storage systems, a series of experimental tests was carried out to evaluate, under realistic operating conditions, the performance of a Ti–Fe redox flow battery in acidic medium. This section focuses on a comparative analysis between two distinct configurations: a reference cell without any additives, and a second configuration in which bismuth (Bi^{3+}) was introduced in the anodic compartment. The main goal of this phase of the work was to assess the extent to which the presence of bismuth affects the overall system performance, with particular attention to enhanced anodic redox kinetics, reduced overpotentials, and improved long-term stability in terms of both energy efficiency and cycling behavior [70].

The tests were conducted using a mixed electrolyte consisting of 1 M Ti (as $TiOSO_4$) and 1 M Fe (as $FeSO_4$) in 3 M H_2SO_4, used simultaneously as both anolyte and catholyte. This formulation offers several advantages from both an operational and electrochemical standpoint. First, the use of a single mixed electrolyte allows for the elimination of redox species crossover, a well-known issue in conventional vanadium redox flow batteries (VRFBs), where the intercompartmental migration of V^{2+}/V^{3+} and VO_2^+/VO_2^+ across the membrane is one of the main causes of efficiency loss, electrolyte imbalance, and the need for frequent rebalancing [109], [110]. In contrast, in the mixed Ti–Fe system, the simultaneous presence of both redox couples in each compartment renders cross-membrane migration negligible, since any diffusion across the membrane does not alter the overall chemical composition of the electrolyte. This results in improved long-term stability and allows for a simplified system design, eliminating the need for additional balancing strategies or external compensation systems. This concept of intrinsic self-balancing has recently been explored in other contexts, such as organic symmetric electrolytes [111] or so-called “single-electrolyte flow batteries” [112]. However, in the case of the inorganic Ti–Fe chemistry, it proves particularly effective due to the excellent chemical compatibility of both redox couples in strongly acidic media and their lack of cross-reactivity, allowing them to coexist stably in the same electrolyte matrix. As a result, there is no need for highly selective separators, which represents a direct advantage in terms of material cost and system durability [113]. From a performance standpoint, the relatively high concentration (1 M) of active species ensures a good compromise between energy density, conductivity, and viscosity, enabling effective operation across a range of current densities without impairing membrane stability or reducing system efficiency [114]. Moreover, the use of concentrated sulfuric acid (3 M) as the supporting electrolyte allows for the stabilization of Ti(IV) in solution via formation of TiO^{2+}–SO_4^{2-} complexes, as discussed in previous sections. In this paragraph, following the detailed description of the electrolyte formulation, materials, and experimental setup provided in earlier sections, we present the results obtained from charge–discharge tests performed in a single flow cell configuration.

Galvanostatic tests were carried out at three different current densities (40, 60, and 80 mA/cm²), within a voltage window of 0.3 to 0.9 V. This experimental strategy was selected to assess the efficiency and internal polarization of the cell across a representative range of operating conditions. In particular, short-term tests (6 cycles at each current density) were performed to evaluate the system's steady-state behavior and to directly compare the two configurations (with and without Bi^{3+}), while a long-term test consisting of 100 consecutive cycles at 80 mA/cm² was carried out to monitor cycling stability, potential degradation phenomena, and long-term performance retention. Long-term testing is essential for identifying cumulative effects, such as progressive deposition of inactive species, membrane degradation, or coulombic efficiency loss, which may not emerge from short-duration tests [115]. The key electrochemical parameters, coulombic efficiency (CE), voltaic efficiency (VE), and overall energy efficiency (EE), were calculated from charge–discharge data acquired under steady-state conditions. Calculations were based on Equations 2.10, 2.11, and 2.12, presented in Chapter 2, where CE refers to the ratio of discharged to charged capacity, VE reflects energy losses due to voltage differences during the two phases, and EE represents the product of the two, quantifying the total energy conversion efficiency of the system For each operating condition, the values were calculated as the average of the last three cycles, in order to exclude initial transient effects related to system adaptation.

These parameters are well-established metrics for the characterization of redox flow batteries, as they allow evaluation of the reversibility of redox processes, the extent of internal losses, and the overall ability of the system to operate efficiently and stably over time [116]. It has been widely reported in the literature that introducing catalytic metals such as bismuth can facilitate the oxidation of Ti(III), lowering the charge transfer resistance at the anode and thereby enhancing voltaic efficiency [117]. The aim of the present study is to quantify this effect systematically, under identical operating conditions, in order to assess the real impact of Bi^{3+} addition on the electrochemical response and long-term behavior of the system. The experimental results for both configurations (with and without bismuth) are presented and discussed in the following sections, with specific focus on charge–discharge curves, efficiency variation as a function of current density and cycle number, and overall system stability over time.

3.8.1 Evaluation of Baseline Performance of the Ti–Fe Redox Flow Battery Without Bismuth

Starting from the reference configuration, a mixed electrolyte containing 1 M titanium and 1 M iron in 3 M H_2SO_4, galvanostatic tests were carried out at varying current densities with the aim of characterizing the electrochemical behavior of the system in the absence of catalytic promoters. This experimental phase is essential for understanding the intrinsic limitations of the Ti-Fe chemistry, and for quantifying in an objective manner the potential effect of adding bismuth, which will be analysed in the subsequent section.

As shown in Figure 3.19, the coulombic efficiencies (CE) obtained during the initial tests remain consistently high, above 97% for all current densities considered (40, 60 and 80 mA cm^{-2}), confirming good reversibility of the redox reactions under controlled conditions. However, both the voltaic efficiency (VE) and the overall energy efficiency (EE) clearly deteriorate with increasing current density: VE declines from 76.34% at 40 mA cm^{-2} to 41.98% at 80 mA/cm², while EE drops from 74.40% to just 42.07%.

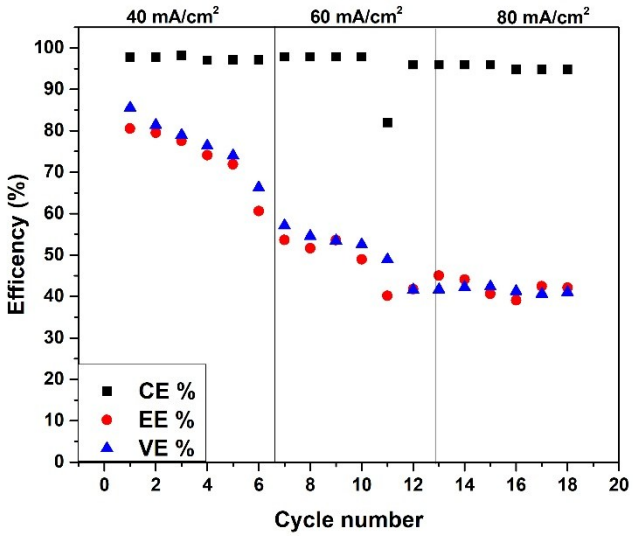


Figure 3.19: Coulombic efficiency (CE), voltaic efficiency (VE), and energy efficiency (EE) of the Ti–Fe flow battery using a mixed electrolyte (1 M Ti / 1 M Fe in 3 M H_2SO_4) without bismuth, during charge/discharge cycling at three different current densities: 40, 60, and 80 mA cm^{-2}.

This behaviour can be attributed to increased ohmic losses and overpotentials, particularly in the anodic process of Ti^{3+} oxidation to TiO^{2+}, which is severely penalised in the absence of catalysts [71], [118]. These early results clearly indicate that although the baseline configuration offers operational simplicity, it requires a specific modification to the anodic compartment to be considered competitive in a real application perspective.

This limitation is well documented in the literature for titanium-based redox systems. The anodic half-reaction $Ti^{3+} \rightarrow TiO^{2+}$ in an acidic environment proceeds via a multi-electron mechanism and involves intermediate complexes such as $Ti(OH)^{2+}$ and $TiOSO_4^{+}$. In the absence of surface promoters, these intermediates may promote passivation phenomena. Furthermore, the potential required for Ti^{3+} oxidation approaches the upper limit of the water stability window, increasing the risk of parasitic reactions such as O_2 evolution, which reduce faradaic efficiency and contribute to electrode degradation [80].

Further information is obtained from the potential-time (V–t) curves shown in Figure 3.20, which show how the cell responds to increasing applied current.

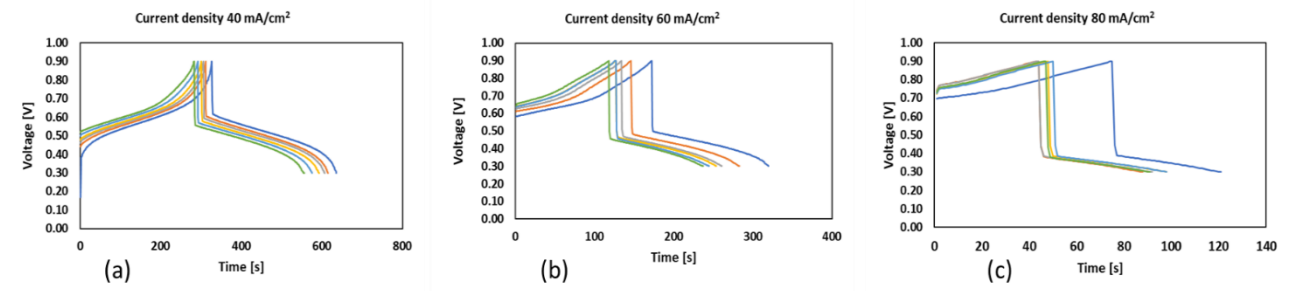


Figure 3.20: Charge/discharge voltage profiles of the Ti–Fe 1M battery with mixed electrolytes at different current densities: (a) 40 mA cm⁻², (b) 60 mA cm⁻², and (c) 80 mA cm⁻², recorded over 6 consecutive charge/discharge cycles in the absence of bismuth, shown with different colours (1st-light blue; 2nd-orange; 3rd-grey; 4th-yellow;5th-blue; 6th-green).

At 40 mA cm^{-2} the charge and discharge profiles are relatively symmetric, with stable plateaux and moderate average voltage. As the current increases, the charge phase requires progressively higher potential, while the discharge phase collapses rapidly, with a significant reduction of the useful energy-release time. This trend signals a progressive increase of internal polarisation, resulting from both ohmic resistance and slow anodic kinetics, as observed in Ti–Fe systems without catalysts [119]. The V–t curves are particularly useful to assess the dynamic behaviour of the cell: the shape of the trace provides direct information on the balance between electrode kinetics and mass transport. A flat and horizontal plateau during charge and discharge indicates efficient and reversible redox reactions, while increasing slopes or unstable segments reflect aggravated internal losses. In particular, a rapid collapse of the discharge potential is often symptomatic of accumulating activation resistances or electrode surface degradation. The V–t curves therefore permit the monitoring of the real-time operational efficiency, by tracking the useful duration of each phase and the actual energy contribution of the cycle [120].

The analysis of the potential-capacity (V–Q) curves, presented in Figure 3.21, is also particularly notable.

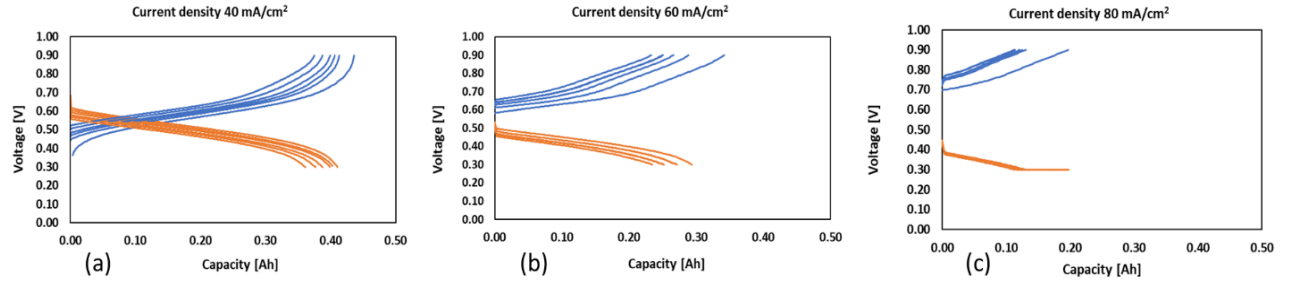


Figure 3.21: Voltage–capacity (V–Q) profiles of the Ti–Fe 1M battery using a mixed electrolyte at different current densities: (a) 40 mA cm⁻², (b) 60 mA cm⁻², and (c) 80 mA cm⁻², recorded over 6 consecutive charge/discharge cycles in the absence of bismuth, shown with different colours (charge blue and discharge orange))

At 40 mA cm^{-2}, the profiles show good symmetry between charge and discharge, with well-defined and relatively broad plateaux, indicating electrochemical behaviour that is efficient and reversible. However, as the current density increases, the plateaux progressively narrow, the voltage gap between the two branches increases and the total transferred capacity reduces. At 80 mA cm^{-2} the charge profile is strongly inclined upward, while the discharge branch shows a rapid collapse of voltage after a short initial segment. The enclosed

area between the curves visibly decreases, demonstrating a significant energetic loss due to polarisation and resistive dissipation. These observations reflect the worsening of performance under severe operating conditions, as extensively documented for the Ti^{3+}/Ti(IV) reaction on unmodified graphite felt [121]. The V–Q curves also serve as a diagnostic tool for assessing cyclic stability: progressive deformations of the profile over time signal irreversible changes in the electrochemical behaviour of the system, often linked to surface degradation or electrolyte composition variations [31].

The quantitative values of capacity, energy and power support the above qualitative considerations. At 40 mA/cm² the recorded capacity is 0.39 Ah, energy delivered is 0.18 Wh and average power is 0.08 W. At 60 mA/cm², despite the theoretical capacity increasing to 0.26 Ah, the useful energy drops to 0.10 Wh due to the reduced average voltage. At 80 mA cm^{-2}, the usable capacity collapses to 0.13 Ah with total energy of just 0.04 Wh, values clearly insufficient for continuous use, highlighting the practical limitations of the baseline configuration.

To evaluate the system stability over time, a long-term test of 100 consecutive cycles at 80 mA cm^{-2} was conducted. As shown in Figure 3.22, the voltage and energy efficiencies are already low from the initial cycles and remain overall limited throughout the entire test, exhibiting fluctuations rather than a progressive degradation trend. This behavior suggests that the poor performance observed at high current density is due to intrinsic limitations of the baseline configuration, likely associated with polarization phenomena and resistive losses, rather than a degradation process developing gradually over time.

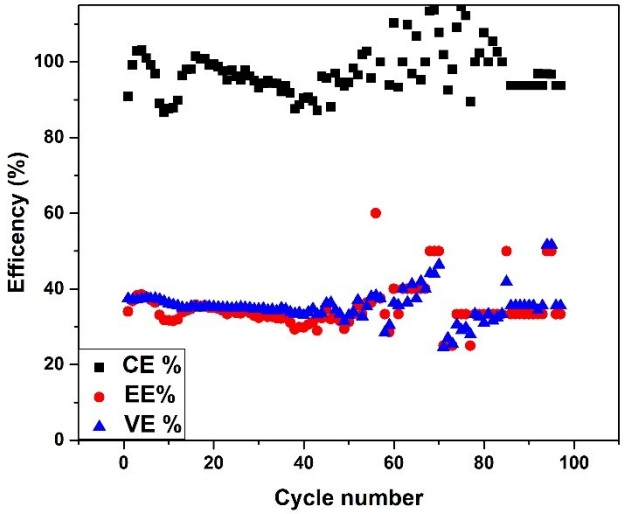


Figure 3.22: Long-term cycling performance of the Ti–Fe 1 M battery using a mixed electrolyte without bismuth at a constant current density of 80 mA cm^{-2} for 100 charge/discharge cycles.

To evaluate the system's stability over time, a long-duration test consisting of 100 cycles at 80 mA/cm² was performed. The results, shown in Figure 3.22, highlight the system's particularly unstable behavior. Unlike what is commonly expected in durability tests, the Coulombic Efficiency (CE) does not follow a monotonic

trend, but rather fluctuates widely throughout the series, with oscillations ranging from values above 100% to sudden drops below 90%. This anomalous behavior could be attributed to a variety of concurrent factors, including the progressive inhomogeneity in the distribution of active species, the appearance of parasitic phenomena (such as water oxidation or anodic side reactions), or malfunction of the pumping system or membrane, which could have altered the charge balance between the two compartments. At the same time, energy efficiency (EE) and voltaic efficiency (VE) also show overall low and relatively stable values in the first few cycles, then gradually deteriorate starting from the 40th–50th cycle. The loss of efficiency is accompanied by a growing oscillation, which indicates unstable electrochemical behavior, often a symptom of electrode degradation or instability of the cell potential. In the literature, similar fluctuations in efficiency have been correlated with the formation of inactive layers, electrochemical delamination phenomena, or internal "soft short-circuiting" processes within the cell, especially in systems based on unmodified titanium [122].
In support of this, Figure 3.23 reports the trend of specific discharge capacity over 100 cycles.

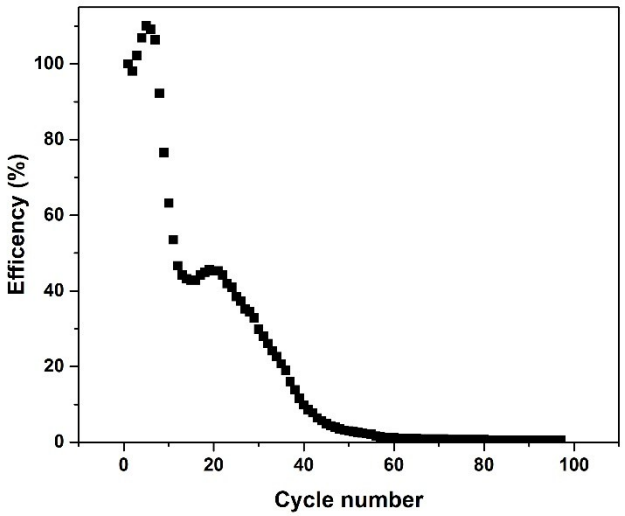


Figure 3.23: *Trend of discharge capacity over 100 charge/discharge cycles for the Ti–Fe 1 M battery using a mixed electrolyte at a constant current density of 80 mA cm⁻², in the absence of bismuth*

curve highlights a tendency towards linear capacity loss, with a marked reduction already after 20–30 cycles and an almost complete exhaustion of useful capacity around the 60th–70th cycle. This evolution suggests the progressive accumulation of inactive species or the irreversible loss of the electrode's active surface, as previously documented in similar vanadium- and titanium-based systems in acidic environments [80].
Overall, the data show that the bismuth-free Ti–Fe system, despite starting from promising initial conditions in terms of CE and potential redox reversibility, exhibits severe electrochemical instabilities when subjected to prolonged high-current charge/discharge regimes. Efficiency fluctuations, progressive loss of discharge capacity, and profile irregularities indicate the presence of significant degradation processes. In this context, the adoption of corrective strategies, such as the selective introduction of a catalytic promoter in the anode

compartment, capable of stabilizing long-term behavior and improving the overall efficiency of the system is warranted.

3.8.2 In-cell performance of the Ti–Fe battery with bismuth: catalytic effect and long-term stabilization

In light of the operational limitations highlighted in the catalyst-free configuration, extensively discussed in the previous section, the possibility of improving the performance of the Ti–Fe battery was investigated by introducing trivalent bismuth (Bi^{3+}) exclusively into the anodic compartment. The inclusion of this species was conceived as a targeted response to the kinetic sluggishness of the $Ti^{3+} \rightarrow TiO^{2+}$ oxidation process, one of the main causes of efficiency loss and premature system degradation [72], [80]. Several studies in the literature have shown that bismuth can deposit in situ as an elemental metal during charge cycles, creating highly active electrocatalytic surfaces that promote the reversibility of the anodic reaction and reduce the overpotential required for the Ti(III) oxidation [123]. In this context, the objective of the present section is to analyze in depth the performance of the modified system, assessing the impact of Bi^{3+} under both short-term operating conditions and extended cycling.

As shown in Figure 3.24, the addition of bismuth results in a marked improvement of the electrochemical performance compared with the additive-free configuration.

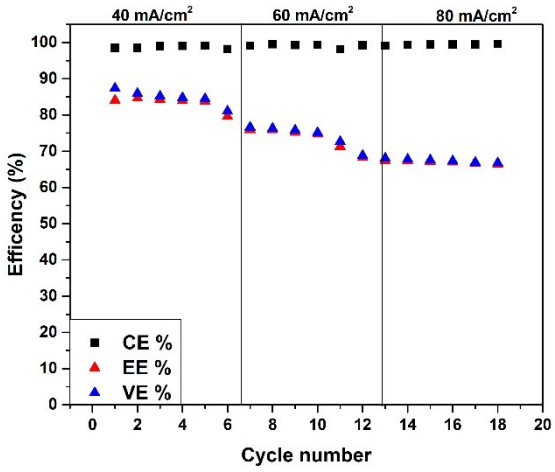


Figure 3.24: Coulombic efficiency (CE), voltaic efficiency (VE), and energy efficiency (EE) of the Ti–Fe flow battery using a mixed electrolyte (1 M Ti / 1 M Fe in 3 M H_2SO_4) with bismuth, during charge/discharge cycling at three different current densities: 40, 60, and 80 mA cm-².

The coulombic efficiencies (CE) remain consistently high, above 98% across the current density range considered (40, 60 and 80 mA cm^{-2}), with mean values of approximately 98.96%, 99.30% and 99.10% respectively. The voltage efficiency (VE) is also significantly more stable and higher relative to the baseline case, registering values of 84.75%, 75.67% and 67.74% at the three current densities. The overall energy

efficiency (EE), directly tied to the preceding two parameters, similarly shows improved stability: at 40 mA cm^{-2} it reaches 84.06%, and at 80 mA cm^{-2} it is 67.49%. Compared to the battery without bismuth, the increase is both evident and systematic, with an average gain exceeding 20 percentage points. This confirms the original hypothesis that Bi acts as a proficient catalytic promoter for the Ti(III)/Ti(IV) redox couple, mitigating energy losses and improving redox reversibility. A more detailed analysis is possible through the voltage-time (V–t) curves presented in Figure 3.25, which allow observation of the cell's dynamic behavior during charge and discharge.

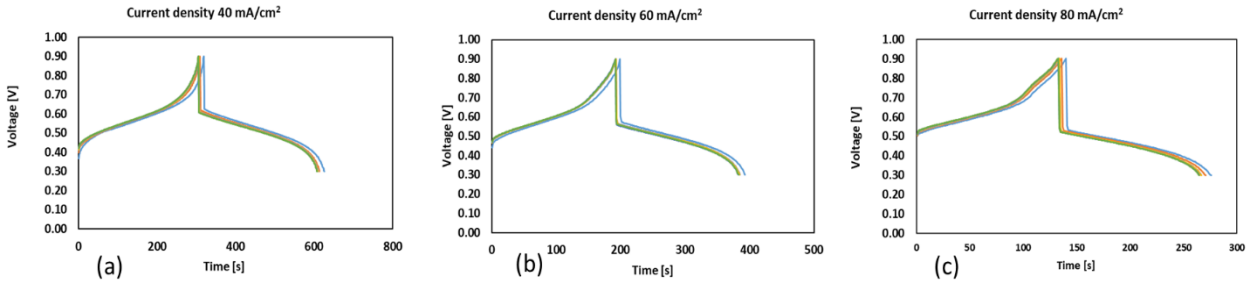


Figure 3.25: Charge/discharge voltage profiles of the Ti–Fe 1 M battery with mixed electrolytes at different current densities: (a) 40 mA cm^{-2}, (b) 60 mA cm^{-2}, and (c) 80 mA cm^{-2}, recorded over six consecutive charge/discharge cycles in the presence of bismuth, shown with different colours (1st-light blue; 2nd-orange; 3rd-grey; 4th-yellow;5th-blue; 6th-green).

At the lower current density (40 mA cm^{-2}), distinct and symmetric plateaus for charge and discharge are observed, indicating an efficient and controlled electrochemical process. As the current increases to 60 and 80 mA cm^{-2}, the curves maintain a regular and coherent shape, showing moderate internal resistance and no sudden voltage collapse. This behavior sharply contrasts with that of the battery lacking bismuth, where higher current densities led to rapid potential drops and significant distortions in discharge profiles. The regular plateau behavior suggests effective mitigation of kinetic barriers, attributable to the presence of metallic Bi, which facilitates charge transfer at the electrode/electrolyte interface [124].

The same positive trend is reflected in the voltage–capacity (V–Q) curves shown in Figure 3.26.

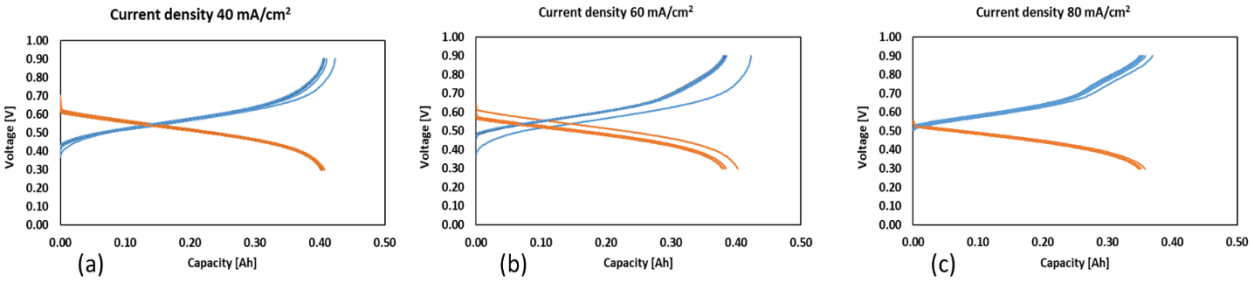


Figure 3.26: Voltage–capacity (V–Q) profiles of the Ti–Fe 1M battery using a mixed electrolyte at different current densities: (a) 40 mA cm^{-2}, (b) 60 mA cm^{-2}, and (c) 80 mA cm^{-2}, recorded over 6 consecutive charge/discharge cycles in the presence of bismuth, shown with different colours (charge blue and discharge orange).

At 40 mA cm^{-2}, the charge curve evolves in a relatively linear manner with moderate slope, and the discharge occurs at stable voltage, yielding a nearly mirror-image shape between the two branches. This is indicative of a reversible process and high energy efficiency. Even at 60 and 80 mA cm^{-2} the curves retain good symmetry and broader plateaus compared to the configuration without Bi, suggesting limited energy loss. The distance between the two branches is significantly reduced, the area enclosed between the curves increases, and the transferred capacity remains high. In literature, maintaining the symmetric form of V–Q curves is regarded as a key diagnostic parameter for evaluating the quality of charge-transfer and the stability of the electrode/electrolyte interface. The gentler slopes of the plateaus and absence of marked deviations indicate low resistive contributions and good integration of Bi on the anodic surface.

The experimental results quantitatively confirm the positive effect of bismuth on the system's performance. At low current densities (40 mA cm^{-2}), the battery shows an electrochemically usable capacity of around 0.40 Ah, a delivered energy of approximately 0.20 Wh and an average power of about 0.08 W. When the current density is increased to 80 mA cm^{-2} under more stressful conditions, the capacity drops only slightly to 0.35 Ah, the energy is around 0.16 Wh and the power about 0.14 W. These values not only surpass those observed in the configuration without Bi, but also demonstrate greater internal coherence and stability. The system appears capable of sustaining the current increase without abrupt performance loss, suggesting that bismuth contributes not only as a temporary promoter, but helps strengthen the entire electrochemical architecture, making it more resilient under demanding operating conditions.

Finally, a long-term test consisting of 100 cycles at 80 mA cm^{-2} was conducted to evaluate the modified system's operational stability. The results, shown in Figure 3.27, reveal a significantly more stable behavior compared to the configuration without Bi (Figure 3.22).

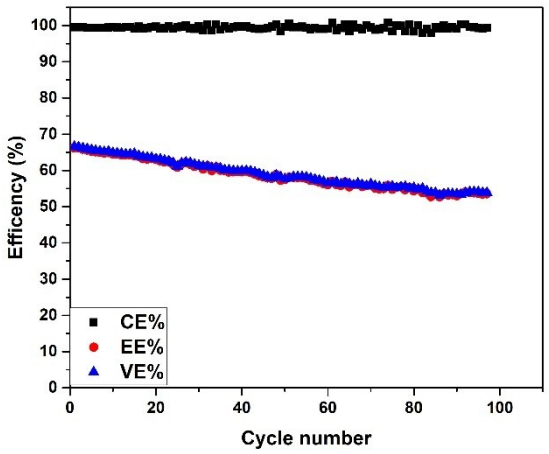


Figure 3.27: Long-term cycling performance of the Ti–Fe 1 M battery using a mixed electrolyte with bismuth at a constant current density of 80 mA cm^{-2} for 100 charge/discharge cycles.

The coulombic efficiency remains above 98% throughout the entire test duration, and the voltage and energy efficiencies (VE and EE) show a gradual decline, but with final values still above 55%. This represents a

dramatic improvement over the collapse observed in the unmodified cell, where capacity was exhausted after only ~60 cycles. Figure 3.28 shows the retained capacity, which stabilizes at 56% after 100 cycles, confirming the protective role of Bi against inactive deposit formation and interface degradation.

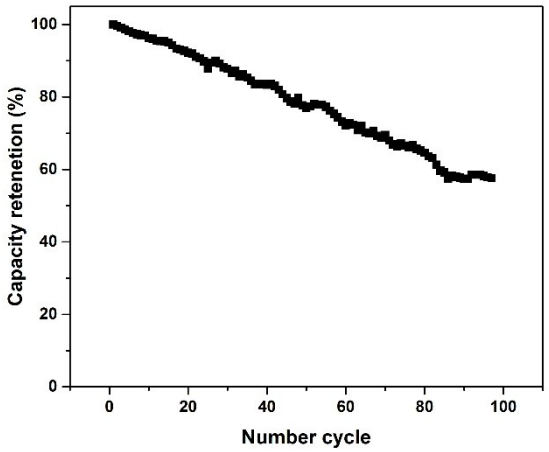


Figure 3.28: Trend of discharge capacity over 100 charge/discharge cycles for the Ti–Fe 1 M battery using a mixed electrolyte at a constant current density of 80 mA cm⁻² with bismuth.

In summary, the introduction of bismuth represents a practical and effective solution to overcome the limitations of the Ti–Fe chemistry. The benefits appear not only in terms of energy efficiency, but also in prolonged cycle stability, positioning the modified configuration as a promising candidate for stationary storage applications. These results open the way for further optimizations through combined strategies of electrode activation and advanced electrolyte management.

3.8.3 Electrochemical Impedance Spectroscopy (EIS) Analysis

To gain deeper insight into the electrokinetic processes and to evaluate the evolution of internal resistance during cell operation, an electrochemical impedance spectroscopy (EIS) analysis was performed on the mixed Ti–Fe 1 M system, both with and without bismuth. As described in 2.1.3, this technique is an extremely sensitive tool capable of distinguishing the resistive, capacitive, and diffusive contributions to the overall electrochemical response of the cell, thus allowing identification of the main factors that limit charge-transfer kinetics and contribute to ohmic losses. The measurements were conducted in a single-cell configuration, under the same operating conditions as those used for galvanostatic tests (T = 25 °C, flow rate = 40 mL min^{-1}), applying a sinusoidal perturbation of 10 mV in the frequency range from 100 kHz to 10 mHz. The Nyquist plots obtained are shown in Figure 3.29, corresponding respectively to the initial state of charge (SOC 0%) and to the fully charged condition (SOC 100%). These two states represent, respectively, the configuration of the system prior to cycling and the condition of maximum oxidation of the Fe^{2+}/Fe^{3+} and Ti^{3+}/TiO^{2+} redox couples after the charging phase.

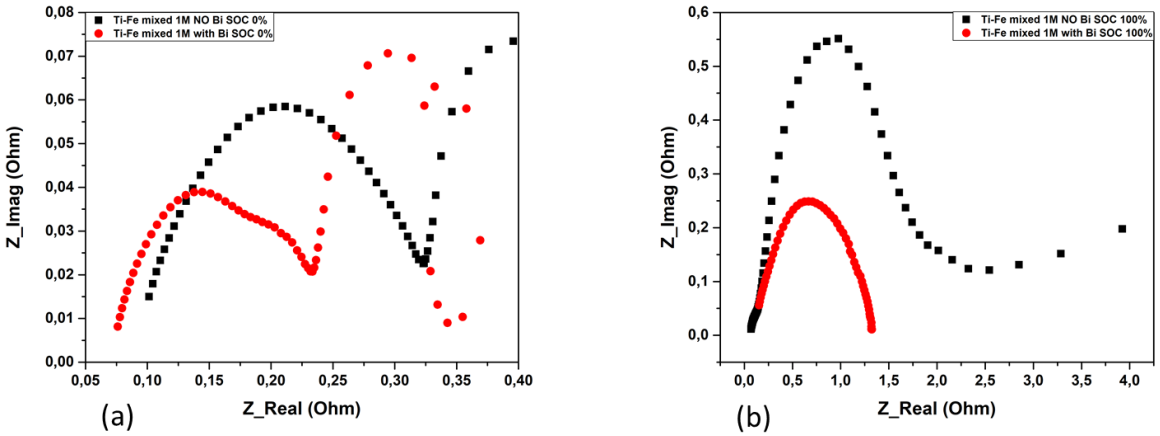


Figure 3.29: Nyquist plots of the mixed Ti–Fe 1 M system with and without bismuth, recorded at (a) SOC 0 % and (b) SOC 100 %. The presence of Bi lowers the charge-transfer resistance and mitigates diffusional limitations after cycling.

In the SOC 0% diagram (Figure 3.29a), both curves display the typical semicircular shape associated with RC-type systems. The intercept on the real axis (Z′) at high frequency corresponds to the total ohmic resistance (R_s), which includes contributions from the electrolyte, membrane, and contacts, while the semicircle diameter represents the charge-transfer resistance (R_{ct}), related to the $Ti^{3+} \rightleftharpoons TiO^{2+}$ redox kinetics. The curve corresponding to the Bi-containing system exhibits a smaller semicircle and a lower intercept, indicating an overall reduction in internal resistance. This behavior suggests that, even under initial conditions, the presence of Bi enhances the interfacial electron exchange between electrode and electrolyte, likely due to the formation of metallic Bi nuclei acting as catalytic centers on the carbon felt fibers. The smaller semicircle radius reflects a notable decrease in the kinetic barrier of the anodic process, while the moderate 45° slope in the low-frequency region indicates a controlled diffusive contribution and effective electrolyte circulation within the porous electrode. The more compact and linear trace observed in the Bi-modified cell further suggests a more homogeneous electrode surface and improved electronic coupling between solid and liquid phases.

The SOC 100% diagram (Figure 3.29b) corresponds to the post-charging condition. In this state, the overall impedance response becomes more resistive, with a visible increase in semicircle diameter for both samples, attributable to the accumulation of oxidized species, higher ionic concentration, and the possible formation of less conductive surface layers during extended polarization. This behavior is typical of metal-based redox systems, where oxidation-state variations modify both the local electrolyte conductivity and the structure of the electrical double layer. Nevertheless, the difference between the two configurations remains evident: the Bi-containing cell retains a more compact arc and a lower intercept, confirming that the catalytic effect of bismuth persists even after repeated cycling, mitigating the increase in charge-transfer resistance and

preserving efficient interfacial conductivity. The ability of bismuth to deposit as a metallic phase on the carbon felt and to remain stable during charge/discharge processes ensures continuous regeneration of active sites, preventing insulating film formation or substrate deactivation. Conversely, the Bi-free system exhibits a marked enlargement of the high-frequency arc and a shift toward higher Z' values, indicating deteriorated kinetic and diffusive behavior, consistent with the formation of passive layers or partial electrode degradation. The enhanced curvature observed in the low-frequency region suggests increased diffusional resistance and less efficient mass transport within the porous structure. It is also noteworthy that, after cycling, the typical diffusion line observed at SOC 0% nearly disappears. This phenomenon indicates that the diffusive contribution has been greatly diminished and that the electrochemical response is now governed predominantly by charge-transfer processes. The presence of Bi promotes the formation of highly conductive metallic surfaces, rendering the system faster and mainly controlled by interfacial kinetics rather than by mass transport. In other words, the disappearance of the Warburg line should be regarded as a positive sign: it demonstrates the reduction of diffusional limitations due to improved electrical contact and greater accessibility of redox species at the active surface. The combined effect of enhanced surface conductivity and efficient ionic exchange within the felt results in an almost purely resistive–capacitive response, characteristic of a more homogeneous, stable, and kinetically favored electrochemical system. Overall, the impedance analysis shows that the charge-transfer resistance is the main contributor to the internal polarization of the cell and is strongly affected by the nature of the anodic surface. The presence of bismuth markedly decreases this resistance both before and after cycling, confirming its catalytic and stabilizing role and indicating improved adhesion between the metallic layer and the carbon substrate. The evolution of the Nyquist profile from SOC 0% to SOC 100% reflects the expected increase in polarization associated with the transition from reduced to oxidized states, but this rise is significantly mitigated by the Bi additive. These findings are fully consistent with the galvanostatic performance results, where the Bi-containing cell exhibited higher energy efficiencies, more regular charge/discharge curves, and greater long-term stability. EIS measurements therefore confirm that the beneficial effect of Bi stems from the reduction of kinetic barriers and the improvement of charge-transfer characteristics at the electrode–electrolyte interface. In perspective, the observed decrease in interfacial resistance can be interpreted as a clear indicator of the long-term stabilization of the Ti–Fe system, implying lower ohmic losses, reduced energy dissipation, and a more uniform current distribution throughout the electrode. These results provide strong experimental evidence for the validity of the catalytic strategy adopted for the optimization of the Ti–Fe system and offer a quantitative and qualitative foundation for the future design of improved configurations in terms of both performance and durability.

3.8.4 Post-cycle morphological analysis of electrodes by SEM

Following the electrochemical tests in mixed-electrolyte configuration, both with and without the addition of bismuth, a detailed morphological investigation of the electrodes was carried out to assess the effects of charge/discharge cycling on the surface structure of the carbon felt. Prior to SEM observation, the electrodes were carefully rinsed with ultrapure water and briefly sonicated in ethanol to remove any residual electrolyte

or loosely bound species. This step ensured that the morphological features observed were attributable to electrochemical effects rather than external contamination. The analysis was conducted by scanning electron microscopy (SEM), previously described in 2.2.1, with the aim of identifying morphological changes and, in particular, metallic deposits resulting from the electrochemical reduction of Bi^{3+} in the anodic compartment.
This stage of the work holds strategic importance, as it enables a direct correlation between electrochemical performance and microscopically observable surface features, offering a complementary perspective to the voltammetric and efficiency data previously discussed. As widely reported in recent literature, the electrochemical deposition of bismuth represents one of the most effective strategies to improve the reversibility of the Ti^{3+}/TiO^{2+} redox couple, which is typically hindered by sluggish kinetics and surface passivation phenomena. Once reduced, bismuth forms a thin metallic layer that distributes over the carbon felt fibers, altering their surface properties and facilitating electron transfer at the electrode/electrolyte interface [72], [123]. SEM analyses, conducted on electrodes extracted from the cell after cycling, revealed the evolution of the electrode surface at various magnifications. At low magnification (250×, Figure 3.30), a continuous and well-preserved fibrillar network was observed, with no macroscopic signs of mechanical damage or structural collapse.

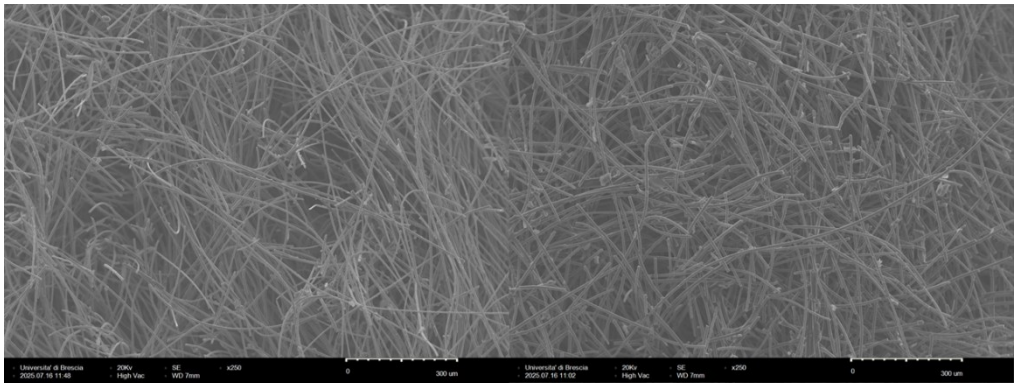


Figure 3.30: SEM images at 250× magnification of carbon felt electrodes after 100 charge/discharge cycles, tested with mixed electrolyte (1 M Ti + 1 M Fe in 3 M H_2SO_4) and added Bi^{3+} :

This indicates that, despite the relatively harsh operating conditions (up to 80 mA cm^{-2} and over 100 consecutive cycles), the carbon substrate maintained its mechanical integrity—a critical requirement for long-term system durability.
At intermediate magnification (1000×, Figure 3.31), localized irregularities and small nodular structures began to emerge along the fiber surfaces.

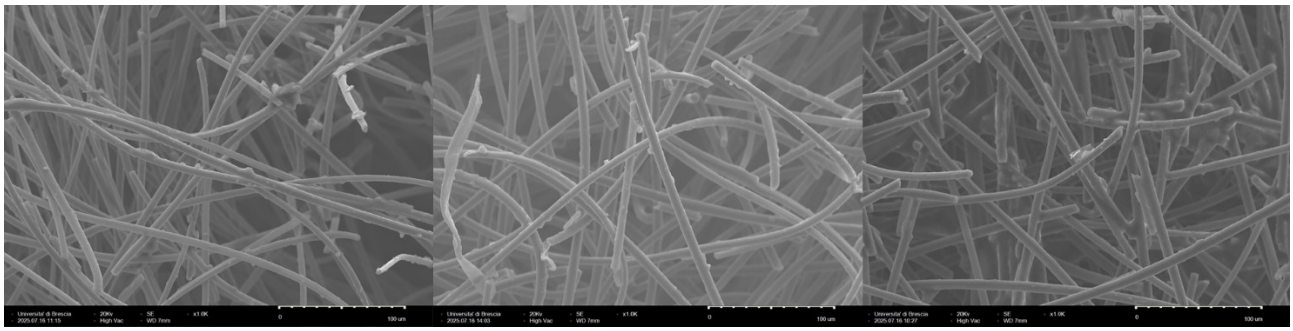


Figure 3.31: SEM images at 1000× magnification of carbon felt electrodes after 100 charge/discharge cycles, tested with mixed electrolyte (1 M Ti + 1 M Fe in 3 M H_2SO_4) and added Bi^{3+}

These features, completely absent in the uncycled electrodes (not shown), are morphologically consistent with metallic electrochemical deposits, most likely bismuth. At higher magnification (3000×, Figure 3.32), sub-micrometric granular agglomerates were clearly visible, typically 200–600 nm in size, uniformly distributed on the outer surface of the fibers.

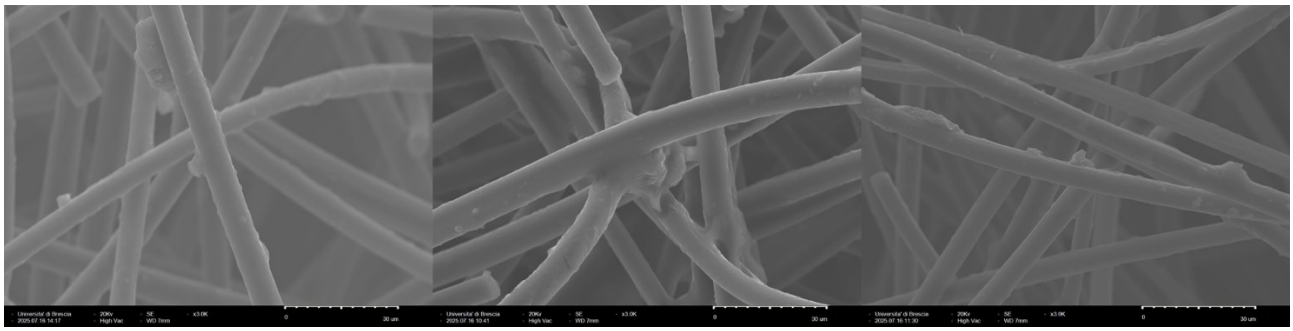


Figure 3.32: SEM images at 3000× magnification of carbon felt electrodes after 100 charge/discharge cycles, tested with mixed electrolyte (1 M Ti + 1 M Fe in 3 M H_2SO_4) and added Bi^{3+}

Although this analysis was purely morphological and not accompanied by elemental mapping (e.g., EDS), the presence of Bi^{3+} in solution, the favorable redox conditions for its reduction, and the consistency with literature reports strongly support the attribution of these deposits to metallic Bi^0. Functionally, the presence of these deposits aligns with the improved electrochemical performance observed in the presence of bismuth, particularly in terms of higher voltaic efficiency, reduced overpotentials, and enhanced cycling stability. SEM images thus provide compelling visual evidence of the catalytic effect of bismuth, confirming that the additive not only remains electrochemically active in solution but also physically integrates into the electrode, generating a conductive metal–carbon hybrid surface. Notably, no signs of critical degradation were observed, such as passivating film formation, fiber cracking, or mechanical fragmentation. On the contrary, the electrode surface retained good porosity and morphological continuity, suggesting excellent compatibility between the carbon felt and the acidic electrolyte environment containing bismuth. This is especially relevant for long-term applications, where substrate stability plays a central role in performance retention.

In summary, the morphological analyses conducted via SEM confirmed the effectiveness of Bi^{3+} addition in modifying the electrode surface in a controlled and beneficial manner. This contributed both to the stabilization

of the Ti–Fe system and to the improvement of its interfacial charge transfer properties. These findings reinforce the hypothesis of a synergistic relationship between surface catalysis and electrochemical optimization, and open the door to further investigations on alternative metal catalysts, electrode pre-treatment strategies, and surface engineering aimed at reducing energy losses in redox flow systems.

3.9 Performance Evaluation of the Ti–Fe System Using Mixed Electrolytes at 0.5 M Ti with Bismuth

To investigate the effect of electrolyte concentration on the electrochemical performance of the Ti–Fe system, a series of galvanostatic tests was carried out using a mixed electrolyte composed of 0.5 M Ti and 0.5 M Fe dissolved in 3 M H_2SO_4. This configuration was designed to explore operating conditions with lower active material content, aiming to reduce overall costs, simplify electrolyte management, and mitigate side reactions, while assessing whether performance could be maintained at acceptable levels. All tests were conducted in the presence of Bi^{3+} in the anolyte, based on previous results obtained with the 1 M configuration, where bismuth was shown to significantly enhance the anodic kinetics of the $Ti^{3+} \rightarrow TiO^{2+}$ reaction by improving redox reversibility and reducing charge-transfer resistance [70], [72]. From a chemical standpoint, dilution of the redox species introduces several interdependent effects. In highly acidic media, Ti(IV) species are stabilized by sulfate complexation—mainly as $[TiO(SO_4)_2]^{2-}$ and $[Ti(OH)_2(SO_4)_2]^{2-}$—which prevents hydrolysis and precipitation [85], [89]. However, at high concentrations, polymerization or the formation of colloidal species may occur, reducing electrochemical availability and diffusion. Lower concentrations, on the other hand, help limit such processes and also improve the electrolyte's fluidity: reduced viscosity enhances infiltration into the porous felt and improves ion transport through the membrane [125], [126]. The aim of this investigation was to assess how concentration affects energy efficiency, charge capacity, and long-term cycling stability under catalytically active conditions.

Short-term galvanostatic tests were conducted at three increasing current densities (40, 60, and 80 mA cm^{-2}), under otherwise identical conditions (Figure 3.33).

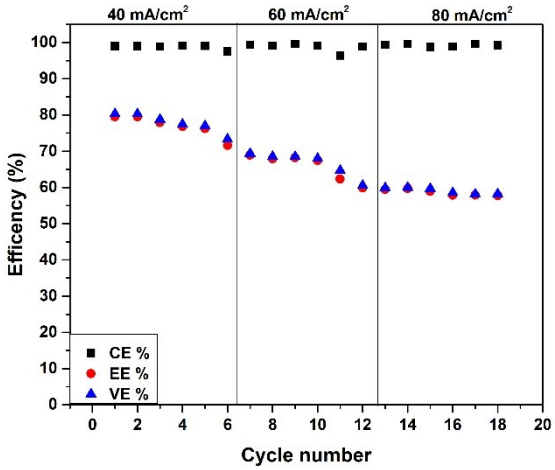


Figure 3.33: Coulombic efficiency (CE), voltaic efficiency (VE), and energy efficiency (EE) of the Ti–Fe flow battery using a mixed electrolyte (0.5 M Ti / 0.5 M Fe in 3 M H_2SO_4) without bismuth, during charge/discharge cycling at three different current densities: 40, 60, and 80 mA cm-².

As shown in Figure 3.33, at 40 mA cm⁻², the cell delivered excellent performance: coulombic efficiency (CE) reached 99.10%, with a voltage efficiency (VE) of 77.68% and an overall energy efficiency (EE) of 77.32%. The discharged capacity per cycle was 0.17 Ah, corresponding to 0.09 Wh of usable energy and an average power output of 0.08 W. These results indicate excellent redox reversibility and low internal losses at low current, thanks to the catalytic action of Bi. At 60 mA cm⁻², performance begins to decline: EE dropped to 67.84%, VE to 67.91%, while CE remained high (99.23%), suggesting that the losses are primarily resistive. At this current, the system still achieved 0.06 Ah capacity and 0.05 Wh of energy output. At 80 mA cm⁻², a marked performance degradation was observed, with a steep reduction in discharge voltage and compressed operating time.

The voltage–time (V–t) profiles shown in Figure 3.34 reflects these trends.

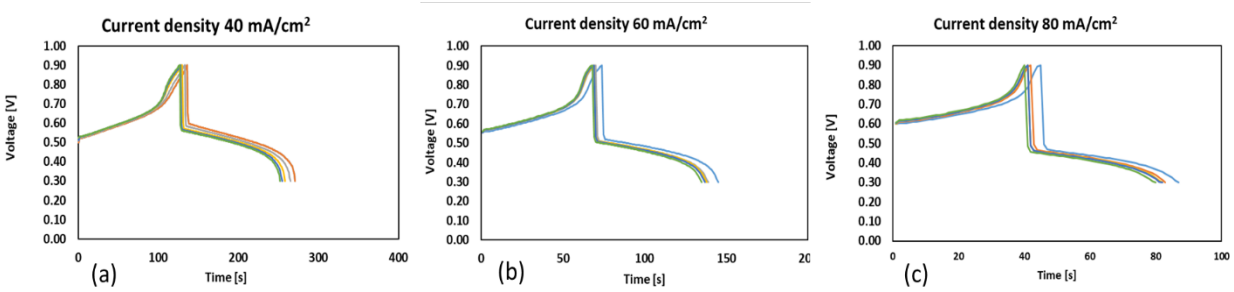


Figure 3.34: Charge/discharge voltage profiles of the Ti–Fe 0.5M battery with mixed electrolytes at different current densities: (a) 40 mA cm⁻², (b) 60 mA cm⁻², and (c) 80 mA cm⁻², recorded over six consecutive charge/discharge cycles in the presence of bismuth, shown with different colours (1st-light blue; 2nd-orange; 3rd-grey; 4th-yellow;5th-blue; 6th-green).

At 40 mA cm⁻², the charge/discharge plateaus were symmetric and flat, indicating well-balanced electrochemical processes. As current increased, the plateaus shortened and sloped, particularly during

discharge. At 80 mA cm^{-2}, the discharge plateau sharply contracts and the average useful potential drops drastically, indicating a marked increase in internal resistance and the system's difficulty in sustaining the high current regime. These observations were confirmed by the voltage–capacity (V–Q) curves in Figure 3.35 which showed a progressive narrowing of the energy-delivering region and widening of the hysteresis between charge and discharge branches.

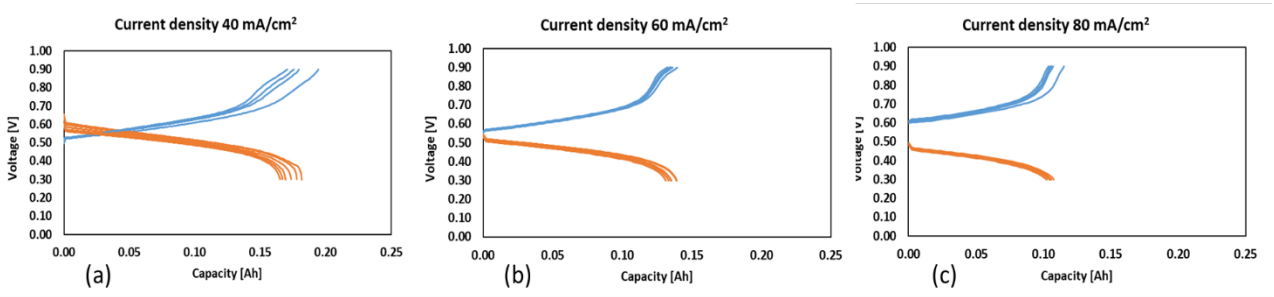


Figure 3.35: Voltage–capacity (V–Q) profiles of the Ti–Fe 0.5 M battery using a mixed electrolyte at different current densities: (a) 40 mA cm^{-2}, (b) 60 mA cm^{-2}, and (c) 80 mA cm^{-2}, recorded over 6 consecutive charge/discharge cycles in the presence of bismuth, shown with different colours (charge blue and discharge orange).

These curves provide a more detailed view of the cell's energy response under different current regimes. At 40 mA cm^{-2}, the profile exhibits a regular and well-developed shape, with good symmetry between the charge and discharge phases and limited hysteresis, indicating high system reversibility and low energy losses. As the current density increases to 60 mA cm^{-2}, the usable area narrows, and a growing separation between the charge and discharge branches is observed, indicating increased internal polarization and ohmic resistance. This trend becomes even more pronounced at 80 mA cm^{-2}, where the discharge curve is visibly compressed and the charge phase extends to higher potentials, significantly distorting the overall profile. The widening of hysteresis and the reduction in effectively utilized capacity suggest that, at higher current densities, the system cannot fully exploit its theoretical capacity due to limitations related to redox reaction kinetics and mass transport. These phenomena have a direct impact on the cell's energy efficiency, confirming the greater sensitivity of the diluted system to polarization effects under high-current operating conditions.

As for long-term stability, a 100-cycle test at 80 mA cm^{-2} was carried out to evaluate the evolution of the system's performance over time. As shown in Figure 3.36, CE remained consistently above 98% throughout the entire test, while VE and EE gradually declined, stabilizing around 57% and 56%, respectively, by the 100th cycle.

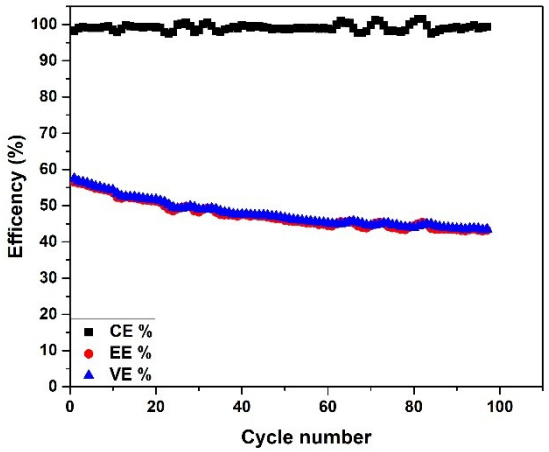


Figure 3.36: Long-term cycling performance of the Ti–Fe 0.5 M battery using a mixed electrolyte with bismuth at a constant current density of 80 mA cm⁻² for 100 charge/discharge cycles.

In parallel, the discharge capacity exhibited a progressive decrease, as illustrated in Figure 3.37, with a total capacity retention of approximately 60% at the end of the test.

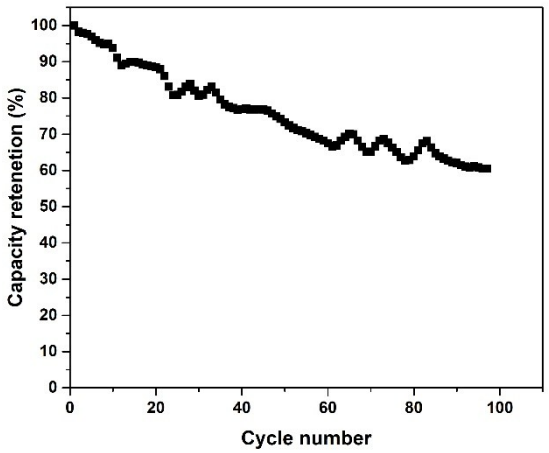


Figure 3.37: Trend of discharge capacity over 100 charge/discharge cycles for the Ti–Fe 0.5 M battery using a mixed electrolyte at a constant current density of 80 mA cm-² with bismuth

This trend suggests a gradual loss of active material or electrode accessibility, possibly due to the accumulation of electrochemically inactive species, clogging of the porous matrix, or partial surface passivation. Despite the observed degradation, the evolution was linear and reproducible, without abrupt capacity drops or signs of electrochemical instability. These results confirm the ability of the diluted system to maintain regular operation under high-current conditions, albeit with a gradual decline in discharge capacity that ultimately limits its long-term energy output. The sustained coulombic efficiency, however, indicates that the degradation mechanisms

are not associated with significant side reactions or charge imbalance, but are more likely related to resistive losses and structural changes within the electrode materials.

Nevertheless, when directly compared to the 1 M mixed electrolyte system with, the limitations of the diluted configuration become apparent. The 1 M system consistently outperformed the 0.5 M system in terms of EE, VE, and capacity retention, particularly under high-current conditions. In the 1 M case, EE remained above 67% even after 100 cycles, whereas the diluted system dropped below 56%. This difference is attributed to the lower available charge density and increased diffusion limitations in the 0.5 M solution, despite the beneficial presence of Bi. In summary, the diluted configuration remains technically viable and electrochemically stable, especially at low-to-moderate current densities, and may be attractive in applications where reduced metal content or lower electrolyte viscosity is advantageous. However, for performance-driven applications aiming to maximize energy efficiency and long-term durability, the 1 M mixed electrolyte system with bismuth remains the optimal configuration for Ti–Fe redox flow batteries.

3.10 Electrochemical Evaluation of the Ti–Fe Cell with Separated Electrolytes

Following the results obtained with the 1 M mixed electrolyte configuration, where the addition of Bi^{3+} significantly improved the electrochemical performance of the Ti–Fe cell, an additional set of experiments was designed employing a separated-electrolyte configuration. In this setup, the anodic compartment contained 1 M $TiOSO_4$ and the cathodic compartment 1 M $FeSO_4$, both dissolved in 3 M H_2SO_4. In this case as well, the anolyte was doped with Bi^{3+}, introduced in the form of $Bi_2(SO_4)_3$, to exploit its catalytic action on the Ti^{3+} oxidation reaction, as previously discussed for the mixed system. The adoption of a separated-electrolyte configuration had two main objectives: on the one hand, to independently study the behavior of the two half-reactions, isolating their contribution to the overall performance; on the other, to investigate the role of ionic crossover between Ti and Fe, which becomes particularly relevant in this type of configuration due to the strong compositional gradient between the two compartments. This approach is consistent with what is proposed in the literature for asymmetric redox systems, where the physical separation of active species helps reduce mutual interference between reactions, though at the cost of increased ionic imbalance and potential operational instabilities [42]. Indeed, in systems with separated electrolytes, the flux of redox species across the membrane from anolyte to catholyte (and vice versa) is significantly amplified, which can lead over time to the formation of inactive products, directly impacting the available capacity and system stability. Furthermore, this separation allows for a more in-depth study of the selectivity of reactions in the two compartments, contributing to the understanding of specific mechanisms that govern the redox balance between the Ti^{3+}/TiO^{2+} and Fe^{3+}/Fe^{2+} couples. Galvanostatic tests at different current densities (40, 60, and 80 mA cm^{-2}) revealed behavior typical of a reversible system affected by kinetic and ohmic limitations. Figure 3.38 shows the evolution of coulombic efficiency (CE), voltage efficiency (VE), and energy efficiency (EE) as a function of the number of cycles.

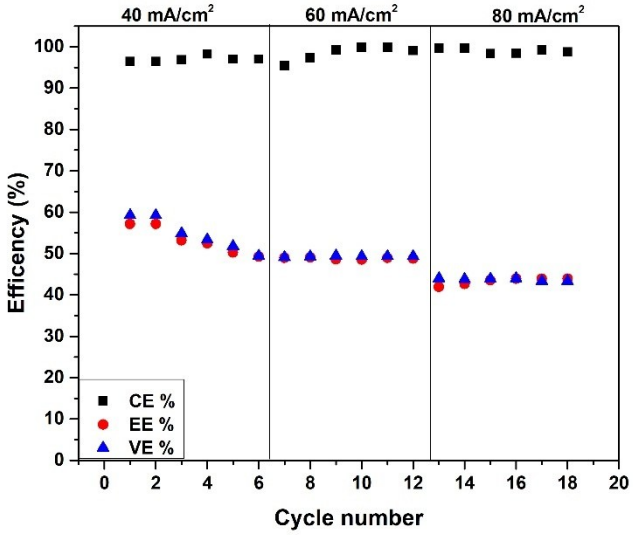


Figure 3.38: Coulombic efficiency (CE), voltaic efficiency (VE), and energy efficiency (EE) of the Ti–Fe flow battery using separated electrolyte (1 M Ti in anolyte side and 1 M Fe in catholyte side both in 3 M H_2SO_4) with bismuth, during charge/discharge cycling at three different current densities: 40, 60, and 80 mA cm^{-2}.

CE remains relatively low for all tested conditions, with average values around 96%, indicating partial irreversibility of the redox reactions and possible phenomena of undesired species migration. Notably, there is no improvement in CE at lower current densities, suggesting that parasitic effects are not limited by the operating conditions. VE and EE are strongly penalized by the applied current density: at 40 mA cm^{-2}, EE reaches 67.2% and VE 69.5%; at 60 mA cm^{-2}, these drop to 47.5% and 48.4%, respectively; while at 80 mA cm^{-2}, EE remains at 47.6% and VE falls to 44.3%. This trend indicates a clearly ohmic regime dominated by internal losses, which increase non-linearly with current density.

The voltage vs. time curves (Figure 3.39a–c) confirm the previously observed behavior: increasing current density leads to a sharp rise in potential during charge, while discharge becomes progressively less stable, with sudden voltage drops and poorly defined plateaus.

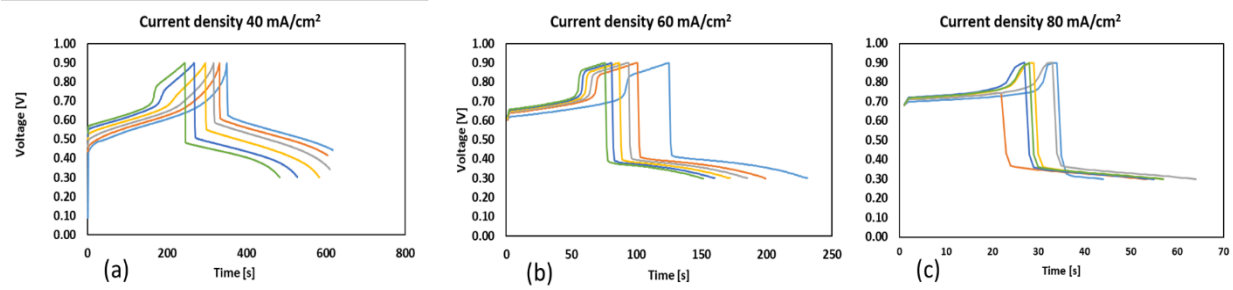


Figure 3.39: Charge/discharge voltage profiles of the Ti–Fe 1M battery with separated electrolytes at different current densities: (a) 40 mA cm^{-2}, (b) 60 mA cm^{-2}, and (c) 80 mA cm^{-2}, recorded over six consecutive charge/discharge cycles in the absence of bismuth, shown with different colours (1st-light blue; 2nd-orange; 3rd-grey; 4th-yellow;5th-blue; 6th-green).

From an electrochemical point of view, the step observed in the initial part of the charge curve at all current densities (Figure 3.39) indicates a transition between two distinct operating regimes. In the first portion of the curve, the potential is governed by non-stationary transient processes, in which double-layer charging, relaxation of concentration gradients, and secondary reactions involving redox species that have crossed the separator are superimposed. At moderate current densities, the system has sufficient time within each cycle to relax these imbalances: the species involved in parasitic reactions are progressively consumed and the charge profile tends to become more regular. In contrast, at 60 and 80 mA cm^{-2} the system is continuously driven far from equilibrium; the characteristic times for diffusion through the separator and for bulk mixing become comparable to, or longer than, the half-cycle duration, and the formation of crossed species and mixed potential states is renewed on each cycle. Under these conditions, the secondary processes do not die out, and the step remains a persistent feature of the charge profile for all cycles. At 40 mA cm^{-2} (Figure 3.39a), the charge plateau extends for approximately 120 s around 0.85 V, while discharge occurs smoothly down to around 0.30 V, with similar duration and symmetrical shape. This indicates good reversibility and low internal resistance. At 60 mA cm^{-2} (Figure 3.39b), the cycle compresses to about 60 s per phase, with a steeper discharge curve and clear ohmic losses. At 80 mA cm^{-2} (Figure 3.39c), the cell quickly reaches the 0.9 V limit, and discharge features a sharp initial drop followed by a short, poorly defined plateau, indicating advanced polarization and high overpotentials. These profiles suggest that, with increasing current, the system enters a progressively non-optimal regime, where electron transfer rates and ionic transport become insufficient to sustain the applied current, leading to a marked decline in energy conversion efficiency. This effect is even more evident in the voltage vs. capacity representation (Figure 3.40a–c).

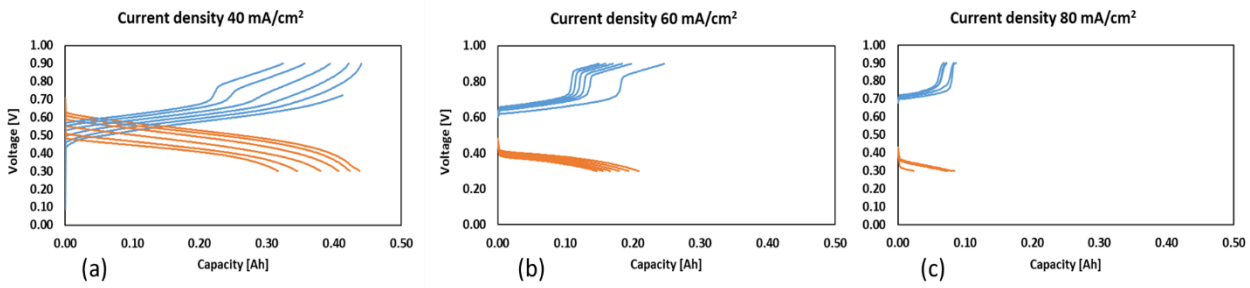


Figure 3.40: Voltage–capacity (V–Q) profiles of the Ti–Fe 1M battery using a separated electrolyte at different current densities: (a) 40 mA cm^{-2}, (b) 60 mA cm^{-2}, and (c) 80 mA cm^{-2}, recorded over 6 consecutive charge/discharge cycles in the presence of bismuth, shown with different colours (charge blue and discharge orange).

At 40 mA cm^{-2} (Figure 3.40a), the charge curve extends smoothly to around 0.22 Ah, while the discharge yields 0.38 Ah, with a relatively small area between the two branches. This implies good energy efficiency, low ohmic losses, and effective utilization of redox-active species. At 60 mA cm^{-2} (Figure 3.40b), the discharged capacity increases to 0.17 Ah, but the gap between charge and discharge branches widens considerably, reflecting higher energy losses due to compromised transport and reaction balance. At 80 mA cm^{-2} (Figure 3.40c), the curve is dramatically compressed: the discharged capacity drops to just 0.07 Ah, and the average voltage decreases sharply due to strong ohmic losses and polarization. In this context, the V vs. Q

curves not only quantify useful capacity but also act as direct indicators of internal energy dissipation: the area enclosed between the branches increases with current, highlighting rising resistive losses and kinetic limitations. These results confirm that the separated-electrolyte configuration suffers significantly under higher current densities due to the accumulation of resistive effects and inefficient charge transfer.

To evaluate long-term system stability, a prolonged cycling test of 100 cycles at 80 mA cm^{-2} was conducted. The results, shown in Figure 3.41, indicate stable and high CE, while VE and EE stabilize at lower but constant values.

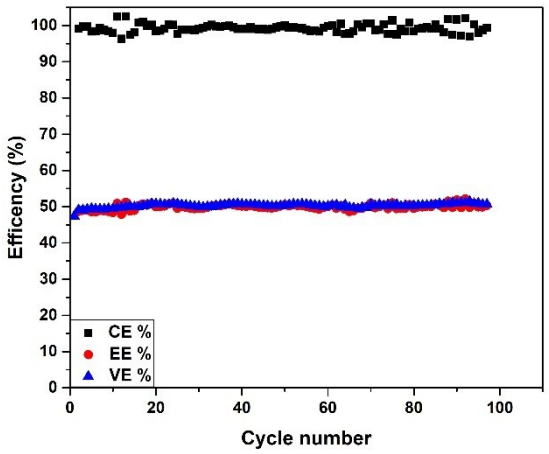


Figure 3.41: Long-term cycling performance of the Ti–Fe 1 M battery using a separated electrolyte with bismuth at a constant current density of 80 mA cm^{-2} for 100 charge/discharge cycles.

However, Figure 3.42, which reports the residual capacity, reveals unusual behavior.

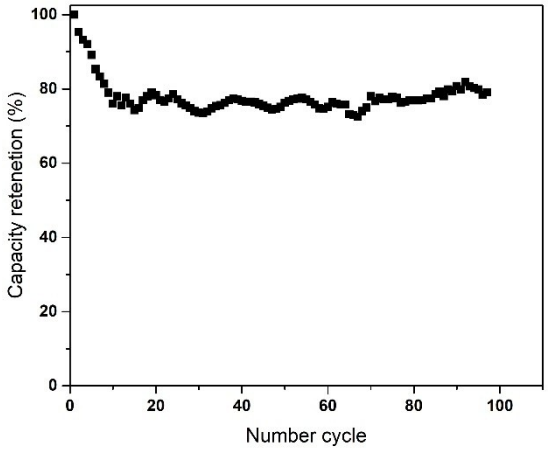


Figure 3.42: Trend of discharge capacity over 100 charge/discharge cycles for the Ti–Fe 1 M battery using a separated electrolyte at a constant current density of 80 mA cm^{-2} with bismuth

After a sharp drop during the first 15–20 cycles (down to 75% of the initial capacity), an unstable plateau emerges, characterized by cyclical fluctuations that persist through the end of the test, stabilizing around 80%. These oscillations, with variable but contained amplitude, show no obvious periodicity, suggesting a dynamic instability driven by multiple, partially uncontrolled phenomena.

The observed residual capacity behavior, atypical compared to the regular linear decline in conventional redox batteries, may be attributed to a complex combination of chemical, electrochemical, and structural factors. Although the hypotheses presented have not yet been experimentally confirmed, they are consistent with both the literature and the behavior observed during testing. One explanation involves enhanced ionic crossover, exacerbated by the steep concentration gradient between compartments in separated-electrolyte systems. This may result in charge imbalance, accumulation of non-regenerable reduced or oxidized species, or the formation of inactive products such as Ti^{4+} or Fe^{0} that no longer contribute to the redox cycle [127]. Another plausible scenario is a chemical stabilization phase occurring during initial cycles, involving precipitation of secondary species (oxides, hydroxides, or poorly soluble sulfates), which reduces the amount of available redox-active material in solution. This could stabilize over time, giving rise to the observed plateau. Similar behaviors have been reported in other multivalent metal-based systems under acidic conditions [42], [128]. A third hypothesis relates to the formation and stabilization of the Bi metal catalytic film on the electrode surface. In the early cycles, this film may be poorly distributed or non-uniform, limiting the $Ti^{3+} \rightarrow TiO^{2+}$ reaction efficiency. Once a stable morphology is reached, the residual capacity also stabilizes, as evidenced by recent work on early-stage behavior of catalytic films [129], [130]. Finally, the high current density imposed (80 mA cm^{-2}) could push the system into an extreme polarization regime, limiting access of redox species to the electrodes and generating local concentration gradients, which may promote cyclical fluctuations in available capacity. All these interpretations should be considered as hypotheses, tentative attempts to rationalize the anomalous behavior, rather than experimentally verified conclusions. Nonetheless, they provide a logical framework for interpreting the data and a foundation for future studies aimed at understanding and controlling long-term stability in asymmetric redox flow systems. These effects were experimentally confirmed by TXRF analysis, which revealed traces of titanium in the catholyte and iron in the anolyte after charge/discharge cycling [127]. Although the separation of redox couples is beneficial for independently analyzing the two half-reactions, it makes membrane selectivity essential. The membrane must ensure effective ionic isolation while still allowing proton transport. The system's ability to maintain the chemical integrity of redox pairs is, in fact, a critical factor for preserving electrochemical properties and ensuring the overall cyclability of the battery.

These results demonstrate that the separated-electrolyte configuration, despite its scientific interest in decoupling the half-cell mechanisms, is not effective from a performance standpoint. Energy efficiencies are significantly lower than those observed in the mixed electrolyte system, and although the residual capacity appears stable in the long term, it is compromised by a sharp initial drop and unstable cyclic behavior. The fluctuations observed point to a non-optimized condition in which multiple phenomena, such as crossover, accumulation of inactive species, and kinetic limitations, act simultaneously and uncontrollably. Therefore, this architecture does not appear suitable for practical and sustainable application in Ti–Fe-based redox flow

systems, especially when compared to the Bi^{3+}-doped mixed electrolyte configuration, which has shown superior performance and greater operational reliability.

3.11 Post-cycling elemental analysis by TXRF

To experimentally verify the occurrence of ionic crossover hypothesized in the separated-electrolyte configuration, an elemental analysis of both cell compartments was performed after the charge–discharge tests using Total Reflection X-Ray Fluorescence (TXRF) spectroscopy. Measurements were carried out at the University of Brescia using the Horizon spectrometer (G.N.R. S.r.l., Italy), already described in 2.2.2, equipped with a molybdenum X-ray tube (Mo Kα) and an internal gallium (Ga) standard for calibration and intensity normalization.

The TXRF spectrum of the catholyte, shown in Figure 3.43, exhibits the main peaks of iron (Fe Kα and Fe Kβ), as expected for the cathodic compartment, but also reveals additional signals corresponding to titanium (Ti Kα and Ti Kβ) and, to a lesser extent, bismuth (Bi Lα, Lβ, Lγ).

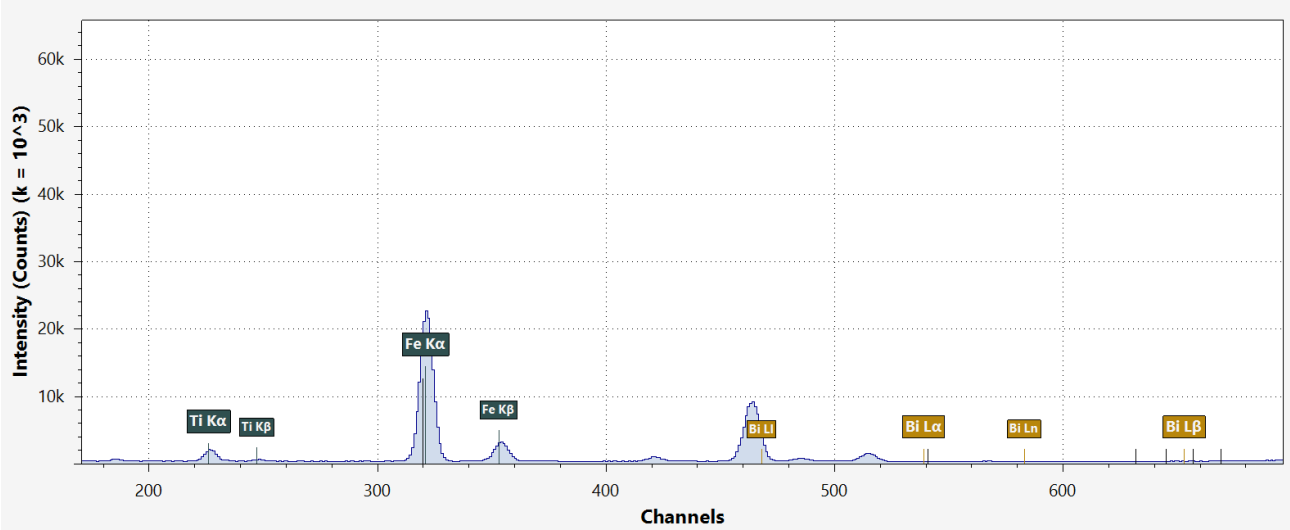


Figure 3.43: TXRF spectrum of the catholyte ($FeSO_4$ 1M in 3M of H_2SO_4) after cycling in the separated-electrolyte Ti–Fe system. The main Fe Kα and Kβ peaks are accompanied by additional signals of Ti and Bi, indicating cross-transfer of species from the anodic compartment.

The appearance of titanium peaks indicates an effective migration of titanium species from the anodic to the cathodic compartment during cell operation, while the presence of bismuth suggests that a small fraction of Bi^{3+} catalyst crossed between the two electrolytes, likely in ionic form. Altogether, these findings provide clear experimental evidence of cross-transfer of metallic species, responsible for a progressive compositional imbalance between the two electrolytes.

A complementary behavior was observed in the spectrum of the anolyte (Figure 3.44), which, besides the characteristic peaks of titanium, shows distinct signals of iron and bismuth.

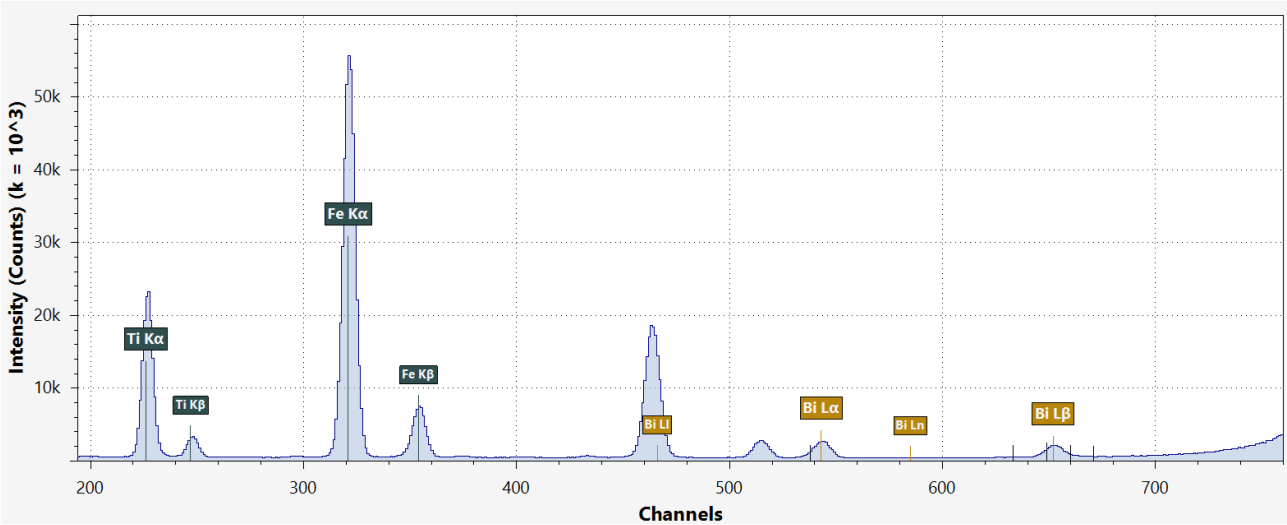


Figure 3.44: TXRF spectrum of the anolyte ($TiOSO_4$ 1M in 3M of H_2SO_4) after cycling in the separated-electrolyte Ti–Fe system. The appearance of Fe peaks in the Ti-based solution confirms bidirectional ionic crossover between the two compartments.

The detection of iron in a compartment where it was initially absent confirms that the crossover is bidirectional, simultaneously involving both redox couples (Ti^{3+}/TiO^{2+} and Fe^{2+}/Fe^{3+}). The presence of bismuth in both compartments further indicates that, although part of the catalyst deposits on the electrode surface, a residual fraction remains in solution and can migrate during cycling.

Quantitative analysis of the elemental concentrations revealed that approximately 12.47% of titanium migrated into the catholyte, 48.26% of iron was detected in the anolyte, and 0.45% of bismuth crossed between the two solutions. These percentages highlight a strong asymmetry in ionic transport, with the mobility of iron being significantly higher than that of titanium. This difference can be rationalized based on the solution speciation and the intrinsic physicochemical properties of the involved species. A concise summary of the elemental migration quantified by TXRF is reported in Table 3.4, providing an immediate visual overview of the crossover extent for each species.

Table 3.4: Percentage migration of Ti, Fe, and Bi across the membrane during cycling

Element	Migration [%]	Notes
Ti	12.47	Low mobility; present as TiO^{2+} / titanium–sulfate complexes with high charge density and large hydrated radius
Fe	48.26	Highest mobility; mainly Fe^{2+}(aq) and $FeSO_4$ (neutral), small hydrated radius, fast diffusion
Bi	0.45	Negligible mobility; partial deposition as metallic Bi°, low solubility in 3 M H_2SO_4

In highly acidic media (3 M H_2SO_4), iron exists mainly as Fe^{2+}(aq) or as a neutral complex $FeSO_4$, characterized by high diffusional mobility and low charge density. These species, with a relatively small hydrated radius (~4 Å), possess higher freedom of motion and greater diffusivity in the aqueous medium. In contrast, titanium is present as the titanyl cation TiO^{2+} or as strongly coordinated sulfate complexes such as $[TiO(SO_4)]$ and $[Ti(OH)_2(SO_4)_2]^{2-}$, with a hydrated radius exceeding 6–7 Å and a high charge density. These features make titanium highly polarized and less mobile in solution. Bismuth, finally, exhibits negligible mobility due to its low solubility in acidic environments, the formation of colloidal species, and its tendency to reduce and deposit as metallic Bi° on the carbon felt electrode. From a chemical and structural standpoint, the observed ionic mobility hierarchy can be expressed as:

$$Fe^{2+} > TiO^{2+} > Bi^{3+}.$$

This relationship is governed not by atomic mass but by the hydrated radius, complexation strength, and charge density. Iron, characterized by a smaller hydrated radius and weaker, reversible Fe–SO_4 bonding, diffuses more readily. Titanium, by contrast, forms stable and bulky complexes that slow down its transport, while bismuth remains almost immobile. Additionally, the concentration gradients generated during galvanostatic cycling—particularly for iron, which undergoes larger oxidation-state variations—enhance its net diffusion toward the anolyte. This molecular picture coherently explains the inferior electrochemical performance of the separated-electrolyte system compared to the mixed-electrolyte configuration. The reciprocal migration of active species leads to a progressive redox imbalance between the two compartments, accumulation of inactive products, capacity fading, and increased internal resistance. The depletion of Ti^{3+} in the anolyte and the ingress of Fe^{2+} into the same compartment alter the chemical composition and ionic strength, producing higher polarization and a lower average discharge potential. Consequently, both voltaic efficiency and energy efficiency decrease, consistent with the reduced electrochemical stability and the enhanced energy losses induced by metallic crossover. Overall, the analysis demonstrates that the main limitation of the separated-electrolyte system does not lie in the reaction kinetics, but rather in the chemical stability and compositional balance between the two electrolytes. The differential migration of metallic species is not only a source of instability but also a direct mechanism of energy loss, as cross-transfer alters the redox balance and reduces the concentration of electroactive species.

In perspective, the results clearly indicate that the most effective strategy to ensure stable and durable operation of the Ti–Fe redox system is the adoption of mixed electrolytes, in which both redox couples coexist within a single compartment. This configuration, by eliminating concentration gradients and preventing ionic crossover, maintains a constant redox balance and ensures a more stable operating potential. As confirmed by the experimental tests, batteries employing mixed electrolytes exhibit higher coulombic and energy efficiencies, reduced voltage losses, and improved reversibility of the redox processes.

This experimental evidence demonstrates that, for redox flow systems based on multivalent metal couples such as Ti–Fe, the control of compositional balance and the choice of electrolyte configuration are key factors for optimizing chemical stability, cycling durability, and overall energy performance of the battery.

3.12 Comparison of the performance of different Ti–Fe battery configurations

A comprehensive analysis of the experimental results provides a clear comparative overview of the electrochemical behavior of the Ti–Fe system as a function of the adopted configuration, systematically evaluating the performance, efficiencies, and cycling stability of the various tested approaches: mixed electrolyte (with and without bismuth), diluted mixed electrolyte, and separated electrolytes.

The mixed-electrolyte battery without Bi^{3+} (1 M Ti + 1 M Fe in 3 M H_2SO_4) initially showed a stable response but progressively degraded after the first few cycles. The coulombic efficiency (CE) remained high, around 97%, but both the voltaic efficiency (VE) and energy efficiency (EE) exhibited a significant decrease with increasing current density: VE dropped from 76.3% to 41.9%, and EE from 74.4% to 42.1%. This degradation highlights an increase in internal polarization and a loss of reversibility due to the sluggish anodic kinetics of the $Ti^{3+} \rightarrow TiO^{2+}$ oxidation reaction in the absence of a catalyst. Although the system functioned adequately during the initial cycles, it proved to be unstable and poorly efficient in the long term, with a rapid decrease in the average discharge potential and a substantial reduction in usable capacity. The addition of Bi^{3+} to the mixed electrolyte drastically changed the battery behavior, significantly improving its performance. The Ti–Fe mixed-electrolyte system with Bi^{3+} exhibited very high coulombic efficiencies, between 98.9% and 99.3%, along with a remarkable enhancement of both VE (from 84.8% to 67.7%) and EE (from 84.1% to 67.5%) with increasing current density. On average, the presence of Bi^{3+} resulted in an approximate 20% increase in overall energy efficiency compared to the catalyst-free configuration. Bismuth is electrochemically reduced to Bi^0, forming a metallic film on the carbon felt surface that acts as an electronic catalyst, facilitating charge transfer and reducing anodic overpotentials. The system maintained stable performance over more than 100 cycles without evident capacity or voltage loss, confirming the effectiveness of bismuth in rendering the battery highly reversible and durable. The diluted mixed-electrolyte configuration (0.5 M Ti + 0.5 M Fe + Bi^{3+}) displayed similar behavior, although with slightly lower energy density. Coulombic efficiencies remained constant (99.1–99.2%), while voltaic and energy efficiencies ranged between 77.7–67.9% and 77.3–67.8%, respectively. Despite the lower concentration of redox-active species, the cell showed good stability and nearly unchanged capacity over prolonged cycling, demonstrating that electrolyte dilution reduces the specific power but does not compromise system reversibility. Finally, the separated-electrolyte configuration highlighted the most significant limitations. Although it allowed independent investigation of the two half-cells, the battery exhibited high polarization and rapid performance decay. Coulombic efficiencies remained close to 96%, but VE dropped from 69.5% to 44.3%, with a corresponding EE decline from 67.2% to 47.6%. These values reflect a strong crossover of Ti and Fe species between the compartments, as confirmed by TXRF analyses, resulting in compositional imbalance, capacity loss, and a reduction of the average discharge voltage. This

configuration, while useful for diagnostic purposes, proved to be energetically inefficient and chemically unstable, unsuitable for long-term cycling operation.

Table 3.5 summarizes the efficiency and stability parameters of the different configurations studied.

Table 3.5: Comparison of Ti–Fe battery performance in different electrolyte configurations

Configuration	Current density	CE	EE	VE	Main observations
	[mA/cm^2]	%	%	%	
Mixed 1 M without Bi^{3+}	40	95.31	74.40	76.34	High polarization; rapid voltage and capacity decay
	60	94.83	51.97	53.79	
	80	94.56	42.07	41.98	
Mixed 1 M with Bi^{3+}	40	98.96	84.06	84.75	High efficiency; outstanding stability and reversibility; effective Bi catalysis
	60	99.10	74.49	74.74	
	80	99.30	67.09	67.40	
Mixed 0.5 M with Bi^{3+}	40	99.10	77.32	77.68	High efficiency; lower energy density but stable behavior
	60	99.23	67.84	67.91	
	80	99.52	59.60	59.83	
Separated electrolytes with Bi^{3+}	40	97.61	67.22	69.53	Strong Ti/Fe crossover; capacity loss and increasing polarization
	60	97.86	47.45	48.45	
	80	99.05	43.63	44.26	

Overall, the comparison among the various configurations demonstrates that the presence of Bi^{3+} is essential to ensure the operational stability and high efficiency of the Ti–Fe system.

The mixed electrolyte without catalyst is kinetically limited and prone to rapid degradation, while the introduction of bismuth stabilizes the anodic titanium reaction, enhancing reversibility and minimizing energy dissipation. The mixed-electrolyte configuration with Bi^{3+} therefore represents the optimal solution, combining high efficiencies (EE ≈ 80%), excellent cycling stability exceeding 100 cycles, and low polarization, clearly outperforming the diluted and separated systems.

Experimental evidence confirms that adopting a Bi^{3+}-catalyzed mixed electrolyte is the most effective strategy to improve the durability, reversibility, and energy efficiency of Ti–Fe-based redox batteries, making them competitive and sustainable systems for stationary energy storage applications. Despite the excellent electrochemical performance achieved, the Ti–Fe system in sulfuric acid still exhibits critical limitations associated with the corrosive nature of the electrolyte and the engineering complexity of the acidic environment, which restrict its scalability. The use of concentrated H_2SO_4 entails issues of material compatibility, progressive deterioration of cell components, and higher maintenance costs, thus lowering the overall sustainability of the system. These challenges—mainly technological rather than chemical—underline the need to develop innovative electrolyte solutions capable of combining electrochemical efficiency with reduced material aggressiveness.

In this context, research efforts are increasingly directed toward novel redox systems based on coordination complexes, capable of preserving the redox properties of titanium and iron in less corrosive and more stable environments. The formation of stable metal–ligand complexes can mitigate electrolyte corrosivity, widen the

operational potential window, and improve material compatibility, thereby enabling more sustainable and longer-lasting cell architectures.

The following chapter will therefore focus on the study of complex-based Ti–Fe systems, aiming to evaluate their chemical and electrochemical behavior and to verify whether complexation can represent a truly innovative pathway for the development of more efficient, safer, and longer-lasting metal-based redox batteries.

4 *Study of Titanium Complexes and Application in the Ti–Fe Battery with EDTA Complexes*

In the previous chapter, the behavior of the Ti–Fe system in sulfuric acid was thoroughly analyzed, highlighting both its electrochemical performance and operational limitations. The results confirmed the potential of this redox couple as an economical and sustainable alternative to conventional vanadium-based systems, but also revealed intrinsic issues related to the chemistry of titanium. In particular, it was found that the stability of Ti(IV) species in solution requires high concentrations of sulfuric acid (≥ 3 M) to prevent hydrolysis and precipitation phenomena. However, such conditions lead to high corrosivity, restrictions in the choice of cell materials, and progressive degradation of performance during long-term cycling. Although the introduction of catalytic promoters such as bismuth improved the anodic kinetics of the $Ti^{3+} \rightarrow TiO^{2+}$ process, the strongly acidic environment remains intrinsically complex and difficult to manage, especially in view of large-scale and long-duration applications. These considerations motivated the exploration of alternative strategies capable of stabilizing titanium in less aggressive media while maintaining good redox reversibility and adequate ionic conductivity. One of the most promising approaches involves the use of coordination complexes as redox-active species. Through the formation of a coordinative bond between the metal center and an organic or organophosphonic ligand, the chemical and electrochemical properties of the metal can be tuned, improving its solubility, stability, and redox selectivity. In the case of titanium—well known for its tendency to hydrolyze and precipitate as TiO_2 in aqueous media—complexation represents an effective strategy to maintain Ti(IV) species in solution at moderately acidic pH values, thus reducing the need for highly acidic environments.

Among the ligands explored in this context, ethylenediaminetetraacetic acid (EDTA) stands out for its strong chelating ability and for forming highly stable complexes with transition metals under mildly acidic or near-neutral conditions. The formation of the $[Ti(EDTA)]^-$ complex allows Ti(IV) to remain stable in aqueous media and to exhibit reversible electrochemical behavior, as demonstrated by the preliminary results obtained at CIC EnergiGune (Vitoria-Gasteiz, Spain). In addition to the Ti–EDTA complex, two other titanium complexes were also investigated — Ti–bpy (2,2′-bipyridine) and Ti–HEDP (hydroxyethylidene diphosphonic acid) — chosen for their different coordination chemistries and donor functionalities. The bpy ligand, an aromatic bidentate chelator, can influence redox potentials through π-delocalization and electronic effects, whereas HEDP, owing to its phosphonate groups, exhibits strong affinity toward tetravalent cations such as

Ti(IV) and enhanced stability under acidic conditions. The comparative study of these systems provides valuable insight into the influence of ligand structure on the stability, solubility, and electron-transfer kinetics of titanium complexes. Based on these premises, the present chapter focuses on the study of titanium complexes with EDTA, bpy, and HEDP, and on their application in a Ti–Fe complex-based battery configuration. The goal is twofold: first, to elucidate the relationship between chemical structure, stability, and electrochemical behavior of titanium complexes; and second, to evaluate the performance of a redox flow battery employing complexed electrolytes as a safer and less corrosive alternative to traditional sulfuric acid systems.

The chapter is organized into a theoretical section describing the fundamentals of coordination chemistry and the ligands investigated, followed by the experimental synthesis and characterization of titanium complexes, the discussion of their electrochemical behavior, and finally, the evaluation of the performance of the Ti–Fe complex-based battery.

4.1 Theoretical background on coordination chemistry

Before delving into the detailed description of the experimental setups and the results obtained in this work, it is essential to build a solid conceptual foundation concerning coordination chemistry in its broadest sense, and then relate it to the specific case of titanium, which is the focus of this study. Coordination chemistry represents a fundamental branch of inorganic chemistry: a coordination complex consists of a central atom or ion, known as the coordination center, bonded to one or more donor species (ligands) that provide electron pairs according to the Lewis acid–base model [131], [132], [133]. The ligands may be neutral molecules or anions, and the resulting complex can be neutral or charged, with counterions ensuring overall charge neutrality. The formation of a coordination complex profoundly modifies the chemical and electronic properties of the central metal, influencing its reactivity, solubility, and redox behavior. Coordination chemistry underpins a wide range of natural and technological phenomena, from homogeneous catalysis and metalloprotein biochemistry to modern applications in electrochemical energy storage systems [134], [135].

From a theoretical standpoint, the understanding of the metal–ligand bond has evolved from the Crystal Field Theory (CFT), developed in the 1930s, to the more sophisticated Ligand Field Theory (LFT), which incorporates the covalent character of the interaction [131], [134]. According to CFT, the electrostatic field generated by the ligands induces a splitting of the d orbitals of the metal ion, the magnitude of which depends on the coordination geometry and the ligand field strength. In an octahedral complex, the d orbitals split into two energy levels: the t_2g set (dxy, dxz, dyz), which is less destabilized, and the eg set (dz^2, $dx^2–y^2$), which lies at higher energy. The energy difference between these two sets, known as Δ_o, or crystal-field splitting energy, determines many of the optical, magnetic, and redox properties of metal complexes. LFT extends this model by including orbital overlap between the metal and the ligand, thus providing a more accurate description of the bonding and metal–ligand interactions. These models are supported by extensive spectroscopic (UV–Vis, Raman, EPR) and computational (DFT) studies conducted on Ti(III) and Ti(IV) complexes, which confirm the strong influence of coordination geometry on the electronic structure and reactivity of the complexes [136].

The formation of a coordination complex in solution is governed by a sequence of equilibria, each characterized by a stepwise formation constant (K_1, K_2, …), whose product defines the overall formation constant (β), a measure of the overall stability of the complex[137], [138]. For the Ti(IV)–EDTA system, for instance, the value of log β_1 ranges between 20 and 25 at 25 °C, depending on the ionic strength and pH of the solution [139], while for ligands such as HEDP the constants are lower (log β ≈ 15–17) but provide higher kinetic stability under acidic condition. These values highlight the remarkable strength of the Ti–O bond, which keeps the metal ion soluble even at moderately acidic or near-neutral pH, reducing its tendency toward hydrolysis. The so-called chelate effect, one of the main factors contributing to complex stability, arises from the formation of ring structures between the metal and the multidentate ligand, increasing the total bond strength and decreasing the number of free species in solution. Thermodynamically, this stabilization is due to both enthalpic (multiple strong M–L bonds) and entropic (fewer species in solution) contributions, as extensively discussed by Martell [134], [136].

An additional interpretative framework is provided by Pearson's Hard and Soft Acids and Bases (HSAB) theory[140], which classifies species based on their polarizability. Titanium, particularly in the Ti(IV) oxidation state, is a hard acid characterized by a small ionic radius (r ≈ 0.745 Å) and high charge density, showing a pronounced affinity for hard ligands containing oxygen donor atoms, such as carboxylates or phosphonates. This explains the exceptional stability of Ti–EDTA and Ti–HEDP complexes compared to those formed with nitrogenated or aromatic ligands like 2,2′-bipyridine (bpy)[132]. Nevertheless, bpy, although thermodynamically less stable, introduces an important electronic component: the π–d interaction between the aromatic ligand and the metal center can modulate redox potentials, stabilizing the Ti(III) reduced form and improving the reversibility of electronic transitions. Such effects have been observed in several Ti(III) coordination systems, where electron delocalization decreases the reduction overpotential and facilitates electron-transfer processes.

In aqueous systems, the stability of titanium complexes plays a decisive role. In the absence of strong ligands, Ti(IV) readily hydrolyzes, forming polymeric species and amorphous TiO_2 precipitates even at pH values slightly above 1. Coordination with multidentate ligands, which saturate the metal's coordination sphere, prevents these processes and keeps the metal soluble under less acidic conditions [132]. The formation of Ti–EDTA, Ti–bpy, and Ti–HEDP complexes therefore represents an effective strategy for obtaining chemically stable and electrochemically reversible solutions, suitable for use in redox systems as alternatives to strongly acidic electrolytes. Among these, EDTA provides the highest stability due to its hexadentate nature, completely encapsulating the metal in an octahedral environment and forming highly stable Ti–O bonds (ΔH ≈ 500 kJ mol^{-1}) [133], [141]. HEDP, though less dentate, forms strongly covalent M–O bonds through its phosphonate groups, maintaining remarkable stability in acidic and high ionic-strength media. In contrast, bpy provides a bidentate and more flexible coordination mode, affecting the electronic distribution around the metal and the redox behavior of the system but with lower long-term stability. From a kinetic perspective, complexes of high-valent transition metals such as Ti(IV) are characterized by slow ligand-exchange rates, a property that confers high kinetic inertness and chemical robustness. This behavior has been confirmed by NMR and UV–

Vis relaxation studies, which report ligand exchange times longer than 10^{-3} s^{-1} for Ti(IV)–EDTA complexes, in contrast to much faster exchange rates observed in systems such as Fe(III)–EDTA[142]. Such kinetic inertness minimizes ligand dissociation and enhances the persistence of the complexes in solution, even under varying pH and temperature. Nevertheless, the strong charge density of Ti(IV) may increase the viscosity and decrease the ionic conductivity of the solution—factors that must be optimized when designing complexed electrolytes for electrochemical applications [143]. The stability and redox reversibility of titanium coordination complexes are therefore essential for their application in aqueous redox systems. Coordination of Ti(IV) by multidentate ligands enables control over redox potentials, improves the reversibility of the Ti(IV)/Ti(III) process, and minimizes the formation of inactive or precipitated species. Moreover, the ligand's chemical nature affects macroscopic properties such as viscosity and conductivity, which in turn determine overall cell performance. Understanding the principles of complex formation and their influence on the redox properties of titanium is thus a prerequisite for the interpretation of the experimental results presented in the following sections, where the synthesis, characterization, and electrochemical behavior of Ti–EDTA, Ti–bpy, and Ti–HEDP complexes will be discussed, along with their application in Ti–Fe complex-based redox systems developed as safer and less corrosive alternatives to traditional sulfuric-acid-based chemistries. The stability and redox reversibility of titanium coordination complexes are therefore essential for their application in aqueous redox systems. Coordination of Ti(IV) by multidentate ligands enables control over redox potentials, improves the reversibility of the Ti(IV)/Ti(III) process, and minimizes the formation of inactive or precipitated species. Moreover, the ligand's chemical nature affects macroscopic properties such as viscosity and conductivity, which in turn determine overall cell performance. Understanding the principles of complex formation and their influence on the redox properties of titanium is thus a prerequisite for the interpretation of the experimental results presented in the following sections, where the synthesis, characterization, and electrochemical behavior of Ti–EDTA, Ti–bpy, and Ti–HEDP complexes will be discussed, along with their application in Ti–Fe complex-based redox systems developed as safer and less corrosive alternatives to traditional sulfuric-acid-based chemistries.

4.2 Experimental Procedure for the Preparation and Electrochemical Characterization of Titanium Complexes

Building upon the theoretical framework discussed in the previous section, the following part focuses on the experimental aspects related to the preparation and electrochemical characterization of titanium complexes. The aim of this phase was to translate the coordination chemistry concepts previously outlined into practical, stable, and reproducible formulations suitable for use as electrolytes in redox flow batteries.

Three different ligands were selected for complex synthesis, representative of distinct coordination behaviors and electronic properties: ethylenediaminetetraacetic acid (EDTA), 2,2′-bipyridine (bpy), and hydroxyethylidene diphosphonic acid (HEDP). In all cases, the metal precursor employed was titanium oxysulfate ($TiOSO_4$, ≥99%), which was first dissolved in ultrapure water (Millipore, 18.2 MΩ·cm) under magnetic stirring until a clear solution was obtained. The complex solutions were prepared following similar

procedures, while adjusting the molar ratio between metal and ligand according to their different coordinating abilities. For the Ti–EDTA complex was adopted a stoichiometric ratio 1:1 (Ti : ligand), for Ti–HEDP complex a 1:2 stoichiometric ratio (Ti : ligand) was adopted and for Ti–bpy a 1:2 and 1:3 ratio (Ti : ligand) was used, to fully saturate the titanium coordination sphere and promote the formation of stable octahedral species. To provide a concise overview of the formulations investigated, Table 4.1 summarizes the ligands employed, their chemical formulae, the Ti:ligand molar ratios adopted, and the pH conditions used for the preparation of the complex solutions.

Table 4.1: Summary of titanium complex formulations used in this work.

Complex ID	Ligand (name)	Ligand (abbrev.)	Ligand chemical formula	Ti : ligand molar ratio	pH
Ti–EDTA	Ethylenediaminetetraacetic acid	EDTA	$C_{10}H_{16}N_2O_8$	1 : 1	5.8
Ti–HEDP	Hydroxyethylidene diphosphonic acid	HEDP	$C_2H_8O_7P_2$	1 : 2	4.3
Ti–bpy	2,2′-Bipyridine	bpy	$C_{10}H_8N_2$	1 : 2	1.6
Ti–bpy	2,2′-Bipyridine	bpy	$C_{10}H_8N_2$	1 : 3	1.6

In each case, the selected ligand was dissolved in approximately 10 mL of ultrapure water in a separate beaker, under constant stirring. The $TiOSO_4$ solution was then added slowly, dropwise, to the ligand solution to ensure a gradual complexation process and to avoid hydrolysis or the formation of colloidal TiO_2.

Particular attention was paid to ensuring experimental reproducibility. Each preparation was carried out under controlled conditions, using acid-cleaned glassware thoroughly rinsed with ultrapure water to eliminate trace metal contamination. After preparation, the final volume was adjusted to 50 mL with ultrapure water, and the pH was continuously monitored using a digital pH meter. The pH was maintained within the stability range between 5,8 for Ti–EDTA, 4.3 for Ti–HEDP, and 1.6 for Ti–bpy. All solutions appeared clear and stable for several hours after preparation, with no evidence of turbidity or precipitation. Before electrochemical analysis, each sample was deaerated by nitrogen bubbling for approximately 15 minutes to remove dissolved oxygen and prevent parasitic redox reactions during voltammetric measurements. As shown in Figure 4.1, the three solutions exhibited distinct colors, indicative of the different nature of the metal–ligand bond and the varying degree of electronic delocalization within the complexes.

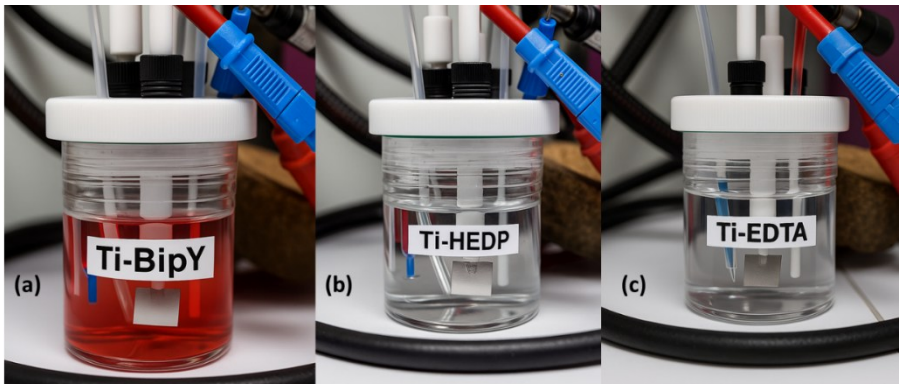


Figure 4.1: Aqueous solutions of titanium complexes prepared for electrochemical analysis: (a) Ti–bpy (pH 1.6), (b) Ti–HEDP (pH 4.3) and (c) Ti–EDTA (pH 5.8). All solutions appear clear and transparent, with no evidence of precipitation or turbidity after several hours.

Electrochemical characterization was carried out using cyclic voltammetry (CV), selected as the primary diagnostic technique to evaluate the reversibility of the Ti(IV)/Ti(III) redox couple and to estimate the main kinetic and diffusional parameters. Measurements were performed using an Autolab PGSTAT204 potentiostat/galvanostat (Metrohm, Netherlands) equipped with a FRA32M impedance module and controlled via NOVA software. The instrument, shown in Figure 4.2, was connected to a conventional three-electrode electrochemical cell consisting of a glassy carbon working electrode (3 mm diameter), an Ag/AgCl reference electrode (saturated KCl), and a platinum counter electrode.



Figure 4.2: Autolab PGSTAT204 potentiostat/galvanostat (Metrohm, Netherlands) used for cyclic voltammetry analysis of titanium complexes. The instrument, equipped with a USB interface and NOVA software, enabled real-time voltammogram acquisition and automated processing of the main electrochemical parameters.

All electrodes were carefully cleaned prior to each measurement following the procedure described in Chapter 2, and the temperature was maintained constant at 25 °C. The potential window was adjusted for each complex to include the full redox range of the Ti(IV)/Ti(III) couple, while avoiding interference from hydrogen or oxygen evolution reactions. Each measurement was repeated at least three times to ensure reproducibility, and the resulting voltammograms were analyzed in terms of anodic and cathodic peak separation, current intensity, and dependence on scan rate. It should be noted that, at this stage, the experimental investigation focused

exclusively on titanium complexes, while iron complexes were not considered. This decision was based on the fact that the electrochemical behavior of Fe(III)/Fe(II) complexes with ligands such as EDTA and HEDP has already been widely reported in the literature, whereas information on Ti(IV)/Ti(III) systems remains limited and fragmented. The present study therefore aimed to fill this gap by systematically analyzing the stability, reversibility, and redox properties of titanium complexes in aqueous media, with the goal of identifying operational conditions that ensure an optimal balance between chemical stability and electrochemical performance.

The results obtained from these preliminary measurements provided valuable insight into the diffusional and kinetic behavior of titanium complexes, allowing the identification of the most suitable conditions of stability and reversibility. These findings were subsequently applied in the preparation of complexed electrolytes for the Ti–Fe flow battery tests discussed in the following sections.

4.3 Electrochemical Study of Titanium Complexes: Objectives and Experimental Studies

Following the preparation and characterization of the titanium complexes described in the previous section, an extensive electrochemical investigation was undertaken to evaluate the redox behavior of titanium in the presence of different complexing ligands.

The main objective of this study was not merely to obtain a qualitative description of the voltammetric response of the systems, but rather to systematically analyze three key parameters, the redox potential of the Ti(IV)/Ti(III) couple, the solubility, and the chemical stability, in order to assess the actual suitability of titanium complexes as active species in redox flow battery electrolytes.

The rationale for this investigation lies in the peculiar chemical nature of titanium, a transition metal which, despite possessing a thermodynamically favorable Ti(IV)/Ti(III) redox couple, exhibits a strong tendency toward hydrolysis and subsequent precipitation as insoluble titanium oxides in aqueous media. These phenomena drastically limit the usable concentration of Ti(IV) and the long-term stability of the system. The use of complexing ligands therefore represents an effective strategy to mitigate such effects, stabilizing the oxidized species through the formation of coordination bonds with oxygen- or nitrogen-donor atoms.

However, coordination does not simply prevent precipitation: it also significantly alters the electronic density of the metal center, thereby shifting the redox potential and affecting the reversibility of the electron-transfer process [144], [145].

Based on these considerations, the primary goal of this work was to experimentally determine the formal potential of the Ti(IV)/Ti(III) redox couple for complexes formed with three ligands of different chemical nature, ethylenediaminetetraacetic acid (EDTA), 2,2′-bipyridine (bpy), and 1-hydroxyethane-1,1-diphosphonic acid (HEDP), and to evaluate their solubility and stability in aqueous solution.

The selection of these ligands was inspired by previous studies demonstrating their capability to modulate the stability and redox activity of coordinated transition-metal centers [146], [147].

In particular, classical work by Miyagawa et all. [144] showed that chelation of trivalent titanium with EDTA induces a marked anodic shift in the redox potential compared to the free Ti^{3+}/Ti^{4+} system, an effect attributed to the enhanced stabilization of the Ti^{3+} state by the ligand.

The solubility of the complexes was investigated experimentally by preparing solutions at progressively increasing concentrations of metal and ligand, from dilute solutions (0.01 M) up to the saturation limit. This approach, already employed for the study of aminopolycarboxylic and phosphonic complexes, allowed the determination of the maximum stable concentration and the identification of the threshold above which colloidal TiO_2 formation or precipitation occurred.

In parallel, the chemical stability of the solutions was examined as a function of pH, varying the conditions from strongly acidic to weakly acidic in order to define the operational range in which each complex maintains its structural integrity without undergoing hydrolysis or decomposition.

Such behavior was interpreted in terms of speciation equilibria and formation constants: for Ti–EDTA, maximum stability was observed in the pH range 5–6, consistent with literature values of the stability constant ($\log \beta \approx 20–25$) [148], while Ti–HEDP complexes exhibited higher tolerance under acidic conditions due to the strong affinity of phosphonate groups for tetravalent cations [149]. Once the solubility and stability domains were established, the stable solutions were subjected to cyclic voltammetry (CV) to determine the formal potential of the Ti(IV)/Ti(III) couple and to evaluate the reversibility of the redox process [148].

The measurements were performed in a conventional three-electrode cell, using a glassy carbon working electrode, a platinum counter electrode, and an Ag/AgCl reference electrode, under controlled temperature (25 °C). The recorded voltammograms enabled the identification of the anodic and cathodic peak positions, the ΔEp separation, and the variation of peak current with scan rate, providing insights into the electron-transfer kinetics and the degree of reversibility of the system.

Overall, this study provided a comprehensive picture of the chemical and electrochemical properties of the three examined complexes, highlighting the critical influence of ligand nature and denticity on both the redox potential and stability of titanium species in aqueous solution.

The following sections will present and discuss in detail the results obtained for each complex, Ti–EDTA, Ti–[150], [151]bpy, and Ti–HEDP, with the aim of correlating ligand structure, complex stability, and redox behavior, ultimately identifying the most promising candidate for use as the anodic electrolyte in the Ti–Fe complex-based redox flow battery.

4.3.1 Electrochemical behavior of the Ti–bipyridine complex

This section presents the study of the titanium complex with 2,2′-bipyridine (Ti–bpy), with the aim of evaluating its stability in aqueous solution and its electrochemical behavior in acidic media. The analysis follows from the theoretical considerations discussed previously, focusing in particular on the influence of the aromatic ligand on the redox window accessible to titanium. Interest in the Ti–bpy system arises from the peculiar electronic interaction between the π^* orbitals of bipyridine and the d orbitals of the metal, which can

induce delocalization effects and modulate the redox properties of the metal center, as already observed in analogous systems with Cu(I) and Fe(II) [150], [151].

The 2,2′-Bipyridine (bpy) is an aromatic bidentate ligand consisting of two pyridine rings joined at position 2, each containing a donor nitrogen atom. The planar and π-conjugated nature of the molecule allows effective interaction between the π* orbitals of the ligand and the d orbitals of the metal, giving bpy strong π-acceptor capability and notable coordination versatility [152], [153]. The molecular structure of 2,2′-bipyridine is shown in Figure 4.3, where the planar geometry and the orientation of the two nitrogen atoms in position 2 can be observed, allowing the formation of stable chelates with octahedral metal cations.

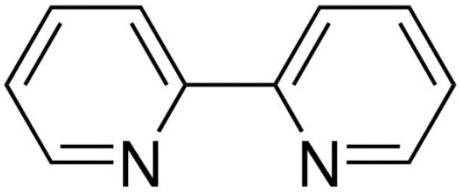


Figure 4.3: Chemical structure of 2,2'-bipyridine (bpy), a planar bidentate ligand composed of two pyridine rings connected at the 2-position. The nitrogen atoms in position 2 act as donor sites, enabling the formation of stable chelate complexes with transition metal ions in octahedral coordination geometries.

This electronic character promotes delocalization of electronic density and metal-to-ligand charge transfer (MLCT) processes, which help stabilize multiple oxidation states of the coordinated metal [141], [154]. These properties make bipyridine a widely used ligand in the study of multielectron redox systems and in the design of electroactive complexes of Fe, Ru, Cu, and Ti [155].

The Ti–bpy complex was prepared following the procedure described in section 4.2, using $TiOSO_4$ as the metal precursor and maintaining Ti:bpy molar ratios of 1:2 and 1:3. The formation of the complex was evaluated in strongly acidic media (pH ≈ 1.3), subsequently adjusted by controlled addition of KOH. It was observed that the solution remains clear and stable up to a maximum pH of about 1.6; above this value, turbidity appears followed by the formation of a whitish precipitate, attributed to complex decomposition and the formation of titanium oxide species ($TiO_2 \cdot xH_2O$). This behavior highlights the limited stability of bipyridine in aqueous acidic environments: protonation of the nitrogen donor sites reduces the ligand's coordination ability, compromising the complex's solubility. Moreover, concentration tests showed that the system remains homogeneous up to 0.2 M, whereas at higher concentrations titanium precipitation occurs even under optimal pH conditions. Figure 4.4 shows a representative image of the whitish precipitate observed in the Ti–bpy solution after a few hours at pH 1.6, visually confirming the limited stability of the system under diluted acidic conditions.

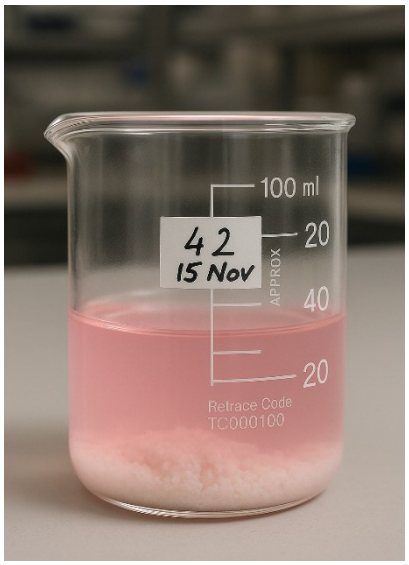


Figure 4.4: Evidence of the formation of a bottom body (whitish precipitate) in the solution containing the Ti–bipyridine complex at pH > 1.6. The precipitation is indicative of the limited stability of the complex under conditions near the upper limit of the experimental stability range.

Cyclic voltammetry (CV) analyses, performed in a three-electrode cell (glassy carbon as working electrode, Ag/AgCl as reference and a platinum electrode as counter electrode), showed a complex and distinctive electrochemical behavior compared to other systems studied. The voltammograms of stable Ti–bpy solutions, shown in Figure 4.5, display two distinct pairs of redox peaks.

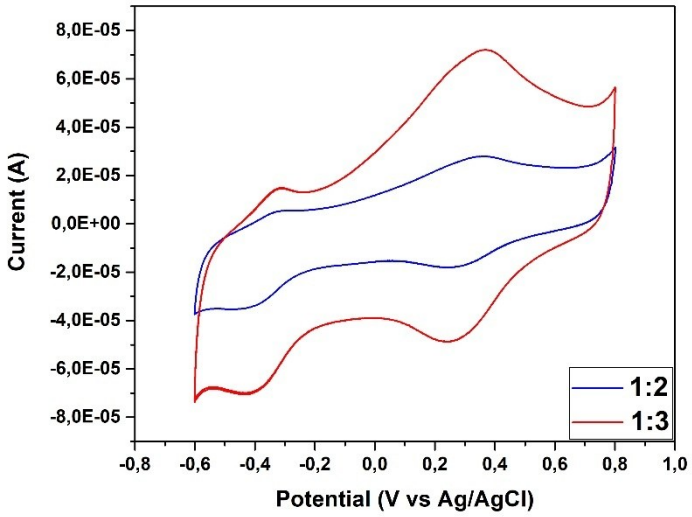


Figure 4.5: Cyclic voltammograms of the Ti–bipyridine complex at pH = 1.5 for Ti:bpy molar ratios of 1:2 (blue curve) and 1:3 (red curve). Measurements were performed in a three-electrode cell using a glassy carbon working electrode, a platinum counter electrode, and an Ag/AgCl reference electrode. The scan rate was 25 mV s^{-1}.

The first pair, located in the negative region, presents an anodic peak at −0.31 V and a cathodic peak at −0.41 V (vs Ag/AgCl), with a mean redox potential of $E^{\circ\prime} = -0.36$ V; the second pair, in the positive region, shows an anodic peak at 0.36 V and a cathodic peak at 0.24 V, with a mean redox potential of $E^{\circ\prime} = +0.30$ V. Although

no specific spectroscopic or theoretical characterizations were carried out, these redox couples can reasonably be attributed, by analogy with other bipyridine-coordinated metal systems, to the Ti(III)/Ti(II) and Ti(IV)/Ti(III) processes, respectively [156]. The peak-to-peak separation (ΔEp) is approximately 100 mV for the negative redox couple (Ti(III)/Ti(II)) and about 120 mV for the positive couple (Ti(IV)/Ti(III)).

As shown in Figure 4.5, the 1:3 molar ratio system exhibits more pronounced and well-defined redox peaks, higher peack currents, and a broader electrochemical window compared to the 1:2 ratio, indicating more effective and stable coordination of titanium in the presence of excess bipyridine. The excess ligand favors the formation of over-coordinated species such as $[Ti(bpy)_3]^{4+}$, which are thermodynamically more stable and capable of facilitating electron transfer. The 1:2 system, on the other hand, shows more damped and partially overlapping waves, suggesting incomplete coordination or partial dissociation of the complex in solution. The electronic effect of bipyridine, due to its π-acceptor nature and ability to interact with d and π* orbitals, enables partial delocalization of electron density from the metal to the ligand. This delocalization reduces the energy gap between the Ti(II), Ti(III), and Ti(IV) states, facilitating multiple reversible redox processes [154], [155], [157]. It is important to note that cyclic voltammetry was carried out at a single scan rate (25 mV/s), and no systematic study of the current response versus the square root of the scan rate was performed, since the complex was quickly excluded from battery applications due to its limited solubility. The experimentally determined maximum solubility of 0.2 M in titanium, even in the presence of excess ligand, was found to be insufficient to achieve meaningful energy densities in a flow system, making further electrochemical investigation of limited practical value. The overall width of the electrochemical window, about 0.66 V, confirms the extent of titanium's redox reversibility in the presence of bpy. The presence of two well-separated redox couples initially suggested the theoretical possibility of developing a fully titanium-based symmetric flow battery, exploiting the Ti(III)/Ti(II) couple as the anodic process and the Ti(IV)/Ti(III) couple as the cathodic one. However, the inability to exceed concentrations of 0.2 M, due to the complex's limited solubility, rendered this hypothesis impractical at the application scale. Despite its interesting electrochemical behavior, the limitations in solubility (≤ 0.2 M) and stability (pH ≤ 1.6) led to the exclusion of bipyridine as an active electrolyte in the Ti–Fe battery configuration, favoring more robust and flow-compatible alternatives.

4.3.2 Electrochemical Behavior of the Ti–HEDP Complex

Among the ligands considered for stabilizing titanium in aqueous solution, 1-hydroxyethylidene-1,1-diphosphonic acid (HEDP) has proven particularly promising due to its strong affinity for highly charged cations and the remarkable chemical stability it imparts to the resulting complexes, even under highly acidic conditions. HEDP is a bidentate organophosphonic ligand, characterized by two $–PO_3H_2$ groups and a central hydroxyl group that serves as an additional electron donor site. These functionalities allow coordination to the metal center via strong covalent Ti–O bonds, ensuring both thermodynamic and kinetic stability. Its molecular structure, shown in Figure 4.6, enables the formation of rigid chelate rings capable of effectively saturating the coordination sphere of Ti(IV), a cation known for its strong tendency to hydrolyze and form colloidal titanium oxide species.

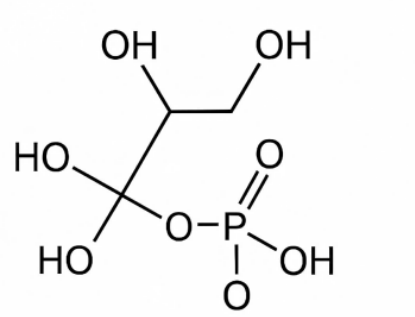


Figure 4.6: Chemical structure of 1-hydroxyethylidene-1,1-diphosphonic acid (HEDP). The molecule features two phosphonate groups (-PO_3H_2) and a central hydroxyl group, providing high coordination ability toward highly charged metal cations such as Ti(IV) through strong Ti–O covalent bonding.

The effectiveness of phosphonate ligands in stabilizing high-valent metal ions is well documented in the literature [139], [140], [158]. In the specific case of titanium, complexation with HEDP offers an effective strategy to suppress hydrolysis and precipitation, maintaining the metal in solution even under moderately acidic conditions [159]. This approach proved especially strategic considering the limitations observed with the Ti–2,2-bipyridine complex, which, despite exhibiting interesting electrochemical behavior, showed significant limitations in terms of solubility (≤ 0.2 M) and chemical stability, making it unsuitable as an active electrolyte for flow batteries. The adoption of a more robust ligand such as HEDP therefore allowed these limitations to be overcome, offering a more reliable basis for electrochemical optimization.

The Ti–HEDP complex was prepared according to the experimental procedure previously described (section 4.2), using a molar ratio of Ti:HEDP = 1:2. Under these conditions, a clear and colorless solution was obtained, which remained stable for several hours at room temperature without signs of turbidity or precipitation. The solution's stability was further investigated by progressively increasing the pH through controlled addition of KOH, in order to define the operational window in which the complex remains intact. It was observed that the Ti–HEDP complex is chemically stable up to approximately pH 9.36. The experimental observations are illustrated in Figure 4.7, which visually documents the solution's appearance across different pH values.

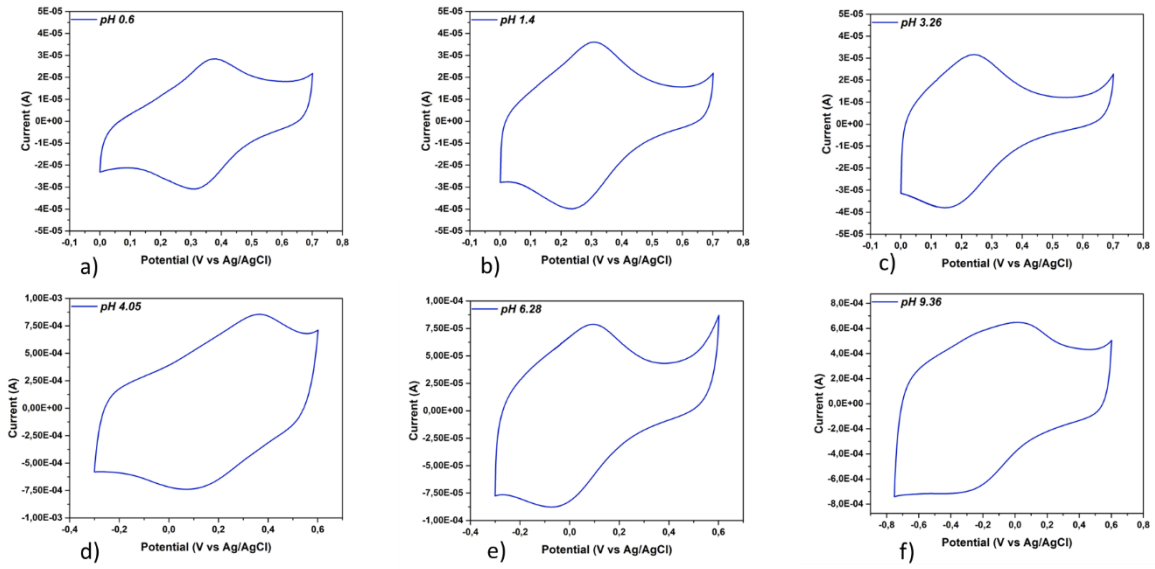


Figure 4.7: Cyclic voltammograms recorded at 25 mV/s for the 0.005 M Ti–HEDP solution at different pH values: a) 0.6; b) 1.4; c) 3.26; d) 4.05; e) 6.28; f) 9.36. The potential window was adjusted in each case to highlight the presence of anodic and/or cathodic peaks.

Figure 4.7 shows the cyclic voltammograms of the 0.005 M Ti–HEDP solution recorded at different pH values. As the pH is increased from 0.6 to 9.36, the Ti(IV)/Ti(III) couple is always visible as a single pair of anodic and cathodic peaks with very similar shape and peak-to-peak separation. Only small shifts in peak potential and moderate changes in current are observed, while no additional redox waves appear. This behaviour indicates that the Ti–HEDP complex remains intact and electrochemically active over the whole pH range investigated, in agreement with the visual observation of a clear solution up to pH 9.36. Beyond the value of pH 9.36, turbidity appeared, indicating decomposition of the complex and precipitation of TiO_2 or hydrolyzed titanium species. This result highlights the excellent robustness of the Ti–HEDP system, offering a much wider pH stability range compared to other complexes such as Ti–bpy, which destabilizes above pH 1.6.

A further evaluation concerned the maximum solubility of the complex in water. Starting from an initial solution containing 0.005 M Ti and 0.01 M HEDP, the titanium concentration was progressively increased up to a maximum stable concentration of 0.5 M, without any precipitation. This result is particularly relevant for practical applications, since the concentration of redox-active species directly affects the energy density in redox flow battery systems. The combination of good solubility and broad pH stability initially suggested that the Ti–HEDP complex could serve as a promising alternative to traditional sulfuric acid-based electrolytes, offering lower corrosiveness and enhanced operational safety.

The electrochemical behavior of the Ti–HEDP complex was analyzed by cyclic voltammetry (CV), with the aim of evaluating the reversibility of the Ti(IV)/Ti(III) redox system and determining its main kinetic and diffusive parameters. The measurement, performed on a solution containing 0.5 M titanium at 25 mV s-1 at pH 3.26 (Figure 4.8), highlighted the presence of a pair of redox peaks with an anodic potential of 0.21 V and a cathodic potential of 0.033 V with respect to the Ag/AgCl electrode, corresponding to a redox mean potential (E_{redox}) of 0.121 V.

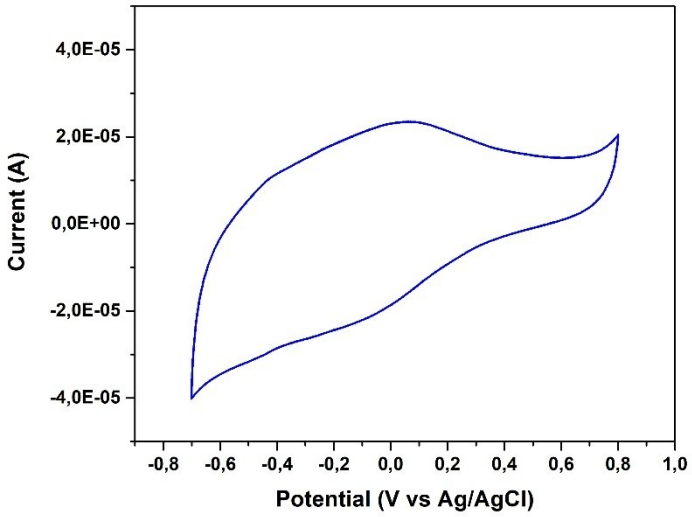


Figure 4.8: Voltammetric cycling of the Ti–HEDP complex at 0.5 M concentration (pH 3.26), performed in aqueous solution using a carbon-glass working electrode, a platinum counter electrode, and an Ag/AgCl reference electrode. The scan was performed in a potential range from –0.70 V to 0.80 V, with a scan rate of 25 mV/s.

The peak separation of approximately 170 mV and the asymmetric shape of the redox waves indicates a quasi-reversible behavior, likely influenced by kinetic limitations or secondary chemical reactions. As the scan rate increased, the redox peaks became progressively less defined and, under higher dynamic conditions, nearly disappeared. Subsequently, several CV tests were performed at variable scan rates, from 5 mV/s to 200 mV/s, in order to evaluate the main electrochemical parameters of the complex, such as the diffusion coefficient and the electron transfer rate (Figure 4.9).

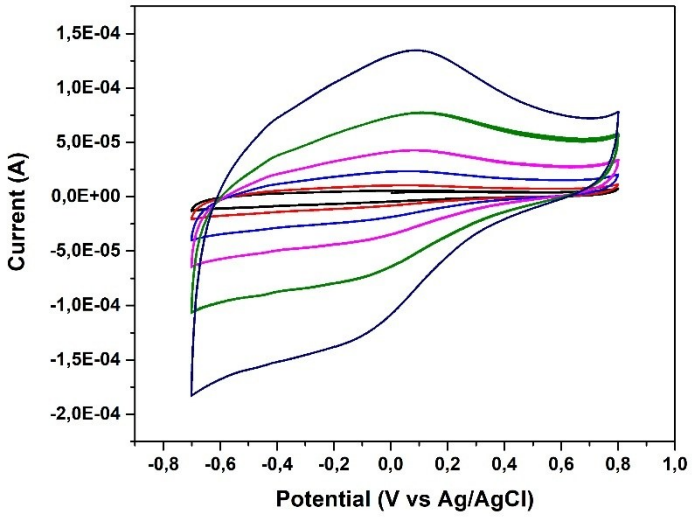


Figure 4.9: Cycle voltammetry of Ti–HEDP complexes recorded at different scan rates (5–200mV/s), under optimal pH conditions (pH=3.26).

As shown in Figure 4.9, the peak current increases steadily with scan rate, as expected for a diffusion-controlled process. However, a progressive separation between the anodic and cathodic peaks is observed, along with a slight increase in asymmetry, indicating a certain contribution of kinetic irreversibility at higher scan rates.The electrochemical analysis of the Ti–HEDP complex was completed with a study of kinetic and diffusional parameters using the Randles–Ševčík and Laviron relations (see Chapter 2 section 2.1.2), to understand both the diffusion-controlled behavior of the species in solution and the kinetics of electron transfer (Figure 4.10).

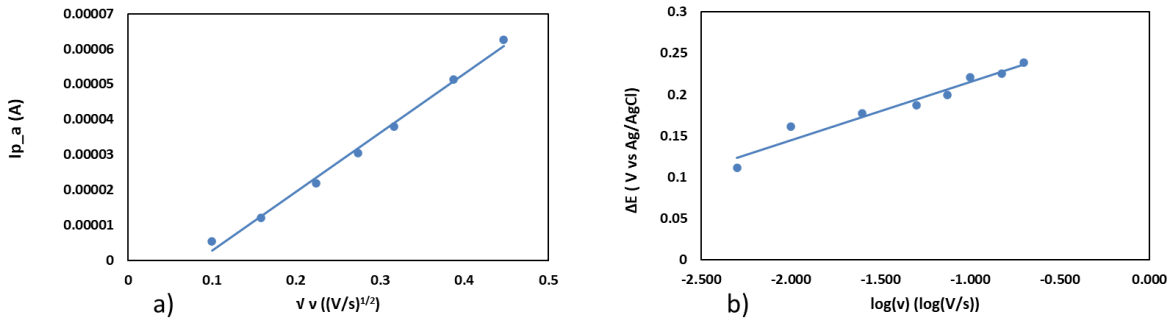


Figure 4.10: Kinetic parameter determination of the Ti–HEDP complex. (a) Plot of anodic peak current (i_p,a) versus the square root of the scan rate (√v), used to calculate the diffusion coefficient according to the Randles–Ševčík equation. (b) Variation of the peak-to-peak separation (ΔE_p) as a function of the logarithm of the scan rate (log v), used for the application of the Laviron model.

The Randles–Ševčík graph (Figure 4.10a) shows the anodic peak current (I_{pa}) as a function of the square root of the scan rate (√v). The observed linearity confirms that, under moderate operating conditions, the Ti(IV)/Ti(III) redox process is predominantly diffusion-controlled. The diffusion coefficient calculated from this graph (D = 9.83 × 10^{-7} cm^2/s) indicates that the complex species are sufficiently mobile in aqueous solution, allowing uniform distribution during the voltammetric cycle. The Laviron analysis (Figure 4.10b) allowed determination of the electron transfer coefficient α = 0.796 and the heterogeneous electron transfer rate constant k^0 = 1.14 cm/s. The α value, close to 0.8, suggests that the electron transfer is highly asymmetric, i.e., the energy barrier for oxidation and reduction is not equivalent, reflecting the influence of possible secondary chemical processes or the complex structure on electron transfer kinetics. The k^0 value indicates that, despite strong Ti–O bonds and stable complexation, electron transfer occurs relatively rapidly, confirming that the complex can support oxidation and reduction cycles, at least at low scan rates. However, the observation of peak broadening and loss of definition at higher scan rates (Figure 4.9) suggests that, at faster scan rates, electron transfer kinetics and mass transport become limiting. This results in decreased reversibility and increased peak asymmetry, indicating that the complex cannot fully sustain the redox reaction at faster timescales. These effects can be attributed to polarization phenomena or the temporary formation of intermediate species that are not fully reversible during the cycle. The integration of Randles–Ševčík and Laviron data therefore provides a comprehensive picture of the electrochemical behavior: while diffusion control ensures that the species are sufficiently mobile to participate in the redox cycle, the limited kinetics at

high scan rates reveal the operational limits of the complex. Overall, these results indicate that, although the complex exhibits good diffusion properties and rapid kinetics at low scan rates, Ti–HEDP does not provide optimal reversibility under high dynamic conditions, limiting its effectiveness as an active electrolyte in redox flow batteries.

4.3.3 Electrochemical Behavior of the Ti–EDTA Complex

Among the ligands used for stabilizing metal cations in aqueous solution, EDTA (ethylenediaminetetraacetic acid) is a particularly effective choice due to its ability to coordinate metals through six donor sites, comprising four carboxylate groups and two nitrogen atoms. This polydentate structure allows the formation of highly stable complexes with highly charged cations such as Ti(IV), preventing precipitation or hydrolysis and ensuring high solubility in water [1][140]. The molecular structure and arrangement of the donor sites can be observed directly in Figure 2.X, which shows the typical coordination of EDTA with Ti(IV).

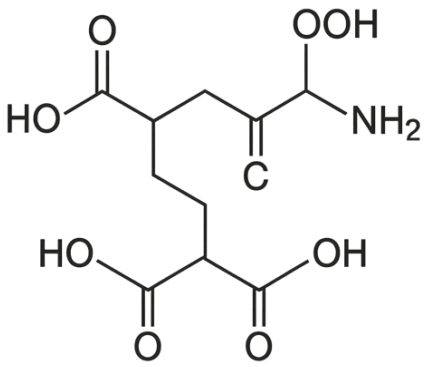


Figure 4.11: Chemical structure of EDTA and schematic of Ti(IV) coordination with the donor sites of the ligand.

The use of the Ti–EDTA complex in this study is motivated by several experimental and practical considerations. Complete coordination of Ti(IV) by EDTA significantly improves solubility and chemical stability, reducing the formation of oxides or polymers and maintaining a clear solution [139], [158]. At the same time, the complex allows operation over a wide pH range, keeping the metal in solution even at neutral or slightly acidic pH, preventing precipitation and providing more flexible operating conditions [147].

The coordination chemistry of Ti(IV) in aqueous solution is characterized by a strong tendency to undergo hydrolysis, leading to the formation of amorphous $Ti(OH)_4$ even at slightly acidic pH, which complicates handling of the cation [147]. The use of EDTA enables the formation of soluble and stable species, although the behavior of the $[TiO(EDTA)]^-$ complex is highly pH-dependent. Previous studies have shown that, between pH 2.0 and 5.2, the complex exists in equilibrium between aqueous/hydrated forms and fully chelated species, with a $\log K \approx 3.43$ and the release of approximately 1.18 protons per mole of complex [160].

From an electrochemical perspective, the polydentate nature of EDTA allows modulation of the redox potential of Ti(IV)/Ti(III), optimizing the cell voltage and the behavior of the system during oxidation and reduction

cycles. In addition, the chemical stability and compatibility of the complex with low-cost materials help to reduce corrosiveness and make the system safer and more reliable for practical applications [161]. Finally, EDTA is a widely studied, inexpensive, and readily available ligand, facilitating experimental use and comparison with literature data. All these factors make the Ti–EDTA complex an ideal candidate for applications in redox flow batteries, as it combines high solubility, chemical stability, and electrochemical control, providing an efficient and reliable electrolyte. In this study, the complex was prepared, characterized, and analyzed in terms of solubility, stability, and electrochemical behavior, with the aim of assessing its suitability as an active electrolyte.

The Ti–EDTA complex was prepared by mixing an aqueous solution of $TiOSO_4$ with an equimolar amount of EDTA, maintaining a 1:1 molar ratio between Ti(IV) and the ligand. The initial pH of the solution, measured immediately after mixing, was 6.35, which falls within the known stability window for the complex [160]. Under these conditions, the solution appeared clear and colorless, indicating complete complexation and the absence of precipitation or turbidity. The preparation was carried out at room temperature with gentle stirring to ensure homogeneous mixing and complete dissolution of the components.

The chemical stability of the complex was assessed by monitoring the solution over several hours. No visible changes were observed, confirming that the Ti–EDTA complex remains stable under these conditions, preventing hydrolysis and the formation of insoluble titanium species. The pH and clarity of the solution were periodically checked to ensure reproducibility and suitability for electrochemical measurements.

Electrochemical characterization of the Ti–EDTA complex was performed using cyclic voltammetry (CV) to investigate the redox behavior of the Ti(IV)/Ti(III) system. The CV measurements were conducted on a 0.1 M Ti–EDTA solution at pH 6.35, as shown in Figure 4.12.

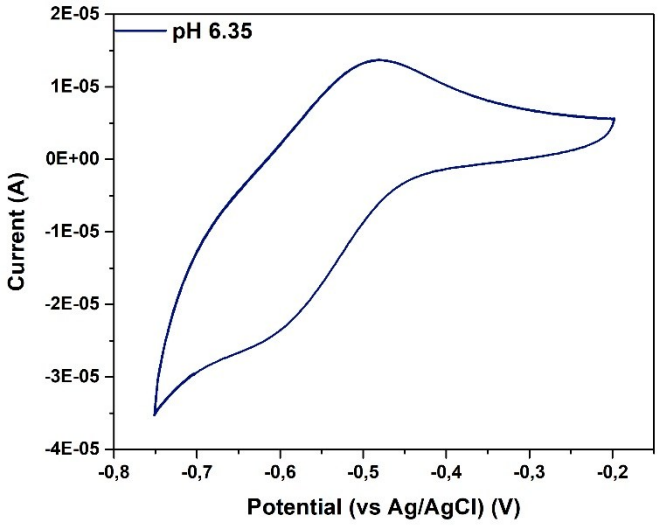


Figure 4.12: CV Ti-EDTA 0.1M. CV was performed using a glassy carbon working electrode, a platinum counter electrode, and an Ag/AgCl reference electrode, in a potential window between –0.75 V and –0.2 V, with a scan rate of 25 mV/s.

A standard three-electrode setup was used, consisting of a glassy carbon working electrode, a platinum counter electrode, and an Ag/AgCl reference electrode. The potential window was set between –0.9 V and –0.1 V, and a scan rate of 25 mV/s was applied. The cyclic voltammogram demonstrates the redox activity of the Ti–EDTA complex under these conditions. Well-defined anodic and cathodic peaks indicate a quasi-reversible process, and the absence of additional peaks or distortions confirms that the complex remains chemically intact and fully soluble during the electrochemical cycle. These observations provide initial evidence for the suitability of the Ti–EDTA complex as an electroactive species for potential applications in redox flow battery systems.
To investigate the electrochemical stability of the Ti–EDTA complex across a wide pH range, cyclic voltammetry was performed at various pH values (Figure 4.13).

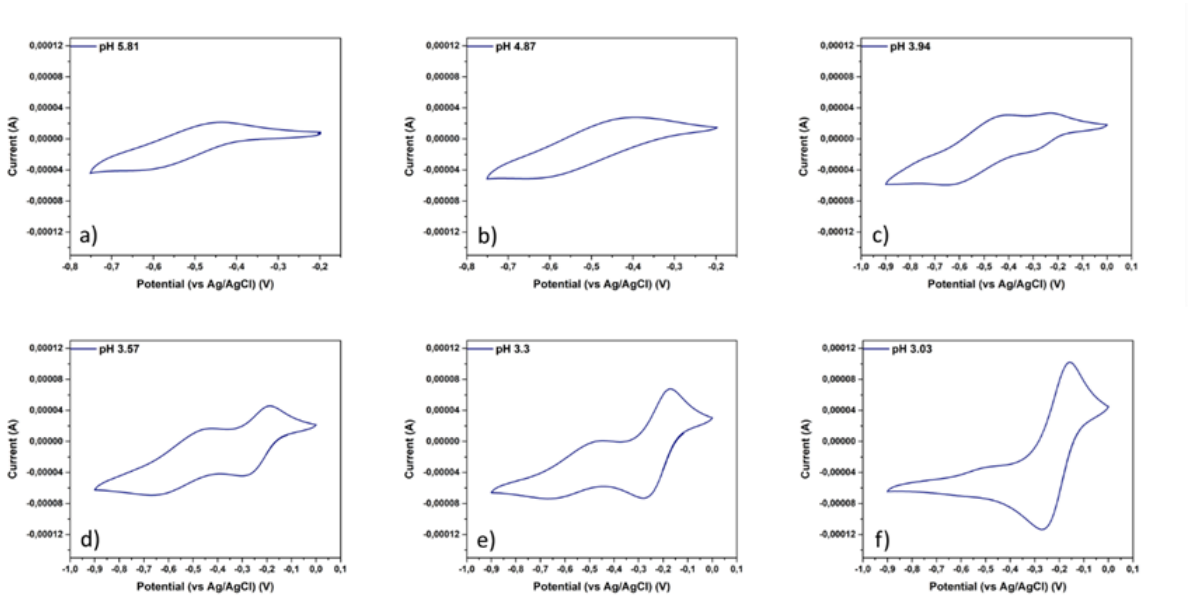


Figure 4.13: Cyclic voltammograms recorded at 25 mV/s for the 0.1 M Ti–EDTA solution at different pH values: a) 5.81; b) 4.87; c) 3.94; d) 3.57; e) 3.30; f) 3.03. The potential window was adjusted in each case to highlight the presence of anodic and/or cathodic peaks.

At higher pH (Figure 4.13a-b) the potential window was expanded towards more positive values to allow the detection of additional redox peaks that were not visible under narrower scan ranges. This adjustment was necessary due to the emergence of new redox signals below pH 4.0, potentially associated with changes in speciation or the presence of decomposition products. It can be seen that, in the pH range of 6.35 to 4.0, the cyclic curve exhibits a broad cathodic peak at -0.58V vs Ag/AgCl and a corresponding anodic peak at -0.42V vs Ag/AgCl, consistent with a quasi-reversible redox process attributed to the Ti(IV)-EDTA/Ti(III)-EDTA couple, considering the potential difference (ΔEp= 159 mV vs Ag/AgCl at 25mV s^{-1}). This behavior is compatible with the presence of the [TiO(EDTA)] species, as reported by Kristine et al. [160]. The stability of the complex within this range is further supported by Berger and Cadoff [147], who observed well-defined polarographic waves at pH 4.7.

Below pH 4.0 (see Figure 4.13c–f), an additional anodic peak at -0.23V vs Ag/AgCl and an additional cathodic peak at -0.28V vs Ag/AgCl emerge in the voltammograms, which are not consistent with the electrochemical profile of the Ti–EDTA complex, indicating the onset of complex instability within this pH range. After standing for some time, turbidity begins to appear in the solution, suggesting the formation of hydrolyzed or insoluble species such as amorphous TiO_2 or $Ti(OH)_4$. At pH 3.03, the characteristic redox peaks of the Ti–EDTA complex almost disappeared, and only single redox peaks are observed: anodic peak at -0.15 V vs Ag/AgCl, and cathodic peak at -0.26V vs Ag/AgCl, matching that of $TiOSO_4$ in H_2SO_4. This suggests that the Ti–EDTA complex has largely dissociated, and the Ti(IV) species exist predominantly as Ti–sulfate complexes. These findings are consistent with the speciation behavior of EDTA: below pH 3.5, it exists predominantly in the fully protonated form, which is unable to effectively coordinate the metal center [162].
The cyclic voltammograms of the Ti–EDTA complex (Figure 4.14) at different scan rate, from 5 mV s^{-1} to 300 mV s^{-1}, exhibit a well-defined redox couple, with an increasing cathodic peak current as the scan rate increases and a corresponding anodic wave, though less intense.

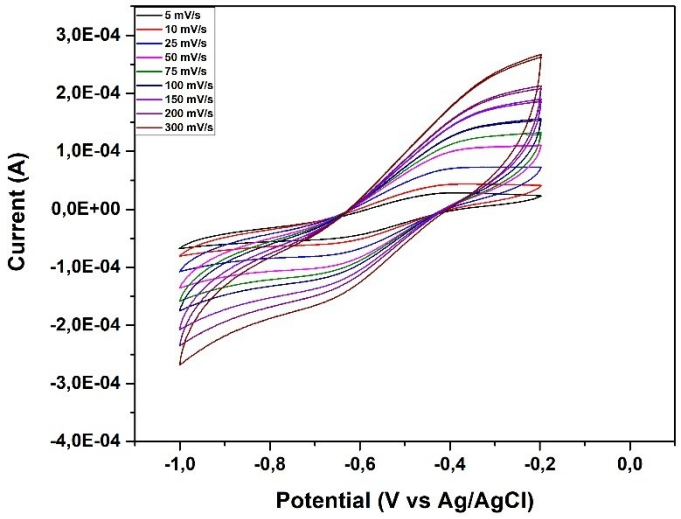


Figure 4.14: Cycle voltammetry of Ti–EDTA complex recorded at different scan rates (5–300mV/s), under optimal pH conditions (pH=5.38).

The regular increase in peak intensity, the absence of asymmetric distortions, and the overlap of successive curves all suggest a diffusion-controlled process [49].
To complete the electrochemical study, CV data at varying scan rates were analyzed to calculate key transport and kinetic parameters using the Randles–Ševčík and Laviron equations (Figure 4.15).

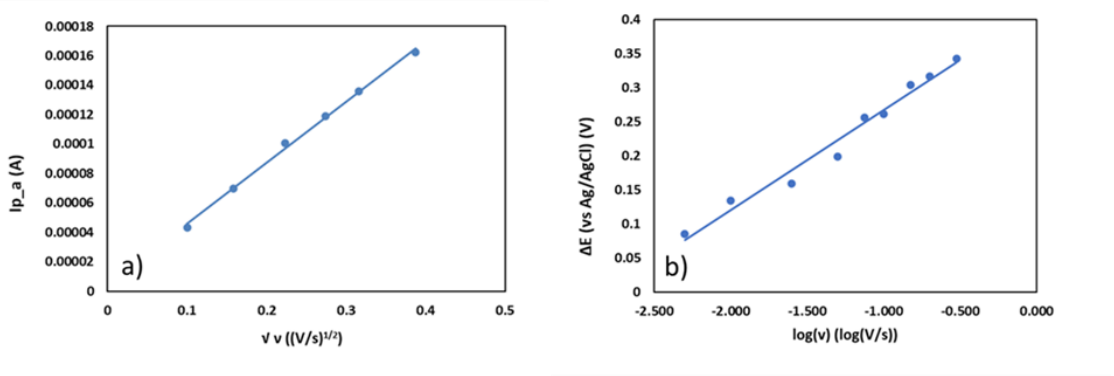


Figure 4.15: Kinetic parameter determination of the Ti–EDTA complex. (a) Plot of anodic peak current (i_p,a) versus the square root of the scan rate (√v), used to calculate the diffusion coefficient according to the Randles–Ševčík equation. (b) Variation of the peak-to-peak separation (ΔE_p) as a function of the logarithm of the scan rate (log v), used for the application of the Laviron model.

The analysis of the anodic peak current as a function of the square root of the scan rate according to Randles–Ševčík yielded a diffusion coefficient D = 9.6 × 10^{-7} cm²/s, consistent with values reported for metal–EDTA complexes in mildly acidic aqueous solutions [161]. Using the Laviron approach, a plot of ΔEp versus log (scan rate) provided an electron transfer coefficient α = 0.403 and a heterogeneous rate constant k^0 = 9 × 10^{-3} cm/s, confirming the quasi-reversible but kinetically slow nature of the Ti(IV)/Ti(III) redox process. These results indicate that, while the complex is electrochemically active and stable in solution, its electron transfer kinetics are slower than analogous systems, requiring careful control of operational conditions for application in redox flow batteries. Nevertheless, Ti–EDTA remains stable and soluble within a well-defined pH window (approximately 4.0–6.35), exhibiting reproducible electrochemical behavior with precisely determined diffusion and electron transfer parameters. Based on these experimental findings, the Ti–EDTA complex was deemed optimal for use as an electrolyte in redox flow batteries, providing reliable and stable electrochemical performance under the intended operating conditions.

4.4 Study of Ti–EDTA and Fe–EDTA Complexes for Redox Flow Batteries

After a detailed comparison of the electrochemical behavior of the Ti–bpy, Ti–HEDP and Ti–EDTA complexes, the results clearly indicate that the Ti–EDTA system represents the most favorable compromise among chemical stability, solubility, and redox reversibility, and therefore constitutes the natural starting point for the design of a fully complexed redox flow battery. Unlike the bipyridine complex, excluded due to its limited solubility (≤ 0.2 M) and narrow pH stability range, and the Ti–HEDP complex, which, despite displaying a broad pH window and good solubility, suffers from suboptimal reversibility at high scan rates, the Ti–EDTA complex combines adequate solubility, a well-defined stability window in moderately acidic conditions, and a reproducible redox behavior under a wide range of operating conditions. These properties, together with the results obtained from Randles–Ševčík and Laviron analyses, which confirmed a diffusion-controlled process and a sufficiently negative formal potential for use as an anolyte, make Ti–EDTA the most suitable candidate for the anodic half-cell of a redox flow battery based entirely on coordination complexes. A

comparative summary of the key chemical and electrochemical parameters guiding the selection of the most suitable complex is reported in the following Table 4.2.

Table 4.2: Electrochemical and chemical comparison among Ti–bpy, Ti–HEDP and Ti–EDTA complexes

Parameter	Ti–bpy	Ti–HEDP	Ti–EDTA
Maximum solubility	≤ 0.2 M	0.5 M	0.5 M
Stable pH range	1.3-1.6	0.6-9.28	4.0–6.35
Chemical stability	Low, multiple species present	High	High within optimal range
CV behavior	Two asymmetric redox couples	Well-defined couple; limits at high scan rates	Sharp and reproducible redox couple
Peaks Potential (vs Ag/AgCl)	I: E_{pa} = –0.31 V E_{pc} = –0.41 V; II: E_{pa} = 0.36 V E_{pc}= 0.24 V	E_{pa} = 0.21 V E_{pc} = 0.03 V	E_{pa} = -0.385 V E_{pc} = -0.651 V
Redox Potential (vs Ag/AgCl)	I: E_{redox} = –0.36 V II: E_{redox} = 0.30 V	E_{redox} = 0.121 V	E_{redox} = –0.518 V
D (cm²/s)	—	9.83×10^{-7}	9.6×10^{-7}
α	—	0.796	0.403
k^0 (cm/s)	—	1.14×10^{-1}	9×10^{-3}

This comparison clearly shows that Ti–EDTA is the only complex capable of simultaneously satisfying the criteria of stability, solubility, and redox reproducibility required for a functional anolyte. Once the anodic system was defined, the next step involved identifying the most appropriate catholyte. In this context, among the candidate complexes evaluated, the Fe–EDTA system emerged as the most suitable due to its combination of high aqueous stability, quasi-reversible redox behavior, good solubility, and significantly faster electron transfer kinetics compared to the Ti–EDTA complex. This choice is strongly supported by classical literature on the Fe(III)/Fe(II)–EDTA system [163], [164], [165], [166], as well as by the experimental results obtained in this work. Unlike titanium, which requires a rigorous pH control to avoid hydrolysis and the formation of colloidal species, iron in the presence of EDTA exhibits robust coordination chemistry and a considerably broader stability range (pH 3.8–6.8). For this reason, an extended pH stability investigation similar to that conducted for Ti–EDTA was deemed unnecessary, and efforts focused instead on verifying the compatibility of the complex with the Ti–EDTA operating pH (4–6.35) and on performing a complete electrochemical characterization.

The stability of the Fe–EDTA complex was verified by cyclic voltammetry at different pH values (Figure 4.16).

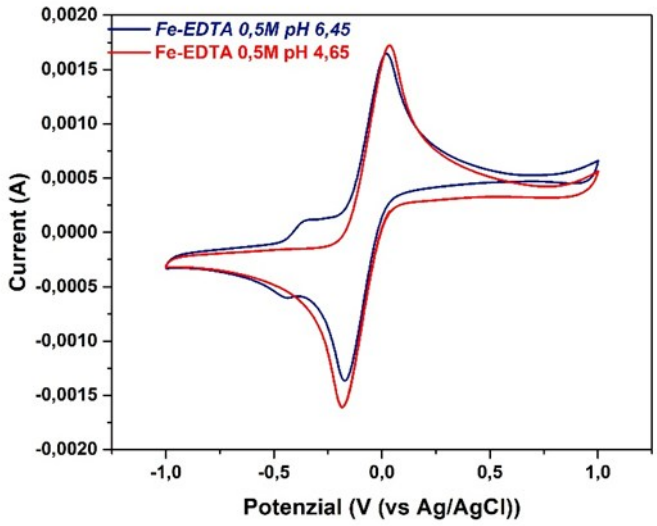


Figure 4.16: Cyclic voltammograms of the Fe (III)–EDTA complex in aqueous solution at 0.5 M concentration at different pH values (4.61 and 6.45).

At pH 4.65, corresponding to the initial pH of the 0.5 M solution, the complex shows a well-defined redox couple, with a cathodic peak centered at −0.180 V Ag/AgCl and an anodic peak at 0.034 V vs Ag/AgCl, and a redox peak (ΔE_{redox}) of about 0.1 V vs Ag/AgCl. The absence of secondary signals or asymmetry indicates a quasi-reversible process, fully consistent with the literature [163], [164]. As the pH is increased to 6.45, the upper stability limit reported for the complex [167], a secondary, small redox signal appears at more negative potentials (–0.3 to –0.4 V vs Ag/AgCl), attributable to the incipient formation of ferric hydroxide species. However, this peak remains significantly less intense than the main couple, demonstrating that Fe–EDTA remains the predominant species even near the upper pH limit. These observations define a well-established stability window between pH 4.0 and 6.3, within which the Fe(III)–EDTA complex remains soluble and stable [166]. Once the stability of the complex within the operating range was confirmed, a complete kinetic-diffusion analysis was conducted via cyclic voltammetry at various scan rates. Figure 4.17 shows the voltammograms recorded between 5 and 300 mV s^{-1}.

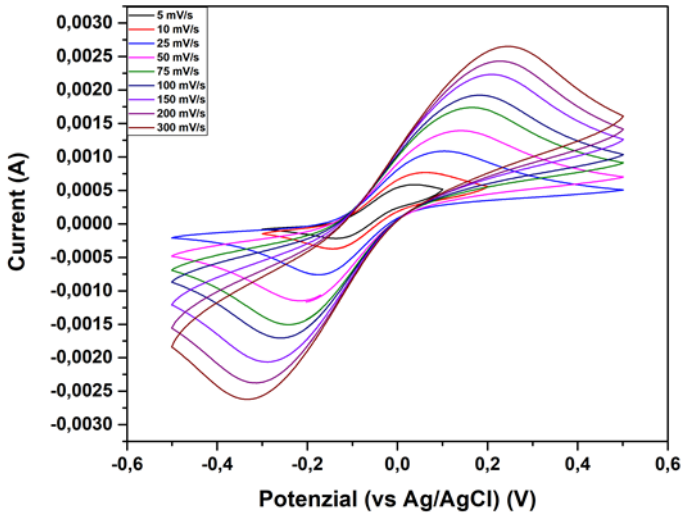


Figure 4.17: Cycle voltammetry of Fe–EDTA complexes recorded at different scan rates (5–300mV/s), under optimal pH conditions (pH=5.00).

The anodic and cathodic peaks increase linearly with √ν, without distortion or asymmetry loss, indicating a diffusion-controlled redox process with no significant kinetic limitations, thus confirming the favorable electrochemical behavior of the Fe–EDTA complex [168].

To quantify mass transport, the anodic peak was analyzed using the Randles–Ševčík equation. The current i_p,a vs √ν plot showed excellent linearity (Figure 4.18a), from which a diffusion coefficient of D = 5.4 × 10^{-7} cm^2 s^{-1} was calculated.

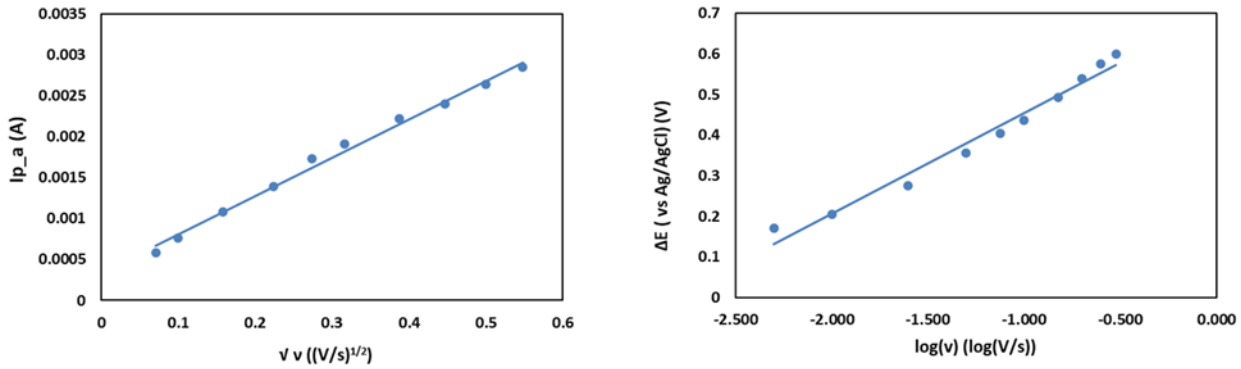


Figure 4.18: Kinetic parameter determination of the Fe–EDTA complex. (a) Plot of anodic peak current (i_p,a) as a function of the square root of the scan rate (√ν), used to calculate the diffusion coefficient via the Randles–Ševčík equation. (b) Relationship between ΔE_p and log(ν) according to the Laviron model.

This value is consistent with that reported for other ferric–EDTA complexes and only slightly lower than that of Ti–EDTA (D ≈ 9.6 × 10^{-7} cm^2 s^{-1}), a difference attributed to variations in electron density and coordination geometry of the metal center [168]. Electron transfer kinetics were evaluated using Laviron's model, analyzing

the ΔEp vs log ν relationship (Figure 4.18b). The resulting parameters were α = 0.228 and a heterogeneous rate constant $k^0 = 2.9 \times 10^{-3}$ cm s^{-1}. This latter value is particularly significant: it is about eight orders of magnitude higher than that of the Ti–EDTA complex ($k^0 \approx 9 \times 10^{-3}$ cm s^{-1}), highlighting the substantially faster electron exchange of the Fe(III)/Fe(II)–EDTA system. These results confirm that Fe–EDTA does not present any kinetic limitation at the cathode, ensuring fast and stable redox activity even at high current densities.

The redox potential of the complex Fe-EDTA, determined as the average of the redox peaks at 25 mV s^{-1}, was −0.074 V vs Ag/AgCl. Combined with redox potential of Ti–EDTA (E_{redox}= −0.518 V vs Ag/AgCl), this yields a theoretical cell voltage of 0.444 V, in perfect agreement with the values observed experimentally in battery tests. To provide a clear overview and distinguish the fully complexed system from the sulfuric acid-based system, the following summary Table 4.3 reports the key parameters of the selected EDTA-based electrolytes:

Table 4.3: Stable pH ranges, redox potentials and achieved concentrations of the Ti- and Fe-complexes.

Electrolytes	pH range for stable complex formation	Redox potential	Obtained concentration
		[V (vs. Ag/AgCl)]	[M]
Ti–sulphate complex	0.3 - 2.5	–0.160 V	1
Fe–sulphate complex	1.0 - 3.0	+0.573 V	1
Ti–EDTA	4 - 6.35	–0.518 V	0.5
Fe-EDTA	4.6 - 6.3	–0.110 V	0.5

Figure 4.19 finally shows the schematic of the Ti–EDTA / Fe–EDTA battery, highlighting the organization of the anolyte and catholyte inside the flow cell and the direction of flow of the electrolytes.

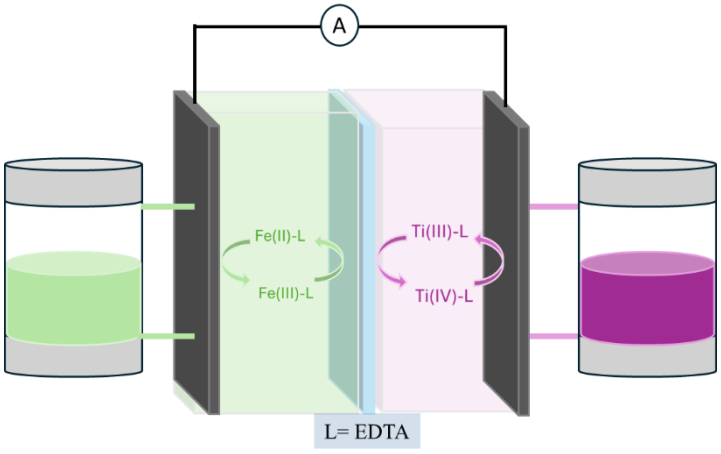


Figure 4.19: Schematic representation of the Ti–EDTA/Fe-EDTA redox flow battery system.

In conclusion, the combination of chemical stability within the pH range 4.6–6.3, reproducible voltammetric behavior, high diffusivity, and fast electron transfer kinetics makes Fe–EDTA the ideal catholyte for a fully complexed redox flow battery. Coupling it with Ti–EDTA allows operation in a moderately acidic, non-corrosive environment, simplifies cell component selection, and enhances operational safety, while

maintaining an adequate and well-defined cell voltage. Based on these results, the following sections will present and analyze in detail the electrochemical performance of the Ti–EDTA / Fe–EDTA battery, evaluating its behavior under real operating conditions.

4.5 Study of Ti–EDTA/Fe–EDTA Battery

After completing the synthesis and characterization of the titanium and iron complexes, and identifying the Ti–EDTA/Fe–EDTA pair as the most promising combination in terms of chemical stability, solubility, and redox efficiency, the work progressed toward evaluating their performance in a redox flow battery configuration. The preliminary studies allowed us to precisely define the operating conditions that ensure the stability of the two electrolytes: the Ti–EDTA complex exhibits reproducible behavior within the pH range 4.0–6.35, while the Fe–EDTA complex is stable between pH 4.6 and 6.3. Moreover, the voltammetric analysis revealed a clear electrochemical complementarity between the two systems, resulting in a theoretical cell potential of 0.44 V, calculated from the difference between their respective redox potentials. The integration of all these elements, stability windows, solubility limits, voltammetric behavior, diffusion parameters, and electron-transfer kinetics, provided a solid foundation for their application in a fully complexed flow battery. On this basis, single-cell experiments were initiated to verify the electrochemical behavior of the Ti–EDTA/Fe–EDTA pair under real operating conditions and to assess its suitability as a less corrosive and safer alternative to the traditional sulfuric-acid-based system.

4.5.1 Ionic Conductivity Study of the Ti–EDTA and Fe–EDTA Complexed Electrolytes

The use of coordination complexes such as Ti–EDTA and Fe–EDTA in a redox flow battery system requires a preliminary and accurate evaluation of the ionic conductivity of the electrolytes, since the prevalence of the metal species in a complexed form reduces the concentration of free ions effectively available for charge transport. Unlike the H_2SO_4-based system, where the high dissociation of sulfuric acid generates a large population of H^+ and SO_4^{2-} ions in solution, EDTA-based electrolytes are characterized by larger species with lower mobility and weaker ionization, resulting in intrinsically lower conductivity values [160], [161]. Excessively low conductivity increases the internal ohmic resistance of the cell and consequently causes a more pronounced voltage drop during charge and discharge processes, with a direct impact on voltage and energy efficiencies at higher current densities. For these reasons, before proceeding with battery electrochemical testing, it was necessary to systematically investigate the transport properties of the complexed electrolytes and to identify appropriate strategies to enhance their conductivity.

The most straightforward strategy to increase the conductivity of the Ti–EDTA and Fe–EDTA solutions consists in increasing the concentration of free ionic species in the medium by introducing a supporting electrolyte that does not interfere with the metal–EDTA complexation equilibria. In this context, potassium chloride (KCl) was selected because of its complete dissociation in water (K^+ and Cl^-), high solubility, good ionic mobility, and chemical inertness toward EDTA complexes. Both K^+ and Cl^- act as spectator ions, contributing to charge transport without significantly competing with EDTA for the metal coordination sphere

or generating alternative side complexes. Furthermore, KCl is inexpensive, readily available, and compatible with the pH range in which Ti–EDTA and Fe–EDTA are stable, making it a suitable choice for aqueous electrolytes. From a theoretical point of view, the addition of KCl increases the ionic strength of the solution, affecting both conductivity and speciation equilibria. A moderate increase in ionic strength improves conductivity by increasing the concentration of charge carriers, whereas an excessive increase may modify activity coefficients and reduce the solubility of certain species, particularly iron-based ones, promoting salting-out phenomena and the formation of less soluble solid phases [169], [170]. The aim of this study was therefore twofold: on the one hand, to maximize conductivity through KCl addition, and on the other hand, to determine the threshold beyond which excessive ionic strength compromises the stability of the Ti–EDTA and Fe–EDTA complexes. Conductivity measurements were performed at controlled temperature (25 °C) on solutions containing Ti–EDTA and Fe–EDTA complexes at fixed concentration (0.5 M), while varying the KCl concentration from 0 M to 4 M. To ensure high reproducibility and precise control of the cell geometry, a dedicated conductivity cell was employed, specifically designed and 3D-printed for this study (Figure 4.20).

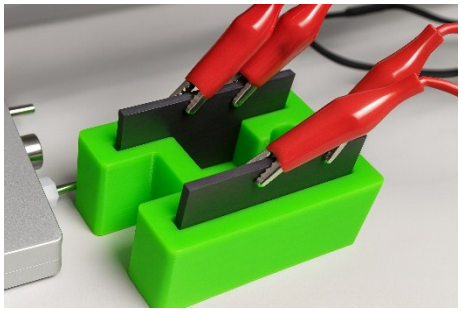


Figure 4.20: Set-up used for electrochemical measurements, consisting of two planar electrodes mounted in a 3D-printed holder and connected by insulated alligator clips. The system allows for stable and reproducible electrode positioning during conductivity measurements.

The cell consists of a PLA (polylactic acid) support, bright green in color, which holds two planar graphite electrodes at a fixed distance, connected to the conductometer via shielded crocodile clips. This configuration allows for a well-defined and reproducible cell constant, while minimizing geometric variations that could affect conductivity measurements. The choice of graphite as electrode material provides excellent chemical inertness, preventing dissolution or undesirable interactions with the EDTA complexes even at high salt concentrations.

In addition to the conductivity measurements, each sample was visually inspected to monitor the potential appearance of turbidity or precipitation as a function of KCl concentration. Figure 4.21 shows the representative images of the Ti–EDTA and Fe–EDTA solutions prepared at different KCl concentrations (from 1M to 4M KCl).

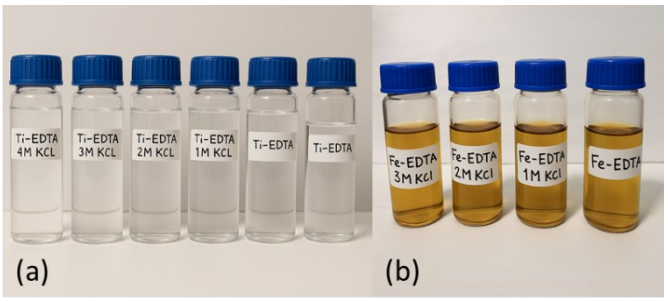


Figure 4.21: Photographs of Ti–EDTA and Fe–EDTA solutions at different KCl concentrations.

The transparent solutions in Figure 4.21a correspond to Ti–EDTA (). It is clearly visible that at 1 M and 3 M KCl the solution remains fully transparent and stable, whereas turbidity appears only at 4 M KCl after 2 hours (Figure 4.22a), indicating the onset of destabilization and formation of titanium hydroxylated species at high ionic strength. The brownish solutions in Figure 4.21b correspond to Fe–EDTA: these also remain perfectly clear up to 2 M KCl, while a marked precipitation occurs at 3 M KCl, consistent with the well-known decrease in solubility of ferric species in high ionic strength media [170]. Figure 4.22b of the Fe–EDTA 3 M KCl sample shows a solid phase deposited at the bottom and strong turbidity in the supernatant, experimentally confirming the threshold of instability of the ferric complex.

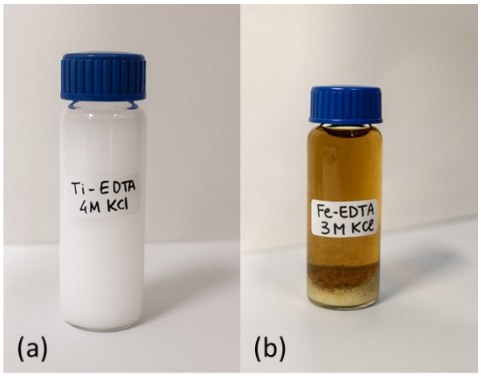


Figure 4.22: Appearance of high ionic strength solutions: (a) 0.5 M Ti–EDTA with 4 M KCl, which shows marked opalescence due to the loss of solubility of the complex; (b) 0.5 M Fe–EDTA with 3 M KCl, in which the formation of a precipitate and the complete destabilization of the ferric complex are evident.

This qualitative analysis made it possible to quickly determine the operating stability limit of the complexes in the presence of KCl: while at low and moderate salt concentrations the solutions remain clear and stable over time, at higher concentrations clear signs of decomposition and loss of solubility are observed, particularly for Fe–EDTA. It is important to emphasize, however, that in your system Fe–EDTA remains completely transparent up to 2 M KCl, whereas turbidity and precipitation appear exclusively at 3 M KCl. This behavior, fully consistent with the literature on ferric species solubility in high ionic strength environments [170], indicates that 2 M still represents a stable condition for the catholyte. Similar, though less pronounced, behavior is observed for Ti–EDTA at higher KCl concentrations (around 4 M), where the solution becomes slightly

opalescent, suggesting the formation of hydroxylated titanium species at high ionic strength [147], [169]. The Table 4.4 summarizes the specifications of KCL electrolytes.

Table 4.4: Visual stability of Ti–EDTA and Fe–EDTA (0.5 M) as a function of KCl concentration

[KCl] (M)	Ti–EDTA Appearance	Ti–EDTA Precipitate	Fe–EDTA Appearance	Fe–EDTA Precipitate	Stability / Notes
0	Clear	No	Clear	No	Stable
1	Clear	No	Clear	No	Stable
2	Clear	No	Clear	No	Stable
3	Slightly opalescent	Traces (Ti)	Marked turbidity	**Yes**	Precipitate after 1 h in Fe-EDTA electrolyte
4	Opalescent	Precipitation	–	–	Tested only for Ti–EDTA

The evolution of the electrical conductivity (σ) as a function of KCl concentration is summarized in Figure 4.23, where the values measured for the 0.5 M Ti–EDTA and Fe–EDTA solutions are shown as a bar chart.

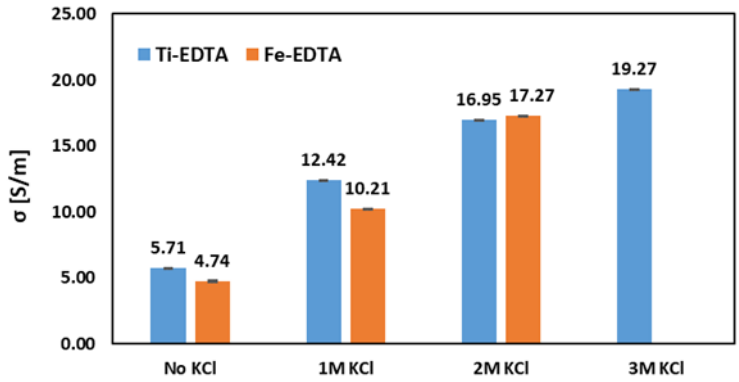


Figure 4.23: Ionic conductivity (σ [S/m]) of Ti–EDTA and Fe–EDTA electrolytes as a function of KCl concentration up to 3 M, measured at 25 °C. Error bars indicate the standard deviation calculated from three independent measurements performed under identical conditions.

The results show a clear increase in conductivity with increasing KCl concentration in both solutions. In the absence of supporting electrolyte, conductivity is relatively low, consistent with the predominance of large, low-mobility complex species. At 1 M KCl, a significant increase in conductivity is already observed, placing the system in a more favorable transport regime for electrochemical applications. Further increases in KCl concentration up to 2 M provide an additional increase in σ, confirming the dominant role of the supporting electrolyte in governing ionic transport. Only at 3 M KCl does the Fe–EDTA complex show signs of instability, with the appearance of turbidity and precipitation, while Ti–EDTA exhibits slight opalescence only near 4 M. Based on the experimental results and the indications provided by the literature, the addition of KCl proved to be an effective strategy for increasing the conductivity of Ti–EDTA and Fe–EDTA solutions, but only within a restricted concentration range. The combined analysis of conductivity data and visual stability clearly indicates that 1 M and 2 M KCl represent the optimal conditions, as both concentrations yield clear and stable solutions with sufficiently high conductivity to mitigate the intrinsic ohmic limitations of the complexed

electrolytes. Higher concentrations (≥ 3 M), although providing slightly higher conductivity, result in significant instability of the Fe–EDTA complex, with precipitation in the catholyte and compromised reproducibility of subsequent electrochemical measurements. From a thermodynamic perspective, this behavior is consistent with studies on protonation and complexation of EDTA-type ligands in high ionic strength media [169], which show that increased ionic strength affects activity coefficients and complex formation equilibria, sometimes promoting solid-phase separation. Therefore, the decision to operate with 1 M and 2 M KCl is not only experimentally justified but also grounded in well-established considerations regarding the speciation and solubility of ferric and titanyl species in aqueous solution [147], [169], [170]. In the following sections, the electrochemical performance of the Ti–EDTA (anolyte) and Fe–EDTA (catholyte) battery system will be presented, employing these two optimal KCl concentrations (1 M and 2 M) to evaluate how ionic conductivity directly influences the overall behavior of the complexed redox flow battery.

4.5.2 Electrochemical performance of Ti–EDTA/Fe–EDTA battery

After defining the optimal stability and conductivity conditions of the Ti–EDTA and Fe–EDTA complexed electrolytes, it was possible to systematically investigate the electrochemical behaviour of the Ti–EDTA/Fe–EDTA battery in a separated-electrolyte configuration. In all experiments, the Ti–EDTA complex was employed as the anolyte and the Fe–EDTA complex as the catholyte, both at a concentration of 0.5 M, operating within the pH range previously identified as compatible with the stability of the complexes (Ti–EDTA at pH 5 and Fe–EDTA at pH 6.28). Based on the conductivity study presented in the previous paragraph, two operating conditions were selected for the supporting electrolyte,1 M and 2 M KCl, which represent the best compromise between increased ionic conductivity and preservation of the chemical stability of the complexes in solution. As previously done for the non-complexed system in sulfuric acid, the anolyte was also additivated with 16 mg L^{-1} of bismuth, added as $Bi_2(SO_4)_3$, in order to exploit the well-known catalytic effect of bismuth on the oxidation of Ti(III). It is known that, under sufficiently cathodic potentials, Bi^{3+} is reduced and electrodeposited in metallic form onto the surface of the graphite felt, forming a thin catalytic layer that enhances the kinetics of the Ti(IV)/Ti(III) redox couple, lowering its overpotential without significantly perturbing the EDTA complexation equilibria [72]. Altogether, these experimental strategies (ligand choice, pH window definition, addition of supporting electrolyte and bismuth) were aimed at demonstrating the feasibility of a fully EDTA-complexed redox flow battery system.

Battery cycling tests were performed in a single-flow cell equipped with a graphite felt as porous electrode in both compartments, a Nafion N212 proton-exchange membrane as separator, and a pumping system delivering a constant flow rate of 40 mL min^{-1} (see Chapter 3 section 3.7.1). The analysis of the cell behaviour at different current densities was conducted through galvanostatic short-run cycles, wherein the battery was subjected to six consecutive charge/discharge cycles at 40, 60 and 80 mA cm^{-2}, maintaining the cell voltage within the range 0.3–0.9 V. From these tests, the main cell efficiencies, coulombic efficiency (CE), voltage efficiency (VE) and energy efficiency (EE), were extracted, as shown in the corresponding Figure 4.24.

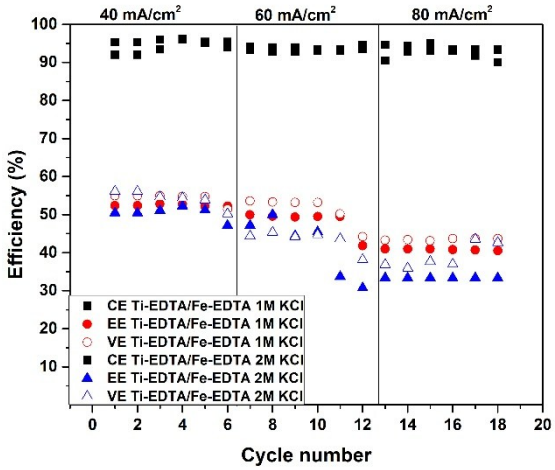


Figure 4.24: Performance of the Ti–EDTA/Fe–EDTA battery at different current densities (40, 60, and 80 mA cm⁻²) at 40 mL min⁻¹

The results first highlight an extremely favourable behaviour in terms of CE, which remains high under all operating conditions, with values between approximately 98% and 99%, essentially independent of both current density and KCl concentration. This indicates that the Ti(IV)/Ti(III) and Fe(III)/Fe(II) redox processes are reversible and that parasitic reactions or active species crossover through the membrane are negligible, in agreement with previous voltammetric observations [147], [164]. Conversely, VE and EE show a much stronger dependence on both the ionic conductivity of the electrolyte and the applied current density: as the current increases, the internal polarisation rises due to the limited ionic mobility of the complexed species and the intrinsic ohmic resistance of the cell, leading to a progressive decrease in VE and EE. The experimental values obtained for the two formulations are summarised in Table 4.5.

Table 4.5: Coulombic efficiency (CE), energy efficiency (EE), and voltage efficiency (VE) of Ti-EDTA/Fe-EDTA battery at different KCl concentration and current densities.

[KCl]	Current density	CE	EE	VE
[M]	mA cm^{-2}	%	%	%
1	40	98.2	61.51	53.77
	60	99.1	48.10	47.82
	80	98.8	42.20	42.70
2	40	99.74	49.89	55.81
	60	98.60	41.90	43.40
	80	98.42	36.64	38.93

Analysis of the table and efficiency plots shows that, for 1 M KCl, CE remains essentially constant across the three current regimes, while VE and EE decrease moderately as current density increases, dropping from about 61.51% and 53.77% at 40 mA cm⁻² to about 42.20% and 42.70% at 80 mA cm⁻². This reflects increasing ohmic and activation losses as the operating regime shifts away from milder conditions, without introducing macroscopic instability in the system. For 2 M KCl, the behaviour is slightly different: at 40 mA cm⁻² VE is comparable to that of the 1 M solution (55.81%) and EE is only slightly lower (49.89%), indicating that the

higher ionic conductivity initially helps to limit voltage losses. However, at higher currents the EE declines more rapidly, reaching 41.90% and 36.64% at 60 and 80 mA cm^{-2}, with VE values of 47.82% and 42.70%, respectively. This behaviour suggests that although increased ionic strength improves charge transport in the short term, it may also amplify other resistive contributions (e.g., membrane or electrode-related) and, as discussed later, promote chemical instability that negatively impacts performance at higher currents. Overall, the short-run tests indicate that both formulations are capable of sustaining charge/discharge cycles under realistic conditions, with high CE and EE values comparable to those reported for other EDTA-based systems [161], [169], while also highlighting that the choice of KCl concentration must consider not only ionic conductivity but also long-term stability. To explore this aspect further, long-run tests were conducted in which the battery was cycled for 100 consecutive cycles at 40 mA cm^{-2}, a current density chosen as a representative condition—high enough to stress the system, but not so high as to induce degradation purely due to excessive electrochemical strain (Figure 4.25).

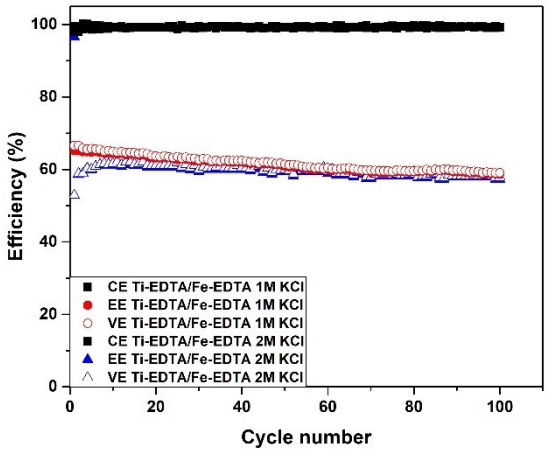


Figure 4.25: Coulombic efficiencies (CE), voltage efficiencies (VE), and energy efficiencies (EE) during 100 cycles at 40 mA cm^{-2}.

The evolution of performance over time shows that, for both formulations, the coulombic efficiency remains practically constant and close to 99% throughout all 100 cycles, confirming the high reversibility of the redox reactions and the absence of significant side processes that would irreversibly consume active species. This result is particularly relevant because it demonstrates that EDTA complexation does not compromise the redox stability of the system even under prolonged operating conditions in a flowing electrolyte environment. In contrast, voltage efficiency and consequently energy efficiency exhibit a progressive decrease as the number of cycles increases. Initially, VE remains at relatively high values, comparable to those observed in the short-run tests at 40 mA cm^{-2}, but with continued cycling a gradual increase in internal polarisation and a reduction in discharge voltage become evident. This phenomenon may be attributed to increasing internal resistances (e.g., microstructural changes on the electrode surface, felt rearrangement, or accumulation of inactive species), as well as potential variations in the transport properties of the electrolyte over time. The effect is present in both formulations but is more pronounced in the 1 M KCl system, where the contribution of

electrolyte ohmic resistance is inherently larger. The most significant difference between the two formulations emerges from the analysis of capacity retention as a function of cycle number (Figure 4.26).

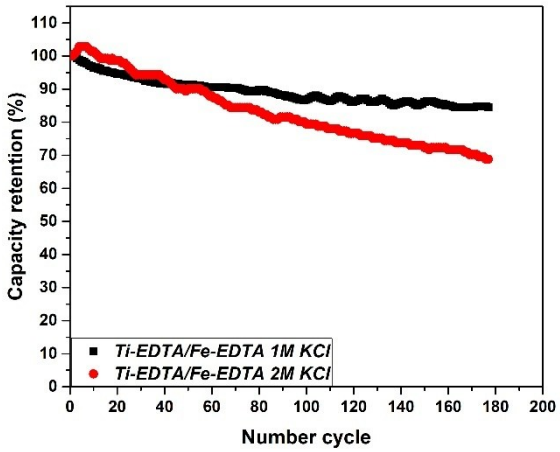


Figure 4.26: Discharge capacity retention during 100 cycles at 40 mA cm⁻².

For the 1 M KCl battery, capacity decreases relatively slowly and smoothly, without abrupt changes or sudden failures: the capacity retention curve shows a moderate decline compatible with expected ohmic and diffusional losses, without any indication of chemical instability of the electrolyte. The Fe–EDTA complex remains in solution, no visual changes occur in the electrolyte, and the cell maintains reproducible behaviour over time. Conversely, for the 2 M KCl formulation a markedly faster and more pronounced capacity fade is observed, with a significantly greater loss of capacity at an equivalent number of cycles. This behaviour correlates with experimental observations made at the end of the test: in the Fe–EDTA catholyte containing 2 M KCl, the presence of a solid precipitate was detected, clearly visible at the bottom of the catholyte reservoir (Figure 4.27).



Figure 4.27: Presence of precipitate in the Fe–EDTA catholyte after 100 battery cycles under operating conditions with 2 M KCl.

Although no specific structural analysis of the precipitate was performed, this behaviour can reasonably be attributed to supersaturation conditions or to a shift in the complexation equilibrium induced by the high ionic strength of the electrolyte. Literature reports indicate that increasing ionic strength, by adding neutral salts such as NaCl, can significantly reduce the solubility of ferric species in solution. In particular, Liu and Millero [170] demonstrated that the solubility of ferric hydroxide decreases markedly with increasing ionic strength, favouring the formation of insoluble species. By analogy, in the Fe–EDTA system at 2 M KCl it is plausible that a fraction of the ferric species, especially those not fully complexed or present in equilibrium with hydrolysed forms, may be driven toward precipitation. The appearance of the precipitate results in a progressive reduction of the concentration of redox-active Fe–EDTA species in solution, and consequently a measurable decrease in discharge capacity: at each cycle, part of the active material becomes unavailable for the redox process, leading to a cumulative and much more rapid capacity loss than in the 1 M KCl system, where no such phenomenon is observed. The correlation between precipitate formation and accelerated capacity fade in the 2 M KCl system is therefore direct and coherent with both the experimental observations and the speciation and solubility considerations drawn from literature [169], [170].

Overall, the results demonstrate that the Ti–EDTA/Fe–EDTA system can sustain charge and discharge cycles under realistic operating conditions, with high CE and good electrochemical stability. However, they also highlight that the choice of KCl concentration must consider not only the need to increase ionic conductivity but also the long-term stability of the complexation equilibria. In light of these findings, the 1 M KCl formulation was identified as the most suitable for subsequent comparative tests with the sulfuric acid-based system, offering the best compromise between conductivity, energy efficiency and chemical stability, avoiding precipitation phenomena in the catholyte and ensuring a more stable capacity throughout cycling, while maintaining bismuth as an effective catalytic additive in the anolyte.

4.5.3 Influence of temperature on Ti–EDTA/Fe–EDTA battery performance

In addition to the investigation carried out at room temperature, the influence of operating temperature on the performance of the Ti–EDTA/Fe–EDTA battery was evaluated in order to understand how thermal parameters affect mass transport, redox kinetics, and, more generally, the overall efficiency of the system. All temperature-dependent tests were conducted using the complexed electrolyte containing 1 M KCl, previously identified as the optimal formulation to ensure a suitable balance between ionic conductivity and long-term chemical stability. The effect of temperature was examined by comparing the cell behaviour at 25 °C (standard condition) and 65 °C, performing galvanostatic charge/discharge cycles at three different current densities: 40, 60, and 80 mA cm^{-2}. The resulting coulombic efficiency (CE), voltage efficiency (VE), and energy efficiency (EE) values obtained under the two thermal conditions are shown in Figure 4.28.

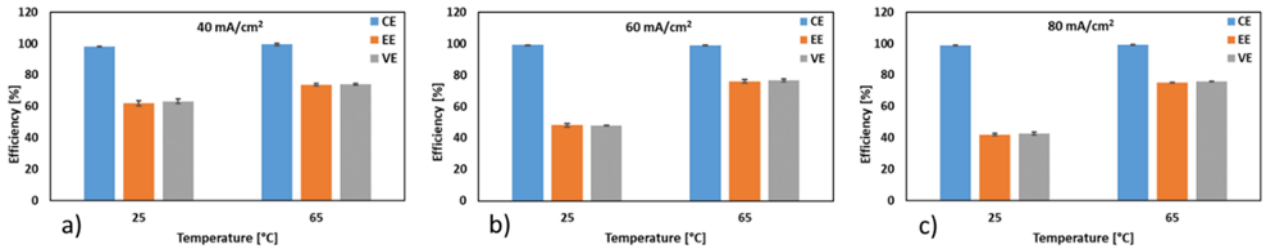


Figure 4.28: Coulombic (CE), voltage (VE), and energy (E) efficiency for the Ti–EDTA/Fe–EDTA battery at 25°C and 65°C, respectively at (a) 40, (b) 60, and (c) 80mA cm-².

Overall, increasing the operating temperature proved to have a strongly beneficial effect on battery performance, although with a magnitude that depends on the applied current density. At 40 mA cm^{-2}, the rise in temperature leads to a significant increase in VE, from approximately 63.1% to over 74.1%, accompanied by a corresponding increase in EE from 61.1% to around 73.9%. CE remains high and unchanged (~99%), confirming that higher temperatures do not compromise the reversibility of the Ti(IV)/Ti(III) and Fe(III)/Fe(II) redox reactions. This indicates that, under low-current conditions, the dominant contribution of temperature is related to the reduction of resistive losses. The effect becomes even more pronounced at 60 mA cm^{-2}, where VE rises from approximately 47.8% to 76.8%, and EE from 48.1% to 76.1%, while CE remains essentially constant (~98.5%). In this regime, elevated temperature reduces both ohmic and activation losses, effects that grow increasingly significant as current density increases due to the stronger polarisation of the system. Even at 80 mA cm^{-2}, where absolute efficiency values are naturally lower due to substantial ohmic losses, the positive influence of temperature remains clear: VE improves from approximately 42.7% to 75.9%, and EE from 42.2% to 75.3%, demonstrating that thermal enhancement remains effective even under more demanding operating conditions.

In Table 4.6, the performance of the Ti–EDTA/Fe–EDTA battery at 25 °C and 65 °C is summarised, highlighting the improvement in CE, VE and EE as the operating temperature increases across all current densities.

Table 4.6: Comparison of electrochemical performance parameters (CE, VE and EE) of the Ti–EDTA/Fe–EDTA system at 25 °C and 65 °C under different current densities.

Complexing Agent	Anolyte	Catholyte	Temperature	Current density	CE	EE	VE
			[°C]	[mA cm-2]	%	%	%
EDTA	0.5 M Ti	0.5 M Fe	25	40	98.2	61.1	63.1
				60	99.1	48.1	47.8
				80	98.8	42.2	42.7
			65	40	99.5	73.9	74.1
				60	99.1	76.1	76.8
				80	99.2	75.3	75.9

This performance enhancement can be attributed to several synergistic physicochemical mechanisms. First, higher temperatures lead to a decrease in electrolyte viscosity, improving ionic mobility and the diffusion of redox-active species [171]. In addition, ionic diffusivity increases according to the Stokes–Einstein relationship, thereby mitigating concentration polarisation effects [172]. Elevated temperatures also accelerate electrode reaction kinetics, reducing activation overpotential and favouring more efficient charge-transfer processes [173]. Furthermore, the proton-exchange membrane exhibits lower resistance at higher temperatures, contributing to improved VE [174].

A key outcome of these experiments is the chemical stability of the system up to 65 °C. Throughout the tests, no precipitation, turbidity, or visible degradation of the complexes was detected, nor were alterations in electrolyte appearance observed. This result is particularly significant, as it demonstrates that the Ti–EDTA/Fe–EDTA system can be operated at moderately elevated temperatures without compromising its chemical integrity, an aspect not always guaranteed in coordination-complex-based systems, which are often more sensitive to thermal variations than inorganic electrolytes. Overall, the results indicate that temperature optimisation is a viable and effective strategy to counterbalance the intrinsically lower conductivity and slower kinetics typical of EDTA-based electrolytes. At the same time, operation at elevated temperatures must be evaluated carefully in practical applications, as long-term cycling under such conditions may lead to secondary effects such as evaporation, local concentration changes, or increased thermal management requirements. In light of these considerations, and as part of a broader effort to characterise both the electrochemical and fluid-dynamic behaviour of the system, the next set of tests focuses on analysing the effect of flow rate, a fundamental parameter in flow batteries as it directly influences electrolyte renewal within the porous electrode, pressure losses, and the overall transport behaviour in the cell.

4.5.4 Influence of flow rate on Ti–EDTA/Fe–EDTA battery performance

As a completion of the parametric analyses carried out on the Ti–EDTA/Fe–EDTA system, and after evaluating the influence of temperature on the electrochemical performance, the role of flow rate was also investigated. Flow rate is a key parameter in redox flow batteries, as it determines the electrolyte renewal within the porous electrode, affects both convective and diffusive transport phenomena, and contributes

significantly to the energy losses associated with pumping. As widely documented in traditional RFB systems, the overall efficiency of the cell strongly depends on the balance between convective transport, ionic diffusion, and hydrodynamic resistances [25], [175]. For this reason, the effect of flow rate was evaluated through short-run tests carried out at 40-, 60-, and 80-mL min^{-1}, combined with three current densities (40, 60, and 80 mA cm^{-2}) and two operating temperatures (25 °C and 65 °C), using the complexed electrolyte containing 1 M KCl, previously identified as optimal for stability and conductivity. The experimental results, reported in Figure 4.29, show that flow rate affects the behaviour of the battery in a nonlinear manner, with effects strongly dependent on the current regime and the operating temperature.

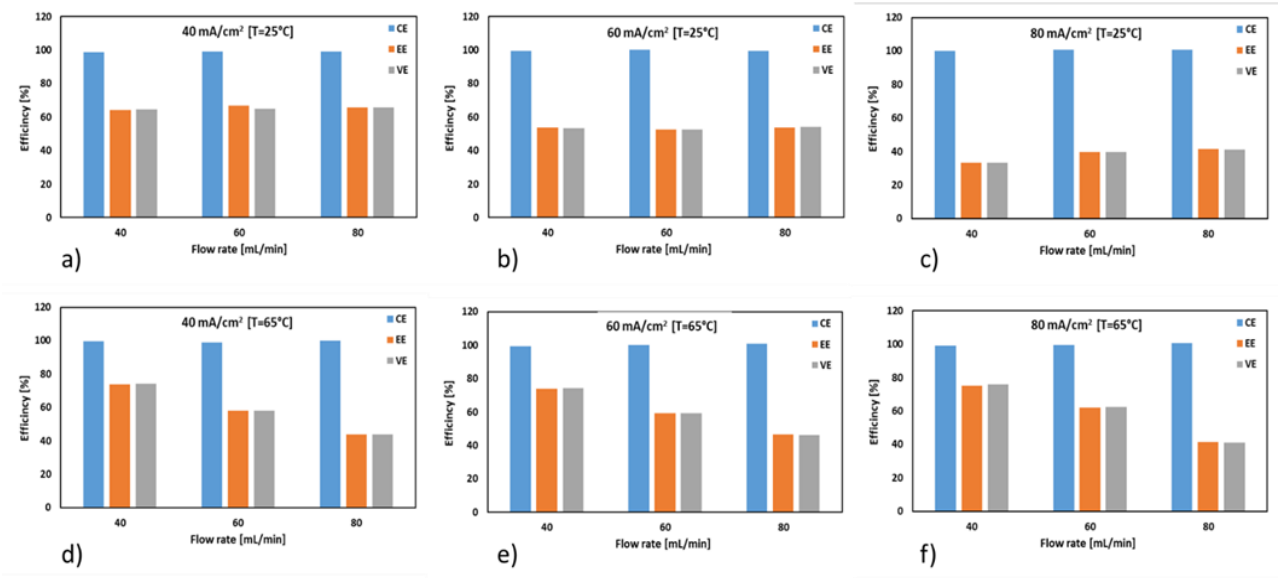


Figure 4.29: Coulombic (CE), energy (EE), and voltage (VE) efficiencies for the Ti–EDTA/Fe–EDTA battery at different flow rates (40–80 mL min^{-1}), for currents of 40 mA cm^{-2}(a, d), 60 mA cm^{-2}(b, e), and 80 mA cm^{-2}(c, f), at 25°C (a–c) and 65°C (d–f), respectively.

At 40 mA cm^{-2}, variations in flow rate produce relatively small changes in efficiencies. At 25 °C, VE and EE are almost independent of flow rate, suggesting that mass transport is not a limiting factor under these conditions. However, at 65 °C, a decrease in VE (from ~72% to ~52%) and EE (from ~70% to ~50%) is observed as the flow rate increases from 40 to 80 mL min^{-1}. This behaviour can be attributed to the reduction in residence time of the electrolyte within the electrode: higher flow rates accelerate electrolyte turnover but reduce the time available for completion of the redox reactions, counterbalancing the benefits associated with enhanced ionic mobility at elevated temperatures. The effect becomes more pronounced at 60 mA cm^{-2}, where a systematic decrease in VE and EE is observed at both temperatures as flow rate increases. CE remains stable and close to 99%, confirming that the performance decline is mainly related to increased ohmic and mass transport losses rather than to irreversible redox processes. This behaviour is consistent with what has been reported in vanadium and iron–chromium systems, where high flow rates can generate concentration inhomogeneities, increased pressure losses, and reduced electrolyte utilisation efficiency [39], [175]. At 80 mA cm^{-2}, the dependence on flow becomes even more evident. Under high current load, mass transport

limitations dominate the cell behaviour, and higher flow rates amplify polarization effects, significantly reducing VE and EE. At such currents, the system requires a longer residence time of the electrolyte within the porous electrode to ensure efficient utilisation of the active species, whereas excessive flow exacerbates internal losses. Overall, these results confirm that flow rate cannot be optimised through simple increase. If excessively low flow rates may limit the supply of active species, excessively high flow rates reduce contact time with the electrode, increase pumping losses, and introduce concentration gradients that penalise energy efficiency, in agreement with previous observations on complexed electrolytes and studies on ionic transport and electrolyte viscosity [103], [173], [174], [176]. In systems based on coordination complexes, characterised by slower kinetics compared to inorganic electrolytes, these effects are particularly relevant and require careful balancing. Based on these considerations, a flow rate of 40 mL min^{-1} emerges as the best compromise between energy efficiency, mass transport, and operational stability for the Ti–EDTA/Fe–EDTA system, as it maximises cell performance while avoiding hydrodynamic penalties. This configuration therefore represents the standard operating condition adopted for the subsequent analyses. The following Table 4.7 shows the optimal configurations for the Ti-EDTA/Fe-EDTA battery.

Table 4.7: Summary of the optimal operating conditions for the Ti–EDTA/Fe–EDTA system

Parameter	Tested values	Experimental outcome	Optimal condition	Motivation
KCl concentration	0–4 M	Conductivity increases; Fe–EDTA precipitation ≥ 3 M Ti-EDTA precipitation ≥ 4M	1-2 M KCl	Best compromise between conductivity and chemical stability
Temperature	25–65 °C	VE and EE increase; no degradation	65 °C	↑ diffusivity, ↓ viscosity, improved kinetics
Flow rate	40–80 mL min^{-1}	High flow rates reduce VE and EE	40 mL min^{-1}	Best balance between mass transport and pumping losses
Cycling stability	100 cycles	Precipitation in Fe–EDTA at 2 M KCl	1 M KCl	No instability observed
Additives	With Bi^{3+}	Improves Ti(III) oxidation kinetics	With Bi^{3+}	↓ anodic overpotential

Overall, these analyses demonstrate that the Ti–EDTA/Fe–EDTA battery is a promising system whose performance can be significantly enhanced through careful optimisation of operating parameters. The behaviour observed as a function of salt concentration, temperature, and flow rate highlights the notable flexibility of the system and its potential scalability. The operating conditions identified therefore provide a solid basis for a direct comparison with the traditional Ti–Fe system in sulfuric acid and for a subsequent evaluation of the material and operating costs of both approaches, topics that will be addressed in Chapter 5.

5 Comparative Assessment of Sulfate-Based and EDTA-Complexed Electrolytes for Ti–Fe Redox Flow Batteries

The experimental work presented in the previous chapters investigated two fundamentally different approaches for stabilizing and operating the Ti–Fe redox couple in aqueous redox flow batteries: a conventional sulfuric-acid-based electrolyte, relying on the intrinsic chemistry of Ti(III)/Ti(IV) and Fe(II)/Fe(III) sulfate species, and a fully coordination-complex-based electrolyte, in which titanium and iron are stabilized through chelation with EDTA ligands. The comprehensive electrochemical, chemical, and operational analysis conducted in Chapters 3 and 4 demonstrated that these two systems differ not only in their redox behaviour, stability, and conductivity, but also in their compatibility with common cell components and, ultimately, in their economic feasibility for large-scale applications. Given the substantial differences between the two electrolyte families, a comparative evaluation becomes essential in order to contextualize the advantages and limitations of each chemistry within the broader framework of redox flow battery development. While the sulfuric acid system offers high ionic conductivity and fast reaction kinetics, it suffers from strong corrosiveness, severe material degradation, and stringent operational constraints. Conversely, the EDTA-complexed system provides a chemically mild environment and high stability of the active species, but at the expense of reduced conductivity and slower electron-transfer kinetics, particularly for the Ti(IV)/Ti(III) couple. The purpose of this chapter is therefore to present a concise yet comprehensive comparison between the two chemistries, integrating chemical, electrochemical, operational, and economic aspects. The analysis builds directly upon the experimental results already discussed, without repeating detailed data, and seeks instead to highlight the key performance indicators that determine the practical feasibility of each system. Particular emphasis is placed on:

- the stability and redox behaviour of titanium and iron species under the two chemistries,
- the resulting cell voltage, efficiencies, and operational limitations,
- the ionic conductivity and its impact on voltage efficiency at various current densities,
- the compatibility of electrolytes with commonly used materials in RFB construction,
- the cost implications, including both electrolyte components and cell hardware.

By synthesizing these elements into a unified comparative framework, this chapter aims to elucidate the relative merits and constraints of sulfate-based and EDTA-complexed electrolytes, providing a critical foundation for the final conclusions and future development pathways discussed in Chapter 6.

5.1 Chemical and Electrochemical Comparison Between Sulfate-Based and EDTA-Complexed Electrolytes

The comparison between sulfate-based electrolytes and EDTA-complexed electrolytes highlights substantial differences in speciation, stability, and electrochemical behavior of the Ti(IV)/Ti(III) and Fe(III)/Fe(II) redox couples, representing a key element in evaluating the two chemistries for redox flow battery applications. In

the sulfuric-acid system, both metal species are extremely stable under the highly acidic conditions employed in this work (pH < 1.5), where Ti(IV) is present as TiO^{2+} or Ti–sulfate species fully soluble in solution [166], [177]. Within this pH range, the risk of hydrolysis is negligible and the electrolytes remain clear and stable over time. Similarly, the Fe(III)/Fe(II) couple exhibits very high stability in strongly acidic media, with no evidence of precipitation or significant changes in speciation [93]. From an electrochemical standpoint, the Ti(IV)/Ti(III) couple displays relatively favorable kinetics in the sulfate environment, further enhanced by catalytic promoters such as bismuth, which lower the anodic overpotential and enable a quasi-reversible behavior [147].

In the EDTA-complexed system, the stability of the metal species is not governed by extreme acidity but rather by the formation of highly robust chelated structures. The Ti–EDTA complex is stable in the pH range 4.0–6.35, while Fe–EDTA remains stable between pH 4.6 and 6.3, yielding clear, hydrolysis-free solutions [144], [146], [160]. The hexadentate coordination of EDTA fully saturates the Ti(IV) coordination sphere and effectively stabilizes the reduced Ti(III) form, preventing any precipitation processes. This high stability arises from strong enthalpic contributions associated with multiple Ti–O and Ti–N bonds, combined with the entropic advantage of the chelate effect [166]. Ligand coordination also induces a marked shift in redox potentials. In the case of Ti–EDTA, the enhanced stabilization of the reduced Ti(III) state results in a significantly more negative formal potential compared to the sulfate system, consistent with coordination-chemistry principles based on differential stabilization of redox states [136]. For iron, the shift is less pronounced but still measurable, and the Fe(III)/Fe(II) couple retains a highly regular and reproducible electrochemical behavior. Reversibility differs distinctly between the two systems: in sulfuric acid, the Ti(IV)/Ti(III) couple can approach quasi-reversible behavior through bismuth catalysis, whereas in the EDTA system the titanium process is slower and limited in reversibility, especially at higher scan rates. Conversely, Fe–EDTA maintains fast kinetics and near-reversible behavior, confirming its high stability under variable operating conditions [178]. The main differences between the two electrolyte families are summarized in Table 5.1.

Table 5.1: Chemical and Electrochemical Comparison of Sulfate-Based and EDTA-Complexed Electrolytes

Parameter	Sulfate system (Ti–Fe)	EDTA-complexed system (Ti–EDTA / Fe–EDTA)
Stable pH range	0.3 – 1.5	4.0 – 6.3
Ti(IV)/ Ti(III) stability	excellent in highly acidic	high, stabilized by chelation
Fe(III)/Fe(II) stability	very high	very high with EDTA
Tendency to precipitation	none under operating conditions	none
Ti reversibility	quasi-reversible with Bi	slow kinetics, limited reversibility
Fe reversibility	good	near-reversible, fast kinetics

Overall, the chemical and electrochemical comparison between the two systems highlights two fundamentally different approaches. The sulfuric-acid electrolyte, under strongly acidic operating conditions, provides excellent metal-species stability and favorable redox kinetics, although it requires the use of materials with high corrosion resistance. In contrast, the EDTA-complexed electrolyte operates in a significantly milder environment and offers exceptional complex stability and safer handling, together with broader compatibility

with less expensive materials. However, the stronger stabilization of the reduced titanium state results in slower kinetics and a lower theoretical cell voltage compared to the sulfate system. These differences form the foundation for interpreting the battery performance observed in single-cell tests, which will be discussed in detail in the following sections.

5.2 Ionic Conductivity

The ionic conductivity of the electrolyte represents one of the most critical parameters governing the internal resistance of the cell and, consequently, the ability of the system to sustain high current densities without significant electrochemical penalties. Ionic transport depends not only on the concentration of charged species, but also on their mobility, transport numbers, and the interactions between ions, solvent, and membrane. The differences between the sulfate-based electrolyte and the EDTA-complexed electrolyte therefore emerge very clearly, as the two systems rely on fundamentally different transport mechanisms.

In the sulfuric-acid system, the presence of a fully dissociated strong acid such as H_2SO_4 generates a highly protonic medium rich in H^+ and SO_4^{2-} ions. In particular, H^+ ions exhibit exceptionally high mobility due to the Grotthuss mechanism, a concerted proton-transfer process occurring along the hydrogen-bond network of water [179]. As a consequence, the proton transport number is very high, meaning that a large fraction of the total current is carried almost exclusively by H^+, which acts as the primary charge carrier. This results in an electrolyte with intrinsically high conductivity, low ohmic resistance, and minimal iR-drop even at elevated current densities. The low viscosity of the medium and the high diffusion coefficients of ionic species further facilitates mass transport, ensuring uniform current distribution within the graphite felt and minimizing local potential gradients. From the membrane standpoint, the behavior is equally favorable: Nafion is specifically designed to facilitate selective proton transport through its perfluoro sulfonic channels, providing highly efficient ionic conduction and extremely low membrane resistance [180], [181]. Under these circumstances, among all acidic electrolytes tested, 1 M H_2SO_4 proved to be the most balanced configuration, providing high conductivity, excellent chemical stability, and limited overpotentials, whereas higher concentrations offered no additional benefit and lower concentrations significantly reduced ionic conductivity.

In contrast, the EDTA-complexed system, the situation is fundamentally different. The intrinsic conductivity of the solution is significantly lower because most of the charge is carried by large, poorly mobile anionic complexes such as $[Ti(EDTA)]^-$ and $[Fe(EDTA)]^-$. Their transport numbers are very small, and their limited mobility contributes to increased internal resistance. Moreover, the absence of protons removes the highly efficient protonic contribution to ionic transport. To mitigate this limitation, the supporting electrolyte KCl is added to increase the concentration of mobile ions such as K^+ and Cl^-. Even in this case, however, the transport number of alkali cations remains substantially lower than that of protons in strongly acidic media [49], and the overall conductivity, although improved, remains significantly inferior to that of the sulfate system. Increasing ionic strength also raises the viscosity of the solution and decreases the diffusivity of the active species, further contributing to diffusive resistance. The interaction with the membrane amplifies these differences even further. In the EDTA system, Nafion does not transport protons but instead conducts K^+ ions, which cross the

membrane with lower mobility and higher resistance [49], [180]. In this work, it was observed that 1 M KCl represents the most favorable condition for the EDTA-based electrolytes, providing the best compromise between enhanced conductivity and chemical stability. The 2 M KCl condition, although stable at rest, led to the formation of a visible precipitate in the catholyte reservoir during battery cycling, indicating that elevated ionic strength and increased viscosity can destabilize the Fe–EDTA complex under dynamic operating conditions. At even higher concentrations, the phenomena become more pronounced: Fe–EDTA precipitates at 3 M KCl, while Ti–EDTA exhibits opalescence at 4 M KCl, clearly indicating the onset of aggregation processes and a loss of colloidal stability.

The differences between the two chemistries become particularly evident when analyzing the electrochemical impedance spectroscopy (EIS) data. Figure 5.1 presents a direct comparison between the spectra obtained for the Ti–EDTA/Fe–EDTA system in 1 M KCl (main plot) and for the Ti–Fe system in 1 M H_2SO_4 (inset Figure 3.29).

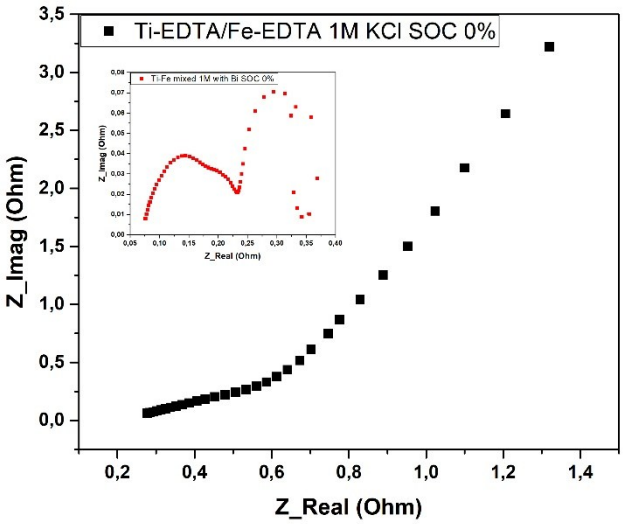


Figure 5.1: EIS spectra at 0% SOC for the Ti–EDTA/Fe–EDTA system in 1 M KCl (main diagram black) and for the Ti–Fe system in 1 M H_2SO_4 (inset red).

The intercept on the real axis, corresponding to the ohmic resistance RΩ, is significantly higher for the EDTA-based electrolyte, confirming its lower ionic conductivity and higher membrane resistance. The large semicircle observed for the EDTA system corresponds to the charge-transfer resistance (R_{ct}) associated with the slow Ti(IV)/Ti(III) kinetics. Its pronounced width indicates a substantial kinetic barrier and a less reactive electrode–electrolyte interface. The inclined low-frequency tail (Warburg-like behavior) further suggests limited mass transport, consistent with the higher viscosity of the solution and the lower mobility of the complexed species. In contrast, the inset showing the sulfuric-acid electrolyte reveals an extremely small ohmic resistance, with an intercept near zero and a very narrow semicircle, indicative of highly favorable charge-transfer kinetics. The absence of a pronounced diffusive tail reflects excellent transport conditions

resulting from high proton mobility, low viscosity, and efficient membrane conduction. Overall, the comparison of the EIS spectra experimentally confirms the theoretical considerations outlined above: the EDTA-based electrolyte exhibits a substantially higher global resistance (ohmic + kinetic + diffusive), while 1 M H_2SO_4 and 1 M KCl clearly emerge as the optimal configurations for the two systems. Taken together, these results demonstrate that ionic conductivity and internal resistance constitute the primary discriminating factors between the two chemistries: the sulfuric-acid electrolyte benefits from highly favorable proton transport and excellent membrane compatibility, whereas the EDTA-based electrolyte, although chemically stable and non-corrosive, is hindered by lower ionic mobility, higher viscosity, greater charge-transfer resistance, and limited stability at high ionic strengths. These differences represent the physical basis responsible for the distinct cell efficiencies of the two systems, as discussed in the following section.

5.3 Short-Run Comparison of Sulfuric Acid and EDTA-Based Ti–Fe Batteries

The comparison between the Ti–Fe system in sulfuric acid and the configuration based on Ti–EDTA and Fe–EDTA complexes, analysed through short-run tests at different current densities, highlights in a clear and systematic way the reasons why the two chemistries exhibit profoundly different electrochemical and operational behaviour. As discussed in the previous sections, the nature of the electrolyte critically influences not only ionic conductivity, but also the stability of the redox-active species, the kinetics of electron-transfer reactions, and the overall internal resistance of the cell. In the case of the sulfuric-acid system, the best performance was obtained using the mixed configuration with 1 M Ti and 1 M Fe in H_2SO_4, which represents the condition where conductivity, kinetic response, and ohmic resistance are most effectively balanced. The strongly protonic environment provided by sulfuric acid enables extremely efficient ionic transport, dominated by proton mobility through the Grotthuss mechanism [179], while simultaneously ensuring high solubility and stability of the Ti(IV)/Ti(III) and Fe(III)/Fe(II) redox couples through the formation of highly soluble sulfate complexes [89], [134]. The addition of bismuth, as reported by Knehr et al. and other authors, further improves the reversibility of the Ti(IV)/Ti(III) couple by reducing the anodic overpotential and promoting quasi-reversible behaviour even at high current densities [72], [123]. Moreover, the high concentration of active species in the mixed configuration reduces ohmic resistance and favours more homogeneous current distribution throughout the porosity of the graphite felt. The combination of these factors explains why, as shown in the comparative efficiency plot, the battery in H_2SO_4 maintains high VE and EE values across the entire current-density range, with only moderate losses as current increases.

The behaviour of the EDTA-complexed system is instead governed by a different set of limitations, primarily related to the nature of the metal–ligand complexes and the absence of an efficient protonic conductor. Since both $[Ti(EDTA)]^-$ and $[Fe(EDTA)]^-$ are large anionic complexes, their mobility in solution is intrinsically low, and the overall ionic conductivity of the electrolyte is strongly dependent on the presence of the supporting electrolyte KCl. For this reason, a systematic conductivity analysis as a function of KCl concentration was carried out prior to battery testing, revealing that increasing ionic strength indeed enhances ionic transport, but also affects the stability of the complexes, particularly in the case of Fe–EDTA. Literature reports have

demonstrated that increasing ionic strength via KCl or NaCl significantly reduces the solubility of ferric species, promoting salting-out phenomena and the formation of poorly soluble hydroxide or chloride-associated species. Consistent with the behaviour described by Liu and Millero for ferric systems in saline solutions [170], preliminary cell tests showed that the configuration containing 2 M KCl resulted in the formation of a precipitate in the anolyte reservoir after cycling, indicating that high ionic strength destabilizes the ferric complex under dynamic operating conditions. Consequently, the configuration selected as the reference for direct comparison with the sulfuric-acid system was the solution containing 1 M KCl, which provides the best compromise between increased conductivity and preservation of chemical stability for both Ti–EDTA and Fe–EDTA, preventing precipitation and ensuring a reproducible electrochemical response.

The direct comparison of short-run performance, carried out specifically between the Ti–Fe system in sulfuric acid (optimal mixed condition: 1 M Ti + 1 M Fe) and the Ti–EDTA/Fe–EDTA system in 1 M KCl, is summarised in Figure 5.2, which reports the trends of the three fundamental cell efficiencies, coulombic efficiency (CE), voltage efficiency (VE), and energy efficiency (EE), as a function of the applied current density.

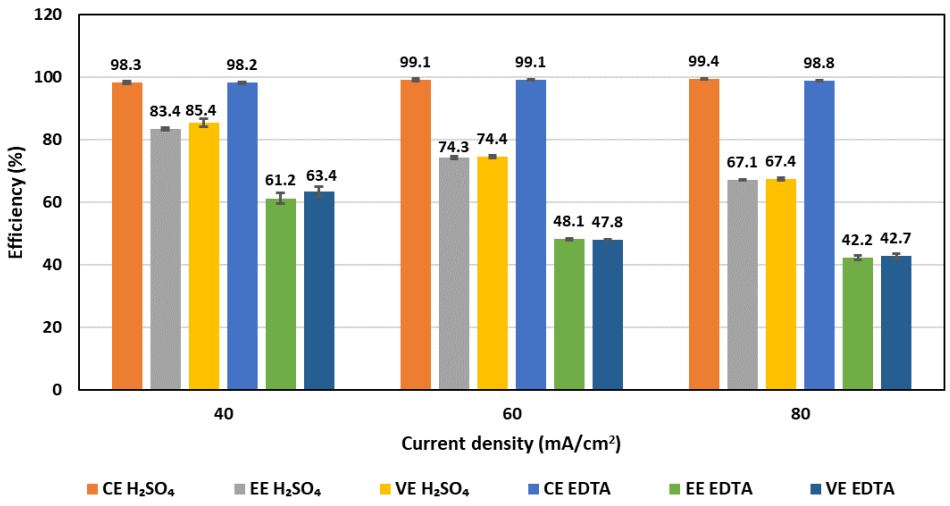


Figure 5.2: Comparison of the coulombic (CE), voltage (VE) and energy (EE) efficiencies of the Ti–Fe system in H_2SO_4 (1 M, mixed electrolyte) and of the Ti–EDTA/Fe–EDTA system in 1 M KCl under the three current density conditions (40, 60 and 80 mA cm^{-2}).

A joint analysis of the plot shows first of all that CE remains very high across all experiments (>98%), confirming the absence of significant crossover or unwanted side reactions in either system. This indicates that the performance gap between the two configurations does not originate from redox instability, but rather from the different ionic-transport mechanisms and resistive phenomena intrinsic to the two electrolytes. The most pronounced differences appear in VE: the sulfuric-acid system exhibits values of ~85% at 40 mA cm^{-2}, ~74% at 60 mA cm^{-2}, and ~67% at 80 mA cm^{-2}, whereas the EDTA-based system reaches ~63%, ~48%, and ~42% under the same conditions. This marked loss in performance reflects the highly resistive nature of the complexed electrolyte, where the absence of protonic conduction and the need to rely on monovalent cations (K^+), which possess much lower diffusional mobility compared to protons, lead to significant ohmic drops.

The low mobility of the anionic complexes further increases internal resistance and amplifies polarisation, especially at higher current densities. EE naturally follows the same trend, with the EDTA system showing a deficit of approximately 20–25 percentage points relative to the sulfuric-acid system across the entire investigated range. A deeper examination of the histogram also reveals that the performance gap widens non-linearly with increasing current density: whereas ohmic losses rise moderately in H_2SO_4, they increase more steeply in the EDTA system. This suggests that the internal resistance of the complexed electrolyte is not constant, but strongly influenced by the limited diffusivity of the active species and the accumulation of concentration gradients within the electrode structure. This behaviour is consistent with the known sluggish kinetics of the Ti(IV)/Ti(III) complexed couple, widely reported in coordination-chemistry studies [182], which becomes the limiting factor at high currents, further increasing anodic overpotential and reducing VE. In contrast, the sulfuric-acid system benefits from the presence of bismuth, higher ionic mobility, and lower viscosity, which work together to contain polarisation within more favourable limits. Overall, the analysis of Figure 5.2 clearly demonstrates that the sulfuric-acid system is intrinsically superior under short-run cycling due to its exceptionally high protonic conductivity, fast redox kinetics, and low membrane-transport resistance. The EDTA-based system, although penalised in terms of energetic efficiency, offers significant advantages in chemical stability, operational safety, and absence of corrosive phenomena. These characteristics make the EDTA chemistry a promising platform for future developments aimed at sustainability and cost reduction, particularly in combination with strategies designed to enhance ionic transport and anodic reaction kinetics.

5.4 Long-run Comparison Between H_2SO_4 and EDTA Systems

The comparison between the Ti–Fe chemistry in sulfuric acid and the configuration based on Ti–EDTA and Fe–EDTA complexes can be further deepened by analysing the behaviour of the cell during extended cycling (long-run tests), where operational stability and the ability to maintain constant efficiency values over time become critical parameters for assessing long-term reliability. In this case too, the comparison was carried out between the optimal configuration of the Ti–Fe system in H_2SO_4 (mixed 1 M Ti + 1 M Fe) and the Ti–EDTA/Fe–EDTA formulation in 1 M KCl. It is, however, essential to emphasise from the outset a critical experimental difference: the sulfuric-acid system was able to operate stably at 80 mA cm^{-2}, whereas the EDTA-complexed battery could only be tested at 40 mA cm^{-2}, since higher current densities caused a pronounced increase in polarisation and operational instability. This difference is not a mere experimental detail but represents direct evidence of the kinetic and resistive limitations of the EDTA chemistry compared with its sulfuric-acid analogue. The evolution of efficiencies over the 100 cycles is shown in Figure 5.3, which reports the trends of coulombic efficiency (CE), voltage efficiency (VE), and energy efficiency (EE) for both chemistries.

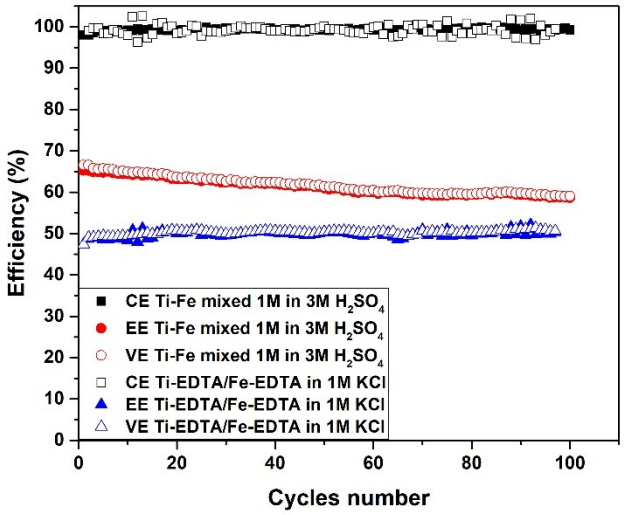


Figure 5.3: Trends of the coulombic (CE), voltage (VE) and energy (EE) efficiencies during 100 cycles for the Ti–Fe system in H_2SO_4 (1 M Ti + 1 M Fe, mixed electrolyte) cycled at 80 mA cm^{-2} and for the Ti–EDTA/Fe–EDTA system in 1 M KCl cycled at 40 mA cm^{-2}.

In the case of the Ti–Fe battery in H_2SO_4, CE remains consistently close to 100% throughout the test, confirming the high redox stability of the Ti(IV)/Ti(III) and Fe(III)/Fe(II) couples in sulfuric acid and the absence of crossover phenomena even under highly demanding electrochemical conditions, further intensified by the use of 80 mA cm^{-2}. VE, although showing a gradual decline as cycling progresses, remains higher than that of the EDTA system, while EE mirrors the same trend, displaying an overall moderate loss over time. For the Ti–EDTA/Fe–EDTA system, CE also remains high and close to 100%, confirming that EDTA chemistry is not limited by redox instability; however, VE and EE start from significantly lower values and exhibit a more pronounced decline during cycling, in line with the higher internal resistance, lower ionic mobility, and slower kinetics of the Ti(IV)/Ti(III) complexed couple.

A more comprehensive evaluation emerges from the analysis of discharge-capacity evolution, shown in Figure 5.4, which reports the capacity retention expressed as a percentage relative to the initial cycle.

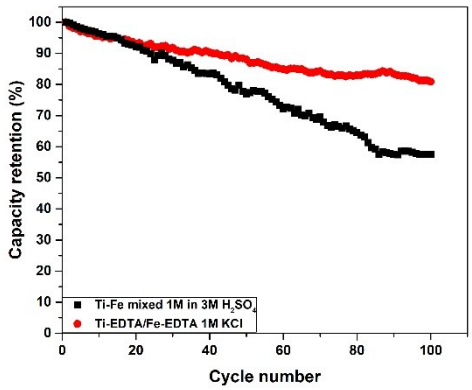


Figure 5.4: Capacity retention during 100 cycles for the Ti–Fe system in H_2SO_4 (1 M Ti + 1 M Fe, mixed electrolyte) cycled at 80 mA cm^{-2} and for the Ti–EDTA/Fe–EDTA system in 1 M KCl cycled at 40 mA cm^{-2}.

In this respect, the Ti–EDTA/Fe–EDTA system displays a slower and more gradual capacity fade compared with the Ti–Fe battery in H_2SO_4. However, it is crucial to underline that this apparent increased stability must not be interpreted as an intrinsic advantage of EDTA chemistry: it is directly related to the different operating conditions. Indeed, the EDTA battery is cycled at 40 mA cm^{-2}, whereas the sulfuric-acid battery operates at 80 mA cm^{-2}, i.e., at double the current density. This difference implies that the complexed system experiences significantly lower electrochemical stress, a condition that naturally mitigates degradation processes, suppresses the formation of concentration gradients, and reduces the accumulation of polarisation within the felt. Conversely, the system in H_2SO_4, forced to operate at higher currents, shows a more rapid capacity decline, likely linked to the greater stress imposed by the strongly acidic environment on the cell components and to the faster onset of structural degradation phenomena.

Overall, the analysis of long-run tests highlights how the two chemistries exhibit complementary behaviours: the Ti–Fe system in sulfuric acid provides superior energetic performance and a greater ability to withstand aggressive operating conditions, although at the expense of a faster capacity decay; the Ti–EDTA/Fe–EDTA system, despite showing lower efficiencies and limited tolerance to high current densities, displays a more gradual capacity fade and enhanced operational stability, thanks to the chemically mild environment of the complexed electrolyte. Taken together, these results confirm that long-term performance and durability depend not only on redox chemistry but on a complex interplay between kinetics, ionic transport, and operating conditions.

5.5 Comparative analysis of different electrolyte configurations

To provide a clear and comparative overview of the experimental results obtained, Table 5.2 summarizes in a systematic manner the average values of coulombic efficiency (CE), energy efficiency (EE), voltage efficiency (VE), and capacity retention after 100 cycles for all the electrolyte configurations investigated. The table also includes a qualitative analysis of the main advantages and limitations of each formulation, allowing for a direct comparison between the performance of the two chemistries under study

Table 5.2: Coulombic efficiency (CE), energy efficiency (EE), and voltage efficiency (VE) of Ti–Fe batteries in 3 M H_2SO_4 for different electrolyte configurations and current densities. Values are reported as the average of cycles 2 to 6, excluding the first cycle and followed by the relative standard deviation, including efficiencies, capacity retention, and key advantages and limitations.

Complexing Agent	Anolyte	Catholyte	Temperature	Current density	CE	EE	VE	Capacity retention 100 cycles	Pros / Cons
			[°C]	[mA/cm^2]	%	%	%	%	
H_2SO_4	1 M Ti + 1 M Fe	1 M Ti + 1 M Fe	25	40	98.3 ± 0.4	83.4 ± 0.4	85 ± 1	~ 57	High efficiency Poor capacity retention Corrosive electrolyte
				60	99.1 ± 0.5	74 ± 2	74 ± 2		
				80	99.4 ± 0.2	67.0 ± 0.4	67.4 ± 0.5		
	0.5 M Ti + 0.5 M Fe	0.5 M Ti + 0.5 M Fe	25	40	99.0 ± 0.1	76 ± 1	80 ± 1	~ 60	Moderate efficiency Poor capacity retention Corrosive electrolyte
				60	99.2 ± 0.3	65.8 ± 0.6	67.8 ± 0.6		
				80	99.2 ± 0.4	58.6 ± 0.9	59.1 ± 0.9		
	1 M Ti	1 M Fe	25	40	98 ± 2	68 ± 1.5	74 ± 3	~ 80	Improved capacity retention Low energy efficiency Corrosive electrolyte
				60	98.2 ± 0.8	47.9 ± 0.6	48.3 ± 0.6		
				80	99 ± 1.5	43 ± 1	43.8 ± 0.5		
EDTA	0.5 M Ti	0.5 M Fe	25	40	98.2 ± 0.2	61 ± 2	63 ± 2	~ 85	Mild electrolyte Improved capacity retention Low energy efficiency Low energy density
				60	99.1 ± 0.1	48.1 ± 0.3	47.8 ± 0.1		
				80	98.8 ± 0.2	42.2 ± 0.8	42.7 ± 0.8		
			65	40	99.5 ± 0.8	73.9 ± 0.6	74.1 ± 0.7	-	Mild electrolyte Improved energy efficiency Long-term stability remains to be validated
				60	99.1 ± 0.1	76.1 ± 0.8	76.8 ± 0.8		
				80	99.2 ± 0.1	75.3 ± 0.2	75.9 ± 0.2		

A broader and more comprehensive comparison among the different electrolyte formulations can be achieved by analysing Table 5.2, which immediately highlights the most significant differences between strongly protonic electrolytes and complexed systems. The table shows that CE remains high and nearly unchanged under all operating conditions, confirming the excellent redox stability of the Ti(IV)/Ti(III) and Fe(III)/Fe(II) couples regardless of the electrolyte medium. In contrast, parameters more sensitive to internal resistance, such as EE and VE, display a strong dependence on the nature of the electrolyte: H_2SO_4-based formulations exhibit markedly higher values, especially at higher current densities, consistent with the higher protonic conductivity, the more favourable electron-transfer kinetics, and the lower resistive contribution of the sulfuric medium. However, these superior performance metrics are accompanied by reduced capacity stability, with a retention of approximately 60% after 100 cycles, reflecting the corrosive impact of the acidic environment on the cell materials. The Ti–EDTA/Fe–EDTA system, on the other hand, shows lower EE and VE values, attributable to its higher internal resistance and the limited mobility of the complexed species, but ensures better long-term capacity retention, with values close to 85% after 100 cycles, owing to the non-corrosive and chemically mild nature of the electrolyte. The "Pros/Cons" section of the table further reinforces this distinction: while H_2SO_4 enables the highest absolute performance, it is characterised by greater corrosivity and lower cycling stability; conversely, the EDTA-based electrolyte emerges as a mild, more durable system, compatible with lower-cost materials. This comprehensive overview complements the analysis of the short-run and long-run experiments and provides the ideal basis for introducing the evaluation of active-material costs, which is addressed in the following paragraph.

5.6 Comparison of active material costs

One of the most relevant aspects in the comparative evaluation of different redox flow battery chemistries is undoubtedly the analysis of the active-material costs. Unlike solid-state batteries, where the cost is distributed among the cathode, anode, separators, and conductive additives, in redox flow batteries the cost of the electrolyte represents a significant portion of the overall investment and directly affects the final cost per stored kWh, especially for large-scale stationary applications where competitiveness is driven more by the energy cost than by the power cost. Recent literature increasingly highlights that the cost of the active materials and the cost of the membrane constitute two fundamental pillars in the economic assessment of emerging RFB technologies, together with cell voltage and electrolyte stability [183], [184]. This holistic approach is essential because electrochemical performance, however promising, is not sufficient unless supported by a sustainable economic framework. For example, in the case of VRFBs, the main limitation is not technical but economic, with the fluctuating price of vanadium driving electrolyte costs above 150–180 $/kWh [183]. In this context, systems based on earth-abundant, low-cost elements such as titanium and iron represent an attractive alternative, but their true economic advantage depends on the way these species are formulated and complexed. Cost analysis therefore complements and gives full meaning to the performance comparison discussed in the

previous sections. The cost of the active materials was estimated using a commonly adopted electrochemical approach based on the following equation 2.3:

$$C = \frac{PM}{nFE} \qquad \text{Eq. 5.1}$$

In this equation, C represents the cost of the active material per unit of stored energy and is expressed in $/kWh. The variable P is the price of the active material in $/kg, M is the molar mass of the active species in g/mol. (since M is expressed in g/mol and P in $/kg, a conversion factor of 1000 is applied in the formula), n indicates the number of electrons transferred in the redox reaction in mol, F is the Faraday constant (96485 C/mol) and E is the cell voltage in volts (V) [185].
The bar chart in Figure 5.5 reports the calculated costs for the different systems.

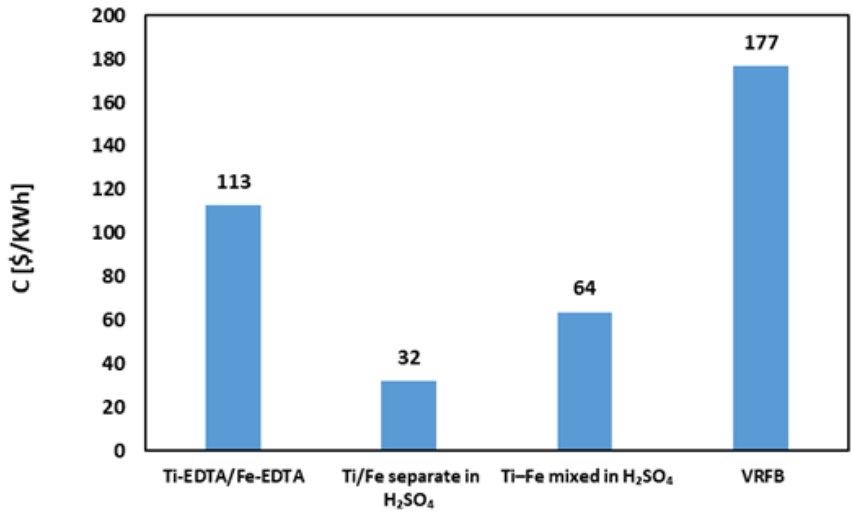


Figure 5.5: Comparison of active material costs for Ti–EDTA/Fe–EDTA, Ti–Fe in H_2SO_4, and VRFB, based on theoretical energy output.

The Ti–EDTA/Fe–EDTA system shows a cost of 113 $/kWh, whereas the H_2SO_4-based formulations are significantly cheaper, amounting to 32 $/kWh (separated Ti/Fe solutions) and 64 $/kWh (mixed). For comparison, a conventional VRFB reaches approximately 177 $/kWh, in full agreement with the values reported in the literature [107], [183]. The cost difference between the EDTA and sulfuric-acid systems arises from several electrochemical and economic factors. First, the cell voltage plays a crucial role: the sulfuric-acid system operates at approximately 0.67 V, whereas the EDTA-based system operates at around 0.44 V. Since voltage appears in the denominator of the cost equation, a lower voltage implies a greater amount of active material required to store the same quantity of energy, thereby increasing the specific cost of the EDTA system. A second contribution comes from the higher cost of EDTA relative to simple metal sulfates, along with the increased molar mass of the complexed species, which further increases the term M, directly raising the electrolyte cost; similar trends have been observed in hybrid and organic complex-based systems [185]. Another economically crucial but often overlooked aspect concerns membrane cost: sulfuric-acid RFBs require

high-selectivity membranes such as Nafion, whose cost can reach 650 $/m² [184], and several comparative studies show that membrane price is one of the major economic limitations of VRFB systems [183]. In contrast, the Ti–EDTA/Fe–EDTA system, operating in a chemically mild and non-corrosive environment, allows the use of low-cost porous membranes such as PVDF-HFP, priced below 10 $/m², about 1.5% of the cost of Nafion [107], leading to a dramatic reduction in stack and maintenance costs. Likewise, the non-corrosive nature of the EDTA electrolyte significantly mitigates material degradation, as documented in Fe–Pb systems and porous nonionic membranes [107] , whereas sulfuric acid accelerates corrosion and wear, requiring more expensive components and more frequent replacements. Integrating performance results with the economic analysis highlights a decisive point: the Ti–Fe mixed 1 M system in H_2SO_4 is not only the most economical among those analysed, but also the best performing, exhibiting the highest VE and EE in short-run tests, excellent long-run efficiency stability, and the unique ability to operate at 80 mA cm^{-2}, thus maximising the delivered energy per unit of active material. Conversely, although the Ti–EDTA/Fe–EDTA system offers advantages in terms of safety, chemical stability, compatibility with low-cost membranes, and reduced corrosivity, it remains penalised by a lower cell voltage, slower kinetics, and the need to operate at half the current density, resulting in a higher overall energy cost and lower electrochemical performance. Therefore, the EDTA chemistry is not yet able to compensate for its performance disadvantage relative to the sulfuric-acid system, making it economically less favourable when considering the actual cost per usable kWh. In conclusion, the Ti–Fe mixed 1 M system in H_2SO_4 stands out as the most competitive solution for large-scale energy storage applications, whereas the Ti–EDTA/Fe–EDTA system represents a valuable alternative in scenarios prioritising safety, material compatibility, and reduced maintenance costs; nevertheless, future developments aimed at increasing cell voltage and improving ionic mobility could significantly narrow the current techno-economic gap.

Conclusions

The work presented in this thesis has enabled a comprehensive and coherent analysis of the chemical and electrochemical behavior of the Ti–Fe system for redox flow battery applications, clearly illustrating how species stability, electron-transfer kinetics, and the mutual interaction between the active redox couples determine the overall efficiency and durability of the cell under realistic operating conditions. The initial part devoted to the sulfuric-acid system demonstrated that Ti(IV) stability requires strongly acidic environments to prevent hydrolysis phenomena, conditions that are essential from a chemical standpoint but intrinsically responsible for the corrosiveness of the medium. Nonetheless, voltammetric characterization and cell-level tests revealed that the mixed Ti–Fe configuration in 1 M sulfuric acid represents the most balanced and functional condition, where the simultaneous presence of both redox couples in the two compartments eliminates crossover-induced imbalances and renders the system intrinsically chemically stable. Although the $Ti^{3+} \rightarrow TiO^{2+}$ oxidation process is inherently sluggish and associated with significant anodic polarization, the introduction of Bi^{3+} as a catalytic promoter effectively overcame these limitations: the in-situ deposition of

metallic Bi onto the carbon felt significantly reduced the charge-transfer resistance, stabilized the electrode surface, and markedly improved the reversibility of the anodic reaction. This resulted in a substantial decrease in overpotentials and the achievement of coulombic efficiencies close to 99%, with voltage and energy efficiencies that reached approximately 84% and 82%, respectively, at 40 mA cm^{-2}. Particularly noteworthy are the long-term results obtained at 80 mA cm^{-2}, where the Ti–Fe 1 M system with bismuth retained more than 50% of its discharge capacity after 100 cycles, in stark contrast with the rapid degradation observed in the catalyst-free configuration. Comparative analysis of mixed, diluted, and separated electrolytes further confirmed that only the mixed-electrolyte configuration—thanks to its intrinsic self-balancing nature—can maintain stable and efficient operation, avoiding the chemical imbalances clearly detected in the separated configuration through TXRF analysis. Altogether, these findings demonstrate that the Ti–Fe mixed electrolyte in 1 M H_2SO_4 with bismuth constitutes one of the most credible and concrete alternatives to vanadium redox flow batteries, offering high electrochemical performance while relying on widely available elements, drastically reduced active-material costs, and compatibility with cost-effective cell components. The second part of the thesis focused on reducing electrolyte corrosiveness through the use of fully complexed systems. The systematic study of Ti–bpy, Ti–HEDP, and especially Ti–EDTA revealed how ligand coordination profoundly impacts the stability and redox properties of titanium. Among the complexes examined, Ti–EDTA and Fe–EDTA proved to be the most stable and best suited for the development of a fully complexed battery. The Ti–EDTA/Fe–EDTA system exhibited excellent chemical stability within their respective pH windows (4–6.35 for Ti–EDTA and 4.6–6.3 for Fe–EDTA), coulombic efficiencies consistently around 99%, and highly reproducible voltammetric behavior, although penalized relative to the sulfuric-acid system by the slower kinetics of the Ti(IV)/Ti(III) couple. Operational parameters such as temperature and flow rate were shown to play a decisive role in improving the performance of the EDTA-based system: increasing the temperature resulted in significant enhancements in voltage and energy efficiencies, particularly at high current density, confirming the diffusional nature of the kinetic limitation; similarly, higher flow rates reduced ohmic and mass-transport losses, stabilizing the cell's electrochemical behavior. Even though the Ti–EDTA/Fe–EDTA system is extremely promising from the standpoint of chemical safety, material compatibility, and reduced aggressiveness, further optimization is required before it can achieve performance levels comparable to those of the catalyzed sulfuric-acid system, especially in relation to the anodic titanium kinetics and ion-transport processes. Overall, the experimental work conducted in this thesis demonstrates that the Ti–Fe chemistry provides a highly competitive platform for large-scale energy storage. On one hand, the mixed Ti–Fe system in 1 M sulfuric acid with bismuth already stands out as one of the few metal-based chemistries capable of approaching, and in some contexts matching, the performance of vanadium redox flow batteries, while benefiting from significantly lower material costs and greater elemental abundance. On the other hand, the fully complexed Ti–EDTA/Fe–EDTA system represents an emerging, safe, and potentially scalable alternative, whose competitiveness will grow through future improvements to the titanium electron-transfer kinetics and ionic-transport optimization. The dual outcome of this study—an acid-based chemistry already capable of high-performance operation and a fully complexed chemistry offering a safer and more sustainable

framework represents the key contribution of this thesis to the development of next-generation flow batteries based on abundant, low-cost and environmentally sustainable elements.

[1] “World Energy Outlook 2020,” Paris, 2020. Accessed: Oct. 01, 2025. Available: https://www.iea.org/reports/world-energy-outlook-2020

[2] European Environment Agency, “Trends and Projections in Europe 2020,” Copenhagen, 2020. Accessed: Oct. 01, 2025. Available: https://www.eea.europa.eu/publications/trends-and-projections-in-europe-2020

[3] REN21, “Renewables 2023 Global Status Report,” Paris, 2023. Accessed: Oct. 01, 2025. Available: https://www.ren21.net/reports/global-status-report/

[4] International Energy Agency, “Energy Storage Tracking Report 2023,” 2023. Accessed: Oct. 01, 2025. Available: https://www.iea.org/reports/energy-storage

[5] Terna S.p.A., “Dati statistici 2023,” 2023. Accessed: Oct. 01, 2025. Available: https://www.terna.it/it/sistema-elettrico/statistiche

[6] International Energy Agency, “CO 2 Emissions in 2023,” 2023. Available: www.iea.org

[7] Global Carbon Project, “CO_2 Emissions Through Time,” 2023. Accessed: Oct. 02, 2025. Available: https://www.visualcapitalist.com/co2-emissions-by-country-over-time/

[8] Intergovernmental Panel on Climate Change (IPCC), “Climate Change 2021: The Physical Science Basis. Sixth Assessment Report,” 2021. Accessed: Oct. 02, 2025. Available: https://www.ipcc.ch/report/ar6/wg1/

[9] United Nations Framework Convention on Climate Change (UNFCCC), “The Paris Agreement,” 2015. Accessed: Oct. 02, 2025. Available: https://unfccc.int/process-and-meetings/the-paris-agreement

[10] European Commission, “Fit for 55: Delivering the EU’s 2030 Climate Target on the way to climate neutrality,” 2021. Accessed: Oct. 02, 2025. Available: https://ec.europa.eu/clima/policies/eu-climate-action/fit-for-55_en

[11] Ministero dell’Ambiente e della Sicurezza Energetica (MASE), “Piano Nazionale Integrato per l’Energia e il Clima – PNIEC (aggiornamento 2023),” 2023. Accessed: Oct. 02, 2025. Available: https://www.mase.gov.it

[12] European Commission, “The European Green Dea,” Brussels, 2019. Accessed: Oct. 16, 2025. Available: https://eur-lex.europa.eu/legal-content/EN/TXT/?uri=CELEX:52019DC0640

[13] European Commission, “‘Fit for 55’: delivering the EU’s 2030 Climate Target on the way to climate neutrality,” Brussels, 2021. Accessed: Oct. 16, 2025. Available: https://eur-lex.europa.eu/legal-content/EN/TXT/?uri=CELEX:52021DC0550

[14] Ministero dell’Ambiente e della Sicurezza Energetica (MASE), “Piano Nazionale Integrato per l’Energia e il Clima – Proposta di aggiornamento 2023,” Roma, 2023. Accessed: Oct. 16, 2025. Available: https://www.mase.gov.it/pagina/pniec

[15] Presidenza del Consiglio dei Ministri, “Piano Nazionale di Ripresa e Resilienza – Revisione 2023,” Roma, 2023. Accessed: Oct. 16, 2025. Available: https://www.governo.it/it/pnrr

[16] F. Bariloche, “SCIENCE AND ACADEMIA AEE-Institute for Sustainable Technologies (AEE-INTEC) Council on Energy, Environment and Water (CEEW).”

[17] I. Energy Agency, “World Energy Outlook Special Report Batteries and Secure Energy Transitions.” Available: www.iea.org

[18] K. Detka and K. Górecki, “Selected Technologies of Electrochemical Energy Storage—A Review,” Jul. 01, 2023, *Multidisciplinary Digital Publishing Institute (MDPI)*. doi: 10.3390/en16135034.

[19] J. Mitali, S. Dhinakaran, and A. A. Mohamad, “Energy storage systems: a review,” Sep. 01, 2022, *B.V.* doi: 10.1016/j.enss.2022.07.002.

[20] M. R. Chakraborty, S. Dawn, P. K. Saha, J. B. Basu, and T. S. Ustun, “A Comparative Review on Energy Storage Systems and Their Application in Deregulated Systems,” Sep. 01, 2022, *MDPI*. doi: 10.3390/batteries8090124.

[21] M. S. Guney and Y. Tepe, “Classification and assessment of energy storage systems,” 2017, *Elsevier Ltd*. doi: 10.1016/j.rser.2016.11.102.

[22] G. L. Soloveichik, “Flow Batteries: Current Status and Trends,” Oct. 28, 2015, *American Chemical Society*. doi: 10.1021/cr500720t.

[23] J. Noack, N. Roznyatovskaya, T. Herr, and P. Fischer, “The chemistry of Redox Flow Batteries,” *Angewandte Chemie*, vol. 127, no. 34, pp. 9912–9947, Aug. 2015, doi: 10.1002/ange.201410823.

[24] A. Z. Weber, M. M. Mench, J. P. Meyers, P. N. Ross, J. T. Gostick, and Q. Liu, “Redox flow batteries: A review,” 2011, *Kluwer Academic Publishers*. doi: 10.1007/s10800-011-0348-2.

[25] M. Skyllas-Kazacos, M. H. Chakrabarti, S. A. Hajimolana, F. S. Mjalli, and M. Saleem, “Progress in Flow Battery Research and Development,” *J. Electrochem. Soc.*, vol. 158, no. 8, p. R55, 2011, doi: 10.1149/1.3599565.

[26] B. R. Chalamala, T. Soundappan, G. R. Fisher, M. R. Anstey, V. V. Viswanathan, and M. L. Perry, “Redox flow batteries: An engineering perspective,” *Proceedings of the IEEE*, vol. 102, no. 6, pp. 976–999, 2014, doi: 10.1109/JPROC.2014.2320317.

[27] A. G. Olabi *et al.*, “Redox Flow Batteries: Recent Development in Main Components, Emerging Technologies, Diagnostic Techniques, Large-Scale Applications, and Challenges and Barriers,” Aug. 01, 2023, *Multidisciplinary Digital Publishing Institute (MDPI)*. doi: 10.3390/batteries9080409.

[28] Jing Sun, Zixiao Guo, Lyuming Pan, Xinzhuang Fan, Lei Wei, and Tianshou Zhao, “Redox flow batteries and their stack-scale flow fields,” *Carbon Neutrality*, vol. 2, no. 1, p. 30, Dec. 2023, doi: 10.1007/s43979-023-00072-6.

[29] M. Rychcik and M. Skyllas-Kazacos, “Characteristics of a new all-vanadium redox flow battery,” *J. Power Sources.*, vol. 22, pp. 59–67, 1988, doi: https://doi.org/10.1016/0378-7753(88)80005-3.

[30] C. Yin, S. Guo, H. Fang, J. Liu, Y. Li, and H. Tang, “Numerical and experimental studies of stack shunt current for vanadium redox flow battery,” *Appl. Energy*, vol. 151, pp. 237–248, Aug. 2015, doi: 10.1016/j.apenergy.2015.04.080.

[31] K. Lourenssen, J. Williams, F. Ahmadpour, R. Clemmer, and S. Tasnim, “Vanadium redox flow batteries: A comprehensive review,” Oct. 01, 2019, *Elsevier Ltd*. doi: 10.1016/j.est.2019.100844.

[32] Q. Ye, J. Hu, P. Cheng, and Z. Ma, “Design trade-offs among shunt current, pumping loss and compactness in the piping system of a multi-stack vanadium flow battery,” *J. Power Sources*, vol. 296, pp. 352–364, Aug. 2015, doi: 10.1016/j.jpowsour.2015.06.138.

[33] M. T. Tsehaye, R. A. Tufa, R. Berhane, F. Deboli, K. A. Gebru, and S. Velizarov, “Modified Membranes for Redox Flow Batteries—A Review,” Sep. 01, 2023, *Multidisciplinary Digital Publishing Institute (MDPI)*. doi: 10.3390/membranes13090777.

[34] L. Pan *et al.*, “Innovations in stack design and optimization strategies for redox flow batteries in large-scale energy storage,” Aug. 26, 2024, *Innovation Press*. doi: 10.59717/j.xinn-energy.2024.100040.

[35] P. Alotto, M. Guarnieri, and F. Moro, “Redox flow batteries for the storage of renewable energy: A review,” 2014, *Elsevier Ltd*. doi: 10.1016/j.rser.2013.08.001.

[36] X. Luo, J. Wang, M. Dooner, and J. Clarke, “Overview of current development in electrical energy storage technologies and the application potential in power system operation,” *Appl. Energy*, vol. 137, pp. 511–536, 2015, doi: 10.1016/j.apenergy.2014.09.081.

[37] M. Shoaib *et al.*, “Advances in Redox Flow Batteries – A Comprehensive Review on Inorganic and Organic Electrolytes and Engineering Perspectives,” Aug. 23, 2024, *John Wiley and Sons Inc*. doi: 10.1002/aenm.202400721.

[38] B. Li and J. Liu, “Progress and directions in low-cost redox-flow batteries for large-scale energy storage,” Jan. 01, 2017, *Oxford University Press*. doi: 10.1093/nsr/nww098.

[39] M. Skyllas-Kazacos, M. H. Chakrabarti, S. A. Hajimolana, F. S. Mjalli, and M. Saleem, “Progress in Flow Battery Research and Development,” *J. Electrochem. Soc.*, vol. 158, no. 8, p. R55, 2011, doi: 10.1149/1.3599565.

[40] M. Skyllas-Kazacos and F. Grossmith, “Efficient Vanadium Redox Flow Cell,” *J. Electrochem. Soc.*, vol. 134, no. 12, pp. 2950–2953, Dec. 1987, doi: 10.1149/1.2100321.

[41] B. Li and J. Liu, “Progress and directions in low-cost redox-flow batteries for large-scale energy storage,” Jan. 01, 2017, *Oxford University Press*. doi: 10.1093/nsr/nww098.

[42] J. Winsberg, T. Hagemann, T. Janoschka, M. D. Hager, and U. S. Schubert, “Redox Flow Battery: From Metals To Organic Redox-Active Materials,” *Angewandte Chemie*, vol. 129, no. 3, pp. 702–729, Jan. 2017, doi: 10.1002/ange.201604925.

[43] K. Gong, Q. Fang, S. Gu, S. F. Y. Li, and Y. Yan, "Nonaqueous redox-flow batteries: Organic solvents, supporting electrolytes, and redox pairs," Dec. 01, 2015, *Royal Society of Chemistry*. doi: 10.1039/c5ee02341f.

[44] Z. Li, T. Jiang, M. Ali, C. Wu, and W. Chen, "Recent Progress in Organic Species for Redox Flow Batteries," Sep. 01, 2022, *Elsevier B.V.* doi: 10.1016/j.ensm.2022.04.038.

[45] M. Park, J. Ryu, W. Wang, and J. Cho, "Material design and engineering of next-generation flow-battery technologies," Nov. 08, 2016, *Nature Publishing Group*. doi: 10.1038/natrevmats.2016.80.

[46] E. B. Agyekum *et al.*, "A state-of-the-art review of electrolyte systems for vanadium redox flow battery – status of the technology, and future research directions," *Energy Conversion and Management: X*, vol. 27, p. 101180, Jul. 2025, doi: 10.1016/j.ecmx.2025.101180.

[47] W. Wang, Q. Luo, B. Li, X. Wei, L. Li, and Z. Yang, "Recent progress in redox flow battery research and development," *Adv. Funct. Mater.*, vol. 23, no. 8, pp. 970–986, Feb. 2013, doi: 10.1002/adfm.201200694.

[48] C. Zhang *et al.*, "Progress and prospects of next-generation redox flow batteries," Nov. 01, 2018, *Elsevier B.V.* doi: 10.1016/j.ensm.2018.06.008.

[49] A. J. . Bard and L. R. . Faulkner, *Electrochemical methods : fundamentals and applications*. John Wiley & Sons, Inc., 2001.

[50] N. Elgrishi, K. J. Rountree, B. D. McCarthy, E. S. Rountree, T. T. Eisenhart, and J. L. Dempsey, "A Practical Beginner's Guide to Cyclic Voltammetry," *J. Chem. Educ.*, vol. 95, no. 2, pp. 197–206, Feb. 2018, doi: 10.1021/acs.jchemed.7b00361.

[51] C. M. A. . Brett and A. M. Oliveira. Brett, *Electrochemistry : principles, methods, and applications*. Oxford University Press, 1993.

[52] Zanello P., "Inorganic Electrochemistry Theory, Practice and Application," Cambridge, 2003. doi: 10.1039/9781847551209.

[53] P. T. Kissinger and W. R. Heineman, "Cyclic Voltammetry," *J. Chem. Educ.*, vol. 60, pp. 702–706, 1983, doi: 10.1021/ed060p702.

[54] J. Heinze, "Cyclic Voltammetry—'Electrochemical Spectroscopy'. New Analytical Methods (25)," 1984. doi: 10.1002/anie.198408313.

[55] K. E. T.-A. John Newman, *Electrochemical Systems*, 3rd edition. Hoboken, New Jersey, 2004.

[56] D. D. MacDonald, "Reflections on the history of electrochemical impedance spectroscopy," in *Electrochimica Acta*, Jan. 2006, pp. 1376–1388. doi: 10.1016/j.electacta.2005.02.107.

[57] A. C. Lazanas and M. I. Prodromidis, "Electrochemical Impedance Spectroscopy─A Tutorial," Jun. 21, 2023, *American Chemical Society*. doi: 10.1021/acsmeasuresciau.2c00070.

[58] J. Abu Qahouq, "An Electrochemical Impedance Spectrum-Based State of Health Differential Indicator with Reduced Sensitivity to Measurement Errors for Lithium–Ion Batteries," *Batteries*, vol. 10, no. 10, Oct. 2024, doi: 10.3390/batteries10100368.

[59] E. M. J. R. Barsoukov, *Impedance Spectroscopy: Theory, Experiment, and Applications*. Wiley-Interscience, 2005.

[60] M. E. ; T. B. Orazem, *Electrochemical Impedance Spectroscopy*. Wiley, 2008.

[61] Zebo Huang, Kaizheng Li, Jianjun Wu, Zhenyu Xiao, and Yilin Liu, "Performance evaluation of vanadium redox flow battery under asymmetric electrolyte flow rate conditions," *J. Power Sources*, vol. 605, p. 233128, 2025.

[62] A. Ashok and A. Kumar, "A comprehensive review of metal-based redox flow batteries: progress and perspectives," 2024, *Taylor and Francis Ltd.* doi: 10.1080/17518253.2024.2302834.

[63] David. Linden and T. B. . Reddy, *Handbook of batteries*, 3rd edition. New York: McGraw-Hill, 2002.

[64] F. Yu *et al.*, "Performance Evaluation of a Scaled-Up Membraneless Organic-Based Hybrid Flow Battery," *Batteries*, vol. 9, no. 7, Jul. 2023, doi: 10.3390/batteries9070336.

[65] H. Chen, G. Cong, and Y. C. Lu, "Recent progress in organic redox flow batteries: Active materials, electrolytes and membranes," Sep. 01, 2018, *Elsevier B.V.* doi: 10.1016/j.jechem.2018.02.009.

[66] D. S. Aaron *et al.*, "Dramatic performance gains in vanadium redox flow batteries through modified cell architecture," *J. Power Sources*, vol. 206, pp. 450–453, May 2012, doi: 10.1016/j.jpowsour.2011.12.026.

[67] A. G. Olabi *et al.*, "Redox Flow Batteries: Recent Development in Main Components, Emerging Technologies, Diagnostic Techniques, Large-Scale Applications, and Challenges and Barriers," Aug. 01, 2023, *Multidisciplinary Digital Publishing Institute (MDPI)*. doi: 10.3390/batteries9080409.

[68] Goldstein, J. I. Newbury, D. E. Joy, D. C. Lyman, and P. C. E. Echlin, "Scanning Electron Microscopy and X-Ray Microanalysis," 2018.

[69] L. Reimer, *Scanning Electron Microscopy: Physics of Image Formation and Microanalysis*, 2th edition. Berlin: Springer-Verlag, 1998. doi: 10.1007/978-3-662-03783-5.

[70] L. Qiao, M. Fang, S. Liu, H. Zhang, and X. Ma, "New-generation iron–titanium flow batteries with low cost and ultrahigh stability for stationary energy storage," *Chemical Engineering Journal*, vol. 434, Apr. 2022, doi: 10.1016/j.cej.2022.134588.

[71] L. Qiao, M. Fang, S. Liu, H. Zhang, and X. Ma, "New-generation iron–titanium flow batteries with low cost and ultrahigh stability for stationary energy storage," *Chemical Engineering Journal*, vol. 434, Apr. 2022, doi: 10.1016/j.cej.2022.134588.

[72] B. Li *et al.*, "Bismuth nanoparticle decorating graphite felt as a high-performance electrode for an all-vanadium redox flow battery," *Nano Lett.*, vol. 13, no. 3, pp. 1330–1335, Mar. 2013, doi: 10.1021/nl400223v.

[73] Beckhoff B., Kanngieber B., Langhoff N., Wedell R., and Wolff H., *Handbook of Practical X-Ray Fluorescence Analysis*. Berlin: Springer, 2006. doi: 10.1007/978-3-540-36719-6.

[74] P. Wobrauschek, "Total reflection x-ray fluorescence analysis - A review," *X-Ray Spectrometry*, vol. 36, no. 5, pp. 289–300, 2007, doi: 10.1002/xrs.985.

[75] D. A. Long, *The Raman Effect*. Wiley, 2002. doi: 10.1002/0470845767.

[76] E. Smith and G. Dent, *Modern Raman Spectroscopy – A Practical Approach*, 1st edition. Wiley, 2005. doi: 10.1002/0470011831.

[77] B. Pettinger, P. Schambach, C. J. Villagómez, and N. Scott, "Tip-enhanced raman spectroscopy: Near-fields acting on a few molecules," 2012, *Annual Reviews Inc.* doi: 10.1146/annurev-physchem-032511-143807.

[78] W. Wang, Y. Liu, T. Xue, J. Li, D. Chen, and T. Qi, "Mechanism and kinetics of titanium hydrolysis in concentrated titanyl sulfate solution based on infrared and Raman spectra," *Chem. Eng. Sci.*, vol. 134, pp. 196–204, Sep. 2015, doi: 10.1016/j.ces.2015.05.006.

[79] P. Sipos, L. Bolden, G. Hefter, and P. M. May, "Raman Spectroscopic Study of Ion Pairing of Alkali Metal Ions with Carbonate and Sulfate in Aqueous Solutions," *Aust. J. Chem.*, vol. 53, no. 10, pp. 887–890, Apr. 2001, doi: 10.1071/CH00126.

[80] S. I. U. Ahmed, M. Shahid, and S. Sankarasubramanian, "Aqueous titanium redox flow batteries—State-of-the-art and future potential," Oct. 10, 2022, *Frontiers Media S.A.* doi: 10.3389/fenrg.2022.1021201.

[81] Y. A. Lisitsyn, N. V. Busygina, Y. I. Zyavkina, and V. G. Shtyrlin, "Electrochemical amination. Ti(IV)/Ti(III) mediator system in aqueous solutions of sulfuric acid," *Russian Journal of Electrochemistry*, vol. 46, no. 5, pp. 512–523, May 2010, doi: 10.1134/S1023193510050046.

[82] I. Cservenyak, G. H. Kelsall, and W. Wang, "Reduction of Ti(IV) species in aqueous sulfuric and hydrochloric acids. I. Titanium speciation," *Electrochim. Acta*, vol. 41, no. 4, pp. 563–572, 1996, doi: 10.1016/0013-4686(95)00343-6.

[83] R. J. H. Clark, D. C. Bradley, and P. Thornton, *The Chemistry of Titanium, Zirconium and Hafnium*. Oxford: Pergamon, 2013.

[84] F. Baillon, É. Provost, W. Fürst, and E. Provost, "Study of titanium(IV) speciation in sulphuric acid solutions by FT-Raman spectrometry," *J. Mol. Liq.*, vol. 143, no. 1, pp. 8–12, 2008, doi: 10.1016/j.molliq.2008.04.010ï.

[85] Y. A. Lisitsyn and N. V. Busugina, "Electrochemical behavior of Ti(IV)/Ti(III) redox couple on dropping mercury electrode in sulfuric acid aqueous and aqueous-organic media," *Russ. J. Gen. Chem.*, vol. 79, no. 7, pp. 1413–1420, Jul. 2009, doi: 10.1134/S1070363209070019.

[86] M. Antoni, "Inorganic Synthesis Methods for Nanostructured Capacitors," Darmstadt, 2015.

[87] I. Cservenyak, G. H. Kelsall, and W. Wang, "Reduction of Ti(IV) species in aqueous sulfuric and hydrochloric acids. I. Titanium speciation," *Electrochim. Acta*, vol. 41, no. 4, pp. 563–572, 1996, doi: 10.1016/0013-4686(95)00343-6.

[88] E. Bishop and P.H. Hitchcock, “Mass and charge transfer kinetics and coulometric current efficiencies. Part IX. An examination of the titanium(IV)–titanium(III) system and the effects of ultratrace impurities in sulphuric acid,” *Analyst*, vol. 98, pp. 563–572, 1973.

[89] S. I. U. Ahmed and S. Sankarasubramanian, “Low pH Titanium Electrochemistry in the Presence of Sulfuric Acid and its Implications for Redox Flow Battery Applications,” *J. Electrochem. Soc.*, vol. 171, no. 6, p. 060538, Jun. 2024, doi: 10.1149/1945-7111/ad5975.

[90] D. Lundberg and I. Persson, “Structure of a Hydrated Sulfonatotitanyl(IV) Complex in Aqueous Solution and the Dimethylsulfoxide Solvated Titanyl(IV) Ion in Solution and Solid State,” *J. Solution Chem.*, vol. 46, no. 2, pp. 476–487, Feb. 2017, doi: 10.1007/s10953-017-0581-3.

[91] C. He *et al.*, “Aqueous iron-based redox flow batteries for large-scale energy storage,” Jul. 01, 2025, *Oxford University Press*. doi: 10.1093/nsr/nwaf218.

[92] A. Okazawa, T. Kakuchi, K. Kawai, and M. Okubo, “Iron-based catholytes for aqueous redox-flow batteries,” Nov. 01, 2023, *American Institute of Physics Inc.* doi: 10.1063/5.0160078.

[93] K. Gong *et al.*, “All-Soluble All-Iron Aqueous Redox-Flow Battery,” *ACS Energy Lett.*, vol. 1, no. 1, pp. 89–93, Jul. 2016, doi: 10.1021/acsenergylett.6b00049.

[94] H. Zhang and C. Sun, “Cost-effective iron-based aqueous redox flow batteries for large-scale energy storage application: A review,” May 01, 2021, *Elsevier B.V.* doi: 10.1016/j.jpowsour.2020.229445.

[95] Shuangbin Zhang *et al.*, “All-soluble all-iron aqueous redox flow batteries: Towards sustainable energy storage,” *Energy Storage Mater.*, vol. 75, Feb. 2025, doi: 10.1016/j.ensm.2024.104004.

[96] H. C. Chi, S. K. Sharma, and D. W. Muenow, “The hydrates and deuterates of ferrous sulfate (FeSO4): A Raman spectroscopic study,” *Journal of Raman Spectroscopy*, vol. 38, no. 1, pp. 87–99, 2007, doi: 10.1002/jrs.1623.

[97] S.K. Sharma, C. H. Chio, and D.W. Muenow, “Raman spectroscopic investigation of ferrous sulfate hydrates,” in *Lunar and Planetary Science Conference XXXVII*, Houston: Lunar and Planetary Institute, 2006, p. Abstract #1078.

[98] L. K. Noda, F. R. Sensato, and N. S. Gonçalves, “Titanyl sulphate, an inorganic polymer: Structural studies and vibrational assignment,” *Quim. Nova*, vol. 42, no. 9, pp. 1112–1115, 2019, doi: 10.21577/0100-4042.20170427.

[99] W. Rudolph, “Structure and dissociation of the hydrogen sulphate ion in aqueous solution over a broad temperature range: A Raman study,” *Zeitschrift fur Physikalische Chemie*, vol. 194, no. 1, pp. 73–95, 1996, doi: 10.1524/zpch.1996.194.part_1.073.

[100] J. Sun, Z. Guo, L. Pan, X. Fan, L. Wei, and T. Zhao, “Redox flow batteries and their stack-scale flow fields,” Dec. 01, 2023. doi: 10.1007/s43979-023-00072-6.

[101] F. Xing, H. Zhang, and X. Ma, “Shunt current loss of the vanadium redox flow battery,” *J. Power Sources*, vol. 196, no. 24, pp. 10753–10757, Dec. 2011, doi: 10.1016/j.jpowsour.2011.08.033.

[102] A. M. Pezeshki, J. T. Clement, G. M. Veith, T. A. Zawodzinski, and M. M. Mench, “High performance electrodes in vanadium redox flow batteries through oxygen-enriched thermal activation,” *J. Power Sources*, vol. 294, pp. 333–338, Jul. 2015, doi: 10.1016/j.jpowsour.2015.05.118.

[103] P. Leung, X. Li, C. Ponce De León, L. Berlouis, C. T. J. Low, and F. C. Walsh, “Progress in redox flow batteries, remaining challenges and their applications in energy storage,” *RSC Adv.*, vol. 2, no. 27, pp. 10125–10156, Nov. 2012, doi: 10.1039/c2ra21342g.

[104] G. Y. Linsen Zhang, “Recent developments in materials and chemistries for redox flow batteries,” *ACS Mater. Lett.*, vol. 5, no. 11, pp. 3007–3009, Nov. 2023, doi: 10.1021/acsmaterialslett.3c00685.

[105] B. Jiang *et al.*, “Insights into the Impact of the Nafion Membrane Pretreatment Process on Vanadium Flow Battery Performance,” *ACS Appl. Mater. Interfaces*, vol. 8, no. 19, pp. 12228–12238, May 2016, doi: 10.1021/acsami.6b03529.

[106] Q. W. S. X. Z. S. Yang Yang, “Research progress on optimized membranes for vanadium redox flow batteries,” *Inorg. Chem. Front.*, vol. 11, no. 14, pp. 4049–4079, May 2024, doi: 10.1039/d4qi00520a.

[107] J. Zhang *et al.*, “Tailoring porous structure in non-ionic polymer membranes using multiple templates for low-cost iron-lead single-flow batteries,” *Energy Materials*, vol. 4, no. 4, May 2024, doi: 10.20517/energymater.2023.113.

[108] Mike L. Perry, James D. Saraidaridis, and Robert M. Darling, “Crossover mitigation strategies for redox-flow batteries,” *Curr. Opin. Electrochem.*, vol. 21, pp. 311–318, Jun. 2020, doi: 10.1016/j.coelec.2020.05.006.

[109] T. Y. George, E. M. Fell, K. Lee, M. S. Emanuel, and M. J. Aziz, “Influence of crossover on capacity fade of symmetric redox flow cells,” *Energy Advances*, vol. 3, no. 12, pp. 2910–2921, Oct. 2024, doi: 10.1039/d4ya00407h.

[110] Á. Cunha, J. Martins, N. Rodrigues, and F. P. Brito, “Vanadium redox flow batteries: A technology review,” Jun. 10, 2015, *John Wiley and Sons Ltd*. doi: 10.1002/er.3260.

[111] Xiaoliang Wei *et al.*, “Materials and Systems for Organic Redox Flow Batteries: Status and Challenges,” *ACS Energy Lett.*, vol. 2, no. 9, pp. 2187–2204, 2017, doi: 10.1021/acsenergylett.7b00650.

[112] I. Iwakiri, T. Antunes, H. Almeida, J. P. Sousa, R. B. Figueira, and A. Mendes, “Redox flow batteries: Materials, design and prospects,” *Energies (Basel).*, vol. 14, no. 18, Sep. 2021, doi: 10.3390/en14185643.

[113] E. S. Beh, D. De Porcellinis, R. L. Gracia, K. T. Xia, R. G. Gordon, and M. J. Aziz, “A neutral pH aqueous organic- organometallic redox flow battery with extremely high capacity retention,” *ACS Energy Lett.*, vol. 2, no. 3, pp. 639–644, Mar. 2017, doi: 10.1021/acsenergylett.7b00019.

[114] P. Leung *et al.*, “Recent developments in organic redox flow batteries: A critical review,” 2017. doi: 10.1016/j.jpowsour.2017.05.057.

[115] Y. Wang, A. Mu, and W. Wang, “Analysis of Capacity Decay and Optimization of Vanadium Redox Flow Battery Based on Operating Conditions,” *J. Electrochem. Soc.*, vol. 172, no. 6, p. 060509, Jun. 2025, doi: 10.1149/1945-7111/adde1a.

[116] H. Zhang, W. Lu, and X. Li, “Progress and Perspectives of Flow Battery Technologies,” Sep. 01, 2019. doi: 10.1007/s41918-019-00047-1.

[117] B. Li *et al.*, “Bismuth nanoparticle decorating graphite felt as a high-performance electrode for an all-vanadium redox flow battery,” *Nano Lett.*, vol. 13, no. 3, pp. 1330–1335, Mar. 2013, doi: 10.1021/nl400223v.

[118] H. Zhang, W. Lu, and X. Li, “Progress and Perspectives of Flow Battery Technologies,” Sep. 01, 2019, *Springer Science and Business Media B.V.* doi: 10.1007/s41918-019-00047-1.

[119] P. Leung, X. Li, C. Ponce De León, L. Berlouis, C. T. J. Low, and F. C. Walsh, “Progress in redox flow batteries, remaining challenges and their applications in energy storage,” *RSC Adv.*, vol. 2, no. 27, pp. 10125–10156, Nov. 2012, doi: 10.1039/c2ra21342g.

[120] J. Zhang *et al.*, “Tailoring porous structure in non-ionic polymer membranes using multiple templates for low-cost iron-lead single-flow batteries,” *Energy Materials*, vol. 4, no. 4, May 2024, doi: 10.20517/energymater.2023.113.

[121] X.-Z. Yuan *et al.*, “A review of all-vanadium redox flow battery durability: degradation mechanisms and mitigation strategies,” *Fuel Cells*, vol. 18, pp. 546–567, 2018, doi: 10.1002/fuce.201800027.

[122] F. Lulay, C. Weidlich, M. Valtiner, and C. M. Pichler, “Membrane degradation in redox flow batteries,” *Green Chem. Lett. Rev.*, vol. 16, no. 1, pp. 227–229, 2023, doi: 10.1080/17518253.2023.2274529.

[123] S. Chen, C. Sun, H. Zhang, H. Yu, and W. Wang, “Electrochemical Deposition of Bismuth on Graphite Felt Electrodes: Influence on Negative Half-Cell Reactions in Vanadium Redox Flow Batteries,” *Applied Sciences (Switzerland)*, vol. 14, no. 8, Apr. 2024, doi: 10.3390/app14083316.

[124] Y. Wu and R. Holze, “Electrocatalysis at electrodes for vanadium redox flow batteries,” *Batteries*, vol. 4, no. 3, 2018, doi: 10.3390/batteries4030038.

[125] J. Jiang, Y. Li, J. Liu, X. Huang, C. Yuan, and X. W. Lou, “Recent advances in metal oxide-based electrode architecture design for electrochemical energy storage,” Oct. 02, 2012. doi: 10.1002/adma.201202146.

[126] S. Yoon, J. H. Jang, B. H. Ka, and S. M. Oh, “Complex capacitance analysis on rate capability of electric-double layer capacitor (EDLC) electrodes of different thickness,” *Electrochim. Acta*, vol. 50, no. 11, pp. 2255–2262, Apr. 2005, doi: 10.1016/j.electacta.2004.10.009.

[127] E. J. Latchem, T. Kress, M. A. de h-Óra, A. Wang, Q. Song, and A. C. Forse, "Revealing and Mitigating Crossover-Driven Side Reactions in Ferrocyanide-Based Redox Flow Batteries," *ACS Electrochemistry*, vol. 1, no. 10, pp. 2071–2084, Oct. 2025, doi: 10.1021/acselectrochem.5c00178.

[128] E. S. Beh, D. De Porcellinis, R. L. Gracia, K. T. Xia, R. G. Gordon, and M. J. Aziz, "A neutral pH aqueous organic- organometallic redox flow battery with extremely high capacity retention," *ACS Energy Lett.*, vol. 2, no. 3, pp. 639–644, Mar. 2017, doi: 10.1021/acsenergylett.7b00019.

[129] J. Schneider *et al.*, "Degradation phenomena of bismuth-modified felt electrodes in vrfb studied by electrochemical impedance spectroscopy," *Batteries*, vol. 5, no. 1, Mar. 2019, doi: 10.3390/batteries5010016.

[130] Z. Yang, Y. Wei, Y. Zeng, and Y. Yuan, "Effects of in-situ bismuth catalyst electrodeposition on performance of vanadium redox flow batteries," *J. Power Sources*, vol. 506, Sep. 2021, doi: 10.1016/j.jpowsour.2021.230238.

[131] C. E. ; S. A. G. Housecroft, *Inorganic Chemistry*, 5th ed. Pearson Education Limited, 2015.

[132] R. J. H. . Clark, D. C. . Bradley, and P. . Thornton, *The Chemistry of Titanium, Zirconium and Hafnium: Pergamon Texts in Inorganic Chemistry*. Elsevier Ltd., 2013.

[133] Robert H. Crabtree, *The Organometallic Chemistry of the Transition Metals*, Fourth Edition. Hoboken, NJ, 2005.

[134] A. E. ; Martell and R. M. Smith, *Critical Stability Constants*. New York: Plenum Press, 1977.

[135] P. W. ; Atkins, T. L. ; Overton, J. P. ; Rourke, M. T. ; A. Weller, and F. A. rmstrong, *Shriver & Atkins' Inorganic Chemistry*, 5th ed. Oxford: Oxford University Press, 2010.

[136] Arthur E. Martell and Robert J. Motekaitis, *Determination and Use of Stability Constants*. New York: VCH Verlagsgesellschaft mbH, 1988.

[137] R. G. Pearson, "Hard and Soft Acids and Bases," *J. Am. Chem. Soc.*, vol. 85, no. 22, pp. 3533–3539, Nov. 1963, doi: 10.1021/ja00905a001.

[138] V. V Pavlishchuk and A. W. Addison, "Conversion constants for redox potentials measured versus different reference electrodes in acetonitrile solutions at 25°C," *Inorganica Chim. Acta*, vol. 298, no. 1, pp. 97–102, Jan. 2000, doi: 10.1016/S0020-1693(99)00407-7.

[139] C. F. ; Baes and R. E. Mesmer, *The Hydrolysis of Cations*. New York: Wiley–Interscience, 1976.

[140] R. G. Pearson, "Hard and Soft Acids and Bases," *J. Am. Chem. Soc.*, vol. 85, no. 22, pp. 3533–3539, 1963, doi: 10.1021/ja00905a001.

[141] C. E. ; Housecroft and A. G. Sharpe, *Inorganic Chemistry*, 5th ed. Oxford: Oxford University Press, 2101.

[142] D. W. Margerum, G. R. Cayley, D. C. Weatherburn, G. K. Pagenkopf, and ., "Kinetics and Mechanisms of Complex Formation and Ligand Substitution Reactions of Metal Ions in Aqueous Solution," *Coord. Chem. Rev.*, vol. 25, pp. 1–50, 1978, doi: 10.1016/S0010-8545(00)80336-0.

[143] X. Han, Y. Lu, and Y. Wang, “Viscosity and Conductivity of Aqueous Solutions of Metal–EDTA Complexes,” *J. Solution Chem.*, vol. 45, pp. 1621–1632, 2016, doi: 10.1007/s10953-016-0536-6.

[144] T. Miyagawa and T. Sakagawa, “Ti^{3+}–EDTA Chelate Developer and Its Developing Action and Redox Potential,” *Bulletin of the Society of Scientific Photography of Japan*, no. 13, pp. 22–27, 1963.

[145] F. J. Kristine, R. E. Shepherd, and S. Siddiqui, “Formation of $Ti(O_2)(edta)^{2-}$ by Two Routes: Peroxo Displacement of Oxo in $TiO(edta)^{2-}$ and Reduction of a Superoxo Transient, $Ti(O_2)(edta)^{-}$,” vol. 20, pp. 2571–2579, 1981, doi: 10.1021/ic50223a028.

[146] J. P. Fackler, F. J. Kristine, A. M. Mazany, T. J. Moyer, and R. E. Shepherd, “The Absence of a Titanyl Oxygen in the Ti(IV)-edta4− Complex: [Ti(edta)(H2O)],” *Inorg. Chem.*, vol. 24, pp. 1857–1860, 1985, doi: 10.1021/ic00205a014.

[147] H. W. Berger and B. C. Cadoff, “Polarographic Analysis of Titanium (IV)-EDTA Complex: Application to Paint Pigments,” vol. 69C, no. 1, pp. 1–7, 1965, doi: 10.6028/jres.069C.001.

[148] C. A. R. M. S. C. A. F. S. and M. V. C. Luciana S. Guinesi, “TITANIUM(IV)–EDTA COMPLEX Kinetics of thermal decomposition by non-isothermal procedures,” *J. Therm. Anal. Calorim.*, vol. 85, no. 2, pp. 301–307, 2006, doi: 10.1007/s10973-005-7354-0.

[149] W. Duan, H. Oota, and K. Sawada, “Stability and structure of ethylenedinitrilopoly(methylphosphonate) complexes of the alkaline-earth metal ions in aqueous solution,” *Journal of the Chemical Society, Dalton Transactions*, pp. 3075–3080, 1999, doi: 10.1039/A903327H.

[150] I. Andrés-Tomé, J. Fyson, F. Baiao Dias, A. P. Monkman, G. Iacobellis, and P. Coppo, “Copper(i) complexes with bipyridyl and phosphine ligands: A systematic study,” *Dalton Transactions*, vol. 41, no. 28, pp. 8669–8674, Jul. 2012, doi: 10.1039/c2dt30698k.

[151] J. Hannonen, A. Kiesilä, U. Mattinen, P. M. Pihko, and P. Peljo, “Electrochemical characterization of redox activity and stability of various tris(2,2‘-bipyridine) derived complexes of iron(II) in aqueous solutions,” *Journal of Electroanalytical Chemistry*, vol. 950, Dec. 2023, doi: 10.1016/j.jelechem.2023.117847.

[152] L. L. Merritt and E. Schroeder, “The crystal structure of 2,2’-bipyridine,” *Acta Crystallogr.*, vol. 9, no. 10, pp. 801–804, Oct. 1956, doi: 10.1107/S0365110X56002175.

[153] W. Kaim, B. Schwederski, and A. Klein, *Bioinorganic Chemistry*, 3rd ed. Weinheim: Wiley-VCH, 2013.

[154] A. Barbieri, G. Accorsi, and N. Armaroli, “Luminescent complexes beyond the platinum group: the d10 avenue,” *Chemical Communications*, no. 19, p. 2185, 2008, doi: 10.1039/b716650h.

[155] G. W. A. Fowles and T. E. Lester, “Bipyridyl complexes of tervalent titanium,” *Journal of the Chemical Society A: Inorganic, Physical, Theoretical*, p. 1180, 1968, doi: 10.1039/j19680001180.

[156] Y. Tachibana *et al.*, “Photosensitization of TiO 2 by [Fe II (2,2′-bipyridine-4,4′-dicarboxylic acid) 2 (CN) 2]: Band Selective Electron Injection from Ultra-Short-Lived Excited States,” 1993.

[157] L. L. Merritt and E. Schroeder, “The crystal structure of 2,2’-bipyridine,” *Acta Crystallogr.*, vol. 9, no. 10, pp. 801–804, Oct. 1956, doi: 10.1107/S0365110X56002175.

[158] B. Nowack, “Environmental chemistry of phosphonates,” *Water Res.*, vol. 37, no. 11, pp. 2533–2546, Jun. 2003, doi: 10.1016/S0043-1354(03)00079-4.

[159] L. Mangold, H. Halleux, S. Leclerc, A. Moncomble, G. Cote, and A. Chagnes, “New insights for titanium(iv) speciation in acidic media based on UV-visible and 31 P NMR spectroscopies and molecular modeling,” *RSC Adv.*, vol. 11, no. 43, pp. 27059–27073, 2021, doi: 10.1039/D1RA04284J.

[160] F. J. Kristine, R. E. Shepherd, and S. Siddiqui, “Formation of $Ti(O_2)(edta)^{2-}$ by Two Routes: Peroxo Displacement of Oxo in $TiO(edta)^{2-}$ and Reduction of a Superoxo Transient, $Ti(O_2)(edta)^{-}$,” *Inorg. Chem.*, vol. 20, pp. 2571–2579, 1981, doi: 10.1021/ic50223a028.

[161] K. Furukawa, Y. Takahashi, and H. Sato, “Effect of the formation of EDTA complexes on the diffusion of metal ions in water,” *Geochim. Cosmochim. Acta*, vol. 71, no. 18, pp. 4416–4424, Sep. 2007, doi: 10.1016/j.gca.2007.07.009.

[162] D. T. Sawer and Jean M. McKinnie, “Properties and Infrared Spectra of Ethylenediaminetetraacetic Acid Complexes,” *J. Am. Chem. Soc.*, vol. 82, pp. 4192–4196, 1960.

[163] K. Shimizu, R. Hutcheson, M. D. Engelmann, and I. Francis Cheng, “Cyclic voltammetric and aqueous equilibria model study of the pH dependant iron(II/III)ethylenediamminetetraacetate complex reduction potential,” *Journal of Electroanalytical Chemistry*, vol. 603, no. 1, pp. 44–50, May 2007, doi: 10.1016/j.jelechem.2007.01.027.

[164] G. Visalakshi, S. V Narasimhan, and K. S. Venkateswarlu, “Polarographic determination of Iron (II) and Iron (III) complexes with EDTA,” *Analytlca Chimica Acta*, vol. 212, pp. 335–339, 1988, doi: 10.1016/S0003-2670(00)82662-0.

[165] M.Kolthoff and Clemens Auerbach, “Studies on the System Iron-Ethylenediamine Tetraacetate,” *Journal of the American Chemical Society*, vol. 74, pp. 1452–1456, 1952.

[166] L. G. Sillén and A. E. Martell, *Stability costant of Metal-ion complexes*. London: The Chemical Society, 1964.

[167] I. González, J. G. Ibaáñez, M. A. Cárdenas, and A. Rojas-Hernández, “The electrochemical behavior of the Fe(II)-Fe(III) system in the presence of EDTA at pH 4.3,” *Electrochim. Acta*, vol. 35, no. 9, pp. 1325–1329, 1990, doi: 10.1016/0013-4686(90)85002-5.

[168] O. García de Alvarez and L. Gierst, “The electrochemical behavior of the Fe(III)-Fe(II) system in strongly alkaline aqueous solutions of ethylenediaminetetraacetate ions,” *Journal of Electroanalytical Chemistry*, vol. 100, pp. 819–829, 1979, doi: 10.1016/S0022-0728(79)80064-5.

[169] A. F. Danil De Namor, D. Alfredo, and P. Tanaka, “Thermodynamics of protonation and complexation of EDTA derivatives and metal cations in water,” *Journal of the Chemical Society, Faraday Transactions*, vol. 94, no. 16, pp. 2439–2446, 1998, doi: 10.1039/A803052C.

[170] X. Liu and F. J. Millero, “The solubility of iron hydroxide in sodium chloride solutions,” *Geochim. Cosmochim. Acta*, vol. 63, no. 19–20, pp. 3487–3497, 1999, doi: 10.1016/S0016-7037(99)00270-7.

[171] W. Lee, G. Park, D. Chang, and Y. Kwon, “The effects of temperature and membrane thickness on the performance of aqueous alkaline redox flow batteries using napthoquinone and ferrocyanide as redox couple,” *Korean Journal of Chemical Engineering*, vol. 37, no. 12, pp. 2326–2333, Dec. 2020, doi: 10.1007/s11814-020-0669-0.

[172] Z. Huang *et al.*, “Operational temperature effects on redox flow batteries performance: A comprehensive review,” Sep. 30, 2025. doi: 10.1016/j.est.2025.117631.

[173] P. Rao and S. Jayanti, “Physics-Based Electrochemical Model of Vanadium Redox Flow Battery for Low-Temperature Applications,” *Batteries*, vol. 9, no. 7, Jul. 2023, doi: 10.3390/batteries9070374.

[174] Y. D. Raka, R. Bock, H. Karoliussen, Ø. Wilhelmsen, and O. Stokke Burheim, “The influence of concentration and temperature on the membrane resistance of ion exchange membranes and the levelised cost of hydrogen from reverse electrodialysis with ammonium bicarbonate,” *Membranes (Basel).*, vol. 11, no. 2, pp. 1–22, Feb. 2021, doi: 10.3390/membranes11020135.

[175] D. A. Ispas-Gil, E. Zulueta, J. Olarte, J. M. Lopez-Guede, and E. Sanchez-Díez, “Study on the Influence of the Flow Factor on the Performance of Vanadium Redox Flow Batteries,” *JOM*, vol. 77, no. 5, pp. 2932–2942, May 2025, doi: 10.1007/s11837-025-07287-1.

[176] R. M. Darling and M. L. Perry, “The Influence of Electrode and Channel Configurations on Flow Battery Performance,” *J. Electrochem. Soc.*, vol. 161, no. 9, pp. A1381–A1387, 2014, doi: 10.1149/2.0941409jes.

[177] A. Anderegg, *Critical Survey of Stability Constants of EDTA Complexes*. Oxford: International Union of Pure and Applied Chemistry (IUPAC), 1982.

[178] P. Kocot, A. Karocki, and Z. Stasicka, “Photochemistry of the Fe(III)-EDTA complexes. A mechanistic study,” *J. Photochem. Photobiol. A Chem.*, vol. 179, no. 1–2, pp. 176–183, Apr. 2006, doi: 10.1016/j.jphotochem.2005.08.016.

[179] N. Agmon, “The Grotthuss mechanism,” *Chem. Phys. Lett.*, vol. 244, no. 5–6, pp. 456–462, Oct. 1995, doi: 10.1016/0009-2614(95)00905-J.

[180] A. Z. Weber and J. Newman, “Transport in Polymer-Electrolyte Membranes,” *J. Electrochem. Soc.*, vol. 151, no. 2, p. A311, 2004, doi: 10.1149/1.1639157.

[181] K. A. Mauritz and R. B. Moore, “State of Understanding of Nafion,” *Chem. Rev.*, vol. 104, no. 10, pp. 4535–4586, Oct. 2004, doi: 10.1021/cr0207123.

[182] L. S. Guinesi, C. A. Ribeiro, M. S. Crespi, A. F. Santos, and M. V. Capela, “Titanium(IV)–EDTA complex: Kinetics of thermal decomposition by non-isothermal procedures,” *J. Therm. Anal. Calorim.*, vol. 85, no. 2, pp. 301–307, 2006, doi: 10.1007/s10973-005-7354-0.

[183] B. Jiang, L. Wu, L. Yu, X. Qiu, and J. Xi, “A comparative study of Nafion series membranes for vanadium redox flow batteries,” *J. Memb. Sci.*, vol. 510, pp. 18–26, Jul. 2016, doi: 10.1016/j.memsci.2016.03.007.

[184] J. Zhao, J. Wang, L. Sun, Q. Chen, and H. Lu, “Novel low-cost cation exchange membrane containing hydrophilic cross-linked structure for enhanced electrodialysis properties,” *J. Taiwan Inst. Chem. Eng.*, vol. 100, pp. 269–276, Jul. 2019, doi: 10.1016/j.jtice.2019.04.016.

[185] B. Huskinson *et al.*, “A metal-free organic-inorganic aqueous flow battery,” *Nature*, vol. 505, no. 7482, pp. 195–198, 2014, doi: 10.1038/nature12909.